2009

Investigation of the structure and dynamics of the M2 transmembrane peptide of the influenza A virus by solid-state nuclear magnetic resonance

Sarah Diane Cady
Iowa State University

Investigation of the structure and dynamics of the M2 transmembrane peptide of the influenza A virus by solid-state nuclear magnetic resonance

by

Sarah Diane Cady

A dissertation submitted to the graduate faculty

in partial fulfillment of the requirements for the degree of

DOCTOR OF PHILOSOPHY

Major: Physical Chemistry

Program of Study Committee:
Mei Hong, Major Professor
Gaya Amarasinghe
Klaus Schmidt-Rohr
Xueyu Song
Edward Yu

Iowa State University

Ames, Iowa

2009

Table of Contents

Acknowledgement

The last five years have been a journey both professionally and personally – heartbreaking, wonderful, frustrating and fulfilling. There are many people whom I wish to thank for taking an interest in my life and goals as a scientist. First and foremost, my PhD advisor, Dr. Mei Hong, has shaped me as a scientist and pushed me to be excellent every day. It is through her guidance and collaboration that I have been able to conduct the research published in this thesis, be prolific with my publications, present my work at national scientific conferences and feel confident among my scientific peers.

I would also like to thank Dr. Klaus Schmidt-Rohr for many helpful theoretical lessons and discussions, and for occasional collaborations on experiments and calculations. Thank you to my committee members, Dr. Xueyu Song, Dr. Hans Stauffer, Dr. Edward Yu and Dr. Gaya Amarasinghe for offering their opinions and guidance on my scientific course of study. Thanks to Dr. William DeGrado and Jun Wang at The University of Pennsylvania for supplying us with peptide and drug molecules for several projects. There are many members of the Iowa State University Department of Chemistry staff that have been of great assistance throughout my years – Dr. Dave Scott and Dr. Shu Xu in the NMR facility, Bev, Carlene, Renee and Lynette in the Chemistry Office, and Wayne in Chemistry Stores. Thank you for always assisting me with a friendly demeanor and helping me out when I needed something done on a tight deadline.

I am grateful for my fellow group members who have been wonderful collaborators, teachers and travel companions throughout graduate school. I would especially like to thank Dr. Tim Doherty for constant help with stupid questions and for being a great friend over the past five years. Dr. Rajee Mani, Dr. Ming Tang and Wenbin Luo have also been excellent mentors, especially in my first few years at Iowa State. Thanks also to Tatiana Mishanina for a great deal of assistance on work published in this thesis. I am thankful for all of the past and present members of the Hong and Schmidt-Rohr groups who have made coming to work every day an enjoyable experience. I would also like to thank Dr. Jay Shore at South Dakota State for getting me started on this crazy journey into solid-state NMR, and for encouragement along the way.

My time in Ames would certainly have not been as enjoyable without the companionship of many friends outside the lab. To my canoeing friends Bill, Gude, Mike, Melanie and Kelly, I thank you for many relaxing summer Sundays on the river. I would particularly like to thank Kelly for being an understanding friend and companion - thank you for sharing so many good times with me, and for tolerating me through the crazy times. Thanks to Erin, Molly, Marilu and Susie for being good friends both inside and outside the walls of Gilman. To my friends from South Dakota and SDSU - Abby, Sarah, Ladene, Becky, Emily, Matt, Josh and Sami, thank you for keeping me grounded and continuing to share your lives with me. Also thanks to my friends Matt, Ryan and Victoria in the West Coast Office for providing encouragement, computer support, and a place to stay during my post-defense victory tour.

Finally, I would like to thank my parents, Kevin and Gary, and my sister Jennifer for unconditional love and support throughout my life. I would especially like to thank my parents for always allowing me to follow my heart, and their enthusiasm for every new project I undertake. I lovingly dedicate this thesis to them.

Abstract

Solid-state nuclear magnetic resonance (SSNMR) is an important tool for the study of structure, function and dynamics of many chemical and biological systems. By using this technique we are able to study molecules that are insoluble or would not be in their native state when dissolved in solution. This is of particular importance in the study of membrane proteins, whose structures have been difficult to analyze through the use of traditional x-ray crystallography or solution NMR techniques. In this thesis, we have studied the transmembrane segment of the M2 proton channel of the influenza A virus. The M2 proton channel is essential to virus replication, as it acidifies the viral interior allowing for the uncoating and release of viral RNA. The M2 transmembrane peptide (M2TMP) is a 25-residue α-helical transmembrane segment that spontaneously forms tetramers in the lipid bilayer. We are interested in the structure and dynamics of M2TMP, and the interaction of the peptide with an anti-influenza drug, amantadine.

We determine the orientation of M2TMP relative to the bilayer normal in model phosphocholine lipid bilayers such as DLPC and POPC, with and without the amantadine drug. This is achieved through the measurement of ^{15}N-^{1}H dipolar coupling and ^{15}N chemical shift anistropy, which are directly related to tensor orientation for a uniaxially rotationally diffusing molecule. From this information we show that the orientation of M2TMP is dependent on lipid bilayer thickness. We also observe that the addition of amantadine affects the orientation of the peptide. We have measured the orientation of both singly and multiply ^{15}N labeled M2TMP.

In order to observe the effects of drug binding on M2TMP secondary structure, we measure the ^{13}C and ^{15}N chemical shifts for 11 sites along the channel, including several proposed binding sites. Chemical shift is known to be very sensitive to local torsion angle perturbations. The largest drug-induced chemical shift change is observed at Serine 31, one of the proposed binding sites. The chemical shifts are used to simulate backbone torsion angles, and an amantadine-bound M2TMP structure is deposited in the Protein Data Bank with accession code 2KAD. We also establish a relationship between ^{13}C chemical shift of sidechain methyl carbons and sidechain torsion angles. Here we show that sidechain rotamer

can be predicted from ^{13}C methyl chemical shift and direct measurement of Val $\chi_1$correlates with the predicted rotamer.

Finally, we have measured the ^{13}C T_2 and ^{1}H $T_{1\rho}$ relaxation rates and ^{13}C linewidths of M2TMP in DLPC bilayers with and without amantadine. Substantial ^{13}C line narrowing occurs when amantadine is bound to the peptide, and the line-narrowing mechanism is attributed to faster peptide motion and a more homogeneous peptide conformation. We observe an increase in ^{13}C T_2 relaxation time for the amantadine-bound peptide relative to the apo state, with the most significant increases occurring near Serine 31. From ^{1}H $T_{1\rho}$ measurements, we are able to calculate the relative activation energies and motional correlation times for uniaxial rotational diffusion of the apo- and amantadine bound peptides. An increase in E_a and a reduction in τ_C was observed for the amantadine-bound state. We propose that the addition of amantadine to the sample results in a more tightly packed and homogeneous tetramer bundle that is able to diffuse faster in the lipid bilayer.

Chapter 1

Nuclear Magnetic Resonance Methodology

1.1 Introduction

Magnetic resonance is an extremely useful physical property that can be measured through the use of nuclear magnetic resonance (NMR) spectroscopy. Magnetic resonance was first discovered by I. I. Rabi in 1938 (*1*) and in the subsequent years was refined for applications to liquids, solids, and for imaging of three-dimensional objects.

Although the applications of magnetic resonance have become wide and varied since the technique was discovered, most chemists today know NMR as the best tool for chemical structure elucidation that is currently available. Solution NMR has many advantages for organic chemists. The spectra have sharp, narrow lines, the technique is extremely sensitive to atomic environment, requires low sample concentrations, and is non-destructive with short measuring times. However, a great deal of important and interesting information is lost when a molecule is solvated and consequently undergoes fast isotropic tumbling in solution. Moreover, many samples cannot be solubilized. Solid-state NMR allows for the study of disordered solids that cannot be studied by other structural techniques such as x-ray crystallography or solution NMR. These include biological solids such as amyloid fibrils and membrane proteins, in addition to natural organic matter and polymers. In the case of membrane proteins, the molecule can be studied in native lipid bilayers that are too large to undergo fast isotropic tumbling. The focus of this work is the application of solid-state NMR to the elucidation of membrane protein structure and dynamics, specifically the M2 transmembrane peptide (M2TMP) of the influenza A virus.

This chapter is intended to provide an overview of the theory and techniques used to conduct NMR experiments in subsequent chapters. This work focuses on two main areas of solid-state NMR experiments. First, we are interested in the motional rate and amplitude of a uniaxially rotating peptide in the lipid bilayer. To observe motional rates we have measured relaxation times such as ^{13}C T_2 and ^{1}H $T_{1\rho}$. By measuring the rate of peptide rotational diffusion, we are able to observe how temperature, membrane environment and drug binding affect peptide motion. To determine motional amplitude we have measured the coupling

strengths of a variety of NMR tensors such as ^{2}H quadrupolar coupling, ^{1}H-^{13}C and ^{1}H-^{15}N dipolar coupling and ^{15}N and ^{13}C chemical shift anisotropy. By measuring motional amplitudes, we are able to extract peptide orientation relative to the lipid bilayer normal. Second, we focus on the determination of protein secondary structure from isotropic chemical shifts. Here we use several chemical shift correlation experiments such as ^{13}C-^{13}C spin diffusion under magic angle spinning, ^{13}C-^{13}C double-quantum filtered single-quantum correlation and ^{13}C-^{15}N heteronuclear correlation. From these experiments we are able to observe chemical shift changes in the protein due to drug binding.

1.2 Relaxation Measurements and Motional Rate

Nuclear spin relaxation in NMR is necessary for pulsed experiments, since without it we would only be able to apply a single pulse to a nucleus and it would remain in an excited state forever. Relaxation can also be a hindrance if it occurs too quickly – the complicated spin gymnastics of many modern pulse sequences require sufficiently long relaxation times in order to complete a series of pulses and have enough remaining signal for acquisition. Relaxation can also be a useful tool for determining motional rates in samples, since the rate of molecular motion is inversely proportional to the locking or decoupling field used in the pulse sequence (*2, 3*). The phenomena described above are due to three types of nuclear spin relaxation – longitudinal or T_1 relaxation, transverse or T_2 relaxation, and T_1 relaxation in the rotating frame or $T_{1\rho}$ relaxation. Nuclear spin relaxation requires randomly fluctuating magnetic fields (*4*). These arise from random molecular motions that cause fluctuations in local interactions such as dipolar coupling or chemical shift anisotropy. These fluctuating local processes produce the randomly fluctuating fields that drive relaxation.

When component of the randomly fluctuating field perpendicular to the static magnetic field fluctuates at the Larmor frequency, it induces nuclear spin transitions similar to those induced by radiofrequency irradiation (*4*). This will occur until the populations return to the initial Bolzmann distribution, and is referred to as T_1 or longitudinal relaxation. T_1 is typically shorter than 1 second for amorphous membrane samples, but can be as long as several minutes to hours in the case of well-ordered crystalline systems.

T_2 relaxation occurs when the fluctuating fields cause the NMR signals from the nuclear spins to become out of phase with one another (*5*). Since the sample contains many spins, the respective signals are no longer in coherence and the detected signal will become progressively lower with increasing time after the initial pulse. T_2 is also inversely proportional to spectral linewidth. This incoherent line broadening is not due to multiple molecular conformations having overlapping isotropic chemical shifts or interactions such as ^1H-^{13}C dipolar coupling (*6*). Incoherent relaxation-induced broadening cannot be reduced by pulse effects such as stronger ^1H decoupling or through faster magic angle spinning.

Finally, $T_{1\rho}$ is defined as T_1 relaxation in the rotating frame. In this experiment, the magnetization is in the transverse plane after a 90° pulse, and is then spin-locked by applying a radiofrequency (rf) field to the nucleus of interest for varying lengths of time. Thus, the magnetization will not undergo precession in the rotating frame, and will decay as a function of spin-lock time.

These three relaxation times are similar in that they are sensitive to molecular motion at a characteristic frequency $\omega_i = \gamma B_i$ (*6-8*). For each relaxation time, the origin and strength of the B_r field is different. For T_1 it is B_0, the static magnetic field; for $T_{1\rho}$ it is the applied spin-locking field with rf strength B_1; and for ^1H decoupled ^{13}C T_2 it is B_1, the ^1H decoupling field (*2*). The rate of relaxation is inversely proportional to the spectral density function, $J(\omega)$, near the characteristic frequency ω_i (*9*):

$$J(\omega_i) = \frac{\tau_C}{1 + \omega_i^2 \tau_C^{\,2}} \tag{1.1}$$

The spectral density function is the Fourier transform of the correlation function $C(t)$ (*4*), where the correlation function describes the variation in a spatial function at time τ relative to time 0. The more random variation in the correlation function, the faster $C(t)$ will decay. The characteristic rate of decay of $C(t)$ is the correlation time, τ_C. Motional correlation times are obtained experimentally by measuring the relaxation time at several different temperatures or field strengths. Here we will consider the temperature-dependent case. Figure 1.1 shows the relationship between relaxation time and correlation time/temperature. Three motional regimes can be observed – fast motion and short correlation times where $\omega_i \tau_c$

<< 1, the intermediate time-scale region where $\omega_i\tau_c \approx 1$, and $\omega_i\tau_c >> 1$, the "slow" or long correlation time limit.

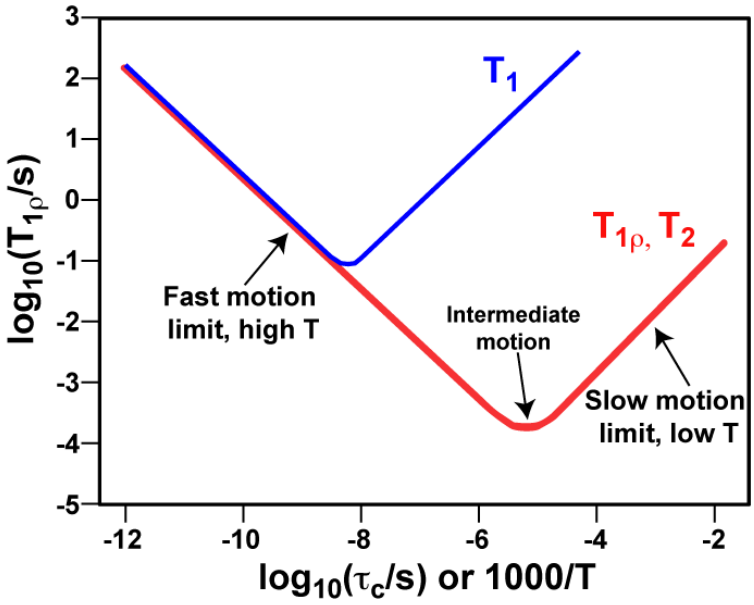

Figure 1.1. Relaxation time versus molecular correlation time/inverse temperature. The correlation time is temperature dependent, and relaxation time will be short when the molecule is moving at a rate inversely proportional to the locking field or decoupling field. Figure adapted from Harris (*4*).

Although the individual derivations for T_1, T_2 and $T_{1\rho}$ relaxation mechanisms are more complex, we will consider a general case for T_i. As stated above, relaxation time is inversely proportional to the spectral density function:

$$T_i^{-1} = C_i \frac{\tau_c}{1 + \omega_i^2 \tau_c^{\,2}} \tag{1.2}$$

where C_i is a constant obtained from the various prefactors that arise from the different derivations of relaxation functions. For the short correlation limit, $\omega_i\tau_C$ is negligible and the equation simplifies to:

$$\omega_i\tau_c << 1, \qquad T_i^{-1} = C_i\tau_c \tag{1.3}$$

Likewise, for the long correlation limit, $\omega_i\tau_C$ is much larger than 1, and the expression for the relaxation rate can be simplified again:

$$\omega_i\tau_c >> 1, \qquad T_i^{-1} = C_i \frac{1}{\omega_i^2\tau_c} \tag{1.4}$$

For the intermediate case, the relaxation rate reaches the maximum value, and the correlation time is at a minimum (Figure 1.1):

$$\omega_i\tau_c = 1, \qquad T_i^{-1} = C_i \tfrac{1}{2}\tau_c \tag{1.5}$$

Since we are studying peptides in a lipid membrane, the minimum in $T_{1\rho}$ and T_2 occurs near the lipid phase transition temperature. Therefore, at high temperatures (fast motion) and low temperatures (slow motion) the relaxation time will be long.

Finally, the correlation time is a function of the activation energy for the motional process. For a simple activated process, the Arrhenius equation can be used to obtain E_a:

$$\tau_c = \tau_0 e^{E_a/RT} \tag{1.6}$$

The relationship between motional correlation time and activation energy will be explored in detail in Chapter 8 through measurement of $T_{1\rho}$ relaxation for the uniaxially mobile M2TMP in DLPC lipid membranes.

In this work we measure ^{13}C T_2 and ^1H $T_{1\rho}$ in order to examine the difference in motional rates for M2TMP at several different temperatures, and the effect of drug binding on M2 motion. In a membrane sample, there are a large number of slow motions that are of little interest here. Since T_2 and $T_{1\rho}$ relaxation probe molecular motion on the microsecond time scale(*2, 3*), we are able to probe fast local motions that are strongly dependent on sample temperature, membrane environment, and ligand binding. As mentioned above, the correlation functions for these relaxation times are dependent on the ^1H decoupling field in the case of T_2 or the ^1H spin-locking field in the case of $T_{1\rho}$.

$T_{1\rho}$ and T_2 relaxation rates are measured by monitoring the rate of signal decay as a function of the length of time B_i is applied to the system. The pulse sequence for the measurement of ^{13}C T_2 relaxation under ^1H decoupling is shown in Figure 1.2, and consists of

a ^{1}H-^{13}C cross polarization period followed by a Hahn echo (*10*) period with varying τ. Several time points are measured by adjusting the delay time, τ, and then the ^{13}C signal intensity is plotted as a function of 2τ. T_2 relaxation is governed by its spectral density function, which is dependent on ^{1}H decoupling field strength during the echo delay. Therefore, stronger decoupling will result in a longer T_2.

There are several disadvantages to the Hahn echo experiment. For example, strong ^{1}H decoupling fields are required and the delay time may be increased to tens of milliseconds, which can put undue stress on the NMR probe. Additionally, ^{13}C-^{13}C *J*-coupling is not eliminated in this simple sequence and may contribute to signal decay. *J*-coupling can be eliminated through the use of a selective 180° pulse on ^{13}C, however this is limiting when many uniformly labeled residues are being measured in a particular sample.

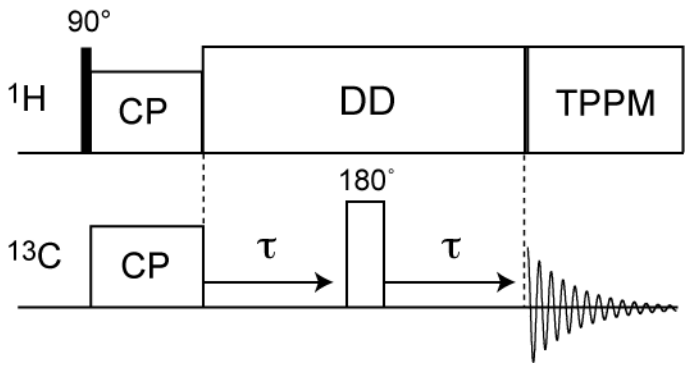

Figure 1.2. Pulse sequence for measurement of ^{13}C T_2 relaxation time.

^{1}H $T_{1\rho}$ relaxation measurements also probe molecular motions on the microsecond time scale. In the pulse sequence, shown in Figure 1.3, a spin-locking field is applied to the ^{1}H channel after the initial 90° pulse, and the magnetization will experience no precession in the rotating frame (*4*). The transverse magnetization will decay as a function of the spin-lock time, τ_{SL}. Here the correlation function is inversely proportional to the locking field (*3*), which is usually at a field strength of 50-100 kHz.

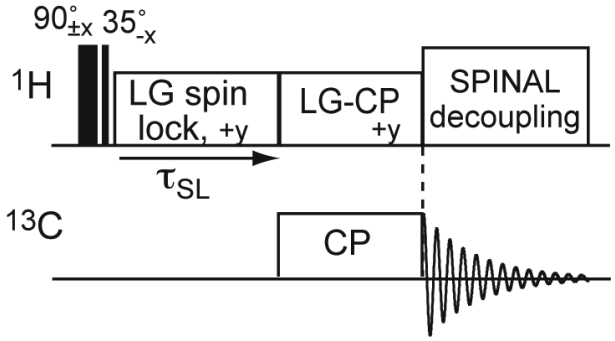

Figure 1.3. Pulse sequence for measurement of ^{1}H $T_{1\rho}$ relaxation time.

Since the signal is detected on the ^{13}C channel, we have employed a Lee-Goldberg spin-lock (*11*) to ensure ^{1}H magnetization transfer to directly bonded carbons. The effective spin lock field is applied at the magic angle, $cos^{-1}\left(1/\sqrt{3}\right)$, by applying a transverse field at a specific field offset such that the effective field is applied at 54.7° relative to B_0. For example, a 50 kHz transverse field will be applied with a field offset of 35.4 kHz, resulting in an effective field of 62.5 kHz at the magic angle.

1.3 Molecular Orientation

The focus of this work is the structure, orientation, and function of the M2TMP of the influenza A virus. The orientation of M2TMP has been studied extensively with aligned samples by Cross and coworkers (*12, 13*), where the peptide is incorporated into lipid membranes on glass plates, and rehydrated to form aligned bilayers. In this sample configuration, the lipid bilayers are aligned parallel to the magnetic field, B_0, and consequently the molecular axes of all of the peptides are also oriented with the same angle β with respect to B_0. Although aligned samples are excellent for orientation determination, it is often difficult to obtain sufficiently good sample alignment. Here we present a method of orientation determination, using unoriented (powder) samples that contain peptides undergoing fast uniaxial motion about the bilayer normal (*14*).

Each molecule in a random powder sample has an orientation relative to the magnetic field B_0, and its NMR frequency ω is dependent upon the orientation as follows (*6*):

$$\omega(\beta,\alpha) = \tfrac{1}{2}\delta(3\cos^2\beta - 1 - \eta\sin^2\beta\cos 2\alpha) + \omega_{iso} \tag{1.7}$$

where (β, α) are the polar coordinates and δ and η are the asymmetry and anisotropy parameters of the principal axis system (PAS) of the spin interaction tensor in the laboratory frame:

$$\eta = \frac{\omega_y - \omega_x}{\omega_z} \quad \text{and} \quad \delta = \omega_z . \tag{1.8}$$

The rigid powder spectrum (dashed line) in Figure 1.4 shows an example of the anisotropic lineshape one would obtain for a non-spinning powder sample with $\eta \approx 0$.

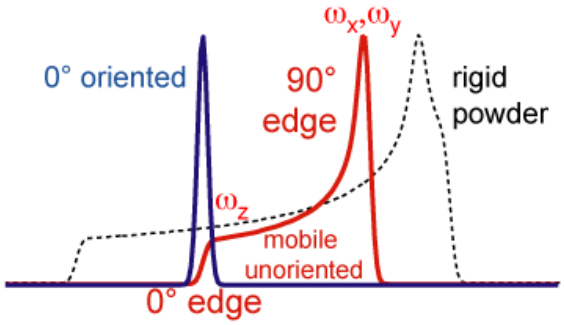

Figure 1.4. Rigid powder spectrum (dashed line) overlaid with $\bar{\eta} = 0$ motionally narrowed powder spectrum (red) and $\theta = 0°$ oriented spectrum. The $\theta = 0°$ edge position is the same for both the oriented and motionally narrowed powder spectra.

Now we consider the orientation of a peptide relative to the lipid bilayer normal. For an aligned sample, the bilayer normal is oriented along the B_0 field. In the aligned sample spectrum, shown in blue in Figure 1.4, the 0° frequency is dependent upon the orientation of the molecule relative to B_0 (in terms of θ, ϕ) and the isotropic chemical shift:

$$\omega_{0^\circ\, aligned} = \tfrac{1}{2}\delta(3\cos^2\theta - 1 - \eta\sin^2\theta\cos 2\phi) + \omega_{iso} \tag{1.9}$$

Here (θ, ϕ) are the polar coordinates for the orientation of the PAS relative to the bilayer normal, $\bar{n}$. As mentioned above, we have aligned the bilayer normal along B_0, thus (θ, ϕ) are also the orientation angles relative to the bilayer normal. Uniaxial rotation about the bilayer

normal does not change the polar coordinates (θ, ϕ), and consequently does not affect the frequency.

In the case of a mobile *unoriented* sample, the averaged anisotropy parameter, $\bar{\delta}$, can be obtained for those liposomes with bilayer normals that are parallel to B_0:

$$\bar{\delta} = \omega_{0^\circ\ aligned} - \omega_{iso} = \tfrac{1}{2}\delta(3\cos^2\theta - 1 - \eta\sin^2\theta\cos 2\phi). \tag{1.10}$$

The averaged anisotropy parameter and the averaged asymmetry parameter of $\bar{\eta} = 0$ define the powder lineshape for a sample composed of uniaxially mobile molecules. The 0° edge of this powder lineshape is defined by (*14*):

$$\bar{\delta}_{//} = \bar{\delta} + \omega_{iso} = \omega_{0^\circ\ aligned} \tag{1.11}$$

which is equal to the peak of the 0° aligned sample (*14*). This is shown in Figure 1.4, where the β = 0° edge of the motionally narrowed powder pattern (red) and the 0° peak of the aligned sample (blue) are at the same position. The β = 90° edge of the motionally narrowed powder pattern is also related to the average anisotropy parameter and the isotropic shift:

$$\bar{\delta}_{\perp} - \omega_{iso} = -\tfrac{1}{2}\bar{\delta} = -\tfrac{1}{2}(\bar{\delta}_{//} - \omega_{iso}) \tag{1.12}$$

Since the $\bar{\delta}_{\perp}$ frequency, or 90° edge of the unoriented powder spectrum is much higher sensitivity than the 0° edge, we read off the 90° frequency when reporting the chemical shift anisotropy of a particular spectrum.

Once $\bar{\delta}$ is known, taking the averaged anisotropy parameter in Equation 1.10 with $\bar{\eta} = 0$, we can determine the orientation θ of a molecule relative to the bilayer normal:

$$\bar{\delta}_{//} - \omega_{iso} = \bar{\delta} = \tfrac{1}{2}\delta\left(3\cos^2\theta - 1\right) \tag{1.13}$$

For dipolar and quadrupolar couplings, the ratio of $\bar{\delta}$ with the rigid limit δ is the bond order paramter, *S:*

$$S = \frac{\bar{\delta}}{\delta} = \tfrac{1}{2}\left(3\cos^2\theta - 1\right). \tag{1.14}$$

Thus, if we measure an averaged NMR interaction for a molecule undergoing fast uniaxial rotational diffusion, we can divide the averaged coupling by the rigid limit coupling, which is generally known. This gives the order parameter S and allows for the extraction of the orientation angle θ. We have shown that the orientation of the NMR interaction tensor is directly related to the order parameter, S. In this work we have measured heteronuclear dipolar couplings, quadrupolar couplings, and chemical shift anisotropies of a uniaxially diffusing peptide, and using the bond order parameter we are able to measure the orientation of the peptide relative to the bilayer normal in an unoriented liposome sample.

1.4 Motional Amplitude and Rates of Diffusion

It has been mentioned in the preceding section that the chemical shift anisotropy narrows for a uniaxially mobile molecule. However, only if a molecule is undergoing diffusion at a rate faster than the NMR interaction being measured will the observed coupling be smaller than the rigid limit. Not all NMR interactions are created equal, and this is reflected in the size of the interaction, otherwise known as the coupling strength. The largest coupling that we have observed in this work is the ^{2}H quadrupolar coupling with a rigid limit of about 120 kHz. This can be contrasted with ^{13}C-^{1}H dipolar coupling of about 22 kHz, and ^{15}N-^{1}H dipolar coupling of about 11 kHz. Chemical shift anisotropy for Cα spans 20-40 ppm giving a coupling of 2-6 kHz, for fields ranging from 400-600 MHz. ^{15}N gives chemical shift anisotropy spans 20-70 ppm for a range of couplings from 2-10 kHz depending on B_0. Rates of rotational diffusion are discussed in detail in Chapters 3 and 8. Here we will present the methods for measurement of ^{2}H quadrupolar and heteronuclear dipolar couplings, and the interpretation of motionally narrowed couplings for uniaxially mobile proteins.

^{2}H Quadrupolar NMR

Measurement of ^{2}H quadrupolar coupling is a convenient method for the observation of molecular motion and motional amplitude. ^{2}H-labeled amino acids are readily available from stable isotope suppliers, and we have measured methyl-deuterated leucine and alanine residues in the peptide. The rigid limit ^{2}H quadrupolar coupling is significantly larger than the dipolar or J-couplings observed in spin-1/2 nuclei, but it is small when compared with the

large quadrupolar couplings observed for nuclei such as ^{85}Rb and ^{25}Mg (*15*). Figure 1.5 shows the quadrupolar echo pulse sequence used to acquire static ^{2}H spectra, where two 90° pulses sandwich two adjustable delay times τ_1 and τ_2. Here, τ_2 is usually 6-10 μs less than τ_1. The quadrupolar echo experiment (*16*) is different from a Hahn echo experiment (*10*) in that it refocuses Hamiltonians that are bilinear (*6*). The two 90° pulses must be 90° out of phase, as shown in Figure 1.5.

Since the ^{2}H lineshape is very broad, it may be necessary to manually adjust τ_1 and τ_2 to obtain a flat baseline after acquisition by left-shifting the FID any number of points. This is attainable when $\tau_2 < \tau_1$, thus causing the acquisition to begin before the echo maxima. Theoretically the number of left shift points can be calculated as $(\tau_1 - \tau_2)$/*dwell time*, where dwell time is the time in between digitized points in the FID. However, the empirical value that gives the best baseline may be slightly different from the calculated value.

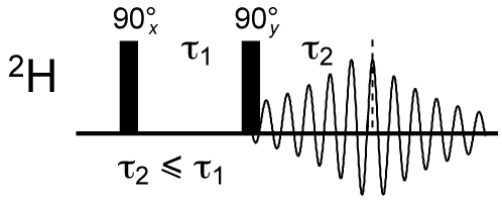

Figure 1.5. Quadrupolar echo pulse sequence. The τ_2 time is generally 6-10 μs less than τ_1 so that acqusition begins before the echo maxima, and the detected FID can be adjusted using left shift.

The rigid limit ^{2}H quadrupolar coupling is approximately 120 kHz, as shown for the CD_2 spectrum in Figure 1.6(c). However, when a methyl group is deuterated, the CD_3 deuterons undergo a three-site jump on the order of 3 x 10^9 Hz (*17*), which is much faster than the rigid quadrupolar coupling of 120 kHz. Since a methyl group has tetrahedral geometry, the deuterons are rotating at an angle of 109.5° with respect to the motional axis, which can be inserted Equation 1.14, giving an order parameter S = 0.34. Thus, the CD_3 lineshape is narrowed by ~1/3 relative to the rigid limit coupling, as shown in Figure 1.6(b).

In the protein, we have selectively replaced alanine residues with CD_3-alanine, so we now have a CD_3 group that is directly bonded to the peptide backbone. The average quadrupolar tensor for the CD_3-alanine residue is along the alanine Cα-Cβ bond, as shown in

Figure 1.7. Alanine has no χ_1 or χ_2 angle, so any observed motional narrowing in Figure 1.6(a) is due to uniaxial rotation of the Cα-Cβ bond, most likely about the bilayer normal. Since the average quadrupolar tensor is along the Cα-Cβ bond, we can now calculate the angle θ between the bond and the bilayer normal. This is achieved by taking the motionally averaged ^{2}H coupling as shown in Figure 1.6(a) divided by the rigid limit CD_3 splitting of about 40 kHz, which gives the Cα-Cβ bond order parameter S as defined by Equation 1.14. The measurement of ^{2}H quadrupolar coupling of CD_3- alanine labeled peptides is a useful test to determine if a peptide is undergoing fast uniaxial motion. If this is the case, we can continue with peptide orientation measurements, which are detailed in Chapters 3 and 4.

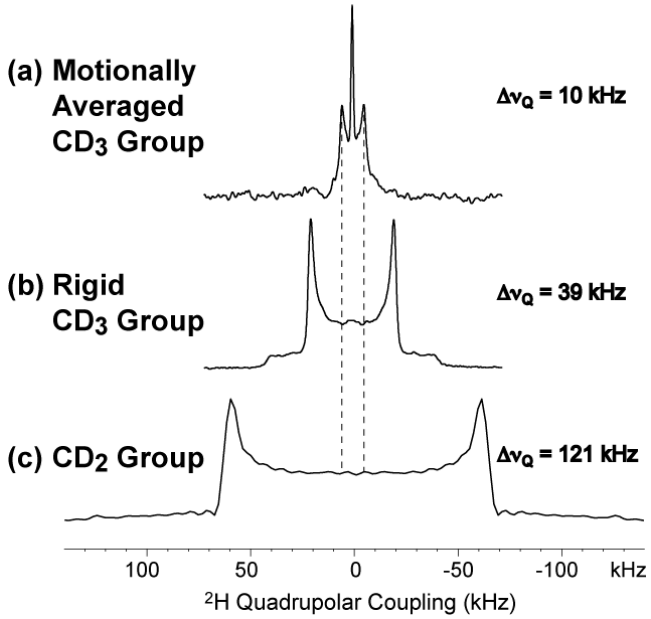

Figure 1.6. Comparison of ^{2}H quadrupolar couplings for (a) a motionally averaged deuterated methyl (CD_3) group, (b) a deuterated methyl group in a rigid crystalline molecule, and (c) a deuterated methylene group (CD_2) in a rigid molecule.

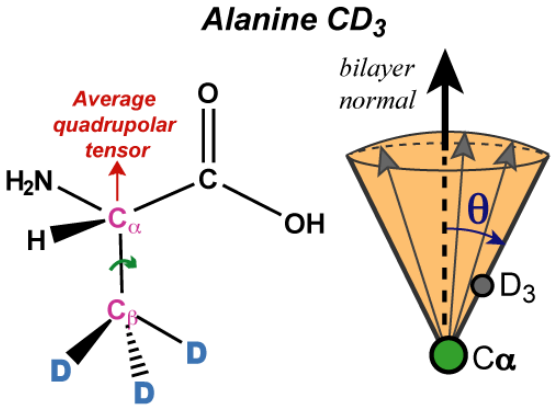

Figure 1.7. Methyl-deuterated (CD_3) alanine. The average quadrupolar tensor is along the Cα-Cβ bond, and the orientation of the bond relative to the bilayer normal can be calculated.

Heteronuclear Dipolar Coupling

The measurement of heteronuclear dipolar couplings has proven to be an important technique throughout this work. In addition to ^{2}H quadrupolar couplings, it has been used extensively to measure peptide motional amplitude and orientation, and these measurements are shown in Chapters 3, 4 and 8. Since the ^{2}H quadrupolar spectrum is quite broad, it is difficult to obtain site-resolved coupling measurements. Additionally, in a traditional 1D magic-angle spinning experiment, the dipolar coupling is averaged out over the rotor period. Thus we require a pulse sequence that recouples the heteronuclear interaction by interfering with the magic angle spinning dipolar averaging. Here we demonstrate the direct, site-resolved measurement of multiple ^{1}H-^{15}N or ^{1}H-^{13}C dipolar couplings for orientation determination

A separated-local field 2D experiment in which chemical shift is detected in one dimension and dipolar coupling in the other was first developed by Munowitz, et al. (*18*) and has been modified by Hong, et al. (*19*) so that the dipolar couplings can be quantum-mechanically "doubled" in order to achieve greater dipolar coupling resolution among sites. This pulse sequence is referred to as dipolar doubled DIPSHIFT. This more recent pulse sequence is used to measure ^{1}H-^{13}C and ^{1}H-^{15}N dipolar couplings in protein samples throughout this work.

We have chosen to measure the ^{1}H-X dipolar couplings of backbone ^{15}N and ^{13}Cα for two reasons. First, the ^{1}H-X bond should have a fixed orientation relative to the peptide backbone that is not subject to torsional motions, given that the only peptide motion is fast uniaxial rotational diffusion. Second, the presence of only one directly bonded ^{1}H makes the analysis of dipolar coupling uncomplicated.

The pulse sequence for dipolar doubled DIPSHIFT is shown in Figure 1.7. The first 180° pulse occurs during homonuclear ^{1}H-^{1}H decoupling, and this doubles the ^{1}H-X dipolar interaction. ^{1}H-^{1}H homonuclear decoupling is applied in order to ensure that only the directly bonded ^{1}H contributes to the dipolar coupling measurement. The second 180° refocuses the chemical shift interaction, which is also doubled during the first 180° pulse. The two 180° pulses are rotor-synchronized and occur at the same time during two subsequent rotor periods. The final experiment consists of a series of 1D spectra obtained for several t_1 increments, and the intensity of the peak of interest can be plotted as a function of t_1.

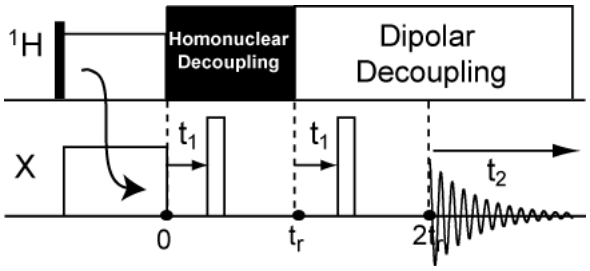

Figure 1.7. Dipolar doubled DIPSHIFT pulse sequence.

1.5 Chemical Shift Correlation

It is well known that ^{13}C chemical shift for Cα, Cβ and CO resonances in the protein backbone are very sensitive to protein secondary structure (*20*). Figure 1.8 shows the chemical shift difference between α-helical and β-sheet peptides. It can be observed that the Cα chemical shift for the β-sheet peptide is more upfield than the α-helical peptide, and the opposite situation is true for the Cβ chemical shift. CO chemical shift follows a trend similar to Cα. Since the M2 transmembrane peptide (M2TMP) forms relatively stable α–helicies in

lipid bilayers (*21*), it is not the main goal of this project to determine the secondary structure of the peptide. Rather, we hope to observe chemical shift perturbations upon binding drug to the channel in order to pinpoint areas most affected by drug binding.

In order to measure ^{13}C chemical shifts, several methods can be employed. The simplest and most common for organic chemists in the solution state would be a 1D ^{13}C spectrum. However, since solid-state NMR samples typically have broad lines, and amino acids in peptides do not have a large range of chemical shifts, spectral overlap is an issue and the importance of 2D correlation experiments becomes apparent.

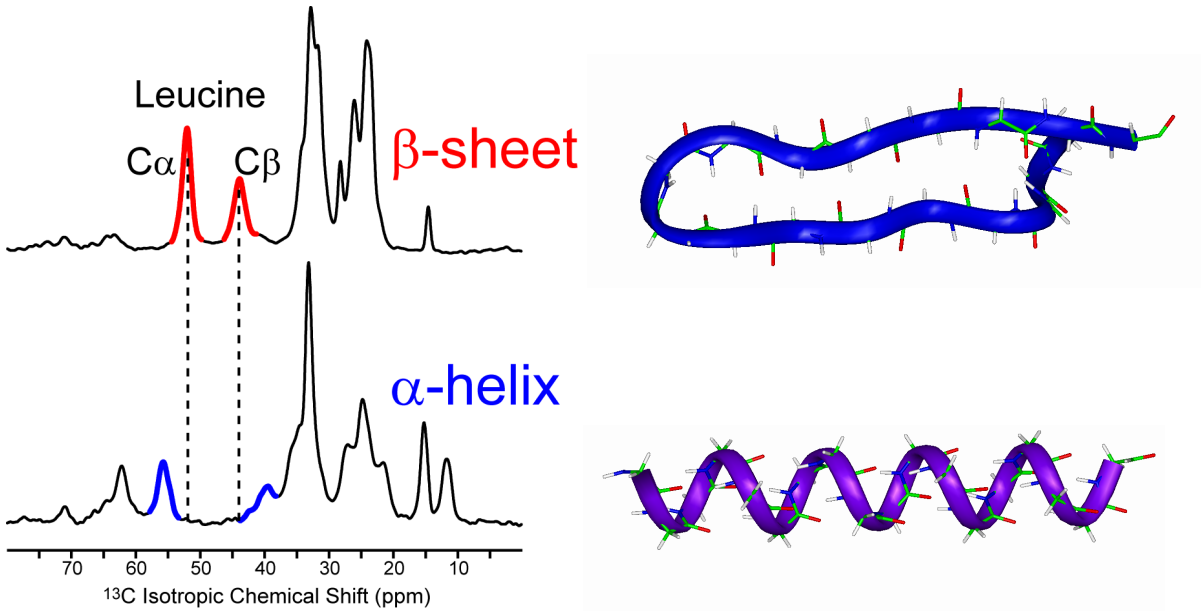

Figure 1.8. Leucine Cα and Cβ chemical shifts shown for a β-sheet protein (KL10) and an α-helical protein (KvAP). (Figure courtesy T. Doherty)

2D ^{13}C-^{13}C Correlation Under ^{13}C-^{1}H Dipolar Assisted Rotary Resonance (DARR)

A simple 2D ^{13}C-^{13}C correlation experiment with high sensitivity the ^{13}C-^{1}H dipolar assisted rotatry resonance or DARR experiment (*22*). This method of polarization transfer combines both a ^{1}H-driven and rotor-driven mechanism. This results in spectral broadening of both the ^{1}H-^{1}H and ^{13}C-^{1}H interactions, and increased spectral overlap and magnetization

transfer (*22*). The ^{13}C-^{1}H dipolar coupling is recoupled by applying a weak ^{1}H rf pulse at the rotor frequency during the chemical shift evolution and mixing times, as shown in Figure 1.9. Spinning speeds for the 4 mm rotor are typically in the 5-8 kHz regime and $\gamma B_1/2\pi$ of the corresponding DARR recoupling pulses equals ν_r. This contrasts with a typical ^{1}H heteronuclear decoupling pulse in the 50-83 kHz regime. Due to the weak field of the ^{13}C-^{1}H recoupling pulse, the mixing time t_m can be as long as 50 ms, resulting in the observation of many long range contacts in the final spectrum.

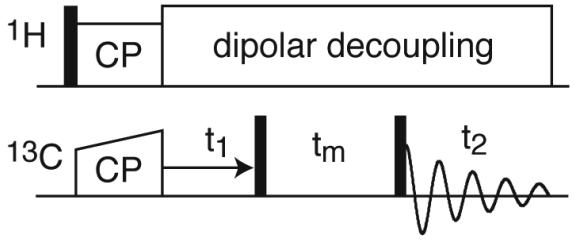

Figure 1.9. Pulse sequence for proton driven ^{13}C-^{13}C spin diffusion experiment with ^{13}C-^{1}H dipolar assisted rotary resonance decoupling.

2D ^{13}C-^{13}C Correlation with Double-Quantum Filtration

Although the DARR experiment has high sensitivity and produces a spectrum with many long-range correlations, it is also desirable to have a ^{13}C-^{13}C correlation experiment that selectively recouples only those ^{13}C spins that are directly bonded to another ^{13}C. Moreover, since the peptides studied are typically bound to a lipid membrane at a ratio of one peptide to fifteen or twenty lipids, the natural abundance ^{13}C signals from the lipid can be the dominant feature in both 1D and 2D spectra. The peptides have been selectively labeled with uniform ^{13}C, ^{15}N amino acids for specific residues, but the lipid contains just 1% natural abundance ^{13}C dispersed randomly throughout the molecule. Thus, the probability that a ^{13}C spin will have a one-bond ^{13}C neighbor in the peptide is 99% (the typical level of enrichment for isotopically labeled amino acids), whereas this probability drops to 1% in lipid molecules. Therefore, selective filtering by recoupling only those ^{13}C spins bonded to other ^{13}C removes all observable lipid signals from the spectrum.

In order to achieve double-quantum recoupling, we have used the SPC-5 pulse sequence (*23*), which is a broadband homonuclear recoupling sequence. This pulse sequence has many predecessors (*24, 25*), which similarly include a rotor-synchronized radiofrequency field and a symmetric pulse. Compared with other double-quantum recoupling sequences, SPC5 has the advantage that the recoupling rf field strength is only $\nu_1 = 5\nu_r$, thus making the requirement of $3*5\nu_r$ for ^{1}H decoupling field more attainable for probe with larger coils, i.e. 4 mm rotor size. For example, most SPC-5 experiments in this work are conducted at ν_r=7 kHz, thus requiring a ^{13}C-^{13}C recoupling field of 35 kHz and ^{1}H decoupling strength of 105 kHz during homonuclear recoupling. Experimentally, ^{1}H decoupling in the range of 71-83 kHz is more than adequate for obtaining maximum transfer efficiency on our equipment.

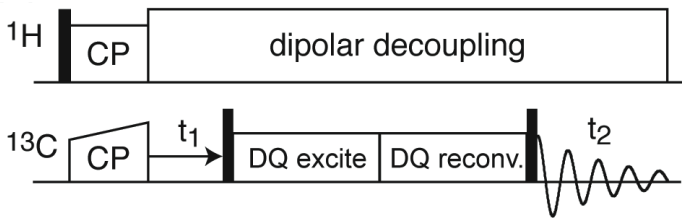

Figure 1.10. Double quantum ^{13}C-^{13}C correlation pulse sequence.

2D ^{15}N-^{13}C Correlation Experiments

Although ^{15}N is an NMR spin of low natural abundance and generally of low sensitivity, the use of ^{13}C, ^{15}N labeled proteins allows us to measure ^{13}C-^{15}N heteronuclear correlation spectra, or CN HETCOR. Unfortunately, due to the weak ^{13}C-^{15}N dipolar coupling, it is difficult to achieve much more than one or two bond correlations. Particularly in this work, the ^{15}N chemical shift has proven to be extremely sensitive to local conformation changes. ^{15}N chemical shifts for helical proteins are not well-resolved, with the ^{15}N shifts for most amino acids falling around 117-124 ppm. Thus, a 2D correlation experiment is useful in separating ^{15}N chemical shifts and observing chemical shift changes.

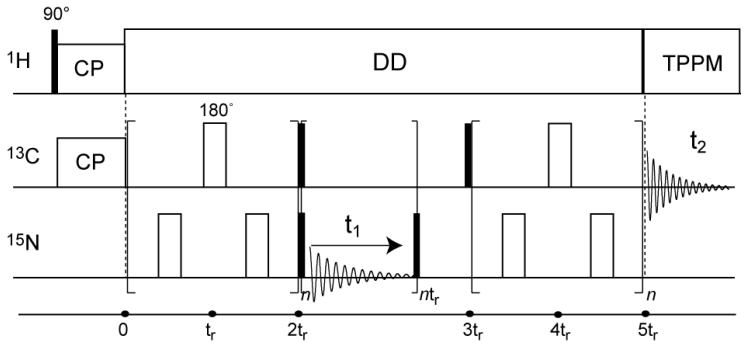

Figure 1.11. 2D ^{13}C-^{15}N HETCOR pulse sequence for a REDOR-like CN magnetization transfer.

The pulse sequence shown in Figure 1.11 is the 2D HETCOR experiment (*26*) using a REDOR-type (*27*) ^{13}C-^{15}N magnetization transfer through dipolar recoupling. The ^{15}N chemical shifts are encoded during the t_1 period. Here it is possible to measure inter- and intra-residue contacts due to the through-space dipolar recoupling that is achieved by the 180° pulses. However, as mentioned above, weak ^{13}C-^{15}N dipolar couplings prohibit long-range couplings from being measured.

1.6 Thesis Organization

This thesis is composed mainly of published journal papers on the structure, orientation and dynamics of the M2 transmembrane peptide of the influenza A virus. Some papers contain supplementary information that was only published in the online edition of the journal, and this data is located at the end of its respective chapter.

Chapter 1 has covered important facets of NMR methodology and has also offered a brief overview of the techniques used for the study of membrane protein structure and dynamics in subsequent chapters. Chapter 2 is a review article that compiles the body of knowledge that is currently about the influenza A M2 protein structure, orientation, dynamics, and the interaction with the anti-influenza drug amantadine. The different crystal, micelle and membrane-bound structures of M2 will be discussed. The debate regarding the location of the amantadine block and the mechanism of H^+ transport through the channel will also be reviewed. In Chapter 3, we show that M2TMP undergoes fast uniaxial motion in a

model phosphocholine lipid bilayer, and use this physical property to show that the orientation of M2TMP is dependent on membrane thickness. This is achieved through the measurement of motionally narrowed ^{2}H and ^{15}N static lineshapes and N-H dipolar couplings. Different sample preparation techniques and the effect they have on the rotational diffusion of the peptide will also be discussed. In Chapter 4, we use the motionally scaled N-H dipolar couplings to measure the orientation of a peptide relative to the bilayer normal in an unoriented sample with several uniformly labeled residues. In Chapter 3, we had only one ^{15}N labeled residue per sample due to the need to measure static ^{15}N chemical shift anisotropy. However, through the use of ^{13}C detection of N-H dipolar couplings, we are able to measure multiple motionally reduced couplings at once. The couplings are plotted on a dipolar wave, which gives the same information regarding peptide orientation as the CSA/dipolar coupling correlated plots discussed in Chapter 3.

In Chapter 5, we begin to discuss the implications of adding the anti-influenza drug amantadine to membrane-bound M2TMP. Through the use of a variety of ^{13}C-^{13}C and ^{13}C-^{15}N correlation techniques, we show significant chemical shift changes occur at several key sites along M2TMP upon amantadine addition. We also show that amantadine increases ^{13}C T_2 times and propose that the increased ^{13}C T_2 is due to a more homogeneous tetramer bundle that is stabilized by amantadine. Chapter 6 extends this work by studying the amantadine-induced chemical shift changes of three more residues, including the proposed binding site Serine 31. We observe large chemical shift changes at S31 for both ^{13}C and ^{15}N, and from the chemical shifts measured for the amantadine-bound and apo peptide, we construct a model using chemical shift-constrained torsion angle calculations using computer simulations. This structure was deposited in the Protein Data Bank with accession number 2KAD.

Chapter 7 extends the idea of chemical shift dependence of torsion angles from protein backbones to sidechains. The chemical shift difference of stereospecifically assigned methyl groups valine γ_1/γ_2 and leucine δ_1/δ_2 was analyzed for several protein structures deposited in the Protein Data Bank. This chemical shift difference was correlated with sidechain rotamer, and a data trend indicates that the difference in methyl chemical shift is correlated with the sidechain torsion angle. This analysis is applied to several valine and leucine sidechains measured in M2TMP with and without amantadine. We show that

chemical shift and direct torsion angle measurement techniques indicate the same sidechain torsion perturbation for Val 27 and Val 28 upon amantadine addition.

Chapter 8 analyzes the observed dynamics changes of M2TMP upon amantadine addition. In previous chapters we have shown that M2TMP is undergoing fast uniaxial rotational diffusion in hydrated DLPC bilayers, and we have also observed that ^{13}C linewidths are narrowed upon the addition of amantadine. To understand the origin of ^{13}C line narrowing, the ^{1}H $T_{1\rho}$ was measured at several temperatures for eleven uniformly labeled residues in M2TMP. From these variable temperature measurements, we are able to extract the activation energy and correlation times of M2TMP in the lipid bilayer. It is shown that the diffusion correlation time of amantadine-bound M2TMP is reduced relative to the apo state, and also that the peptide has an increased activation energy for the diffusion process.

Finally, three appendices are located at the end of the thesis. Appendix A covers the synthesis of ^{15}N labeled amantadine in great detail. Appendix B covers the ^{207}Pb temperature calibration experiments that were conducted on the 4 mm probe on the 600 MHz machine. Lastly, Appendix C covers the sample transfer technique for hydrated liposome samples.

1.7 Copyright Permission

Chapters 2, 3, 4, 5, 6, 7 and 8 are reprints of published papers. With the exception of Springer, the copyright permissions do not require a license for re-use in a thesis or dissertation. Copyright permissions have been obtained from the following publishing groups:

Chapters 2, 3 and 7: American Chemical Society

Chapters 4 and 6: Elsevier, Inc.

Chapter 5: National Academy of Sciences

Chapter 8: Springer, license number 2237680916222

References

1. Rabi, I. I., Millman, S., Kusch, P., and Zacharias, J. R. (1938) The Magnetic Moments of Li63, Li73 and F199, *Phys. Rev. 53*, 495.
2. Rothwell, W. P., and Waugh, J. S. (1981) Tranverse relaxation of dipolar coupled spin systems under rf irradiation: detecting motions in solids., *J. Chem. Phys. 74*, 2721-2732.
3. Schaefer, J., Stejskal, E. O., and Buchdahl, R. (1977) Magic-Angle C-13 NMR Analysis of Motion in Solid Glassy Polymers, *Macromolecules 10*, 384-405.
4. Harris, R. K. (1986) *Nuclear Magnetic Resonance Spectroscopy*, Longman, Essex, England.
5. Levitt, M. H. (2001) *Spin Dynamics*, Wiley, West Sussex, England.
6. Schmidt-Rohr, K., and Spiess, H. W. (1994) *Multidimensional Solid-State NMR and Polymers*, Academic Press, San Diego, CA.
7. Abragam, A. (1961) *The Principles of Nuclear Magnetism*, Oxford University Press, London.
8. Slichter, C. P. (1990) *Principles of Nuclear Magnetic Resonance, 3rd ed.*, Springer, Berlin.
9. Lipari, G., and Szabo, A. (1982) Model-Free Approach to the Interpretation of Nuclear Magnetic-Resonance Relaxation in Macromolecules .1. Theory and Range of Validity, *J. Am. Chem. Soc. 104*, 4546-4559.
10. Hahn, E. L. (1950) Spin echoes, *Phys. Rev. 80*, 580-594.
11. van Rossum, B. J., de Groot, C. P., Ladizhansky, V., Vega, S., and de Groot, H. J. M. (2000) A method for measuring heteronuclear (H-1-C-13) distances in high speed MAS NMR, *J. Am. Chem. Soc. 122*, 3465-3472.
12. Hu, J., Asbury, T., Achuthan, S., Li, C., Bertram, R., Quine, J. R., Riqiang, F., and Cross, T. A. (2007) Backbone Stucture of the Amantadine-Block Trans-Membrane Domain M2 Proton Channel from Influenza A Virus, *Biophys. J. 92*, 4335-4343.
13. Tian, C., Gao, P. F., Pinto, L. H., Lamb, R. A., and Cross, T. A. (2003) Initial structural and dynamic characterization of the M2 protein transmembrane and amphipathic helices in lipid bilayers, *Protein Sci. 12*, 2597-2605.

14. Hong, M., and Doherty, T. (2006) Orientation determination of membrane-disruptive proteins using powder samples and rotational diffusion: A simple solid-state NMR approach, *Chem. Phys. Lett. 432*, 296-300.
15. Hung, I., and Schurko, R. W. (2003) A Solid-State Mg-25 C13 NMR Study of Bis(cyclopentadienyl)magnesium, *Solid State Nucl. Magn. Reson. 24*, 78-93.
16. Davis, J. H., Jeffrey, K. R., Bloom, M., Valic, M. I., and Higgs, T. P. (1976) Quadrupolar echo 2H NMR in ordered hydrocarbons, *Chem. Phys. Lett. 42*, 390-394.
17. Batchelder, L. S., Niu, C. H., and Torchia, D. A. (1983) Methyl Reorientation in Polycrystalline Amino-Acids and Peptides - a H-2 Nmr Spin-Lattice Relaxation Study, *J. Am. Chem. Soc. 105*, 2228-2231.
18. Munowitz, M. G., Griffin, R. G., Bodenhausen, G., and Huang, T. H. (1981) Two-Dimensional Rotational Spin-Echo Nuclear Magnetic Resonance in Solids: Correlation of Chemical Shift and Dipolar Interactions, *J. Am. Chem. Soc. 103*, 2529-2533.
19. Hong, M., Gross, J. D., Rienstra, C. M., Griffin, R. G., Kumashiro, K. K., and Schmidt-Rohr, K. (1997) Coupling amplification in 2D MAS NMR and its application to torsion angle determination in peptides, *J. Magn. Reson. 129*, 85-92.
20. Zhang, H., Neal, S., and Wishart, D. S. (2003) RefDB: A database of uniformly referenced protein chemical shifts, *J. Biomol. NMR 25*, 173-195.
21. Stouffer, A. L., Ma, C., Cristian, L., Ohigashi, Y., Lamb, R. A., Lear, J. D., Pinto, L. H., and DeGrado, W. F. (2008) The interplay of functional tuning, drug resistance, and thermodynamic stability in the evolution of the M2 proton channel from the influenza A virus, *Structure 16*, 1067-1076.
22. Takegoshi, K., Nakamura, S., and Terao, T. (2001) C-13-H-1 dipolar-assisted rotational resonance in magic-angle spinning NMR, *Chem. Phys. Lett. 344*, 631-637.
23. Hohwy, M., Rienstra, C. M., Jaroniec, C. P., and Griffin, R. G. (1999) Fivefold symmetric homonuclear dipolar recoupling in rotating solids: application to double-quantum spectroscopy., *J. Chem. Phys. 110*, 7983-7992.
24. Gregory, D. M., Mitchell, D. J., Stringer, J. A., Kiihne, S., Shiels, J. C., Callahan, J., Mehta, M. A., and Drobny, G. P. (1995) Windowless dipolar recoupling: the detection of

weak dipolar couplings between spin 1/2 nuclei with large chemical shift anisotropies, *Chem. Phys. Lett. 246*, 654-663.

25. Tycko, R., and Dabbagh, G. (1990) Measurement of nuclear magnetic dipole-dipole couplings in magic angle spinning NMR, *Chem. Phys. Lett. 173*, 461-465.
26. Hong, M., and Griffin, R. G. (1998) Resonance Assignment for Solid Peptides by Dipolar-Mediated 13C/15N Correlation Solid-State NMR, *J. Am. Chem. Soc. 120*, 7113-7114.
27. Gullion, T., and Schaefer, J. (1989) Rotational echo double resonance NMR, *J. Magn. Reson. 81*, 196-200.

Chapter 2

Structure and Function of the Influenza A M2 Proton Channel

A paper published in Biochemistry

2009, vol. 48 pp. 7356-7364

Sarah D. Cady, Wenbin Luo, Fanghao Hu, and Mei Hong

Abstract

The M2 protein of influenza A viruses forms a tetrameric pH-activated proton-selective channel that is targeted by the amantadine class of anti-viral drugs. Its ion channel function has been extensively studied by electrophysiology and mutagenesis; however, the molecular mechanism of proton transport is still elusive, and the mechanism of inhibition by amantadine is controversial. We review the functional data on proton channel activity, molecular dynamics simulations of the proton conduction mechanism, and high-resolution structural and dynamical information of this membrane protein in lipid bilayers and lipid-mimetic detergents. These studies indicate that elucidation of the structural basis of M2 channel activity and inhibition requires thorough examination of the complex dynamics of the protein and the resulting conformational plasticity in different lipid bilayers and lipid-mimetic environments.

A. Function of the M2 proton channel of influenza A viruses

The M2 protein of influenza A and B viruses forms tetrameric proton channels that are important for the viral life cycle. After the virus enters the infected cell by endocytosis, the M2 proton channel opens in response to the low pH of the endosome, allowing proton flux into the virus, which triggers the dissociation of the viral RNA from the matrix proteins and the fusion of the viral and endosomal membranes. These events release the viral RNA to the cytoplasm for replication by the host cell (*1*). In a later stage of virus replication, the M2 protein maintains the high pH of the trans-Golgi network and prevents premature

conformational changes of hemagglutinin in viruses with a high pH optimum of hemagglutinin-induced fusion (*2*).

The influenza A M2 (AM2) protein contains a short N-terminal periplasmic domain, a transmembrane (TM) domain, and a C-terminal cytoplasmic tail (Figure 2.1). It is one of the smallest ion channel proteins and thus an excellent system for elucidating the structure-function relation of ion channels. Extensive mutagenesis, electrophysiology (*3, 4*) and sedimentation equilibrium experiments (*5*) have been conducted to characterize the function and stability of AM2 (for recent reviews, see (*6, 7*)). The AM2 proton channel is also the target of the amantadine class of drugs, one of only two anti-influenza drugs currently available. However, the efficacy of amantadine dropped by two orders of magnitude since 2002, mainly due to the S31N mutation in the TM domain (*8*). Thus, elucidating the mechanism of amantadine inhibition of AM2 has great public health relevance.

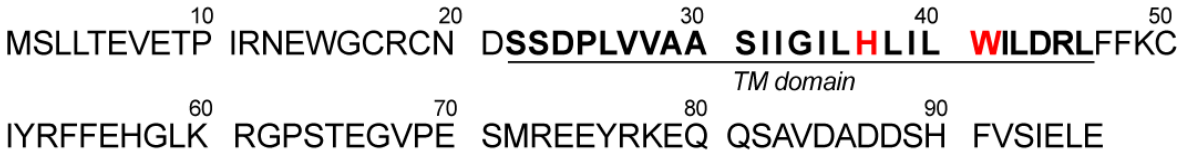

Figure 2.1. Amino acid sequence of influenza A/Udorn/72 M2 protein. The TM domain containing the crucial His_{37} and Trp_{41} residues (red) are underlined.

Recently, several high-resolution structural studies have been carried out to determine the structural basis of AM2 proton conductance and inhibition. In this article, we summarize the main functional data of AM2 and high-resolution structural information available on the TM domain, to promote future investigations of this intriguing and far from understood membrane protein.

Proton transport, selectivity, and activation. The proton conductance of AM2 has been well studied both in vivo and in vitro since its discovery as an ion channel (*3*). The gold

standard of M2 functional assays is the replication of live viruses in infected cells, followed by the "silver standard" of whole-cell conductance data in *Xenopus laevis* oocytes. The wild-type protein is activated below pH 6.2 and its current is sensitive to amantadine. The single-channel activity under a -130 mV voltage is ~0.16 μA/ng protein at pH 6.2 for the A/Udorn/72 strain of M2 (*4*), which corresponds to 12 aA per channel or a conductance of ~100 aS. Extraction of single-channel currents requires quantification of the amount of protein, and the assumption that all proteins form open channels or the knowledge of the fraction of open channels.

For in-vitro liposome assays, several additional factors such as the orientation of the protein in the membrane, the size and buffering capacity of the liposomes, and the fluxes of other monovalent ions (Na^+ and K^+) can affect the measured conductance. One of the most reliable liposome assays employed an intravesicular pH-sensitive dye to measure proton fluxes, and obtained a single-channel current of 2.7 aA at pH 5.7 and 18˚C (conductance = 29 aS) for full-length M2 in DMPC/DMPS vesicles (*9*). These values agree well with the oocyte result (*4*). Several other liposome assays gave more divergent values due to different experimental designs and protein constructs (*10-12*). However, the general consensus is that the single-channel conductance of M2 ranges from tens of aS to a few hundred aS, indicating low transport rates of ten to several hundred protons per second at mildly acidic pH. It is thought that the low currents are a result of the low physiological proton concentration (*9*), although the idea that M2 may have some characteristics of transporters has also been proposed (*13*).

There is general consensus that AM2 is selective for protons over Na^+ and K^+ by a factor of 1.5–3.0 x 10^6 (*9, 14, 15*), and that the increased proton current at low exterior pH (pH_{out}) is due to true activation of the channel rather than mere mass action, since increased pH_{out} stops the outward current of acidified cells (*15, 16*). The site of activation is His_{37}, the only residue in the TM domain that can be protonated within the relevant pH range. Mutation of His_{37} to either Gly or Glu results in channels that are no longer modulated by pH_{out} (*17*). Solid-state NMR (SSNMR) studies of His_{37} in the TM peptide M2(22-46) suggest that it is the third protonation at pH 6.3 that opens the channel (*18*).

His_{37} selectivity filter and Trp_{41} gate in the TM domain. His_{37} and Trp_{41} are the two most conserved residues in the M2 protein of influenza A strains (*19*) and are essential for channel function. His_{37} protonation is responsible for the activation and selectivity of the channel. The wild-type (WT) A/Udorn/72 M2 protein has 50-fold conductance difference between pH_{out} of 4.5 and 8.2. In contrast, many His_{37} mutants, while still forming channels, are toxic to oocytes and have pH-independent currents, indicating non-specific conductance of other cations (*17*). These mutants can be neither activated effectively by low pH_{out} (H37G, H37S and H37T) (*20*) nor inactivated by high pH_{out} (H37G, H37E and H37A) (*17*). The mutant channels are not proton selective and are only partially and reversibly blocked by amantadine (*20*), in contrast to the WT protein (*16*). Analytical ultracentrifugation (AUC) experiments indicate that H37A and H37F mutants are about 3.1 and 1.8 kcal/mol less stable than the WT peptide in DPC micelles (*21*).

When a high concentration of imidazole buffer is added to the bathing solution, proton-selective conductance and gating are partially restored to the His_{37} mutants (*20*). This chemical rescue is specific to imidazole and does not require interaction with Trp_{41}. Thus, His_{37} was proposed to be an intermediate proton acceptor and donor, consistent with SSNMR titration data of the TM peptide (*18*).

The M2 proton channel responds exclusively to external pH: low pH_{out} activates the channel and high pH_{out} closes the channel, regardless of the interior pH. Mutagenesis data indicates that Trp_{41} acts as the gate in concert with His_{37} (*22*). At high pH_{out} and low pH_{in}, the WT protein does not exhibit outward current while W41A/C/F mutants do, indicating loss of gating by the mutants (*22*). Further, intracellular Cu^{2+} inhibited the open W41A channel but not the WT channel, indicating that Trp_{41} shields His_{37} from coordination by Cu^{2+} (*22, 23*). These data suggest that the indole rings adopt distinct conformations at different pH_{out} to obstruct or open the pore. Resonance Raman data indicate that the Trp_{41} conformational change must be small to keep its environmental hydrophobicity unchanged (*24*). Concerted conformational changes seem necessary for His_{37} to act as the selectivity filter and Trp_{41} as the gate. Compared to His_{37}, the two Trp_{41} mutants that abolish gating (W41A and W41F)

(*22*) actually have enhanced tetramer stability in DPC micelles (*21*), indicating that this residue has evolved for function rather than stability.

Mechanism of proton transport. Molecular dynamics (MD) simulations have been used extensively to study the M2 proton transport mechanism. The basic premise is that protons hop along a water wire via the Grotthuss mechanism, but the water wire is broken at the narrow His_{37} constriction (and possibly other locations along the channel). Thus, the mechanism of proton passage through the His_{37} tetrad is the central question. Two main models have been proposed: the gating model and the shuttle model. In the gating model, protonation of the His_{37} tetrad at low pH causes pore opening by electrostatic repulsion, so that a continuous water wire is formed (*25*). Conformational changes of the His_{37} and possibly Trp_{41} are necessary in this model. MD simulations suggest that a 60° change of the His_{37} χ_2 angle may be sufficient to open the pore (*26*), and the excess proton may form a Zundel complex with two water molecules on the extra- and intracellular side of the histidine rings (*27, 28*). Early MD simulations postulated various charged states of His_{37} for channel activation (*29*). However, with SSNMR data indicating the third protonation of the His_{37} tetrad to be responsible for channel opening (*18*), recent simulations confirmed that the +3 state has the lowest proton permeation free energy (*30*). The channel water molecules that transport the protons were calculated to have three-fold lower diffusion coefficients than bulk water (*27, 31*).

The second proton transport model is the shuttle model, where the imidazole nitrogen facing the extracellular side binds one proton to form a biprotonated intermediate, then the other nitrogen releases the proton on the intracellular side and returns the imidazole to the neutral form (*32*). The initial state is then recovered by tautomerization or ring flip of the imidazole. This model explains the low proton transport rate and low-pH saturation of the channel, since both would be associated with the limiting rate of His_{37} sidechain torsional motion or tautomerization.

Simulations of the protein conformation at different pH also shed light on the mechanism of proton transport. One proposal is that in addition to His_{37}, Val_{27} may act as a

secondary gate that breaks the water wire, especially in the presence of amantadine (*33*). The two gates may not be static but instead may move synchronously in response to His_{37} protonation: at high pH the Val_{27} region opens while the His/Trp region narrows, and the opposite is found at low pH (*13*). Thus, instead of equating high pH with the closed state and vice versa, these simulations suggest a more complex view of an $Open_{out}$-$Closed_{in}$ conformation at high pH and $Closed_{out}$-$Open_{in}$ conformation at low pH. This model reconciles the different helix orientations and packing in different high-resolution structures (*34-37*).

Inhibition of the AM2 channel. Three classes of M2 inhibitors have been identified so far: the adamantane analogs (*38, 39*), the spirene-containing compounds (*40*), and Cu^{2+} ions. The FDA approved amantadine achieves its antiviral effect by inhibiting the M2 proton channel activity (*3*): 100 μM amantadine nearly irreversibly blocks > 90% of the channel activity of A/Udorn/72 (H3N2) M2 in several minutes at both acidic and neutral pH (*16, 41, 42*). For some other influenza strains the amantadine block is stronger at neutral pH than at low pH (*16*). The Hill coefficient of the amantadine block is 1, consistent with the scenario that a single drug inhibits each functional channel (*16*).

Naturally occurring mutations in the TM domain that confer amantadine resistance include L26, V27, A30, S31, and G34, all N-terminal to G34 (*8, 38, 43, 44*) (Figure 2.1). Extensive whole-cell conductance studies have been carried out on these mutants. S31N, the most common resistant mutant (*8*), has an IC_{50} of 199.9 μM, more than ten times higher than that of the WT (IC_{50} = 16 μM) (*41*). The resistance is not due to altered channel activity, as S31N has very similar specific activity and acid activation as the WT (*4, 42*). L26F has ~35% higher channel activity than S31N but is more sensitive to amantadine (*42*). G34E has a 3-fold higher specific activity than S31N and is about 5-fold less sensitive to amantadine than S31N (*4*). V27 mutants have mixed phenotypes: V27A and V27S are amantadine resistant but V27T is amantadine sensitive, and all V27 mutants have significantly increased (~ 3 fold) channel activities than WT (*4*). In contrast, the A30T mutant has a greatly reduced but still detectable activity, while the A30P mutant is inactive (*4*). Thus, residue 30 appears to be important for maintaining a functional structure of the protein. Among the resistant mutants,

S31N was found by thiol-disulfide exchange experiments to be stable in both bilayers and micelles (*42*), suggesting a reason for its dominance in current flu strains that is independent of the selective pressure of amantadine. The stability and similar channel activity of S31N to the WT protein argue against the model that the S31N variant is resistant to amantadine by destabilizing the closed state and favoring the open state of the channel (*45*). The latter hypothesis was made based on the larger NMR linewidths of S31N than WT proteins in the presence of rimantadine. However, since S31N does not bind rimantadine, the correct comparison should be between S31N and the apo WT protein, which is known to exhibit broad linewidths as well.

In the C-terminal region of the TM domain, L38F, W41A, and D44A mutants incorporated into influenza viruses showed similar growth as the WT protein in infected cells, and the growth is sensitive to amantadine (*41*) (despite the fact that the W41A mutant does not gate properly (*22*)). Electric recordings in oocytes indicate that the IC_{50} of D44A is 15.8 μM, indistinguishable from the WT protein. Thus, no amantadine-resistant mutations have been found C-terminal to G34, implicating the segment between L26 and G34 to be the amantadine-binding region (*41*). Further, when residues 6-18 of the amantadine-insensitive BM2 were replaced by AM2 residues 24-36, the chimeric protein showed amantadine-sensitive currents in oocytes (*41*), strongly indicating that the C-terminal region of the AM2 TM helix is not required for amantadine binding. In contrast, a recent liposome proton flux assay of M2(18-60) found the D44A mutant to be resistant to rimantadine while the S31A mutant to be sensitive, supporting a C-terminal binding model (*34, 45*). This liposome assay result is in serious contradiction with the finding from the "gold standard" assay that replication of live virus bearing the D44A mutation is inhibited by rimantadine (*41*).

The second class of M2 inhibitors are spirene-containing compounds, initially discovered from a growth impairment assay where the M2 toxicity to yeast cells due to its proton channel activity is reversed by inhibitors (*40*). The first compound, BL-1743 (2-[3-azaspiro(5,5)undecanol]-2-imidazoline), has similar inhibition rate, Hill coefficient, and spectra of resistance as amantadine (*46*). However, BL-1743 inhibition is reversible (~12 minutes) while amantadine block is irreversible on the experimental time scale (~30 minutes). BL-1743 also differs from amantadine in its interaction with I35: the I35T mutant

is resistant to BL-1743 but is reversibly inhibited by amantadine (*46*). The cause of this difference is suggested by a recent SSNMR study of the analogous spirene-piperidine compound, 3-azaspiro (5,5) undecane hydrochloride (IC_{50} = 0.92 μM) (*47*). This compound reduces the dynamic disorder of the G34-I35 backbone of AM2, suggesting that spirene-amine inhibitors bind more extensively and strongly with the TM helices than the adamantane inhibitors.

B. High-resolution structure of AM2 TM domain

Orientation of the TM helices in lipid bilayers. The TM peptide of AM2 has been a prime target for high-resolution structure investigation by a number of biophysical techniques. Both global structural information such as helix orientation and site-specific information of key residues have been obtained. The orientation of the TM helices in lipid bilayers has been extensively studied by SSNMR, EPR and IR techniques. The majority of SSNMR studies measured orientation-dependent ^{15}N tensors on glass-plate aligned M2(22-46) (*37, 48-51*) and to a small extent on aligned full-length M2 (*52, 53*). From 1D ^{15}N chemical shift anisotropies (CSA), Cross and coworkers obtained a helix tilt angle of 33°-37° for M2(22-46) in DMPC bilayers (*49, 50*) and 33° in DOPC bilayers. 2D NMR spectra correlating ^{15}N-^{1}H dipolar couplings and ^{15}N CSAs gave more precise orientational constraints, including both the tilt angle (τ) and the rotation angles (ρ) of individual residues. From these 2D spectra, the tilt angle of apo M2(22-46) in DMPC bilayers was refined to 38° (*51*), while the rotation angles are consistent with the pore- or lipid-facing positions of residues inferred from functional data (PDB: 1NYJ).

Prior to 2001, the oriented NMR studies were conducted on peptides that were first mixed with lipids in organic solvents before hydration. These samples were not pH controlled and may be acidic due to residual TFA. After 2001, the oriented membranes were prepared by an aqueous protocol where M2 was reconstituted into lipid bilayers by detergent dialysis at controlled pH before alignment on glass plates. The amantadine-bound M2(22-46) and the full-length M2 were studied in this way. In DMPC/DMPG lipid bilayers, the 2D spectra of uniformly ^{15}N-labeled full-length M2 at pH 8.0 showed a TM helix with a 25° tilt,

which is smaller than the tilt of the TM peptide alone, and an 80˚ tilted helix, which is attributed to an amphipathic helix C-terminal to the TM domain (*52*). Hydrogen/deuterium exchange of full-length M2 showed that the TM helix underwent fast H/D exchange, consistent with its participation in forming an aqueous pore, while the 80˚-tilted helix resisted H/D exchange, indicating that it is shielded from water. Full resonance assignment is necessary to elucidate the orientation and depth of this C-terminal amphipathic helix.

Upon amantadine binding, M2(22-46) exhibits a pronounced kink at G34 in DMPC bilayers, with a tilt angle of 31˚ for the N-terminal segment and 20˚ for the C-terminal segment (PDB: 2H95) (Figure 2.5a) (*48*). While it is tempting to conclude that amantadine caused this kink, the bound peptide spectra were obtained from aqueous prepared samples at pH 8.8, under which condition there is no comparable apo peptide data. It is thus possible that the kink may already be present in the apo state, especially given the known propensity of Gly to perturb α-helices. Indeed, other high-resolution structures of AM2 suggest a G34 kink already in the apo state. For example, MAS-NMR data of DLPC-bound M2 suggest a kink of 5° for the bound peptide and 8˚ for the apo peptide (*36*), while the crystal structure of apo M2 at neutral pH shows a distribution of helix kink angles (*35*).

Direct comparison of the orientation of apo and amantadine-bound M2(22-46) prepared under the same conditions was reported recently (*54*). Using unoriented DLPC vesicles and dialysis reconstituted M2(22-46), Hong and coworkers determined the helix orientations by exploiting the uniaxial diffusion of the helical bundles around the bilayer normal. The N-terminal half of the TM segment was found to have a tilt angle of 35˚ in the apo state and a slightly larger tilt of 38˚ in the amantadine-bound state (*55*) (Figure 2.5d), indicating that the drug slightly enlarges the pore vestibule.

The TM helix orientation is also sensitive to membrane thickness. EPR spectra of N-terminus nitroxide labeled M2(22-46) reconstituted into DLPC, DMPC, DOPC, and POPC bilayers showed the least dipolar broadening in the thinnest DLPC membrane and the strongest broadening in the thickest POPC membrane (*56*). The broadening is attributed to shorter interhelical distances as the peptide decreases its tilt angle in the thicker membrane. The orientational change was detected directly in SSNMR spectra of unoriented M2(22-46).

The TM helices showed a tilt angle of 35˚ in DLPC bilayers but a much smaller angle of 26˚ in the thicker POPC bilayers (*54*). These results are consistent with AM2 adjusting its TM helix orientation to minimize the hydrophobic mismatch with the lipid bilayer, as also observed for other membrane peptides (*57, 58*). These results revise an earlier conclusion that the M2 helix orientation is intrinsic to the peptide and unaffected by the membrane (*50*), made based on the fortuitously similar orientations of the peptide in DMPC and DOPC bilayers because of the similar thickness of these two bilayers.

The SSNMR and EPR orientational studies do not detect evidence of rotational angle change of M2 by pH: both the organic-solvent prepared samples, which likely have acidic pH, and the aqueous samples at high pH, gave the same rotation angles. These results are consistent with the functional requirement for a hydrophilic pore. Distances between the Trp_{41} indole 5-^{19}F of neighboring helices were also found to be the same (11.8 Å) at pH 7.5 and pH 4.5 (Figure 2.2), consistent with the lack of ρ change (*59*). Thus, it is surprising that a recent IR study of M2(22-46) in DMPC bilayers reported a one-residue (100˚) rotation of the helices between low and high pH (*60*). The ρ angle of the low pH samples was found to agree well with early SSNMR data (*37, 51*) while that of the high pH samples differ by ~100˚. When the ρ angles were combined with the +3 protonated His_{37} tetrad, MD simulations found that the rotated helices reduce His_{37} exposure to water at high pH, thus rationalizing channel closure (*61*). The ρ angles were extracted from diagonal linewidths of 2D IR spectra, which reflect the electrostatic environment of the $^{13}C=^{18}O$ groups, the main contributor of which is thought to be the water contact. However, the 2D lineshape analysis requires the distinction of homogeneous and inhomogeneous linewidths, consideration of population relaxation times, and consideration of water-independent electrostatic effects such as hydrogen bond network of the peptide. Thus the origin of the diagonal linewidth change is complex. In addition, linear FT-IR dichroism data for the high pH samples reported in this work do not show a clear sinusoidal dependence with the residue number, casting further doubt on the high pH ρ angle result (*60*).

Tetramer stability and packing. In mammalian cells and oocytes the functional state of M2 is tetrameric, as shown by sucrose gradient, chemical cross-linking (*62*) and conductance experiments (*5*). In detergents and lipid bilayers, the TM peptide retains the tetrameric state under a wide range of conditions, and the monomer-tetramer equilibrium is readily shifted by membrane thickness, pH, amantadine binding, cholesterol, and amino acid sequence. The environmental effects on the free energy of tetramer association have been the focus of study using AUC in micelles (*21, 63*) and thiol disulfide exchange in lipid vesicles (*64*). It was shown that M2(19-46) tetramers are increasingly stabilized in the direction of detergents << DLPC < DMPC < POPC. Among lipid bilayers the hydrophobic-thickness matched bilayers produce the most stable tetramers (*64*), but even the thinnest bilayer (DLPC) induces 100-fold tighter tetramer association than detergents. Both amantadine and cholesterol shift the equilibrium to tetramers (*64, 65*). Compared to external environmental factors, the sequence requirement for tetramer formation is much more lenient: Ala and Phe mutations of a number of pore residues retain stable M2(22-46) tetramers in DPC micelles, with the exception of the functionally essential His_{37} (*21*). However, more stable tetramers are often less functional tetramers, as manifested by their reduced ability to bind amantadine (*63*). For example, the most amantadine-resistant S31N mutant forms 0.4 kcal/mol more stable tetramers than the WT protein (*42*). This inverse relationship between stability and function suggests that the multiple M2 functions –proton conduction, gating and inhibitor binding – may require conformational flexibility, which cannot be provided by highly stable mutants locked in the wrong conformational minima.

Direct distance constraints for M2 tetramers in lipid bilayers were recently reported based on ^{19}F spin diffusion SSNMR experiments that probe ^{19}F-^{19}F distances in the ~10 Å range (*66, 67*). So far, four interhelical ^{19}F-^{19}F distances have been reported for M2(22-46) in DMPC bilayers. On 4-^{19}F labeled A30F M2, the ^{19}F spin diffusion equilibrium value of 1/4 directly proved the tetrameric state, and the decay trajectory yielded a distance of 8.5 ± 0.6 Å between nearest neighbor helices (Figure 2.2a). This distance rules out helix tilt angles smaller than 20° and constrains the Phe χ_1 angle. The ^{19}F NMR data of V27F suggest incomplete tetramer formation (partial dimers), which is consistent with the reduced stability

of this mutant seen in AUC experiments (*21*). The L38F NMR data also indicated distance heterogeneities (*59*).

His_{37} and Trp_{41} sidechain conformation. A semi-quantitative ^{13}C-^{15}N distance between His_{37} Nπ and Trp_{41} Cγ was measured on DMPC-bound M2(22-46) at pH 7 and 38˚C using SSNMR REDOR experiments (*37*). Significant dipolar dephasing was observed that corresponded to a minimal coupling of 63±12 Hz (*37*) or a maximum distance of 3.9 Å. The limiting nature of this result is because the measurements were done at physiological temperature where M2(22-46) undergoes uniaxial diffusion around the bilayer normal, which averages the dipolar coupling (*50, 54*). Scanning the possible His and Trp rotameric states indicate that this C-N distance must be between helices *i* and *i*+1, and suggested that His_{37} adopts the t-160 (χ_1=180˚, χ_2=-160˚) rotamer while Trp_{41} adopts the t-105 rotamer (PDB code: 1NYJ) (*37*). Subsequent reexamination of the conformational space of the two residues indicates that other possible solutions also exist: His_{37} can adopt the t-160 or the t60 rotamer, while Trp_{41} can adopt the t-105 or the t90 rotamer. Density functional theory calculations and MD simulations suggest that the most stable combination is (t60, t90) (*26*).

^{19}F spin diffusion NMR experiments provided a direct distance constraint on the Trp_{41} sidechain conformation. The *i* - *i*+1 distance between 5-^{19}F-Trp_{41} of M2(22-46) was measured to be mainly 11.8 Å at pH 7.5 (*59*) (Figure 2.2a), and the value does not change significantly with amantadine binding and pH. When the helix orientation is fixed to 35˚ and the channel diameter is fixed to 10.2 Å between G34 Cα, the only Trp_{41} rotamer that is consistent with the ^{19}F-^{19}F distance is t90, which is consistent with the MD prediction (*26*). Combined with the measured His_{37}-Trp_{41} C-N distance, the (t-160, t90) rotamer pair was proposed for the closed state of His_{37} and Trp_{41} (*59*). This conformation suggests that it may not be Trp_{41} alone but rather the cation-π interaction between His_{37} and Trp_{41} that is responsible for gating and the shielding of His_{37} from intracellular ions (Figure 2.2b).

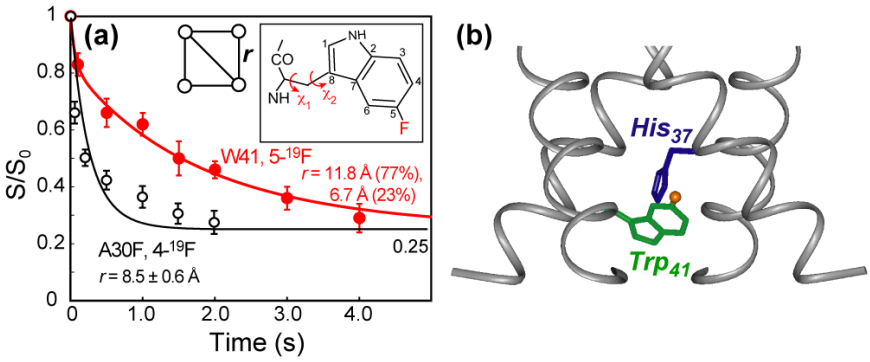

Figure 2.2. (a) Interhelical ^{19}F-^{19}F spin diffusion data of 5-^{19}F-Trp_{41} WT M2 (red) and 4-^{19}F-A30F M2 (black) in DMPC bilayers (*59, 67*). The best-fit distances confirm the tetrameric state of the peptide, and constrain the Trp_{41} sidechain (χ_1, χ_2) torsion angles (inset). (b) Trp_{41} t90 and His_{37} t-160 rotamers proposed from the distance data.

A third Trp_{41} rotamer of (χ_1=-100°, χ_2=+100) was proposed for the high pH state of M2 based on analysis of ^{19}F NMR lineshapes under the combined effects of ^{19}F CSA and ^{19}F-^{19}F interhelical dipolar couplings (*68*). However, the presence of intermediate time scale broadening of the spectra and the lack of information on the orientational angles between the ^{19}F chemical shift tensor and the F-F dipolar tensors make this analysis a severely under-determined problem. The resulting rotamers are also inconsistent with any of the computational predictions (*26*).

His_{37} protonation state. The charged state of His_{37} gives crucial information on the activation of the M2 proton channel. The pK_a of His_{37} in micelle-bound M2(22-46) was measured by ^1H solution NMR to be 6.8 for the monomer and 6.4 for the tetramer in the absence of drug (*65*). Amantadine decreases the tetramer pK_a to 5.8. UV resonance Raman experiments on M2(22-46) in POPE/POPS membranes found a pK_a of 5.7 based on the intensity of the 1407 cm^{-1} band (*24*). This imidazole band has the same intensity in liposomes and in SDS micelles at pH 4.0, indicating that all four His residues are protonated at pH 4.0 (*24*).

By far the most definitive study of His_{37} protonation states came from ^{15}N SSNMR experiments of M2(22-46) in DMPC/DMPG bilayers by Cross and coworkers (*18*), who monitored the imidazole Nδ1 and Nε2 ^{15}N isotropic chemical shifts as a function of pH. Two neutral tautomers were found at pH 8.6, with the unprotonated nitrogen exhibiting a large isotropic shift of ~230 ppm. Between pH 8.0 and pH 7.0, two +1 dimer species, His-$HisH^+$, were concluded. Based on the relatively large ^{15}N linewidths in this pH range, which suggest intermediate time scale motion, low-barrier hydrogen bonds between imidazole and imidazolium within each dimer were proposed. Below pH 6.5 and pH 5.0, the third and fourth His are protonated. Quantification of the spectral intensities yielded four pKa's at 8.2, 8.2, 6.3 and < 5.0. Thus, the first two histidines titrate cooperatively at higher pH than the aqueous pK_a of His (6.0). Since the +1 dimers already exist at neutral pH, they are proposed to form a histidine-locked state that occludes the pore (*18*). The binding of the third proton below pH 6.3 was proposed to break the two-fold symmetry of the +1 dimers and thus activates the channel.

Amantadine binding changes the titration curve of the His_{37} tetrad (*69*). The 230 ppm unprotonated ^{15}N peak persisted to a much lower pH of 6.0 in the presence of the drug. Intensity analysis shows that the bound peptide has only one pK_a near 5.4. The nature of this apparently highly cooperative protonation event is still unknown. In addition, the ^{15}N peak associated with the His-$HisH^+$ dimer is no longer observed in the amantadine-bound peptide, suggesting that the neutral tautomers directly form biprotonated histidines in the presence of amantadine. Further studies are necessary to elucidate the amantadine-induced changes of His_{37} protonation.

Extensive conformational dynamics of AM2. The M2 homo-tetramer exhibits extensive conformational dynamics in lipid bilayers and lipid-mimetic detergents, as well documented by SSNMR and solution NMR spectra. Membrane-bound apo M2(22-46) shows dynamically broadened lines in both unoriented vesicle spectra (*36, 55*) and oriented spectra (*70*) at ambient temperature in a range of model membranes: DLPC, DMPC/DMPG, and POPC. The fact that the line broadening is mainly dynamic in origin rather than due to static

conformational distributions is proved by the temperature dependence of the linewidths. The broadest lines are observed between 298 K and 263 K (*54*), above and below which the lines narrow (Figure 2.3a). Acidic pH broadens the lines compared to neutral pH for both membrane-bound M2(22-46) (*70*) and detergent-bound M2(18-60) (*34*). In all solvent environments and for both M2(22-46) and M2(18-60), amantadine noticeably narrows the linewidths (Figure 2.3b). The line broadening or narrowing occur for all residues, thus it reflects the dynamic property of the whole protein rather than segmental motion.

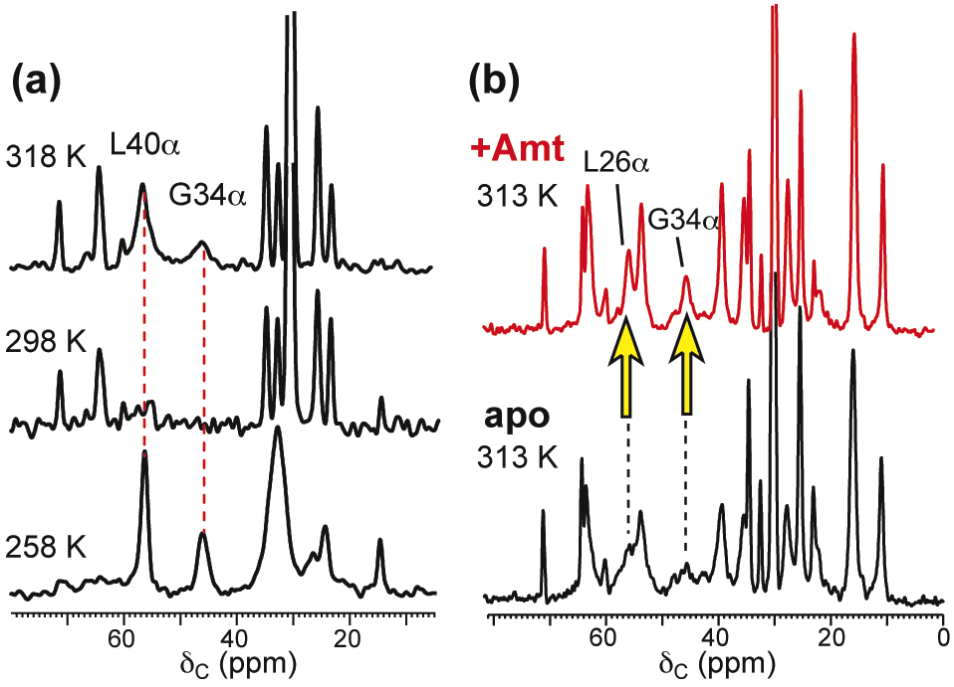

Figure 2.3. ^{13}C MAS spectra of DLPC-bound M2(22-46). (a) Variable temperature ^{13}C MAS spectra indicate large-amplitude intermediate timescale motion at ambient temperature (*54*). (b) Amantadine narrows the linewidths of most residues at 313 K (*55*).

The origin of the broad linewidths and their narrowing by amantadine has been examined in detail by SSNMR (*54, 71*). The main motion accounting for the broad linewidth is the whole-body uniaxial diffusion of the tetramers around the bilayer normal, as shown by motionally averaged ^{2}H, ^{15}N and ^{13}C NMR lineshapes (Figures 2.4a, b) (*54*). The correlation

time of this uniaxial diffusion has been estimated from relaxation studies to be ~3 μs (*71*) for DLPC-bound apo M2(22-46) at 313 K, which is very close to the time scale of the radio-frequency pulses and nuclear spin interactions (2-4 μs), thus causing intermediate time scale broadening. Amantadine binding reduces the correlation time by 2-3 fold at 313 K (*71*) (Figure 2.4c), thus avoiding exchange broadening and narrowing the NMR lines. The larger diffusion rates strongly suggest that amantadine promotes the formation of more homogeneous helical bundles (Figure 2.4d), which is consistent with the increased tetramer stability observed in thiol disulfide exchange experiments (*64*). The NMR relaxation data also indicate that excess amantadine in the bilayer increases the membrane viscosity. Since protein rotational diffusion is generally sensitive to membrane viscosity, cholesterol-rich virus-mimetic membranes immobilize this diffusion, and was found to suppress exchange broadening and give rise to high-resolution NMR spectra in a wide temperature range (*72*).

Whether the whole-body uniaxial diffusion has functional importance is not known. If the viral envelope is in a liquid-ordered phase, then M2 is most likely immobilized. But if the virus envelope contains significant liquid-disordered domains, then the fact that M2 is poorly incorporated into raft-like microdomains (*73*) should promote uniaxial diffusion in the functional state. Most spectroscopic studies so far were carried out on M2 bound to non-cholesterol-containing membranes or bound to detergents, which favor the whole-body motion. Thus site-specific conformational dynamics have not been separated from the whole-body motion. In this light, the larger linewidths of M2 at low pH are at least partly due to global motional changes, and their interpretation in the context of pH activation needs to be considered carefully (*34, 70*).

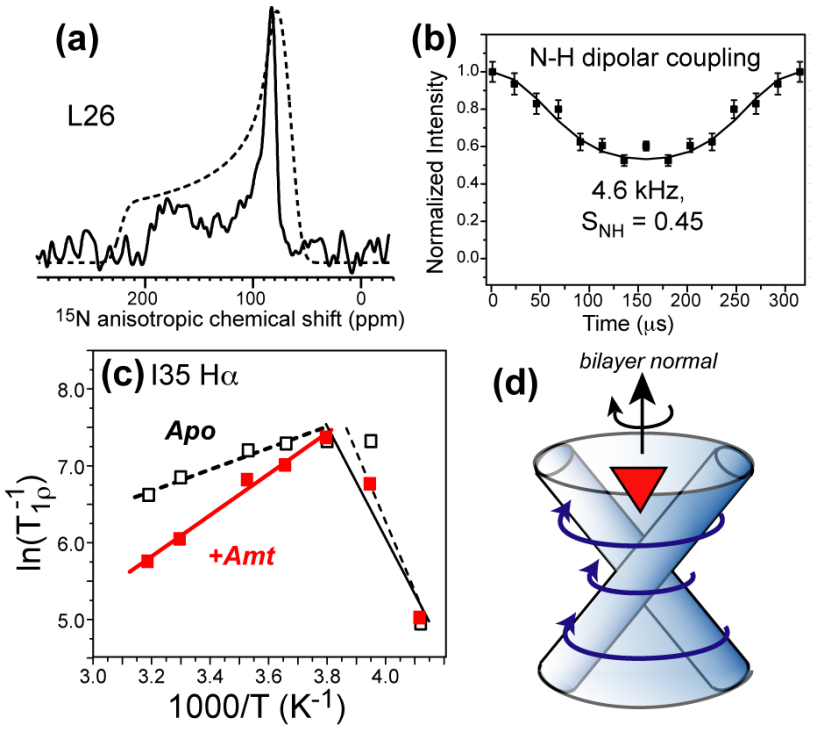

Figure 2.4. Uniaxial diffusion of M2(22-46) helical bundles around the bilayer normal. (a) ^{15}N CSA of L26 is uniaxially averaged from the rigid-limit pattern (dashed line) (*54*). (b) L26 N-H dipolar coupling is reduced from the rigid-limit coupling. (c) Amantadine decreases ^{1}H $T_{1\rho}$ relaxation rates at high temperature, indicating it speeds up protein motion (*71*). (d) Schematic of M2 uniaxial diffusion. Amantadine binding creates better packed tetramers, thus speeding up rotational diffusion.

Amantadine binding in high-resolution structures. Two atomic-resolution structures of TM-containing portions of AM2 were recently solved using X-ray crystallography and solution NMR, which shed light on the pH activation of the channel and led to two different models of M2 inhibition (*74*).

The crystal structures were solved on M2(22-46) in octyl-β-D-glucopyranoside (OG) at pH 7.3 in the absence of amantadine (PDB: 2BKD) (2.0 Å resolution) and at pH 5.3 in the presence of amantadine (PDB: 3C9J) (3.5 Å resolution) (*35*). In both structures, the N-terminal half of the TM domain has a tilt angle of ~35°, consistent with SSNMR data (*51, 54*). The orientation of the C-terminus half of the TM helix depends on the pH: at low pH the helices are uniformly straight and diverge toward the C-terminus, creating an open cavity,

but at pH 7.3 two of the four helices bend and create a small pore at the His_{37}/Trp_{41} region. The amantadine-bound structure, solved with a 1.3 : 1 protein : amantadine molar ratio, shows a single drug molecule in the pore, surrounded by residues that confer drug resistance (Figure 2.5b). Thus, the amantadine binding site and stoichiometry agree with electrophysiology data (*16*), and the crystal structure supports a occlusion model for channel inhibition.

The solution NMR structure was solved on rimantadine-bound M2(18-60) in DHPC micelles at pH 7.5 (PDB: 2RLF) (*34*). The sample contains 0.75 mM protein, 40 mM rimantadine and 300 mM DHPC, thus the drug is in 53-fold excess to the protein or ~210 fold excess to the channel. The TM helix is tilted by ~15˚ from the bilayer normal and the C-terminal amphipathic helix is roughly perpendicular to the TM helix. Low pH broadens the linewidths and increases the millisecond motion of Trp_{41}. Four protein-rimantadine NOEs were found to lipid-facing residues L40, I42, L43, and R45 near the C-terminus of the TM helix, with four rimantadine molecules per tetramer (Figure 2.5c). Since this surface binding site is inconsistent with the large body of mutagenesis data that place drug-resistant mutations at pore-facing residues at the N-terminus, the authors proposed that rimantadine inhibits the channel by stabilizing its closed state and making the channel harder to open, whereas drug-resistant mutations destabilize the closed channel and make it easier to open. However, this allosteric inhibition model is inconsistent with the one-drug-per-channel stoichiometry of amantadine (*16*), and also contradicts virus replication and whole cell conductance data that showed D44A and R45A mutants to be amantadine sensitive (*41*). The drug – protein NOEs involve residues in the headgroup region of the micelle, exactly where the amphiphilic rimantadine is located based on paramagnetic relaxation NMR data (*75, 76*). At the high concentration of 40 mM, rimantadine constitutes 12 mol% of the micelle, making the surface binding site a likely secondary lipid binding site rather than the true inhibition site. Given the abundant reorientational dynamics of the peptide and amantadine discussed above (*55, 71*), the lack of NOEs between the N-terminal pore residues and rimantadine could arise from motion on unfavorable time scales that broadens the NMR signals and/or make the NOE intensity vanish. Thus, while this work shows the presence of rimantadine on

the outside of the protein, they do not provide strong evidence against an additional binding site within the pore.

It is unlikely for the different protein lengths to be the cause for the drug binding site difference, since the TM peptide is capable of binding amantadine, folding into appropriate tetramers, and having at least 50% of the proton conductance of full-length M2 (*77*).

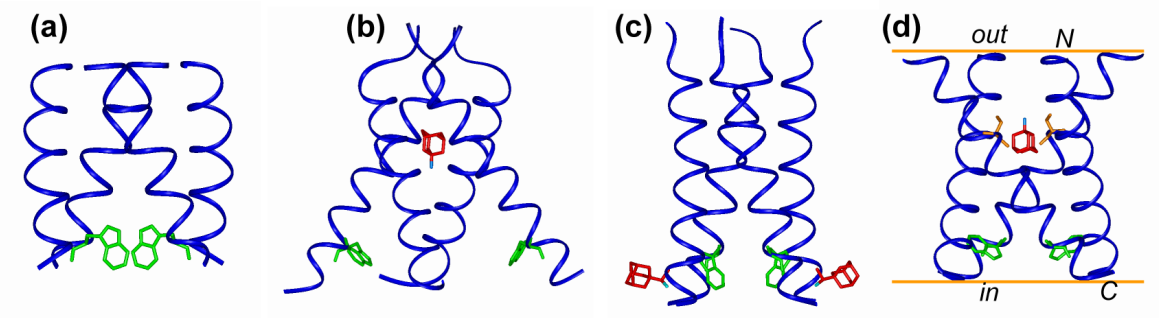

Figure 2.5. High-resolution structures of the TM domain of AM2. (a) Amantadine-bound orientational structure of M2(22-46) in DMPC bilayers at pH 8.8 from oriented-membrane SSNMR (PDB: 2H95) (*48*). The drug binding site was not directly studied but was implicitly assumed to be in the pore at the N-terminus side. (b) Amantadine-bound crystal structure of M2(22-46) in OG at pH 5.3 (PDB: 3C9J) (*35*). (c) Rimantadine-bound solution NMR structure of M2(18-60) in DHPC micelles at pH 7.5 (PDB: 2RLF) (*34*). Only the TM part is shown. (d) Amantadine-bound structure of M2(22-46) in DLPC bilayers at pH 7.5 from MAS SSNMR (PDB: 2KAD) (*36*). The amantadine position is hypothesized based on chemical shift perturbation of S31. The bilayer planes are drawn for reference. In each structure, two of the Trp_{41} indole rings (green) are shown, and the drug molecules are shown in red. IN (c), only two rimantadine molecules are shown for clarity.

The above two high-resolution structures were solved in detergents and micelles. Recently, an amantadine-bound structure of M2(22-46) in DLPC bilayers was reported based on MAS SSNMR data (*36, 55*). The experiments were carried out at a peptide : amantadine : DLPC molar ratio of 1 : 8 : 15. The main conformational constraints came from ^{13}C and ^{15}N isotropic chemical shifts (CS) measured at 243 K where the protein dynamics is frozen.

Comparison of the apo and bound peptide chemical shifts indicated that the M2(22-46) conformation is most perturbed by amantadine at S31, with a large ^{15}N CS change of 7 ppm, strongly suggesting drug binding near S31 (Figure 2.6a). The CS perturbation is also high for G34 and V28, while the C-terminal L38 and D44 are minimally affected (Figure 2.6b). The chemical-shift predicted (ϕ, ψ) angles for the apo and bound monomers also show that the apo peptide has a slightly larger kink than the amantadine-bound peptide. The monomer structure was combined with the helix orientation and inter-helical ^{19}F-^{19}F distances to lead to a tetramer structure for M2(22-46) at pH 7.5 (PDB: 2KAD). The tetramer has larger N-terminus vestibule than the other structures, and differs in the Trp_{41} conformation (*36*) (Figure 2.5d). SSNMR studies also found that amantadine slightly perturbs the sidechain conformations of V27 and V28 (*78*).

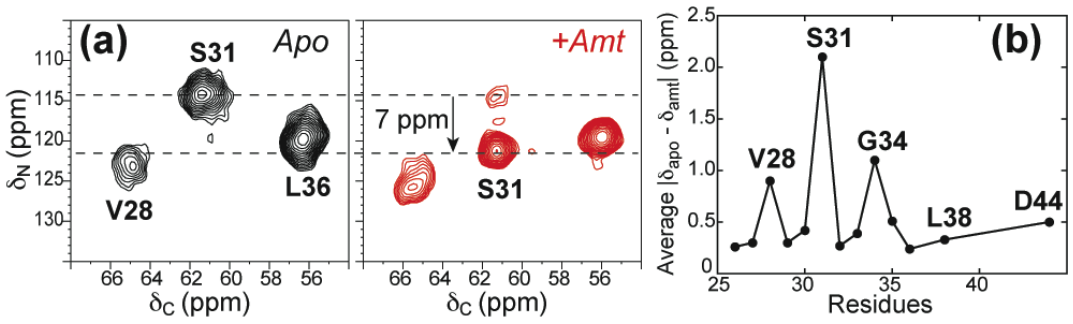

Figure 2.6. SSNMR evidence for amantadine binding near S31. (a) 2D ^{15}N-^{13}C correlation spectra of DLPC-bound M2(22-46) in the absence (black) and presence (red) of amantadine (*36*). (b) Chemical shift perturbation by amantadine in bilayer-bound M2(22-46).

C. Future directions

While a large amount of biochemical and structural information have been obtained for the M2 proton channel, many open questions remain about this fascinating multi-functional protein. So far the most complete three-dimensional structures were solved in detergents and micelles, which are only partial mimics of lipid bilayers. Given the plasticity of the protein, high-resolution structural studies in lipid bilayers that mimic the virus

envelope will be very valuable. Most structural studies so far used partial constructs of the full-length protein, thus future studies of the full-length protein will clearly be desirable, especially to understand the role of the C-terminal amphipathic helix, which was found to be able to affect ion channel function by interacting with the TM helix (*79*). Elucidating how M2 changes its conformation and dynamics between high pH and low pH is central to understanding its activation, and will require atomic-resolution information of His_{37} and Trp_{41} conformation as a function of pH. Clearly, protein-drug distances in lipid bilayers will be essential for resolving the controversy of M2 inhibition. Finally, the ultimate public health benefit of this research is to develop new antiviral drugs to target the dominant mutants of influenza A viruses to prevent future influenza pandemics. Achieving this end will require a combination of pharmacological, biochemical, and structural studies.

References

1. Lamb, R. A., Holsinger, K. J., and Pinto, L. H. (1994) The Influenza A virus M2 ion channel protein and its role in the influenza virus life cycle, in *Cellular Receptors of Animal Viruses* (Wemmer, E., Ed.), pp 303-321, Cold Spring Harbor Lab Press, Plainview, NY.
2. Sugrue, R. J., Bahadur, G., Zambon, M. C., Hall-Smith, M., Douglas, A. R., and Hay, A. J. (1990) Specific structural alteration of the influenza haemagglutinin by amantadine, *EMBO J. 9*, 3469-3476.
3. Pinto, L. H., Holsinger, L. J., and Lamb, R. A. (1992) Influenza virus M2 protein has ion channel activity, *Cell 69*, 517-528.
4. Holsinger, L. J., Nichani, D., Pinto, L. H., and Lamb, R. A. (1994) Influenza A virus M2 ion channel protein: a structure-function analysis, *J. Virol. 68*, 1551-1563.
5. Sakaguchi, T., Tu, Q., Pinto, L. H., and Lamb, R. A. (1997) The active oligomeric state of the minimalistic influenza virus M2 ion channel is a tetramer *Proc. Natl. Acad. Sci. USA 94*, 5000-5005.
6. Pinto, L. H., and Lamb, R. A. (2006) The M2 Proton Channels of Influenza A and B Viruses, *J. Biol. Chem. 281*, 8997-9000.

7. Pinto, L. H., and Lamb, R. A. (2007) Controlling influenza virus replication by inhibiting its proton channel, *Mol. Biosyst. 3*, 18-23.
8. Bright, R. A., Medina, M. J., Xu, X., Perez-Oronoz, G., Wallis, T. R., Davis, X. M., Povinelli, L., Cox, N. J., and Klimov, A. I. (2005) Incidence of adamantane resistance among influenza A (H3N2) viruses isolated worldwide from 1994 to 2005: a cause for concern, *Lancet 366*, 1175-1181.
9. Lin, T. I., and Schroeder, C. (2001) Definitive assignment of proton selectivity and attoampere unitary current to the M2 ion channel protein of influenza A virus, *J. Virol. 75*, 3647-3656.
10. Moffat, J. C., Vijayvergiya, V., Gao, P. F., Cross, T. A., Woodbury, D. J., and Busath, D. D. (2008) Proton transport through influenza A virus M2 protein reconstituted in vesicles, *Biophys. J. 94*, 434-445.
11. Vijayvergiya, V., Wilson, R., Chorak, A., Gao, P. F., Cross, T. A., and Busath, D. D. (2004) Proton conductance of influenza virus M2 protein in planar lipid bilayers, *Biophys. J. 87*, 1697-1704.
12. Duff, K. C., and Ashley, R. H. (1992) The transmembrane domain of influenza A M2 protein forms amantadine-sensitive proton channels in planar lipid bilayers, *Virology 190*, 485-489.
13. Khurana, E., Dal Peraro, M., DeVane, R., Vemparala, S., DeGrado, W. F., and Klein, M. L. (2009) Molecular dynamics calculations suggest a conduction mechanism for the M2 proton channel from influenza A virus, *Proc. Natl. Acad. Sci. U. S. A.... 106*, 1069-1074.
14. Chizhmakov, I. V., Geraghty, F. M., Ogden, D. C., Hayhurst, A., Antoniou, M., and Hay, A. J. (1996) Selective proton permeability and pH regulation of the influenza virus M2 channel expressed in mouse erythroleukaemia cells, *J. Physiol. 494*, 329-336.
15. Mould, J. A., Drury, J. E., Frings, S. M., Kaupp, U. B., Pekosz, A., Lamb, R. A., and Pinto, L. H. (2000) Permeation and activation of the M2 ion channel of influenza A virus, *J. Biol. Chem. 275*, 31038-31050.
16. Wang, C., Takeuchi, K., Pinto, L. H., and Lamb, R. A. (1993) Ion channel activity of influenza A virus M2 protein: characterization of the amantadine block, *J. Virol. 67*, 5585-5594.

17. Wang, C., Lamb, R. A., and Pinto, L. H. (1995) Activation of the M2 ion channel of influenza virus: a role for the transmembrane domain histidine residue, *Biophys. J. 69*, 1363-1371.
18. Hu, J., Fu, R., Nishimura, K., Zhang, L., Zhou, H. X., Busath, D. D., Vijayvergiya, V., and Cross, T. A. (2006) Histidines, heart of the hydrogen ion channel from influenza A virus: toward an understanding of conductance and proton selectivity, *Proc. Natl. Acad. Sci. U.S.A. 103*, 6865-6870.
19. Ito, T., Gorman, O. T., Kawaoka, Y., Bean, W. J., and Webster, R. G. (1991) Evolutionary analysis of the influenza A virus M gene with comparison of the M1 and M2 proteins, *J. Virol. 65*, 5491-5498.
20. Venkataraman, P., Lamb, R. A., and Pinto, L. H. (2005) Chemical rescue of histidine selectivity filter mutants of the M2 ion channel of influenza A virus, *J. Biol. Chem. 280*, 21463-21472.
21. Howard, K. P., Lear, J. D., and DeGrado, W. F. (2002) Sequence determinants of the energetics of folding of a transmembrane four-helix-bundle protein, *Proc. Natl. Acad. Sci. USA 99*, 8568-8572.
22. Tang, Y., Zaitseva, F., Lamb, R. A., and Pinto, L. H. (2002) The Gate of the Influenza Virus M2 Proton Channel Is Formed by a Single Tryptophan Residue, *J. Biol. Chem. 277*, 39880-39886.
23. Gandhi, C. S., Shuck, K., Lear, J. D., Dieckmann, G. R., DeGrado, W. F., Lamb, R. A., and Pinto, L. H. (1999) Cu(II) inhibition of the proton translocation machinery of the influenza A virus M2 protein, *J. Biol. Chem. 274*, 5474-5482.
24. Okada, A., Miura, T., and Takeuchi, H. (2001) Protonation of Histidine and Histidine-Tryptophan Interaction in the Activation of the M2 Ion Channel from Influenza A Virus, *Biochemistry 40*, 6053-6060.
25. Sansom, M. S., Kerr, I. D., Smith, G. R., and Son, H. S. (1997) The influenza A virus M2 channel: a molecular modeling and simulation study, *Virology 233*, 163-173.
26. Wu, Y., and Voth, G. A. (2005) A Computational Study of the Closed and Open States of the Influenza A M2 Proton Channel, *Biophys. J. 89*, 2402-2411.

27. Smondyrev, A. M., and Voth, G. A. (2002) Molecular dynamics simulation of proton transport through the influenza A virus M2 channel, *Biophys. J. 83*, 1987-1996.
28. Wu, Y., and Voth, G. A. (2003) Computational studies of proton transport through the M2 channel, *FEBS Lett. 552*, 23-27.
29. Zhong, Q., Newns, D. M., Pattnaik, P., Lear, J. D., and Klein, M. L. (2000) Two possible conducting states of the influenza A virus M2 ion channel, *FEBS Lett. 473*, 195-198.
30. Chen, H., Wu, Y., and Voth, G. A. (2007) Proton transport behavior through the influenza A M2 channel: insights from molecular simulation, *Biophys. J. 93*, 3470-3479.
31. Forrest, L. R., Kukol, A., Arkin, I. T., Tieleman, D. P., and Sansom, M. S. P. (2000) Exploring models of the influenza A M2 channel: MD simulations in a phospholipid bilayer, *Biophys. J. 78*, 55-69.
32. Pinto, L. H., Dieckmann, G. R., Gandhi, C. S., Papworth, C. G., Braman, J., Shaughnessy, M. A., Lear, J. D., Lamb, R. A., and DeGrado, W. F. (1997) A functionally defined model for the M2 proton channel of influenza A virus suggests a mechanism for its ion selectivity, *Proc. Natl. Acad. Sci. USA 94*, 11301-11306.
33. Yi, M., Cross, T. A., and Zhou, H. X. (2008) A secondary gate as a mechanism for inhibition of the M2 proton channel by amantadine, *J. Phys. Chem. B 112*, 7977-7979.
34. Schnell, J. R., and Chou, J. J. (2008) Structure and mechanism of the M2 proton channel of influenza A virus, *Nature 451*, 591-595.
35. Stouffer, A. L., Acharya, R., Salom, D., Levine, A. S., Di Costanzo, L., Soto, C. S., Tereshko, V., Nanda, V., Stayrook, S., and DeGrado, W. F. (2008) Structural basis for the function and inhibition of an influenza virus proton channel, *Nature 451*, 596-599.
36. Cady, S. D., Mishanina, T. V., and Hong, M. (2009) Structure of amantadine-bound M2 transmembrane peptide of influenza A in lipid bilayers from magic-angle-spinning solid-state NMR: the role of Ser31 in amantadine binding. , *J. Mol. Biol. 385*, 1127-1141.
37. Nishimura, K., Kim, S., Zhang, L., and Cross, T. A. (2002) The closed state of a H+ channel helical bundle combining precise orientational and distance restraints from solid state NMR, *Biochemistry 41*, 13170-13177.
38. Hay, A. J., Wolstenholme, A. J., Skehel, J. J., and Smith, M. H. (1985) The molecular basis of the specific anti-influenza action of amantadine, *EMBO J. 4*, 3021-3024.

39. Grambas, S., Bennett, M. S., and Hay, A. J. (1992) Influence of amantadine resistance mutations on the pH regulatory function of the M2 protein of influenza A viruses, *Virology 191*, 541-549.

40. Kurtz, S., Luo, G., Hahnenberger, K. M., Brooks, C., Gecha, O., Ingalls, K., Numata, K., and Krystal, M. (1995) Growth impairment resulting from expression of influenza virus M2 protein in Saccharomyces cerevisiae: identification of a novel inhibitor of influenza virus, *Antimicrob. Agents Chemother. 39*, 2204-2209.

41. Jing, X., Ma, C., Ohigashi, Y., Oliveira, F. A., Jardetzky, T. S., Pinto, L. H., and Lamb, R. A. (2008) Functional studies indicate amantadine binds to the pore of the influenza A virus M2 proton-selective ion channel, *Proc. Natl. Acad. Sci. USA 105*, 10967-10972.

42. Stouffer, A. L., Ma, C., Cristian, L., Ohigashi, Y., Lamb, R. A., Lear, J. D., Pinto, L. H., and DeGrado, W. F. (2008) The interplay of functional tuning, drug resistance, and thermodynamic stability in the evolution of the M2 proton channel from the influenza A virus, *Structure 16*, 1067-1076.

43. Schmidtke, M., Zell, R., Bauer, K., Krumbholz, A., Schrader, C., Suess, J., and Wutzler, P. (2006) Amantadine resistance among porcine H1N1, H1N2, and H3N2 influenza A viruses isolated in Germany between 1981 and 2001, *Intervirology 49*, 286-293.

44. Tang, J. W., Ngai, K. L., Wong, J. C., Lam, W. Y., and Chan, P. K. (2008) Emergence of adamantane-resistant influenza A(H3N2) viruses in Hong Kong between 1997 and 2006, *J. Med. Virol. 80*, 895-901.

45. Pielak, R. M., Schnell, J. R., and Chou, J. J. (2009) Mechanism of drug inhibition and drug resistance of influenza A M2 channel, *Proc. Natl. Acad. Sci. U. S. A. 106*, 7379-7384.

46. Tu, Q., Pinto, L. H., Luo, G., Shaughnessy, M. A., Mullaney, D., Kurtz, S., Krystal, M., and Lamb, R. A. (1996) Characterization of inhibition of M2 ion channel activity by BL-1743, an inhibitor of influenza A virus, *J. Virol. 70*, 4246-4252.

47. Wang, J., Cady, S. D., Balannik, V., Pinto, L. H., DeGrado, W. F., and Hong, M. (2009) Discovery of spiro-piperidine inhibitors and their modulation of the dynamics of the M2 proton channel from influenza A virus, *J. Am. Chem. Soc. 131*, 8066-8076.

48. Hu, J., Asbury, T., Achuthan, S., Li, C., Bertram, R., Quine, J. R., Riqiang, F., and Cross, T. A. (2007) Backbone Stucture of the Amantadine-Block Trans-Membrane Domain M2 Proton Channel from Influenza A Virus, *Biophys. J. 92*, 4335-4343.

49. Kovacs, F. A., and Cross, T. A. (1997) Transmembrane four-helix bundle of influenza A M2 protein channel: structural implications from helix tilt and orientation, *Biophys. J. 73*, 2511-2517.

50. Kovacs, F. A., Denny, J. K., Song, Z., Quine, J. R., and Cross, T. A. (2000) Helix tilt of the M2 transmembrane peptide from influenza A virus: an intrinsic property, *J. Mol. Biol. 295*, 117-125.

51. Wang, J., Kim, S., Kovacs, F., and Cross, T. A. (2001) Structure of the transmembrane region of the M2 protein H(+) channel, *Protein Sci. 10*, 2241-2250.

52. Tian, C., Gao, P. F., Pinto, L. H., Lamb, R. A., and Cross, T. A. (2003) Initial structural and dynamic characterization of the M2 protein transmembrane and amphipathic helices in lipid bilayers, *Protein Sci. 12*, 2597-2605.

53. Tian, C., Tobler, K., Lamb, R. A., Pinto, L. H., and Cross, T. A. (2002) Expression and initial structural insights from solid-state NMR of the M2 proton channel from influenza A virus, *Biochemistry 41*, 11294-11300.

54. Cady, S. D., Goodman, C., Tatko, C. D., DeGrado, W. F., and Hong, M. (2007) Determining the orientation of uniaxially rotating membrane proteins using unoriented samples: a 2H, 13C, and 15N solid-state NMR investigation of the dynamics and orientation of a transmembrane helical bundle, *J. Am. Chem. Soc. 129*, 5719-5729.

55. Cady, S. D., and Hong, M. (2008) Amantadine-Induced Conformational and Dynamical Changes of the Influenza M2 Transmembrane Proton Channel, *Proc. Natl. Acad. Sci. U.S.A 105*, 1483-1488.

56. Duong-Ly, K. C., Nanda, V., DeGrado, W. F., and Howard, K. P. (2005) The conformation of the pore region of the M2 proton channel depends on lipid bilayer environment, *Protein Sci. 14*, 856-861.

57. de Planque, M. R., Greathouse, D. V., Koeppe, R. E., Schafer, H., Marsh, D., and Killian, J. A. (1998) Influence of lipid/peptide hydrophobic mismatch on the thickness of

diacylphosphatidylcholine bilayers. A 2H NMR and ESR study using designed transmembrane alpha-helical peptides and gramicidin A, *Biochemistry 37*, 9333-9345.

58. Park, S. H., and Opella, S. J. (2005) Tilt angle of a trans-membrane helix is determined by hydrophobic mismatch, *J. Mol. Biol. 350*, 310-318.
59. Luo, W., Mani, R., and Hong, M. (2007) Sidechain conformation and gating of the M2 transmembrane peptide proton channel of influenza A virus from solid-state NMR, *J. Phys. Chem. 111*, 10825-10832.
60. Manor, J., Mukherjee, P., Lin, Y. S., Leonov, H., Skinner, J. L., Zanni, M. T., and Arkin, I. T. (2009) Gating mechanism of the influenza A M2 channel revealed by 1D and 2D IR spectroscopies, *Structure 17*, 247-254.
61. Leonov, H., and Arkin, I. T. (2009) pH-driven helix rotations in the influenza M2 H(+) channel: a potential gating mechanism, *Eur Biophys J.*, Epub ahead of print.
62. Holsinger, L. J., and Lamb, R. A. (1991) Influenza virus M2 integral membrane protein is a homotetramer stabilized by formation of disulfide bonds, *Virology 183*, 32-43.
63. Stouffer, A. L., Nanda, V., Lear, J. D., and DeGrado, W. F. (2005) Sequence determinants of a transmembrane proton channel: an inverse relationship between stability and function, *J. Mol. Biol. 347*, 169-179.
64. Cristian, L., Lear, J. D., and DeGrado, W. F. (2003) Use of thiol-disulfide equilibria to measure the energetics of assembly of transmembrane helices in phospholipid bilayers, *Proc. Natl. Acad. Sci. USA 100*, 14772-14777.
65. Salom, D., Hill, B. R., Lear, J. D., and DeGrado, W. F. (2000) pH-dependent tetramerization and amantadine binding of the transmembrane helix of M2 from the influenza A virus, *Biochemistry 39*, 14160-14170.
66. Buffy, J. J., Waring, A. J., and Hong, M. (2005) Determination of Peptide Oligomerization in Lipid Membranes with Magic-Angle Spinning Spin Diffusion NMR, *J. Am. Chem. Soc. 127*, 4477-4483.
67. Luo, W., and Hong, M. (2006) Determination of the oligomeric number and intermolecular distances of membrane protein assemblies by anisotropic 1H-driven spin diffusion NMR spectroscopy, *J. Am. Chem. Soc. 128*, 7242-7251.

68. Witter, R., Nozirov, F., Sternberg, U., Cross, T. A., Ulrich, A. S., and Fu, R. (2008) Solid-state 19F NMR spectroscopy reveals that Trp41 participates in the gating mechanism of the M2 proton channel of influenza A virus, *J. Am. Chem. Soc. 130*, 918-924.

69. Hu, J., Riqiang, F., and Cross, T. A. (2007) The Chemical and Dynamical Influence of the Anti-Viral Drug Amantadine on the M2 Proton Channel Transmembrane Domain, *Biophys. J. 93*, 276-283.

70. Li, C., Qin, H., Gao, F. P., and Cross, T. A. (2007) Solid-state NMR characterization of conformational plasticity within the transmembrane domain of the influenza A M2 proton channel, *Biochim. Biophys. Acta 1768*, 3162-3170.

71. Cady, S. D., and Hong, M. (2009) Effects of amantadine binding on the dynamics of membrane-bound influenza A M2 transmembrane peptide studied by NMR relaxation, *J. Biomol. NMR*, in press.

72. Luo, W., Cady, S. D., and Hong, M. (2009) Immobilization of the Influenza A M2 Transmembrane Peptide in Virus-Envelope Mimetic Lipid Membranes: A Solid-State NMR Investigation, *Biochemistry*, Epub ahead of print.

73. Leser, G. P., and Lamb, R. A. (2005) Influenza virus assembly and budding in raft-derived microdomains: a quantitative analysis of the surface distribution of HA, NA and M2 proteins, *Virology 342*, 215-227.

74. Miller, C. (2008) Ion channels: coughing up flu's proton channels, *Nature 451*, 532-533.

75. Wang, J., Schnell, J. R., and Chou, J. J. (2004) Amantadine partition and localization in phospholipid membranes: a solution NMR study, *Biochem. Biophys. Res. Commun. 324*, 212-217.

76. Li, C., Yi, M., Hu, J., Zhou, H. X., and Cross, T. A. (2008) Solid-state NMR and MD simulations of the antiviral drug amantadine solubilized in DMPC bilayers, *Biophys. J. 94*, 1295-1302.

77. Ma, C., Polishchuk, A. L., Ohigashi, Y., Stouffer, A. L., Scho¨n, A., Magavern, E., Jing, X., Lear, J. D., Freire, E., Lamb, R. A., DeGrado, W. F., and Pinto, L. H. (2009) Identification of the Functional Core of the Influenza A Virus A/M2 Proton-Selective Ion Channel *Proc. Natl. Acad. Sci. U.S.A.*, in press.

78. Hong, M., Mishanina, T. V., and Cady, S. D. (2009) Accurate measurement of methyl 13C chemical shifts by solid-state NMR for the determination of protein sidechain conformation: the influenza M2 transmembrane peptide as an example, *J. Am. Chem. Soc. 131*, 7806-7816.

79. Nguyen, P. A., Soto, C. S., Polishchuk, A., Caputo, G. A., Tatko, C. D., Ma, C., Ohigashi, Y., Pinto, L. H., DeGrado, W. F., and Howard, K. P. (2008) pH-induced conformational change of the influenza M2 protein C-terminal domain, *Biochemistry 47*, 9934-9936.

Chapter 3

Determining the Orientation of Uniaxially Rotating Membrane Proteins Using Unoriented Samples

A paper published in Journal of the American Chemical Society

2007 vol. 129 (17) pp. 5719-5729

Sarah D. Cady, Catherine Goodman, Chad D. Tatko, William F. DeGrado and Mei Hong

Abstract

Membrane protein orientation has traditionally been determined by NMR using mechanically or magnetically aligned samples. Here we show a new NMR approach that abolishes the need for preparing macroscopically aligned membranes. When the protein undergoes fast uniaxial rotation around the bilayer normal, the 0°-frequency of the motionally averaged powder spectrum is identical to the frequency of the aligned protein whose alignment axis is along the magnetic field. Thus one can use unoriented membranes to determine the orientation of the protein relative to the bilayer normal. We demonstrate this approach on the M2 transmembrane peptide (M2TMP) of influenza A virus, which is known to assemble into a proton-conducting tetrameric helical bundle. The fast uniaxial rotational diffusion of the M2TMP helical bundle around the membrane normal is characterized via ^{2}H quadrupolar couplings, C-H and N-H dipolar couplings, ^{13}C chemical shift anisotropies, and ^{1}H $T_{1\rho}$ relaxation times. We then show that ^{15}N chemical shift anisotropy and N-H dipolar coupling measured on these powder samples can be analyzed to yield precise tilt angles and rotation angles of the helices. The data show that the tilt angle of the M2TMP helices depends on the membrane thickness to reduce the hydrophobic mismatch. Moreover, the orientation of a longer M2 peptide containing both the transmembrane domain and cytoplasmic residues is similar to the orientation of the transmembrane domain alone, suggesting that the latter regulates the orientation of this protein and that structural information obtained from M2TMP may be extrapolated to the longer peptide. This powder-

NMR approach for orientation determination is generally applicable and can be extended to larger membrane proteins.

Introduction

Orientation determination of membrane proteins by solid-state NMR traditionally requires mechanically or magnetically aligned proteins (*1, 2*). A uniformly aligned protein produces resolved spectra where the anisotropic frequency - chemical shift or dipolar coupling – reports the orientation of the molecule-fixed spin interaction tensor, from which the orientation of the protein can be obtained. However, this approach is constrained by the degree of alignment. Poor alignment can occur for many reasons: the size of the protein may be too large; the protein-lipid molar ratio may be too high, which is important for achieving sufficient sensitivity but deleterious for alignment; the protein may be inherently membrane-disruptive by causing curvature and non-lamellar phases (*3, 4*); and often only a narrow set of lipids is conducive to alignment for a specific protein, thus the dependence of orientation on environmental parameters such as membrane thickness and membrane composition is difficult to study. These factors severely restrict the determination of membrane protein orientation.

It is thus desirable to develop alternative approaches for determining membrane protein orientation that do not require macroscopic alignment, but use straightforward unoriented liposomes. We demonstrate here that this is possible as long as the membrane protein undergoes fast uniaxial rotational diffusion around the bilayer normal on the timescale of the NMR spin interactions. Under this condition, the protein orientation can be extracted with high precision using unoriented membranes and magic-angle spinning (MAS) or static experiments. The elimination of macroscopic alignment also increases the sample amount in the radiofrequency (rf) coil by removing the alignment media, thus giving intrinsically higher sensitivity.

The M2 protein of the influenza A virus is a well studied proton channel that initiates the release of the viral ribonuclear protein complex into the host cell, which is necessary for viral replication (*5, 6*). The transmembrane domain of the M2 protein, M2TMP (residues 22-

46), has been extensively studied by a number of biophysical techniques, including electrophysiological measurements (*7, 8*), analytical ultracentrifugation (*9, 10*), solid-state NMR (*11, 12*), neutron diffraction (*13*), and molecular dynamics simulation (*14-17*). The results indicate that M2TMP has the essential characteristics of the intact protein: it forms tetrameric helical bundles with proton-conducting abilities in the lipid membrane (*18*). Cross and coworkers used glass-plate aligned membranes and 2D ^{15}N correlation experiments to show that the helices in this tetrameric bundle are tilted by 38°±3° (*11*) from the bilayer normal in DMPC bilayers. The availability of this information makes M2TMP an excellent model system to test the principle of orientation determination using powder samples. Moreover, the orientation of M2TMP has been measured in detail only in DMPC (14:0) bilayers. A more limited set of NMR data on M2TMP bound to DOPC bilayers, which have longer acyl chains (18:1) than DMPC (14:0), found a similar orientation as that in DMPC bilayers (*19*). This was interpreted to suggest that M2TMP orientation is an inherent property of the protein and is independent of the membrane thickness. However, a more recent EPR study of M2TMP bound to DLPC, DMPC, POPC, and DOPC bilayers suggested that the peptide orientation does change with the membrane thickness (*20*). Thus, further experiments are of interest to resolve this discrepancy.

Another issue investigated in the current paper is the role of a C-terminal helix, which occurs just beyond the transmembrane helix. Previously, limited proteolysis of full length M2 protein in micelles and CD spectroscopy were used to identify a cytoplasmic amphiphilic helix that follows the transmembrane helix in the sequence of M2 (*21*). The C-terminal helix increases the stability of the tetramer (relative to a peptide spanning only the TM helix), and this cytoplasmic helix was also essential to obtain full proton channel activity when deletion mutants were expressed in oocytes (*7*). The role of this C-terminal segment in stabilizing the channel is currently not known. Originally, it was suggested that the cytoplasmic helix might have one of two orientations: in one model it formed an extension of the transmembrane helix, possibly explaining the increased stability of the tetramer. In a second model, the helix was proposed to lie parallel to the membrane surface, radiating out from the transmembrane helix bundle in a rosette-like structure with a radius of 35 to 40 Å (*21*). Subsequent solid-state NMR studies of the full-length M2 protein (*22*) were more consistent with the rosette

model, although there were also features in these experiments that were difficult to understand. Hydrogen-deuterium exchange data indicated that the amide NH groups of all residues in the transmembrane helix exchanged with solvent very rapidly, irrespective of whether they faced the phospholipid acyl chains or the transmembrane pore. By contrast, in the cytoplasmic helix, the putative lipid-facing amides were found to exchange very slowly with the bulk water (*22*). However, because the studies were not conducted with site-specifically labeled proteins, there remained some ambiguity in the conclusions. Thus, in this paper, we include initial data on a 42-residue peptide spanning both the transmembrane and the cytoplasmic helix.

In this work, we first examine the rotational dynamics of the M2TMP helical bundle under different sample preparation conditions and in lipid bilayers of different thicknesses. Multiple NMR spin interactions, including ^{2}H quadrupolar couplings, ^{13}C chemical shift anisotropy (CSA), C-H dipolar couplings, and ^{1}H rotating-frame relaxation time ($T_{1\rho}$), are used to examine the amplitude and rate of M2TMP rotational diffusion. We then measure the ^{15}N-^{1}H dipolar couplings and ^{15}N CSAs of site-specifically labeled M2TMP in unoriented membranes under MAS or static conditions. These anisotropic couplings are summarized in the same 2D correlation patterns – "PISA" wheels – as those obtained from oriented membrane samples. These powder PISA wheel spectra show that the orientation of M2TMP does depend on the lipid bilayer thickness: it decreases from 35°±3° in DLPC bilayers to 26°±3° in POPC bilayers. Finally, we show that the longer segment of the M2 protein encompassing both the transmembrane domain and cytoplasmic residues has the same orientation in DLPC bilayers as M2TMP, suggesting that the transmembrane domain regulates the orientation of the protein.

Material and Methods

Peptides and lipids

1-Palmitoyl-2-oleoyl-*sn*-glycero-3-phosphocholine (POPC), 1,2-dimyristoyl-*sn*-glycero-3-phosphocholine (DMPC), and 1,2-dilauroyl-*sn*-glycero-3-phosphocholine (DLPC) were obtained from Avanti Polar Lipids (Alabaster, AL). ^{13}C, ^{2}H, and ^{15}N labeled Leu and

Val (Sigma) were FMOC-protected in house using standard methods (*23*). Other FMOC-protected amino acids were purchased from Sigma (Miamisburg, OH) and Cambridge Isotope Laboratories (Andover, MA).

The transmembrane domain (residues 22-46) of the M2 protein of the A/Udorn/307/72 (H3N2) influenza A virus (SSDPLVVAASIIGILHLILWILDRL) (*24*) was synthesized and purified by Primm Biotech (Cambridge, MA). These samples contain various site-specific ^{2}H, ^{13}C, and ^{15}N labels. One sample contains a L38F mutation to allow a 4-^{19}F label at the phenylene ring. This L38F variant is found in the Weybridge (FPVW27) strain of the influenza A virus (*24*) and has similar biological activity as the Udorn strain (*25*).

Membrane sample preparation

Peptide-containing membrane samples were prepared either by an aqueous-mixing method or by an organic-phase mixing method. The aqueous samples were prepared by mixing the peptide with pH 7.5 lipid vesicle solutions at a peptide/lipid molar ratio (P/L) of 1:15. The lipid solution was vortexed, freeze-thawed 6-8 times to create uniform vesicles of < 200 nm diameter (*26*), then added to the appropriate amount of M2TMP. The solution was incubated at 30 °C for 2 days, after which it was ultracentrifuged at 150,000 g for 3 hours above the lipid main phase transition (T_m) temperature. The resulting pellet typically contained ~50% water by mass. UV-VIS absorption and a photometric assay of the supernatant (*27, 28*) show that ~98% of the peptide is bound to the pellet. The organic-phase mixed samples used P/L = 1:20 and were prepared by codissolving M2TMP with lipids in trifluoroethanol, drying the mixture with nitrogen gas, redissolving it in cyclohexane, lyophilization, then rehydration to 50% water by mass using a phosphate buffer (pH 8.1). We refer to these two types of samples as “aqueous samples” and “organic samples”, even though the final products are both well-hydrated proteoliposomes.

Importantly, we have confirmed by independent ^{19}F spin diffusion experiments that the oligomeric state of M2TMP is indeed tetramer at the peptide concentrations used here, whether the sample is prepared by aqueous-phase mixing or organic-phase mixing (*18, 29*).

This is manifested as an equilibrium value of ~0.25 at long spin diffusion mixing times. Thus, the mobility and orientation observed in this work are those of the tetrameric M2 peptide.

Solid-state NMR spectroscopy

NMR experiments were carried out on a Bruker AVANCE-600 (14.1 Tesla) spectrometer and a DSX-400 (9.4 Tesla) spectrometer (Karlsruhe, Germany). The ^{2}H experiments were carried out using a quadrupolar echo pulse sequence with a ^{2}H 90° pulse length of 5 μs. Static ^{15}N chemical shift spectra were measured using a Hahn-echo sequence. ^{13}C-^{1}H and ^{15}N-^{1}H dipolar couplings were measured using the 2D DIPSHIFT experiment (*30*) at 2.4 – 3.5 kHz MAS with MREV-8 for ^{1}H homonuclear decoupling. Pulse lengths of 3.5 – 5.2 μs were used in the MREV-8 pulse train, the longer values due to the rf power loss on some of the hydrated membrane samples. Tests on the model compound ^{15}N-acetyl-valine indicate that the measured dipolar coupling is unaffected by the varying MREV-8 field strengths within the range used. The N-H DIPSHIFT experiments were performed with dipolar doubling (*31, 32*) to increase the precision of the measured couplings. The ^{13}C chemical shift anisotropy (CSA) was measured using the 2D SUPER experiment (*33*) under 2.5 kHz MAS. The corresponding ^{13}C field strength was 30.3 kHz. ^{1}H $T_{1\rho}$ was measured using a spin-lock field strength of 62.5 kHz.

The ^{2}H and ^{13}C 1D spectra were recorded between 243 K and 313 K. All ^{15}N chemical shift and N-H dipolar coupling experiments were carried out at 313 K where the peptide is mobile to determine the helix orientation.

Results and Discussion

Equivalence of aligned and powder samples for uniaxially mobile molecules

For a membrane protein undergoing fast uniaxial rotational diffusion around the bilayer normal, the 0°-frequency, $\bar{\delta}_{//}$, of the motionally average powder spectrum is identical

to the frequency when the protein is uniformly aligned, with the alignment axis parallel to the magnetic field (0°-aligned sample) (*34*):

$$\bar{\delta}_{//} = \omega_{0^\circ\ aligned} = \frac{1}{2}\delta\left(3\cos^2\theta - 1 - \eta\sin^2\theta\cos 2\phi\right) + \omega_{iso} \qquad (3.1)$$

Here $\delta = \delta_{zz}-\delta_{iso}$ and $\eta = (\delta_{yy} - \delta_{xx})/\delta$ are the anisotropy and asymmetry parameters, respectively, of the rigid-limit interaction tensor. The angles (θ, ϕ) are the polar coordinates of the magnetic field B_0 in the principal axis system of the spin interaction tensor. Equation 3.1 can be derived, as we showed recently (*34*), by considering consecutively the frequency of an aligned sample without motion, then the frequency of an aligned sample undergoing uniaxial rotation around the alignment axis of bilayer normal, then the motionally averaged anisotropy parameter of the same aligned and mobile sample, finally the powder spectrum of the mobile sample without alignment. The essential link between the frequency of a 0°-aligned aligned sample and that of an unoriented sample is the realization that $\bar{\delta}_{//}$ of the motionally averaged powder pattern is obtained when B_0 is along the motional axis, the bilayer normal. This is identical to the geometry of a 0°-aligned sample, when B_0 coincides with the alignment axis, also the bilayer normal.

Once $\bar{\delta}_{//}$ is known, the motionally averaged anisotropy parameter, $\bar{\delta}$, and the frequency of the powder pattern maximum, $\bar{\delta}_{\perp}$, are also known, since these are related by

$$\bar{\delta}_{\perp} - \omega_{iso} = -\frac{1}{2}\left(\omega_{0^\circ\ aligned} - \omega_{iso}\right) = -\frac{1}{2}\left(\bar{\delta}_{//} - \omega_{iso}\right) = -\frac{1}{2}\bar{\delta}. \qquad (3.2)$$

Thus one can extract the orientation information by measuring the high-sensitivity $\bar{\delta}_{\perp}(90^\circ)$ edge, rather than the low-intensity $\bar{\delta}_{//}$ edge, of the uniaxially averaged spectrum.

Predicted rates of rotational diffusion of membrane proteins

The prerequisite for this powder-sample orientation determination approach is that the membrane protein must undergo uniaxial rotational diffusion at a rate larger than the NMR spin interaction. The rotational diffusion rate of proteins in two-dimensional membranes is given by the Saffman-Delbrück equation (*35*):

$$D_r = \frac{kT}{4\pi\eta r^2 h} \tag{3.3}$$

where the diffusion coefficient, D_r is directly proportional to the temperature T and inversely proportional to the membrane viscosity η, the square of the radius (r) of the diffusing cylinder, and the height (h) of the cylinder.

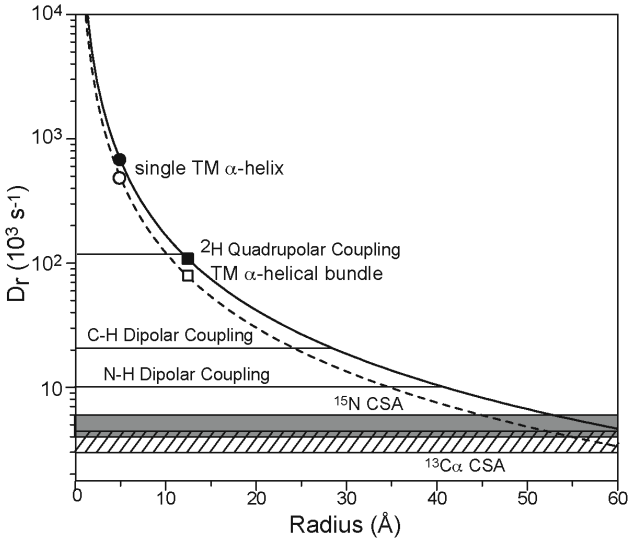

Figure 3.1. Calculated rotational diffusion rates of membrane proteins as a function of radius compared to various NMR spin interactions. The rotational rates of a single TM α-helix (circles) and a tetrameric α-helical bundle (squares) are indicated. For the calculated curves, a membrane viscosity of 10 poise and a temperature of 298 K are used. A diffusion cylinder height (h) of 19.5 Å (solid line) and 27 Å (dashed line) are used, corresponding to the hydrophobic thickness of DLPC and POPC bilayers, respectively. Superimposed are the ^{2}H quadrupolar coupling strength, C-H and N-H dipolar couplings, and ^{15}N and ^{13}Cα chemical shift anisotropies for magnetic field strengths of 9.4 – 14.1 Tesla.

Equation 3.3 allows us to estimate the diffusion rates of membrane proteins of varying sizes. Figure 3.1 plots the calculated rotational diffusion rates D_r as a function of *r* at T = 298 K, with *h* = 19.5 Å for DLPC bilayers and 27 Å for POPC bilayers, and assuming a membrane viscosity of 10 poise (*35*), A single TM α-helix, which has a radius of ~5 Å, gives a D_r of ~6.7 x 10^5 s^{-1} and 4.9 x 10^5 s^{-1} for DLPC and POPC bilayers, respectively. These rates are much larger than any spin interactions in proteins, thus a single TM helix in liquid-crystalline bilayers should give motionally narrowed spectra.

If the α-helix is surface-bound instead of transmembrane, the radius of the diffusing cylinder will be on the order of the length of the helix while *h* is roughly the radius of the helix. For a 25-residue α-helix, using *r* = 37.5 Å and *h* = 5 Å, we find a D_r of ~4.7 x 10^4 s^{-1}. This is smaller than the ^{2}H quadrupolar coupling of 125 kHz. Indeed, a recent ^{2}H NMR study of an in-plane 26-residue α-helix found the peptide to be immobilized on the ^{2}H NMR timescale (*36*).

A TM helical bundle has a larger *r* than a single helix, thus should have a lower rotational diffusion rate. The M2TMP tetramer is estimated to have a radius of ~12.5 Å based on the existing structural model (PDB code: 1NYJ). The resulting D_r is ~10^5 s^{-1}, which is comparable to the ^{2}H quadrupolar interaction and much larger than any spin-1/2 interactions such as C-H dipolar couplings and ^{15}N CSA (Figure 3.1). Since the membrane viscosity used in the calculation is an estimated value and since T is an adjustable parameter, the rotational diffusion rate may exceed the ^{2}H quadrupolar interaction under experimentally accessible conditions. Certainly, the rotational diffusion of this tetrameric helical bundle is sufficiently fast to average spin-1/2 interactions.

It is important to note that the fast uniaxial rotation relevant for orientation determination is the rotation of the entire helical bundle together around the membrane normal, and that the individual helices do not rotate around their own molecular axes. That the bilayer normal is the motional axis is dictated by the two-dimensional nature of the membrane, which makes intermolecular potentials symmetric around this bilayer normal. Moreover, the bundle axis is parallel to the bilayer normal, making the orientation of all

helices relative to the bilayer normal identical, since only a single anisotropic NMR signal was observed for each residue (*9, 11*). Thus, rotation around the membrane normal is also rotation around the bundle axis.

^{2}H spectra of M2TMP in lipid membranes: conditions for fast uniaxial rotation

Previous ^{15}N spectra of glass-plate aligned M2TMP with the alignment axis perpendicular to the magnetic field showed narrow peaks that indicate the presence of fast uniaxial rotation of this helical bundle (*37*). However, whether this motion is fast on the timescales of larger spin interactions such as ^{2}H quadrupolar coupling is not known, and the rates and amplitudes of the motion have also not been characterized. We first measured the ^{2}H spectra of site-specifically deuterated M2TMP in various lipid membranes to provide a lower limit of the rotational diffusion rates. Figure 3.2 shows the ^{2}H spectra of 5,5,5-d_3-L38-M2TMP in POPC bilayers at several temperatures. In the Lα-phase of the membrane, the Leu_{38} CD_3 group experiences methyl three-site jumps, χ_1 and χ_2 torsional motion, and possible backbone motion. The methyl three-site jumps reduce the rigid-limit ^{2}H quadrupolar coupling to 40 kHz (*38*). Any further coupling reduction must be a result of the two other motional mechanisms.

The ^{2}H spectra in Figure 3.2 show different dynamics for different sample preparation conditions. For the organic sample (a), the spectra show $\bar{\eta} = 0$ lineshapes and couplings of < 15 kHz in the Lα phase (Figure 3.2a). For the aqueous sample, the spectra show couplings of > 25 kHz and non-uniaxial lineshapes at the same temperatures. Mildly below the phase transition temperature, the same trend is seen: organic mixing yielded a splitting of 16 kHz whereas aqueous mixing yielded a coupling of 31 kHz. Since χ_1 and χ_2 torsional motion is inherently non-uniaxial, the $\bar{\eta} = 0$ lineshape (Figure 3.2a) at high temperatures cannot be solely due to the sidechain motion, but the helix backbone must undergo uniaxial rotation faster than the rigid-limit ^{2}H quadrupolar coupling of 125 kHz. Moreover, since the backbone motion should have a higher energy barrier than sidechain motion, the couplings of 26 – 31 kHz in the aqueous sample (Figure 3.2b) must reflect χ_1/χ_2 torsional motions while the backbone rotation has stopped.

The different backbone mobility of M2TMP in the two sample preparation methods suggests different aggregation states of the protein. Mixing the peptide and lipid in organic solvents before the assembly of lipid bilayers in water may result in a homogeneously mixed membrane mixture in which the tetrameric bundles are well isolated from each other. In contrast, mixing M2TMP with preformed lipid vesicles may not fully solubilize the peptide in the membrane, leading to aggregates of tetramers that inhibit fast rotation on the ^{2}H timescale.

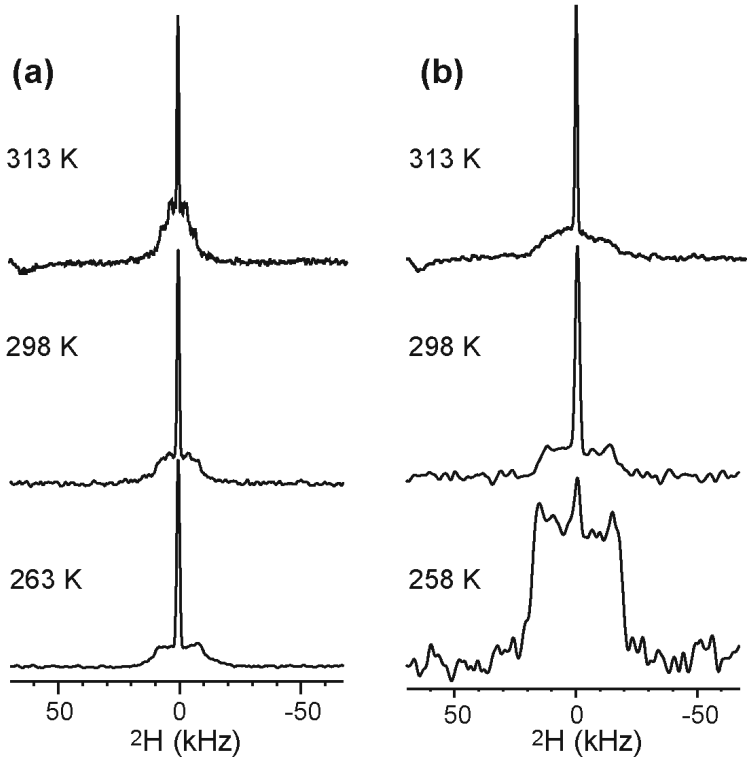

Figure 3.2. ^{2}H spectra of d_3-L38-M2TMP in POPC membranes prepared via (a) organic mixing and (b) aqueous mixing at various temperatures. Quadrupolar splittings of the organic sample are 13.8 kHz, 15.0 kHz, and 16.0 kHz from top to bottom (a). Quadrupolar splittings of the aqueous sample are 26.0 kHz, 26.0 kHz, and 31.0 kHz from top to bottom (b).

To confirm the backbone motion of the helical bundles in the organic samples, we measured the ^{2}H spectra of d_3-A29 labeled L38F-M2TMP in DLPC and POPC bilayers above and below the T_m of 271 K. Since the Ala methyl group is directly attached to the backbone,

there is no sidechain torsional motion other than the methyl three-site jump, and quadrupolar couplings smaller than 40 kHz must be attributed to backbone reorientation. Figure 3.3 shows that above T_m, the peptide exhibits uniaxial lineshapes and 16 kHz couplings in both DLPC and POPC membranes, confirming that the helical bundles undergo fast uniaxial rotation. Below T_m, between 243 K and 262 K, the ^2H spectra broaden to 32 kHz in the DLPC membrane and 39 kHz in the POPC membrane. The prediction that rotational diffusion should be slower in the thicker membrane (larger *h*) is confirmed by the larger quadrupolar couplings in the gel-phase POPC membrane at the same reduced temperature as the DLPC sample. In addition, the zero-frequency signal is more completely suppressed in POPC bilayers than in DLPC bilayers.

The fact that the M2TMP spectra in the Lα-phase are the same between DLPC and POPC membranes with different *h* suggests that as long as the rotational diffusion rate exceeds the coupling strength, it gives the same motionally averaged couplings, which depend only on the orientation of the spin interaction tensor, in this case the Cα-Cβ bond, with respect to the bilayer normal. Equation 3.1 indicates that an order parameter can be defined: $S \equiv \bar{\delta}/\delta = \bar{\delta}/40\ \text{kHz}$, that is related to the angle θ of the Cα-Cβ bond relative to the bilayer normal as $S = \frac{1}{2}\left(3\cos^2\theta - 1\right)$. Thus, the measured splitting of 16 kHz in fluid DLPC and POPC membranes indicates a Cα-Cβ bond orientation of 39° (or 141°) for S = +0.4 or 75° (or 105°) for S = -0.4. The existing M2TMP tetramer model gives a Cα-Cβ bond orientation of 92°, in reasonable agreement with one of the predicted values (105°). However, this Ala Cα-Cβ constraint, while easy to obtain, is not very sensitive to the helix axis orientation because the Cα-Cβ bond is roughly perpendicular, rather than parallel, to the helical axis. It has been shown that multiple Ala CD_3 groups need to be measured to obtain accurate helix tilt angles (*39*).

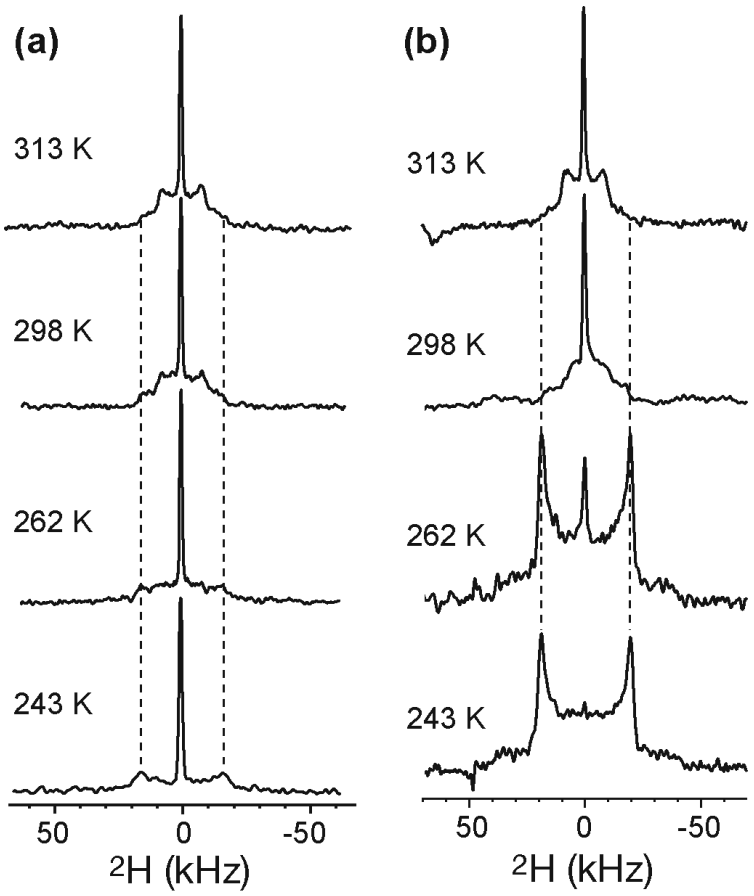

Figure 3.3. ^{2}H spectra of d_3-A29 L38F-M2TMP in (a) DLPC and (b) POPC membranes at various temperatures. Both samples were prepared by organic mixing. The quadrupolar splittings in (a) are 16 kHz, 16 kHz, 32 kHz, and 32 kHz from top to bottom. The quadrupolar splittings in (b) are 16 kHz, 20 kHz, 38 kHz, and 39 kHz from top to bottom.

Rates of M2TMP uniaxial rotational diffusion

We characterized the rotational diffusion rates of the M2TMP tetramers by ^{13}C cross-polarization (CP) MAS spectra as a function of temperature. Figure 3.4 shows the ^{13}Cα signals of L40 and G34 in DLPC membrane between 258 K and 318 K. The sample was prepared by organic-phase mixing. The two Cα signals are strong below the phase transition temperature, disappear between 288 K and 298 K, then reappear above 313 K. The same trend is observed in the organic POPC membrane whereas the aqueous POPC sample showed strong signals that are independent of temperature (spectra not shown). The suppression of

the ^{13}C signals at intermediate temperatures in the organic samples is a classic signature that motions with similar rates as the C-H dipolar coupling and the ^{1}H decoupling strength, 20,000–50,000 s^{-1}, are present (*40*). When this motion is either frozen or sped up by varying the temperature, the ^{13}C signals reappear.

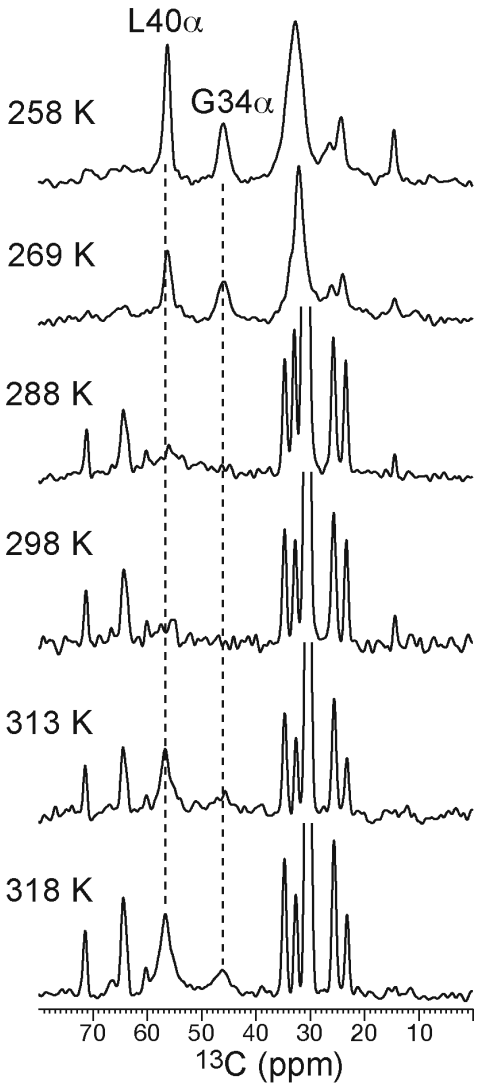

Figure 3.4. Temperature-dependent ^{13}C spectra of [$^{13}C\alpha$-L40, $^{13}C\alpha$-G34] M2TMP in DLPC membrane prepared by organic mixing. Below T_m (271 K), the L40α and G34α signals are strong. With increasing temperature, the peak intensities decrease and almost disappear due to intermediate timescale motion (288 – 298 K). The signals reappear as the peptide reaches the fast motion limit (313 – 318 K).

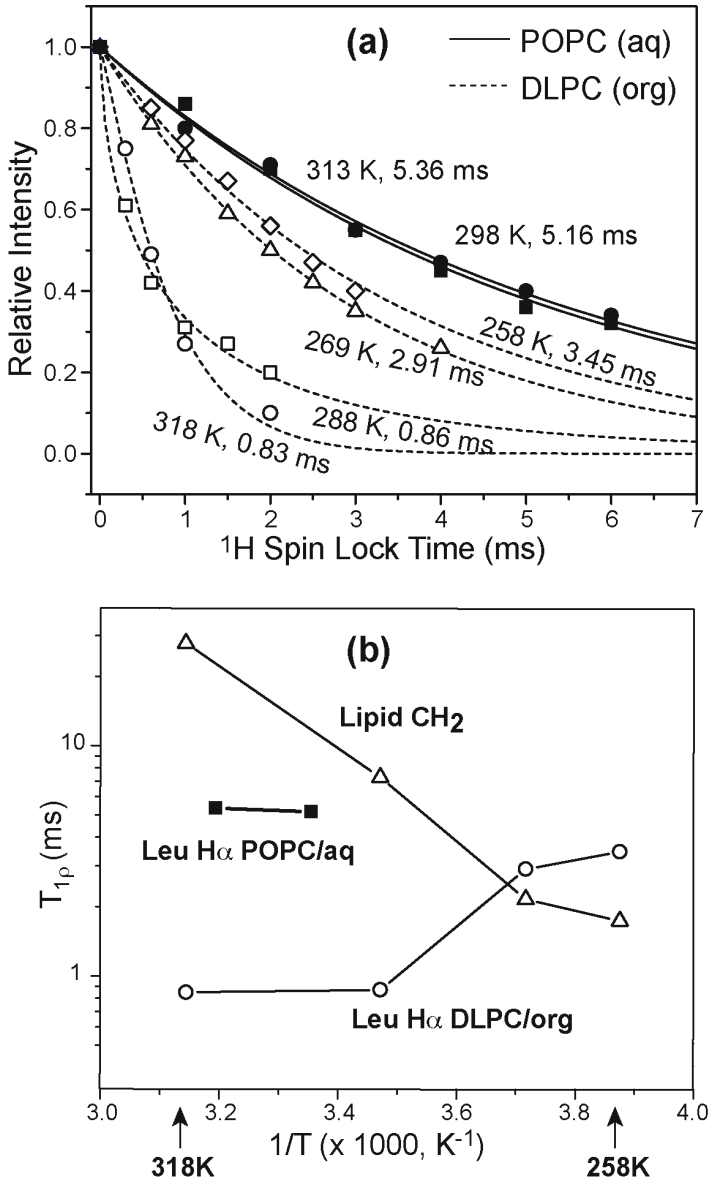

Figure 3.5. Temperature-dependent ^{1}H $T_{1\rho}$ of M2TMP in different lipid membranes**.** (a) ^{13}C-detected ^{1}H $T_{1\rho}$ curves of L40α at various temperatures. The aqueous POPC sample is shown with filled symbols and solid fit curves. The organic DLPC sample is shown with open symbols and dashed fit curves. (b) ^{1}H $T_{1\rho}$ versus inverse temperature for lipid CH_2 and L40α in the organic DLPC sample, and L40α in the aqueous POPC sample.

Motions with rates of 10^5 s^{-1} are readily detectable in rotating-frame spin-lattice relaxation time ($T_{1\rho}$) measurements. Figure 3.5a shows the ^{13}C-detected L40 Hα $T_{1\rho}$ relaxation curves at various temperatures under a ^1H spin-lock field of 62.5 kHz. In the aqueous POPC membrane, the peptide has a long ^1H $T_{1\rho}$ of > 5 ms that is independent of the temperature between 298 K and 313 K. In contrast, the organic DLPC sample gave much shorter and temperature-dependent ^1H $T_{1\rho}$ values. Above T_m, the ^1H $T_{1\rho}$ is only 0.8 ms whereas below T_m, the ^1H $T_{1\rho}$ increases to 3.45 ms at 258 K. Figure 3.5b plots the ^1H $T_{1\rho}$ of the lipid CH_2 and L40 Hα in the two samples as a function of temperature. The lipid CH_2 groups show increasing $T_{1\rho}$ with increasing temperature, indicating that they are in the fast motional limit in the temperature range examined (Figure 3.5c). The organic DLPC sample shows decreasing $T_{1\rho}$ with increasing temperature, indicating that the peptide motion is near the minimum of the $T_{1\rho}$ curve. Finally, the temperature-independence and long $T_{1\rho}$ of the aqueous POPC sample indicates that M2TMP is in the slow motional limit.

Amplitudes of backbone motion from ^{13}C-^1H dipolar coupling and ^{13}C CSA

Direct evidence of backbone motion can be obtained from Cα-Hα dipolar couplings and Cα CSAs. Figure 3.6 shows the L40 Cα-Hα dipolar coupling curves in three different samples obtained from the indirect dimension of the 2D DIPSHIFT spectra. In the aqueous POPC membrane, a coupling of 10.6 kHz was measured (Figure 3.6a). Taking into account the MREV-8 scaling factor (0.47), this corresponds to an unscaled coupling of 22.6 kHz, which is the rigid limit C-H dipolar coupling. In contrast, POPC and DLPC organic membranes (b, c) gave significantly reduced couplings of 3.4 kHz and 4.0 kHz, respectively, which correspond to order parameters of ±0.32 and ±0.37. The sign degeneracy, similar to the ^2H quadrupolar interaction, is due to the uniaxial nature of the dipolar interaction. The negative S values indicate a Cα-Hα angle of 70° (110°) for POPC and 73° (107°) for DLPC with respect to the bilayer normal. The existing M2TMP structural model, obtained from experiments conducted on DMPC bilayers, gives a Cα-Hα orientation of 73° or 107° from the bilayer normal, in excellent agreement with the present data.

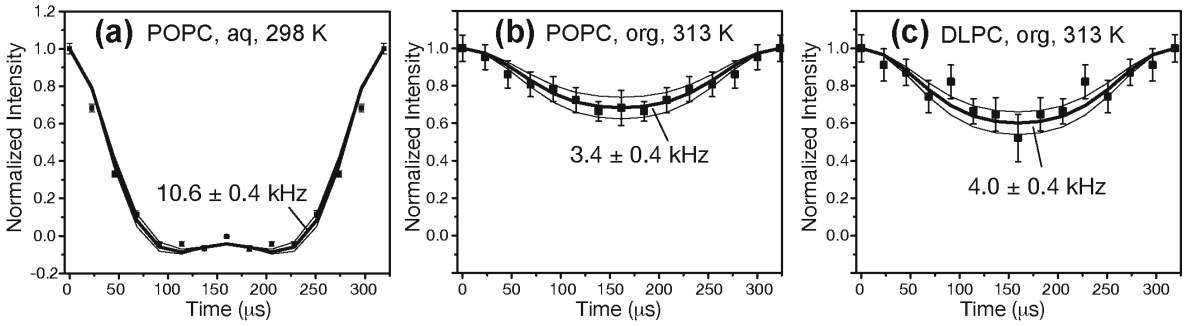

Figure 3.6. ^{13}C-^{1}H DIPSHIFT curves of $^{13}C\alpha$-L40 in M2TMP in different membrane samples. (a) POPC aqueous sample (P/L = 1:20). (b) POPC organic sample (P/L = 1:15). (c) DLPC organic sample (P/L = 1:15). The POPC aqueous sample (a) gave a rigid-limit ^{13}C-^{1}H dipolar coupling whereas the two organic samples (b, c) have motionally averaged dipolar couplings.

The similarity of the two C-H couplings belies the fact that the helix orientation is detectably different between the two membranes, as we show by ^{15}N experiments below. Again, this is a result of the roughly perpendicular orientation of the Cα-Hα bond to the helix axis, which makes it not extremely sensitive to the helix tilt angle.

The same backbone uniaxial rotation also averages the Cα CSA, which can be measured under MAS using the recoupling experiment SUPER (*33, 41*). Figure 3.7 shows the CSA spectra of L40 in various membranes, obtained from the indirect dimension of the 2D SUPER spectra. Only the organic DLPC sample in the liquid crystalline phase shows a motionally narrowed CSA ($\bar{\delta}$=9.2 ppm) while the gel-phase sample or aqueous samples gave CSAs of 18 ppm, which is the rigid-limit CSA of α-helical Leu predicted by quantum chemical calculations (*42*).

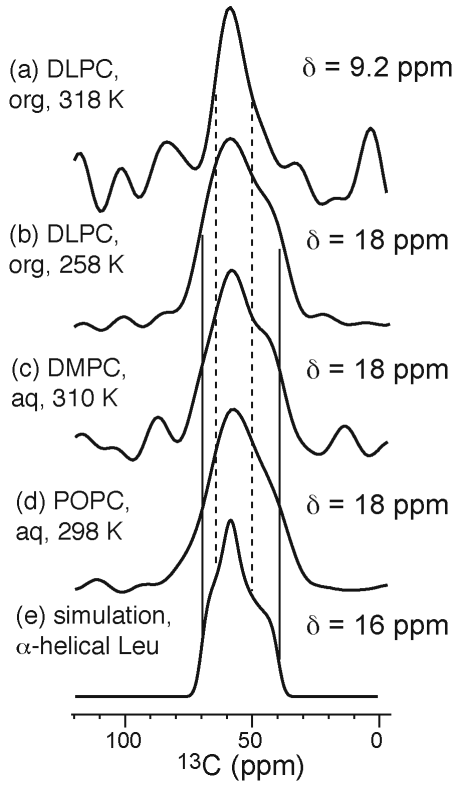

Figure 3.7. ^{13}C CSA spectra of the ^{13}Cα-L40 in M2TMP in various membranes, extracted from the indirect dimension of 2D SUPER spectra. (a) DLPC organic sample at 318 K. (b) DLPC organic sample at 258 K. (c) DMPC aqueous sample at 310 K. (d) POPC aqueous sample at 298 K. Spectra (b-d) show rigid-limit CSAs, as simulated in (e). Spectrum (a) is the only one narrowed by fast backbone motion of the peptide.

M2TMP orientation from powder samples using ^{15}N NMR

To determine the orientation of α-helical peptides with high angular resolution, the most sensitive nuclear spin interactions are the N-H dipolar coupling and ^{15}N CSA, as both tensors are roughly parallel to the helix axis. The PISEMA experiment, commonly used for aligned samples, correlates these two spin interactions in a 2D spectrum, producing wheel-like patterns called "PISA wheels". The size and frequency position of the PISA wheels depend on the tilt angle of the helices whereas the residue position on the wheel depends on the rotation angle around the helix axis (*43, 44*). Figure 3.8a shows the calculated PISA wheels for tilt angles of 15°–45° for 0°-aligned membranes. The center of the wheels shifts

towards lower frequencies in both dimensions as the tilt angle increases. When the alignment axis is perpendicular to the magnetic field, and the protein undergoes fast rotational diffusion, "90° PISA wheels" are obtained that are half-sized mirror images of the 0° PISA wheels (Equation 3.2), reflected around the isotropic shift and zero dipolar coupling axis (Figure 3.8b). These 90° wheels have been observed in membrane proteins bound to "unflipped" bicelles (*45*).

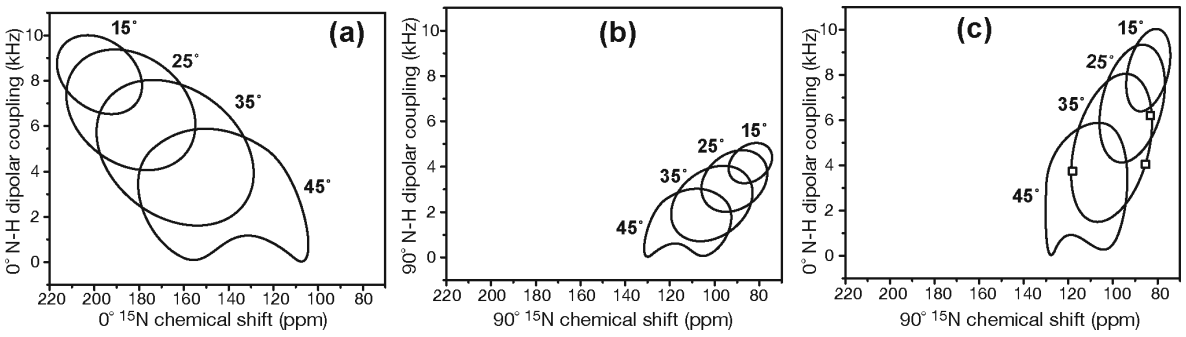

Figure 3.8. Calculated PISA wheel spectra for (a) 0°-aligned membranes, (b) 90°-aligned membranes, and (c) 0° N-H coupling and 90° ^{15}N chemical shift from unoriented membranes. Tilt angles of 15°–45° are shown. In (c), the resonances of A30, V28, and L26 at a tilt angle of 35° and with rotation angles reproducing the previous glass-plate aligned data are shown (*11*).

The presence of protein uniaxial rotation enables PISA wheels to be obtained from powder samples using MAS and static experiments. For example, N-H dipolar couplings can be measured in a site-specific fashion using the 2D DIPSHIFT (*46*) or LG-CP (*47*) experiments under MAS, giving the $\bar{\delta}_{//}$ frequency or 0° dipolar coupling. The ^{15}N CSA can be obtained from the $\bar{\delta}_{\perp}$ singularity of the static ^{15}N spectra of site-specifically labeled samples or by CSA recoupling experiments under MAS on multiply labeled samples. When the 0° dipolar coupling is correlated with the 90° chemical shift, we obtain 0°/90° PISA wheels (Figure 3.8c). Whichever PISA wheels to use, multiple ^{15}N-labeled residues are necessary to determine both the tilt and the rotation angles of the helix.

We demonstrate this powder orientation determination approach by measuring the ^{15}N chemical shift and N-H dipolar couplings of site-specifically labeled M2TMP. Figure 3.9 shows static ^{15}N spectra of M2TMP in DLPC and POPC organic membranes. L26, V28, and A30 were ^{15}N-labeled to cover different rotational angles around the helix axis. Most spectra show well-defined $\bar{\delta}_{\perp}$ singularities, $\bar{\delta}_{//}$ edges, and $\bar{\eta}$ = 0 lineshapes and a "magic-angle hole" at the isotropic shift.

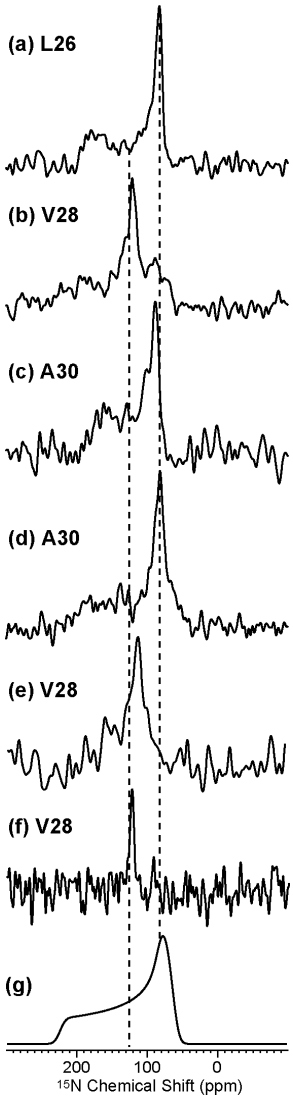

Figure 3.9. ^{15}N static spectra of ^{15}N-labeled M2 peptides in DLPC and POPC bilayers. (a) L26 of M2TMP in DLPC bilayers. (b) V28 of M2TMP in DLPC bilayers. (c) A30 of M2TMP in DLPC bilayers. (d) A30 of L38F-M2TMP in POPC bilayers. (e) V28 of M2TMP in POPC bilayers. (f) V28 of M2(19-60) in DLPC bilayers. (g) Calculated rigid-limit ^{15}N powder pattern.

This magic-angle hole results from the collinearity of the chemical shift tensor and the dipolar coupling tensor in uniaxially mobile molecules (*48*). The exception is V28, whose $\bar{\delta}_\perp$ singularity nearly coincides with the isotropic shift in various samples so that the magic-angle hole is not visible (Figure 3.9b, e, f). This indicates that the V28 main ^{15}N chemical shift tensor axis, which is near its N-H bond, is incidentally aligned near the magic angle with respect to the bilayer normal, so that the CSA tensor is motionally averaged to vanishing anisotropies. Also observed is a 6 ppm difference in the A30 $\bar{\delta}_\perp$ frequency between DLPC and POPC bilayers (Figure 3.9c, d), indicating that the helix orientation differs between the two lipid bilayers.

Figure 3.10 shows the N-H dipolar-doubled DIPSHIFT curves of the same ^{15}N labeled residues. A range of couplings from 2.6 kHz to 8.5 kHz is observed. After taking into account the dipolar doubling and MREV-8 scaling factor, we find unscaled couplings from 4.7 kHz to 9.0 kHz (Table 3.1). The rigid-limit one-bond N-H dipolar coupling is 10.5 kHz, thus these N-H bonds are variably tilted from the bilayer normal.

Table 3.1: ^{15}N 90° chemical shifts (ω_N) and N-H dipolar couplings (ω_{NH}) of several residues in M2 peptides in various lipid membranes.

^{15}N-labeled peptide	lipid bilayer	ω_N (ppm)	ω_{NH} (kHz)
L26, M2TMP	DLPC	78±3	4.8
V28, M2TMP	DLPC	117±4	2.8
V28, M2TMP	POPC	106±4	6.3
V28, M2(19-60)	DLPC	123±3	NA
A30, M2TMP	DLPC	87±2	5.1
A30, L38F-M2TMP	POPC	81±3	9.0

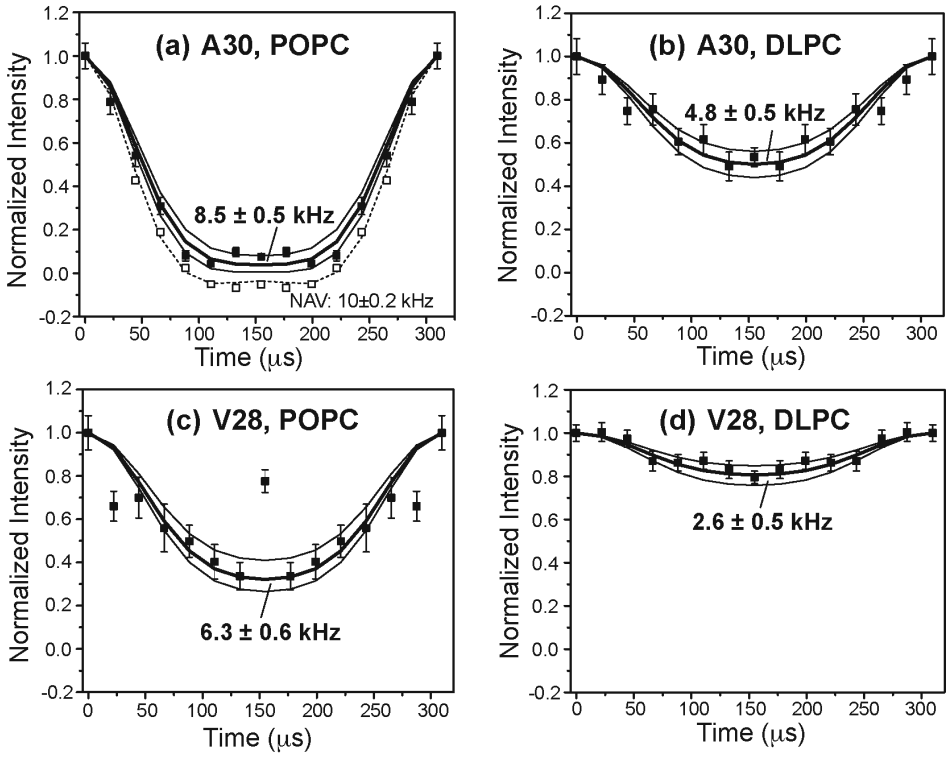

Figure 3.10. N-H dipolar-doubled DIPSHIFT curves of selected residues of M2TMP in DLPC and POPC bilayers. (a) A30 of L38F-M2TMP in POPC bilayers. (b) A30 of M2TMP in DLPC bilayers. (c) V28 of M2TMP in POPC bilayers. (d) V28 of M2TMP in DLPC bilayers. The DIPSHIFT curve of crystalline rigid N-acetyl-valine (NAV) is shown in (a) for comparison. The best-fit N-H dipolar coupling (bold solid lines) is indicated for each site. All spectra were measured at 313 K under 3.23 kHz MAS.

Figure 3.11 summarizes the N-H dipolar coupling and the $\bar{\delta}_{\perp}$ ^{15}N chemical shift of A30, V28, and L26 in DLPC and POPC bilayers. Superimposed on the experimental data are the best-fit 0°/90° PISA wheels calculated using the ideal α-helical geometry. The DLPC data (filled squares) are best fit to a 0°/90° PISA wheel of $\tau = 35° \pm 3°$. The rotation angle, determined by the relative positions of the three sites on the wheel, is 105°, where $\rho = 0°$ is defined by the Ser_{22} CO – Ser_{23} N peptide bond direction. With the same reference, the oriented-membrane ^{15}N data gave a rotation angle of ~95° (*11*). L26 shows an ^{15}N chemical shift that falls outside the calculated 35° PISA wheel, but the measured N-H dipolar coupling

is consistent with the predicted frequency for $\tau = 35^\circ$. This may result from a deviation of the ^{15}N chemical shift tensor magnitude or orientation at this site from the literature value used in the simulation of the PISA wheel. Indeed, ^{15}N chemical shift tensor variations in proteins can be significant, as shown by a recent study of the protein GB1 (*49*). Fortunately, the dipolar coupling information is intrinsically more accurate, which is the reason that N-H dipolar couplings only are used in the dipolar wave analysis for orientation determination (*50*). In POPC bilayers, the A30 and V28 data are best fit by a tilt angle of $26^\circ \pm 3^\circ$ and the same rotation angles. The N-H dipolar couplings are significantly larger than in DLPC bilayers and the $\bar{\delta}_\perp$ chemical shifts are further away from the isotropic chemical shift. Both indicate larger anisotropies, which shift the 0°/90° PISA wheels to a smaller tilt angle. Interestingly, as the PISA wheels become smaller, the tilt angle resolution improves, thus although the rotation angle is defined only by two residues, the precision of the tilt angle is still high.

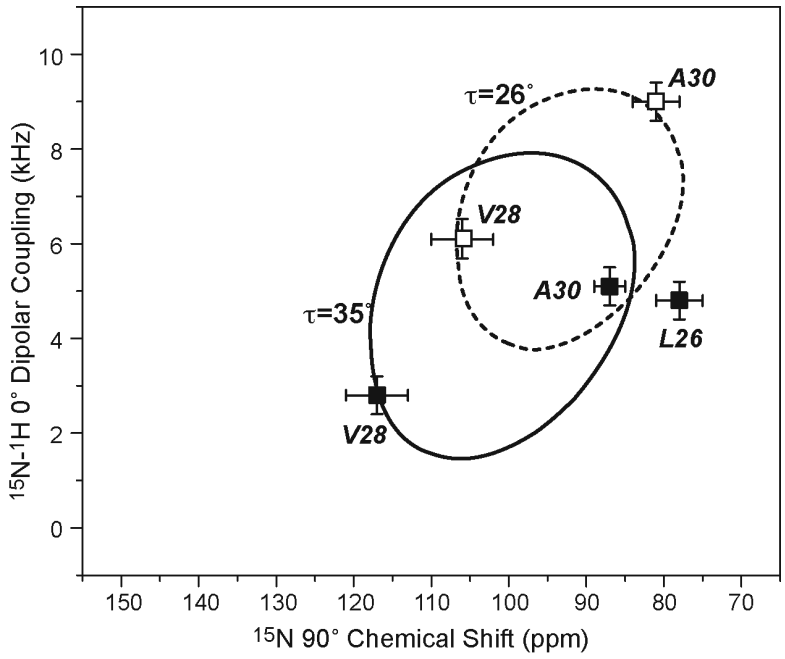

Figure 3.11. Orientation of M2TMP using 0°/90° PISA wheels constructed from data collected from unoriented samples. The DLPC membrane results of A30, V28, and L26 are shown in filled squares and solid lines. The POPC membrane data are shown in open squares and dashed lines.

The comparison between the DLPC and POPC data indicates clearly that the M2TMP helix tilt angle is affected by the membrane thickness: increasing the membrane thickness decreases the tilt angle, as expected for the hydrophobic thickness of the peptide to match the hydrophobic thickness of the lipid bilayer. The similar rotation angle between the two membranes is also expected, since the residues facing the pore lumen must be maintained to carry out the proton-conducting function (*51*). Mutation of key channel-facing residues can destabilize the channel (*10, 52*).

The tilt angle of 35±3° in the DLPC membrane is similar to, instead of larger than, the tilt angle found in the thicker DMPC membrane (*11*). This may be a result of the competition between increasing the tilt angle to minimize the hydrophobic mismatch and the need to maintain channel stability through sufficient hydrophobic contacts between the residues on different helices. The similarity suggests that a tilt angle of 35°-38° is the maximum achievable for this peptide while still maintaining its tetrameric state.

Below this maximum tilt angle, M2TMP orientation appears to still depend on the membrane thickness. The current result that the peptide orientation differs between DLPC and POPC bilayers supports a recent EPR study showing that the intermolecular distance between spin-labeled M2 helices changes with the membrane thickness (*20*). The previous observation by Cross and coworkers that the M2TMP orientation doesn't change significantly between DMPC and DOPC bilayers (*19*) may be coincidental: DOPC lipids differ from DMPC lipids not only in the chain length but also in having a double bond per chain, thus the lateral pressure of the two membranes differs. The unsaturated DOPC bilayer may laterally expand to adopt a similar thickness as the saturated DMPC bilayer, thus giving the same tilt angle for the M2 helices.

Figure 3.12 summarizes the orientation of M2TMP determined from the current study. M2TMP shows different tilt angles between DLPC and POPC bilayers. The P-P distances of the two membranes are ~30 Å and ~45 Å, respectively. The 25-residue M2TMP has a length of 37.5 Å if the ideal rise of 1.5 Å per residue is used. Thus a tilt angle of 35° and 26° yields, respectively, a vertical length of 31 Å and 34 Å, respectively. The former agrees well with the DLPC P-P distance, while the latter is shorter than the POPC P-P

distance but closer to the average between the estimated POPC hydrophobic thickness of 27 Å and the P-P distance (*20*).

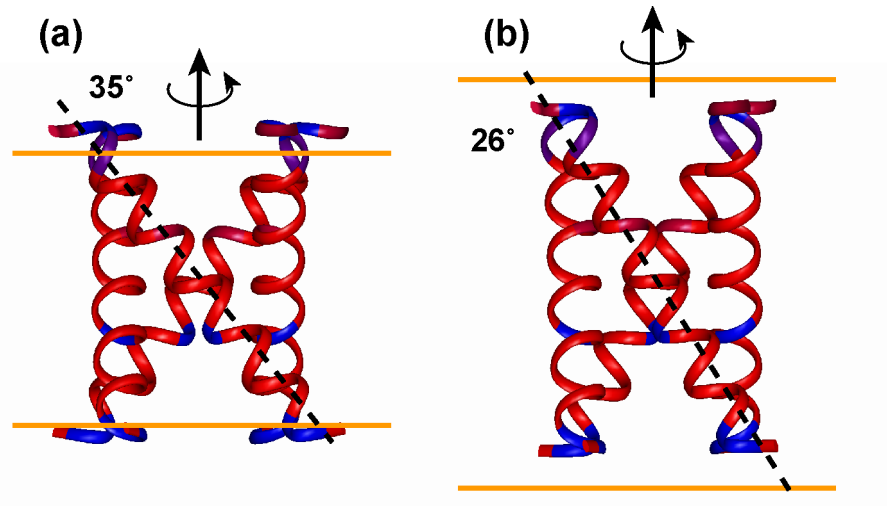

Figure 3.12. Orientation of M2TMP helical bundles in membranes of different thicknesses. (a) DLPC bilayer. (b) POPC bilayer. The P-P boundaries of the bilayer are shown in orange. The peptide lengths and P-P distances are shown to scale. Red: hydrophobic residues. Blue: polar and charged residues. The tilt angle of M2TMP is 35˚ in DLPC bilayers and 26˚ in POPC bilayers.

M2(19-60) orientation from powder samples using ^{15}N NMR

Finally, we apply this powder orientation determination technique to a longer construct of the M2 protein, M2(19-60), whose orientation has not been determined before. This construct encompasses all the structured regions of the M2 protein, and has been shown to be functional in oocytes (*7*). With a molecular weight of 4878, the M2(19-60) peptide would be more difficult to align than M2TMP. Figure 3.9e shows the static ^{15}N spectrum of V28 in M2(19-60) bound to DLPC bilayers: a chemical shift of 123 ppm is observed, similar to the value found for M2TMP in the same membrane. Since the rotation angle of the protein is fixed, the similarity in the ^{15}N CSA indicates that M2(19-60) has the same tilt angle as M2TMP within experimental uncertainty. This implies that structural conclusions made on the M2TMP helical bundle can be reasonably extrapolated to the longer peptide.

Interestingly, the V28 ^{15}N chemical shift lineshape in M2(19-60) is much narrower than in M2TMP, suggesting that the inclusion of the extra-membrane residues creates a conformationally more homogeneous peptide.

Although a complete investigation of M2(19-60) is beyond the scope of the current paper, the data is quite interesting with respect to the role of the C-terminal helix in influencing the properties of the M2 proton channel. Previous studies of M2TMP suggested that the tetramer formed by this peptide had multiple conformations, some of which could be stabilized by specific mutations to its sequence (*53*). The decrease in heterogeneity in M2(19-60) versus M2TMP suggests that the C-terminal helix helps specifically stabilize one or a small subset of conformations within the transmembrane helix. Furthermore, the C-terminal helix lies just C-terminal to and structurally interacts with the His_{37}-Trp_{41} pair that forms the proton selectivity filter in M2. Thus, it might modulate the properties of this essential motif, which is known to be required for proton conduction. Finally, while we have not yet made measurements involving labeled residues in the C-terminal helix, it is clear that the present approach has considerable promise for examining the conformation of this region of the protein.

Conclusion

We have shown that in the presence of fast uniaxial rotational diffusion, orientation-dependent PISA wheels in a 2D N-H/N correlation pattern can be obtained from unoriented membrane protein samples. This allows membrane protein orientation to be determined without macroscopic alignment, thus offering an important opportunity for studying membrane proteins that naturally disrupt lipid bilayers or that are difficult to align. In this work the M2TMP samples are studied under conditions where the peptide forms tetrameric helical bundles, as determined by separate ^{19}F spin diffusion experiments. Thus, the observed fast uniaxial motion of the whole helical bundle, with a total molecular weight of 10.9 kDa, indicates that membrane proteins with an effective size smaller than 100 residues have the requisite uniaxial mobility to give orientation-dependent NMR spectra for interactions as large as the ^{2}H quadrupolar coupling. But since the spin interactions most sensitive to helix

orientations are ^{15}N-related tensors, the minimum required rotational diffusion rates is much lower (Figure 3.1), and membrane proteins with a radius as large as 30 Å should be accessible to this powder sample approach using ^{15}N NMR. Further experiments are necessary to show whether uniaxial rotations fast compared to the ^{15}N NMR timescale are indeed general in larger proteins. In addition to the protein molecular weight, the P/L ratio may also affect the uniaxial rotational rate. The motionally averaged spectra shown here were obtained from samples containing relatively high mass concentrations of peptide, ~20%. This suggests that it is not necessary to lower the protein concentration significantly to ensure motion. Instead, it is more important to maintain the protein or peptide assembly in their natural functional states without non-specific aggregation, as indicated by the dramatically different mobilities observed between the organically mixed and aqueous mixed M2TMP samples.

The powder samples allow MAS experiments to be used for orientation determination. Combining ^{13}C and ^{15}N labeling, one can in principle employ multidimensional correlation experiments to simultaneously extract multiple orientational constraints. While for demonstration we only measured site-specifically ^{15}N-labeled samples here, the 2D N-H DIPSHIFT and ^{15}N CSA filter experiments can be extended to three dimensions, where an additional ^{13}C chemical shift dimension can be used to resolve multiple residues in the protein. The main challenge will be to conduct these experiments in the liquid-crystalline phase of the membrane where the protein is mobile, with motionally averaged dipolar couplings for polarization transfer.

Acknowledgement: The authors thank Tim Doherty for help with the synthesis of Fmoc-protected amino acids. This work is supported by NSF grant MCB-0543473 to M. H. and NIH grant GM56423 to W.F. D.

References

1. Opella, S. J., and Marassi, F. M. (2004) Structure determination of membrane proteins by NMR spectroscopy, *Chem. Rev. 104*, 3587-3606.

2. Hong, M. (2006) Oligomeric structure, dynamics, and orientation of membrane proteins from solid-state NMR, *Structure 14*, 1731-1740.
3. Buffy, J. J., McCormick, M. J., Wi, S., Waring, A., Lehrer, R. I., and Hong, M. (2004) Solid-State NMR Investigation of the Selective Perturbation of Lipid Bilayers by the Cyclic Antimicrobial Peptide RTD-1, *Biochemistry 43*, 9800-9812.
4. Hallock, K. J., Lee, D. K., and Ramamoorthy, A. (2003) MSI-78, an Analogue of the Magainin Antimicrobial Peptides, Disrupts Lipid Bilayer Structure via Positive Curvature Strain, *Biophys. J. 84*, 3052-3060.
5. Lamb, R. A., Holsinger, K. J., and Pinto, L. H. (1994) The Influenza A virus M2 ion channel protein and its role in the influenza virus life cycle., in *Cellular Receptors of Animal Viruses* (Wemmer, E., Ed.), pp 303-321, Cold Spring Harbor Lab Press, Plainview, NY.
6. Pinto, L. H., and Lamb, R. A. (2006) The M2 Proton Channels of Influenza A and B Viruses, *J. Biol. Chem. 281*, 8997-9000.
7. Pinto, L. H., Holsinger, L. J., and Lamb, R. A. (1992) Influenza virus M2 protein has ion channel activity, *Cell 69*, 517-528.
8. Tang, Y., Zaitseva, F., Lamb, R. A., and Pinto, L. H. (2002) The Gate of the Influenza Virus M2 Proton Channel Is Formed by a Single Tryptophan Residue, *J. Biol. Chem. 277*, 39880-39886.
9. DeGrado, W. F., Gratkowski, H., and Lear, J. D. (2003) How do helix-helix interactions help determine the folds of membrane proteins? Perspectives from the study of homo-oligomeric helical bundles., *Protein Sci. 12*, 647-665.
10. Howard, K. P., Lear, J. D., and DeGrado, W. F. (2002) Sequence determinants of the energetics of folding of a transmembrane four-helix-bundle protein, *Proc. Natl. Acad. Sci. USA 99*, 8568-8572.
11. Wang, J., Kim, S., Kovacs, F., and Cross, T. A. (2001) Structure of the transmembrane region of the M2 protein H(+) channel, *Protein Sci. 10*, 2241-2250.
12. Nishimura, K., Kim, S., Zhang, L., and Cross, T. A. (2002) The closed state of a H+ channel helical bundle combining precise orientational and distance restraints from solid state NMR, *Biochemistry 41*, 13170-13177.

13. Duff, K. C., Gilchrist, P. J., Saxena, A. M., and Bradshaw, J. P. (1994) Neutron diffraction reveals the site of amantadine blockade in the influenza A M2 ion channel, *Virology 202*, 287-293.
14. Wu, Y., and Voth, G. A. (2005) A Computational Study of the Closed and Open States of the Influenza A M2 Proton Channel, *Biophys. J. 89*, 2402-2411.
15. Fischer, W. B., and Sansom, M. S. (2002) Viral ion channels: structure and function, *Biochim. Biophys. Acta 1561*, 27-45.
16. Zhong, Q., Husslein, T., Moore, P. B., Newns, D. M., Pattnaik, P., and Klein, M. L. (1998) The M2 channel of influenza A virus: a molecular dynamics study, *FEBS Lett. 434*, 265-271.
17. Zhong, Q., Newns, D. M., Pattnaik, P., Lear, J. D., and Klein, M. L. (2000) Two possible conducting states of the influenza A virus M2 ion channel, *FEBS Lett. 473*, 195-198.
18. Luo, W., and Hong, M. (2006) Determination of the Oligomeric Number and Intermolecular Distances of Membrane Protein Assemblies by Anisotropic1H-Driven Spin Diffusion NMR Spectroscopy, *J. Am. Chem. Soc. 128*, 7242-7451.
19. Kovacs, F. A., and Cross, T. A. (1997) Transmembrane four-helix bundle of influenza A M2 protein channel: structural implications from helix tilt and orientation, *Biophys. J. 73*, 2511-2517.
20. Duong-Ly, K. C., Nanda, V., Degrado, W. F., and Howard, K. P. (2005) The conformation of the pore region of the M2 proton channel depends on lipid bilayer environment, *Protein Sci. 14*, 856-861.
21. Kochendoerfer, G. G., Salom, D., Lear, J. D., Wilk-Orescan, R., Kent, S. B., and DeGrado, W. F. (1999) Total chemical synthesis of the integral membrane protein influenza A virus M2: role of its C-terminal domain in tetramer assembly., *Biochemistry 38*, 11905-11913.
22. Tian, C., Tobler, K., Lamb, R. A., Pinto, L. H., and Cross, T. A. (2002) Expression and initial structural insights from solid-state NMR of the M2 proton channel from influenza A virus, *Biochemistry 41*, 11294-11300.
23. Carpino, L. A., and Han, G. Y. (1972) The 9-Fluorenylmethoxycarbonyl Amino-Protecting Group, *J. Org. Chem. 37*, 3404-3409.

24. Ito, T., Gorman, O. T., Kawaoka, Y., Bean, W. J., and Webster, R. G. (1991) Evolutionary analysis of the influenza A virus M gene with comparison of the M1 and M2 proteins, *J. Virol. 65*, 5491-5498.
25. Wang, C., Takeuchi, K., Pinto, L. H., and Lamb, R. A. (1993) Ion channel activity of influenza A virus M2 protein: characterization of the amantadine block, *J. Virol. 67*, 5585-5594.
26. Traikia, M., Warschawski, D. E., Recouvreur, M., Cartaud, J., and Devaux, P. F. (2000) Formation of unilamellar vesicles by repetitive freeze-thaw cycles: characterization by electron microscopy and 31P-nuclear magnetic resonance, *Eur. Biophys. J. 29*, 184-195.
27. Pace, C. N., Vajdos, F., Fee, L., Grimsley, G., and Gray, T. (1995) How to measure and predict the molar absorption coefficient of a protein, *Protein Sci. 4*, 2411-2423.
28. Smith, P. K., Krohn, R. I., Hermanson, G. T., Mallia, A. K., Gartner, F. H., Provenzano, M. D., Fujimoto, E. K., Goeke, N. M., Olson, B. J., and Klenk, D. C. (1985) Measurement of Protein Using Bicinchoninic Acid, *Anal. Biochem. 150*, 76-85.
29. Luo, W., Mani, R., and Hong, M. (2007) Sidechain conformation and gating of the M2 transmembrane peptide proton channel of influenza A virus from solid-state NMR, *J. Phys. Chem. B. 111*, 10825-10832.
30. Munowitz, M. G., Griffin, R. G., Bodenhausen, G., and Huang, T. H. (1981) Two-dimensional rotational spin-echo NMR in solids: correlation of chemical shift and dipolar interactions, *J. Am. Chem. Soc. 103*, 2529-2533.
31. Hong, M., Gross, J. D., Rienstra, C. M., Griffin, R. G., Kumashiro, K. K., and Schmidt-Rohr, K. (1997) Coupling Amplification in 2D MAS NMR and Its Application to Torsion Angle Determination in Peptides, *J. Magn. Reson. 129*, 85-92.
32. Huster, D., Yamaguchi, S., and Hong, M. (2000) Efficient b-Sheet Identification in Proteins by Solid-State NMR Spectroscopy, *J. Am. Chem. Soc. 122*, 11320-11327.
33. Liu, S. F., Mao, J. D., and Schmidt-Rohr, K. (2002) A robust technique for two-dimensional separation of undistorted chemical-shift anisotropy powder patterns in magic-angle-spinning NMR, *J. Magn. Reson. 155*, 15-28.

34. Hong, M., and Doherty, T. (2006) Orientation determination of membrane-disruptive proteins using powder samples and rotational diffusion: a simple solid-state NMR approach, *Chem. Phys. Lett. 432*, 296-300.
35. Saffman, P. G., and Delbruck, M. (1975) Brownian motion in biological membranes, *Proc. Natl. Acad. Sci. USA 72*, 3111-3113.
36. Aisenbrey, C., and Bechinger, B. (2004) Investigations of polypeptide rotational diffusion in aligned membranes by 2H and 15N solid-state NMR spectroscopy, *J. Am. Chem. Soc. 126*, 16676-16683.
37. Song, Z., Kovacs, F. A., Wang, J., Denny, J. K., Shekar, S. C., Quine, J. R., and Cross, T. A. (2000) Transmembrane domain of M2 protein from influenza A virus studied by solid-state 15N polarization inversion spin exchange at magic angle NMR, *Biophys. J. 79*, 767-775.
38. Palmer, A. G., Williams, J., and McDermott, A. (1999) Nuclear magnetic resonance studies of biopolymer dynamics, *J. Phys. Chem. 100*, 13293-13310.
39. Strandberg, E., Wadhwani, P., Tremouilhac, P., Durr, U. H., and Ulrich, A. S. (2006) Solid-state NMR analysis of the PGLa peptide orientation in DMPC bilayers: structural fidelity of 2H-labels versus high sensitivity of 19F-NMR, *Biophys. J. 90*, 1676-1686.
40. Rothwell, W. P., and Waugh, J. S. (1981) Tranverse relaxation of dipolar coupled spin systems under rf irradiation: detecting motions in solids., *J. Chem. Phys. 74*, 2721-2732.
41. Tycko, R., Dabbagh, G., and Mirau, P. A. (1989) Determination of Chemical-Shift-Anisotropy Lineshapes in a Two-Dimensional Magic-Angle-Spinning NMR Experiment, *J. Magn. Reson. 85*, 265-274.
42. Sun, H., Sanders, L. K., and Oldfield, E. (2002) Carbon-13C NMR shielding in the twenty amino acids: comparisons with experimental results in proteins., *J. Am. Chem. Soc. 124*, 5486-5495.
43. Marassi, F. M., and Opella, S. J. (2000) A solid-state NMR index of helical membrane protein structure and topology, *J. Magn. Reson. 144*, 150-155.
44. Wang, J., Denny, J., Tian, C., Kim, S., Mo, Y., Kovacs, F., Song, Z., Nishimura, K., Gan, Z., Fu, R., Quine, J. R., and Cross, T. A. (2000) Imaging membrane protein helical wheels, *J. Magn. Reson. 144*, 162-167.

45. Park, S. H., Mrse, A. A., Nevzorov, A. A., De Angelis, A. A., and Opella, S. J. (2006) Rotational diffusion of membrane proteins in aligned phospholipid bilayers by solid-state NMR spectroscopy, *J. Magn. Reson. 178*, 162-165.
46. Munowitz, M., Aue, W. P., and Griffin, R. G. (1982) Two-dimensional separation of dipolar and scaled isotropic chemical shift interactions in magic angle NMR spectra, *J. Chem. Phys. 77*, 1686-1689.
47. vanRossum, B. J., deGroot, C. P., Ladizhansky, V., Vega, S., and deGroot, H. J. M. (2000) A method for measuring heteronuclear (1H-13C) distances in high speed MAS NMR, *J. Am. Chem. Soc. 122*, 3465-3472.
48. Yamaguchi, S., Huster, D., Waring, A., Lehrer, R. I., Tack, B. F., Kearney, W., and Hong, M. (2001) Orientation and Dynamics of an Antimicrobial Peptide in the Lipid Bilayer by Solid-State NMR, *Biophys. J. 81*, 2203-2214.
49. Wylie, B. J., Franks, W. T., and Rienstra, C. M. (2006) Determinations of 15N chemical shift anisotropy magnitudes in a uniformly 15N,13C-labeled microcrystalline protein by three-dimensional magic-angle spinning nuclear magnetic resonance spectroscopy, *J. Phys. Chem. B. 110*, 10926-10936.
50. Mesleh, M. F., Lee, S., Veglia, G., Thiriot, D. S., Marassi, F. M., and Opella, S. J. (2003) Dipolar waves map the structure and topology of helices in membrane proteins, *J. Am. Chem. Soc. 125*, 8928-8935.
51. Pinto, L. H., Dieckmann, G. R., Gandhi, C. S., Papworth, C. G., Braman, J., Shaughnessy, M. A., Lear, J. D., Lamb, R. A., and DeGrado, W. F. (1997) A functionally defined model for the M2 proton channel of influenza A virus suggests a mechanism for its ion selectivity, *Proc. Natl. Acad. Sci. USA 94*, 11301-11306.
52. Wang, C., Lamb, R. A., and Pinto, L. H. (1995) Activation of the M2 ion channel of influenza virus: a role for the transmembrane domain histidine residue, *Biophys. J. 69*, 1363-1371.
53. Stouffer, A. L., Nanda, V., Lear, J. D., and DeGrado, W. F. (2005) Sequence determinants of a transmembrane proton channel: an inverse relationship between stability and function., *J. Mol. Biol. 347*, 169-179.

Chapter 4

Simultaneous Extraction of Multiple Orientational Constraints of Membrane Proteins by ^{13}C-Detected N-H Dipolar Couplings Under Magic Angle Spinning

A paper published in Journal of Magnetic Resonance

2008 vol. 191 pp. 219-225

Sarah D. Cady and Mei Hong

Abstract

A ^{13}C-detected N-H dipolar coupling technique is introduced for uniaxially mobile membrane proteins for orientation determination using unoriented samples. For proteins undergoing rigid-body uniaxial rotation in the lipid bilayer, the intrinsic equality between the dipolar coupling constants measured in unoriented samples and the anisotropic coupling measured in static oriented samples has been shown recently. Here, we demonstrate that the orientation-sensitive backbone N-H dipolar couplings can be measured with ^{13}C detection using 2D and 3D MAS correlation experiments, so that maximal site resolution can be achieved and multiple orientational constraints can be extracted from each experiment. We demonstrate this technique on the M2 transmembrane peptide of the influenza A virus, where the N-H dipolar couplings of various residues fit to a dipolar wave for a helical tilt angle of 37°, in excellent agreement with data obtained from singly ^{15}N-labeled samples.

Introduction

Orientation determination of membrane proteins by solid-state NMR traditionally requires mechanically or magnetically aligned proteins under the static condition (*1, 2*). The alignment results in resolved spectra with anisotropic frequencies - chemical shift or dipolar coupling – indicative of the protein orientation relative to the membrane normal. While this approach has been successfully used to determine the orientation of many membrane peptides and proteins (*1, 3*), macroscopic alignment is a rate-limiting step to this technique.

High-quality alignment usually requires extensive optimization of sample conditions such as the types of lipids, the protein/lipid molar ratio, and the degree of hydration. These factors can severely restrict the determination of membrane protein orientation. To facilitate membrane protein orientation determination, we have recently introduced a powder sample approach that relies on the presence of uniaxial rotational diffusion of the protein in the lipid bilayer (*4, 5*). When the protein undergoes rigid-body uniaxial rotation with respect to the bilayer normal, the NMR order parameters depend on the angle between the molecule-fixed spin interaction tensor and the motional axis. Thus, by measuring the motionally averaged dipolar couplings or chemical shift anisotropies in powder samples, one can extract the same orientation information as in aligned samples.

We previously demonstrated this powder-sample orientation determination technique on a tetrameric α-helical bundle, the M2 transmembrane domain (M2TMP) of the influenza A virus, by measuring, on singly ^{15}N-labeled samples, the static ^{15}N chemical shift powder patterns and the N-H dipolar couplings under magic-angle spinning (MAS) using the DIPSHIFT (*6*) method (*4*). The choice of ^{15}N spin interactions is natural because their principal axis systems are approximately along the helix axis, thus their spectra are sensitive to the tilt and rotation angles of the helical axis. However, to obtain many orientational constraints simultaneously, static chemical shift anisotropy (CSA) measurement with no site resolution is clearly undesirable. Even if MAS-based 2D ^{15}N CSA or N-H dipolar recoupling techniques are used to give site-resolved information, the ^{15}N isotropic shift resolution is usually limited compared to the ^{13}C spectra. The chemical shift ranges for α-helical proteins, defined as twice the standard deviations, are about 6.0 ppm for ^{15}N and 8.5 ppm for ^{13}Cα (*7*). Considering that the typical ^{13}C linewidths of membrane proteins are 1-2 ppm whereas the ^{15}N linewidths are often about 3 ppm, the effective resolution, estimated as the shift range/linewidth ratio, is 2-4 times higher for ^{13}Cα than ^{15}N. Moreover, ^{13}C detection has higher sensitivity than ^{15}N. Thus, it is desirable to convert the ^{15}N-detected N-H dipolar coupling experiment to ^{13}C detection. Further, it would be desirable to use two chemical shift dimensions instead of one to resolve the resonances and using a third dimension to sample the N-H dipolar evolution. The challenge is to carry out the necessary coherence transfer between ^{13}C and ^{15}N nuclei under the condition that the protein is mobile, which entails

reduced dipolar couplings and possibly unfavorable relaxation properties. Provided that this coherence transfer is feasible, the N-H dipolar couplings from multiple residues can be measured simultaneously with ^{13}C detection to map out the orientation of the protein. It is not essential to measure the ^{15}N chemical shift anisotropies since the N-H dipolar couplings exhibit a periodicity with respect to residue number that is already sufficient for determining the helix orientation. The residue-periodic N-H dipolar couplings yield the so-called dipolar wave (*8*), which contains full information on the tilt and rotation angles of the protein. In this work, we show that such a ^{13}C-detected N-H dipolar wave method is indeed feasible under MAS for an unoriented membrane protein with the requisite uniaxial mobility.

Materials and Methods

Uniformly ^{13}C, ^{15}N-labeled and Fmoc-protected amino acids were either obtained from Sigma (Miamisburg, OH) and Cambridge Isotope Laboratories (Andover, MA), or prepared in house. The transmembrane domain of the M2 protein of the Udorn strain of influenza A virus (*9*) was synthesized by PrimmBiotech (Cambridge, MA) and purified to >95% purity. The amino acid sequence is SSDPLVVAASIIGILHLILWILDRL. Two peptide samples each containing four U-^{13}C, ^{15}N-labeled residues were synthesized. The first sample contains ^{13}C, ^{15}N-labeled residues at L26, A29, G34 and I35. The second sample contains labels at V27, A30, I33 and L38.

M2TMP was reconstituted into liposomes by a detergent dialysis protocol (*10*). Briefly, 1,2-dilauroyl-*sn*-glycero-3-phosphatidylcholine (DLPC) (Avanti Polar Lipids) was suspended in 1 mL phosphate buffer (10 mM Na_2HPO_4/NaH_2PO_4, 1 mM EDTA, 0.1 mM NaN_3, 10 mM amantadine) at pH 7.5. 10 mM amantadine is present in all solutions. The lipid solution was vortexed and freeze-thawed to make uniform vesicles of about 200 nm in diameter. M2TMP was codissolved with the detergent octyl-β-D-glucopyranoside (OG) in 2 mL phosphate buffer at an OG concentration of 30 mg/mL. The M2TMP/OG solution was then mixed with the DLPC vesicle solution, reaching an OG concentration of 15 mg/mL. The mixture was vortexed for 1 hour, allowed to stand for 6-8 hours at room temperature, and dialyzed against 1 L phosphate buffer at 4°C while changing the buffer every 8-12 hours for 3 days. The dialyzed M2TMP/DLPC solution was centrifuged at 150,000 g for 3 hours at

10°C to give a membrane pellet that is about 50 wt% hydrated. The final protein/lipid molar ratio is 1:15. UV-VIS absorption and photometric assay of the supernatant showed 98% binding of the peptide to the membrane.

Solid-state NMR experiments were carried out on a Bruker AVANCE-600 (14.1 Tesla) spectrometer using a 4 mm triple-resonance MAS probe. Typical 90° pulse lengths for ^{1}H, ^{13}C and ^{15}N were 4 μs, 5 μs and 6 μs respectively. ^{1}H decoupling strengths were 71 kHz during ^{13}C-^{15}N REDOR and acquisition, and 76.5 kHz FSLG homonuclear decoupling during N-H dipolar dephasing.

N-H dipolar waves for various orientations were calculated using a home-written Fortran program. A 25-residue ideal α-helix is used as the input structure for the calculation and is rotated to different tilt angles with respect to the z-axis. The calculated N-H dipolar couplings are plotted against the residue number and fit to a sinusoidal equation $y(\tau,\rho) = C(\tau) + A(\tau)\sin\left(\left(2n \cdot \frac{100}{360} + \phi(\rho)\right)\pi\right)$, where the offset C(τ) and amplitude A(τ) reflect the tilt angle while the phase φ(ρ) of the wave depends on the rotation angle ρ. The rotation angle in the simulation was fixed to within 10° by our previous orientation data obtained in DLPC bilayers (*4, 11*) and the data of Cross and coworkers measured in DMPC bilayers (*12*). It was subsequently held constant in the simulations. This is reasonable because the proton channel function of the M2TMP helical bundle dictates that the helices have a well defined rotation angle that places certain residues in the channel lumen to carry out the proton conduction and gating functions (*13*).

Results and Discussion

Pulse sequence

Figure 4.1 shows the ^{13}C-detected N-H dipolar coupling pulse sequences in the 2D or 3D mode. ^{13}C-^{15}N two-spin coherences are generated from ^{13}C magnetization by a REDOR pulse train (*14*). The resulting ^{15}N antiphase magnetization is allowed to evolve under the scaled N-H dipolar coupling for a period t_1. Subsequently, ^{15}N chemical shift evolution may be added as the t_2 dimension if the 3D experiment is desired. The ^{15}N antiphase

magnetization is then reconverted back to ^{13}C magnetization using an identical REDOR pulse train, and detected in the t_3 period. Thus, the ^{13}C and ^{15}N coherence transfer is achieved in an out-and-back heteronuclear single-quantum coherence fashion (*15*).

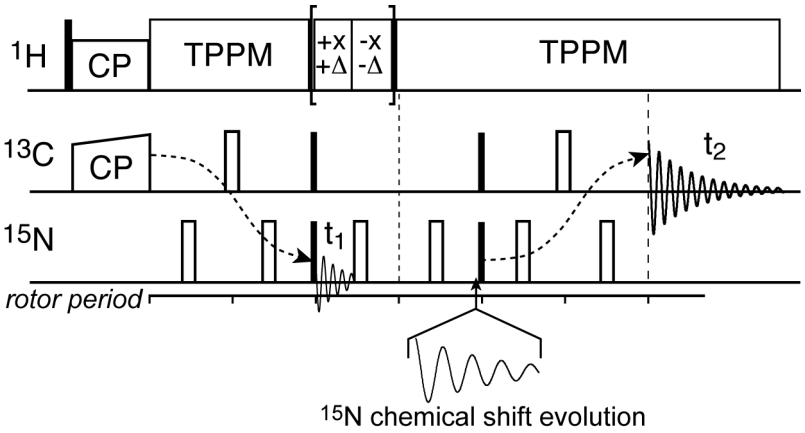

Figure 4.1. Pulse sequence for the ^{13}C-detected N-H dipolar coupling measurement. The ^{1}H homonuclear decoupling sequence depicted is FSLG. The optional ^{15}N chemical shift evolution period can be inserted to make this a 3D experiment to enhance site resolution.

During the N-H dipolar evolution period, frequency-switched Lee-Goldburg (FSLG) ^{1}H homonuclear decoupling (*16*) was applied for a whole rotor period, while a ^{15}N 180° pulse was moved through the rotor period to induce dipolar dephasing. A second rotor period with ^{1}H heteronuclear decoupling and a synchronously moving ^{15}N 180° pulse refocuses the chemical shift anisotropy encoded in the first rotor period while retaining the N-H dipolar phase. As shown before, this method doubles the dipolar dephasing compared to the case of incrementing the ^{1}H homonuclear decoupling period (*17*). Due to the short cycle time of the FSLG sequence, relatively fast spinning speeds of 7-10 kHz can be used, which is necessary for suppressing residual ^{13}C-^{13}C dipolar interactions in uniformly ^{13}C labeled proteins.

Model peptide formyl-MLF

We first demonstrate this ^{13}C-detected N-H dipolar coupling experiment on U-^{13}C, ^{15}N-labeled formyl-MLF, a rigid crystalline peptide with good spectral resolution (*18, 19*). Figure 4.2 shows the ^{15}N 1D CP-MAS spectrum and the ^{13}C spectrum after passing through

the ^{13}C-^{15}N REDOR filter. For this well ordered crystalline peptide, the ^{15}N spectrum is already resolved for the three sites; however this is not generally true for membrane proteins. Figure 4.2c-d show the 2D ^{13}C-^{15}N correlation spectra with no N-H dipolar evolution (c) and with half a rotor period of dipolar evolution (d), measured using the 3D mode of the pulse sequence in Figure 4.1. Both spectra were plotted with the same absolute-intensity contour levels to show the intensity reduction after 65 μs of N-H dipolar evolution. At 7 kHz MAS, 65 μs corresponds to half a rotor period of net evolution. A ^{1}H FSLG t_{360° pulse length of 13.06 μs was used in the experiment.

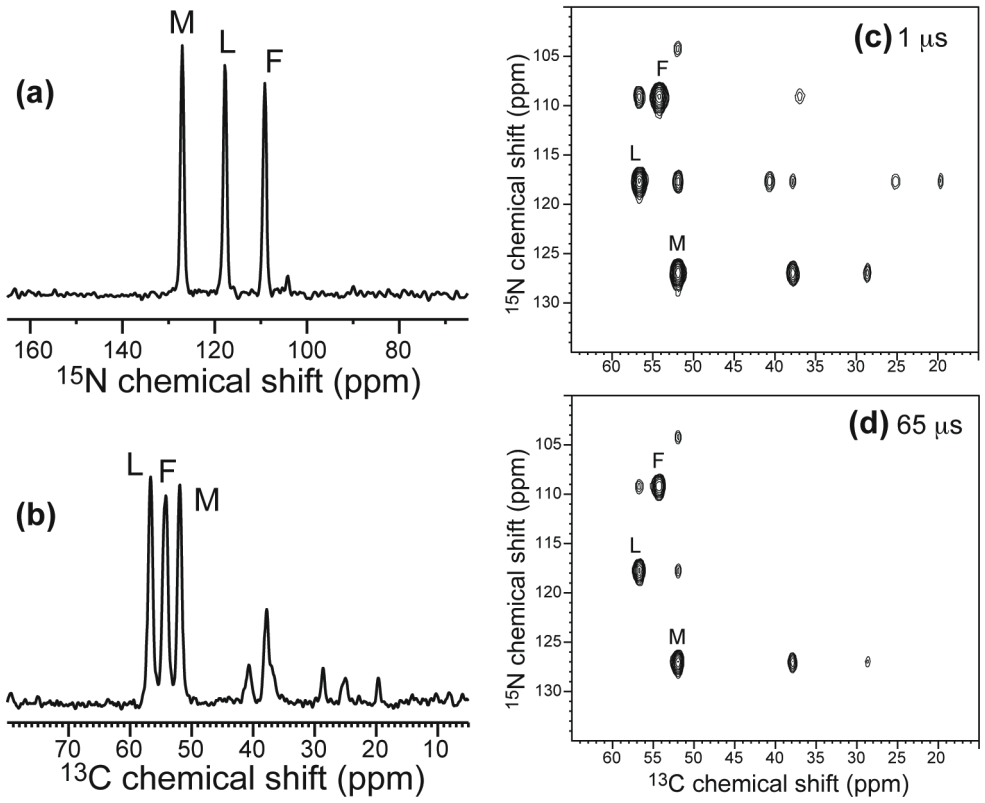

Figure 4.2. Detecting N-H dipolar dephasing of formyl-MLF by ^{13}C detection. (a) ^{15}N CP-MAS spectrum. (b) ^{13}C MAS spectrum after a 1.42 ms ^{13}C-^{15}N REDOR filter. (c) 2D ^{13}C-^{15}N correlation spectrum with no N-H dipolar dephasing. (d) 2D ^{13}C-^{15}N correlation spectrum with 65 μs N-H dipolar dephasing. The data were obtained under 7 kHz MAS at ambient temperature.

The N-H dipolar dephasing curves of the three residues are plotted in Figure 4.3. The data of three experiments are shown: the normal 2D ^{15}N-detected DIPSHIFT curves (triangles), the 2D ^{13}C-detected DIPSHIFT curves (open squares) using the pulse sequence of Figure 4.1 without ^{15}N chemical shift evolution, and the 3D ^{13}C-^{15}N resolved DIPSHIFT curves (filled squares). All three methods produced the same couplings of 11.7 kHz for each residue within experimental uncertainty, which is ±0.5 kHz or smaller. The ^{13}C-detected spectra were obtained using a ^{13}C-^{15}N REDOR mixing time of 1.42 ms, including the excitation and reconversion periods. When shorter ^{13}C-^{15}N mixing times were used, we found that the ^{13}C-detected N-H dipolar couplings decreased by ~10%, indicating incomplete powder averaging that biases the N-H dipolar couplings. With 1.42 ms of ^{13}C-^{15}N REDOR coherence transfer, the sensitivity of the experiment on formyl MLF is about 10% of CP. Overall, the consistency between the ^{13}C-detected and ^{15}N-detected N-H dipolar dephasing indicates that the technique indeed works as expected.

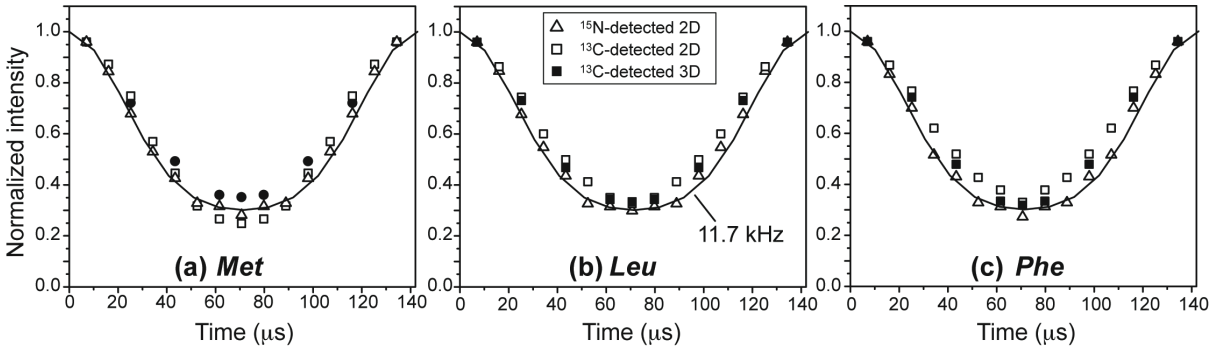

Figure 4.3. N-H dipolar dephasing curves of the three residues of formyl-MLF, measured by three methods: ^{15}N-detected 2D DIPSHIFT (open triangles), ^{13}C-detected 2D DIPSHIFT (open squares), and ^{13}C-^{15}N resolved 3D DIPSHIFT (filled squares).

Influenza A virus M2 transmembrane peptide

For motionally averaged proteins in lipid membranes, the intrinsic sensitivity of the ^{13}C-detected N-H dipolar coupling experiment is lower due to the small amount of protein in a sample that is largely composed of lipid, and due to the lower efficiency of the ^{13}C-^{15}N coherence transfer. Due to motion, the ^{13}C-^{15}N dipolar coupling driving the coherence

transfer is scaled by the order parameter $S \equiv \bar{\delta}/\delta = \frac{1}{2}\left(3\cos^2\theta - 1\right)$, where θ is the angle between the C-N bond and the motional axis. It is thus necessary to test the feasibility of this technique in a real membrane protein under the condition of uniaxial mobility. We chose the M2 transmembrane protein of the influenza A virus, since its tetrameric helical bundle (*20*) has been shown to undergo rigid-body uniaxial rotational diffusion around the bilayer normal in DLPC, DMPC and POPC bilayers (*4, 21*). We carried out the experiment on M2TMP reconstituted in DLPC bilayers with the drug amantadine present (*22*). The use of amantadine is essential for the experiment because the drug significantly orders the peptide structure (*11*), which is manifested by much higher spectral resolution and longer ^{13}C T_2 relaxation times (*11*). Without amantadine, the Cα T_2 values are only 1.0 – 1.8 ms, which makes the efficiency of ^{13}C-^{15}N coherence transfer prohibitively low. With amantadine, the Cα T_2 increases to 2.1 – 3.5 ms (*11*).

Figure 4.4a shows the ^{15}N CP-MAS spectrum of one of the M2TMP samples. While the linewidth is quite narrow for a membrane protein, two of the sites still overlap completely. The corresponding ^{13}C spectrum after 1.42 ms of REDOR filter (Figure 4b), on the other hand, shows complete resolution of the Cα signals. The use of the ^{13}C-^{15}N REDOR filter not only selected the Cα signals of the protein but also completely removed the lipid background ^{13}C signals, thus significantly simplifying spectral assignment. Two representative N-H dipolar dephasing curves, for residues I35 and G34, are shown in Figure 4.4(c-d). The curves were measured with ^{13}C detection without ^{13}C-^{15}N correlation. The two residues show very different N-H dipolar couplings of 3.0 kHz and 6.1 kHz, indicating the difference in their N-H bond orientations relative to the motional axis. The two residues have very different sensitivities in the ^{13}C spectrum; but even the less sensitive G34 signal gave a self-consistent dephasing curve.

A total of six N-H dipolar couplings were resolved and measured in this way. They are plotted with respect to the residue number and shown in Figure 4.5. Indeed, the data fit to a periodic pattern, which is best represented by a dipolar wave for an ideal helix whose axis is tilted by 37° from the bilayer normal. This is in good agreement with the recently measured M2TMP tilt angle in the DLPC bilayer using singly ^{15}N-labeled samples (*4, 11*).

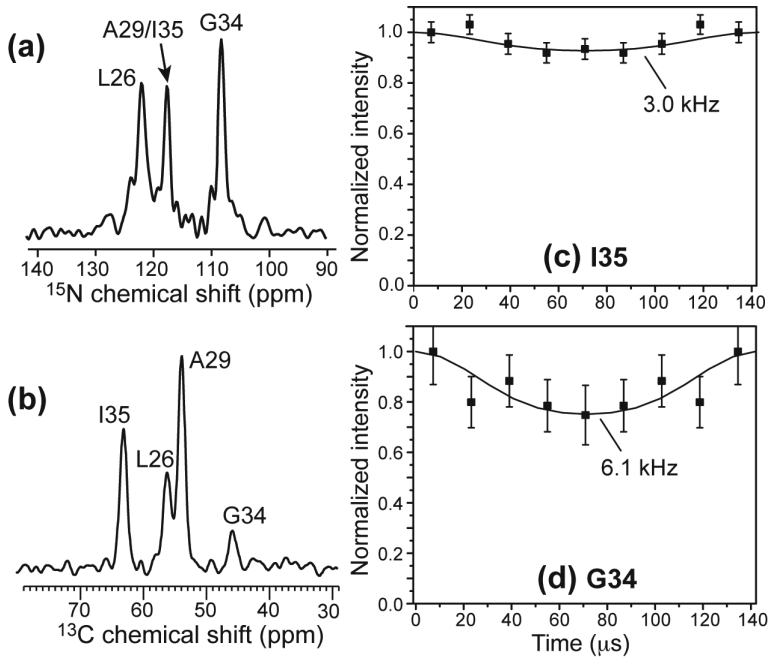

Figure 4.4. N-H dipolar couplings of ^{13}C, ^{15}N-labeled amantadine-bound M2TMP in DLPC bilayers at 313 K. (a) 1D ^{15}N CP-MAS spectrum. Two of the four ^{15}N labels overlap completely. NS = 5120. (b) ^{13}C MAS spectrum after 1.42 ms ^{13}C-^{15}N REDOR filter. All four $^{13}C\alpha$ labels are resolved. NS = 27,648. (c, d) ^{13}C-detected N-H dipolar dephasing curves for I35 (c) and G34 (d). The couplings indicated are the true values after dividing the fit values by 1.154 = 0.577 x 2 to take into account the FSLG scaling factor 0.577 and the doubling factor of 2. The experiment was conducted under 7 kHz MAS.

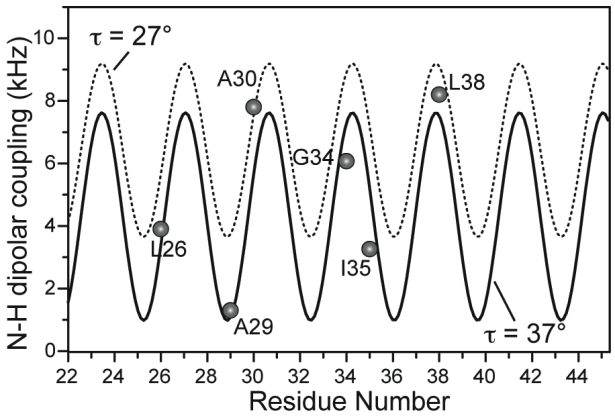

Figure 4.5. ^{13}C-detected N-H dipolar couplings of M2TMP as a function of residue number. The peptide is bound to DLPC bilayers with the drug amantadine present. The calculated wave corresponds to a tilt angle τ of 37°. The calculated wave for a tilt angle 27° is also shown for comparison (dotted line).

In Figure 4.5, two sites, A30 and L38, exhibit couplings significantly larger than the expected values for the 37˚ dipolar wave. At present we do not know the exact reason for these outliers. They may partly reflect a true helix axis orientation difference. Cross and coworkers recently reported that the helical segment C-terminal to G34 in M2TMP is kinked from the N-terminal segment in the presence of amantadine (*23*). Using glass-plate aligned DMPC membranes, they found a tilt angle of 30˚ for residues N-terminal to G34 but 20˚ for residues C-terminal to it. A similar helix kink may be present in the current DLPC bilayers as well, which could then explain the L38 data. More residues C-terminal to G34 need to be measured to test this hypothesis. Alternatively, the larger couplings could result from deviation of the helix from the ideal backbone conformation. It is certain that the abnormally large couplings do not result from the lack of uniaxial rotation, since the ^{2}H spectrum of CD_3-labeled A29 in the same sample showed a quadrupolar coupling of 15.5 kHz (not shown), which is much narrower than the 40 kHz expected when methyl rotation is the only motion. In other words, the peptide backbone must undergo reorientational motion to reduce the Cα-Cβ order parameter of A29 to an effective value of 0.39 (relative to the methyl group rigid limit of 40 kHz). We can also rule out segmental motion of A30 and L38 as the reason for the outliers, since any internal motion additional to the whole-body motion can only make the couplings smaller, instead of bigger, than the expected values. Thus, either a true helix orientation change or non-ideal backbone conformation at these residues account for the abnormal N-H couplings.

Sensitivity of the MAS ^{13}C-detected N-H dipolar wave experiment

The ^{13}C-detected N-H DIPSHIFT data on the amantadine-complexed M2TMP samples required signal-averaging of 23,000-27,000 scans per t_1 slice and nine t_1 slices, thus resulting in a total experimental time of about 5 days per sample. The efficiency of the experiment compared to CP is 5-15%, depending on the ^{13}C T_2 of the individual residues. To increase the sensitivity of the experiment, one could use an alternative method for C-N coherence transfer, which is double cross polarization (CP). The ^{15}N magnetization can be directly polarized from ^{1}H and evolves under the N-H dipolar coupling. It can then be transferred to $^{13}C\alpha$ by frequency-specific CP (*24*). Our tests on formyl-MLF showed that

indeed this SPECIFIC-CP method has a higher efficiency of ~40% compared to REDOR at a ^{15}N-^{13}C contact time of 3 ms. However, with 3 ms contact, the ^{13}C-detected N-H dipolar couplings were about 12% weaker than the rigid-limit value (10.4 kHz instead of 11.7 kHz) measured using the direct ^{15}N-detected DIPSHIFT experiment, suggesting incomplete powder averaging. Increasing the N–C CP contact time to as much as 7 ms did not change the situation. The dephasing value at the middle of the rotor period for Leu was 0.39 for the ^{13}C-detected DIPSHIFT experiment versus 0.31 for the direct ^{15}N-detected experiment. For all sites, a 25-50% increase in the intensity in the middle of the rotor period is seen, indicating weaker dipolar couplings. Moreover, using a long C-N contact time places a higher demand on the probe due to the simultaneous radiofrequency (rf) irradiation. In real membrane proteins with the requisite mobility, long contact times may also cause potential $T_{1\rho}$ losses. These shortcomings may be circumvented, however, if the reduced dipolar couplings due to incomplete powder averaging can be calculated and corrected for, in which case this CP-based DIPSHIFT method would be significantly more sensitive.

Conclusion

In conclusion, we have demonstrated an MAS ^{13}C-detected N-H dipolar coupling technique to simultaneously extract multiple orientational constraints of membrane proteins in unoriented lipid bilayers by virtue of their uniaxial motion. The enhanced site resolution provided by ^{13}C chemical shifts is a significant advantage over the ^{15}N-detected experiment, and the ability to extend this approach to 3D to further resolve resonances makes this approach more applicable to larger membrane proteins. The elimination of sample alignment and the adoption of MAS technology for orientation determination are major advantages of this approach. In this way, multiple orientation-dependent N-H dipolar couplings can be measured to yield dipolar waves, from which both the helix orientation and helical structure defects can be detected.

For this ^{13}C-detected ^{15}N-^{1}H dipolar wave technique to be generally applicable, long ^{13}C T_2 is essential to facilitate the ^{13}C-^{15}N coherence transfer. In the case of the M2TMP helical bundle, the use of a natural channel blocker, amantadine, made the dynamic property of the protein sufficiently favorable to be amenable to this technique. Future development of

more efficient coherence transfer techniques for mobile systems will be desirable to further increase the sensitivity of this class of techniques.

Acknowledgement: This work is funded by National Science Foundation grant MCB-0543473.

References

1. Opella, S. J., and Marassi, F. M. (2004) Structure determination of membrane proteins by NMR spectroscopy, *Chem. Rev. 104*, 3587-3606.
2. Hong, M. (2006) Oligomeric structure, dynamics, and orientation of membrane proteins from solid-state NMR, *Structure 14*, 1731-1740.
3. Ketchem, R. R., Hu, W., and Cross, T. A. (1993) High resolution conformation of Gramicidine A in a lipid bilayer by solid-state NMR, *Science 261*, 1457-1460.
4. Cady, S. D., Goodman, C., Tatko, C. D., DeGrado, W. F., and Hong, M. (2007) Determining the orientation of uniaxially rotating membrane proteins using unoriented samples: a 2H, 13C, AND 15N solid-state NMR investigation of the dynamics and orientation of a transmembrane helical bundle, *J. Am. Chem. Soc. 129*, 5719-5729.
5. Hong, M., and Doherty, T. (2006) Orientation determination of membrane-disruptive proteins using powder samples and rotational diffusion: a simple solid-state NMR approach, *Chem. Phys. Lett. 432*, 296-300.
6. Munowitz, M. G., Griffin, R. G., Bodenhausen, G., and Huang, T. H. (1981) Two-Dimensional Rotational Spin-Echo Nuclear Magnetic Resonance in Solids: Correlation of Chemical Shift and Dipolar Interactions, *J. Am. Chem. Soc. 103*, 2529-2533.
7. Zhang, H., Neal, S., and Wishart, D. S. (2003) RefDB: A database of uniformly referenced protein chemical shifts, *J. Biomol. NMR 25*, 173-195.
8. Mesleh, M. F., Lee, S., Veglia, G., Thiriot, D. S., Marassi, F. M., and Opella, S. J. (2003) Dipolar waves map the structure and topology of helices in membrane proteins, *J. Am. Chem. Soc. 125*, 8928-8935.

9. Ito, T., Gorman, O. T., Kawaoka, Y., Bean, W. J., and Webster, R. G. (1991) Evolutionary analysis of the influenza A virus M gene with comparison of the M1 and M2 proteins, *J. Virol. 65*, 5491-5498.
10. Luo, W., Mani, R., and Hong, M. (2007) Sidechain conformation and gating of the M2 transmembrane peptide proton channel of influenza A virus from solid-state NMR, *J. Phys. Chem. B 111*, 10825-10832.
11. Cady, S. D., and Hong, M. (2007) Amantadine-induced conformational and dynamical changes of the influenza M2 transmembrane proton channel, *Proc. Natl. Acad. Sci. U.S.A. in press*.
12. Wang, J., Kim, S., Kovacs, F., and Cross, T. A. (2001) Structure of the transmembrane region of the M2 protein H(+) channel, *Protein Sci. 10*, 2241-2250.
13. Pinto, L. H., Dieckmann, G. R., Gandhi, C. S., Papworth, C. G., Braman, J., Shaughnessy, M. A., Lear, J. D., Lamb, R. A., and DeGrado, W. F. (1997) A functionally defined model for the M2 proton channel of influenza A virus suggests a mechanism for its ion selectivity, *Proc. Natl. Acad. Sci. USA 94*, 11301-11306.
14. Gullion, T., and Schaefer, J. (1989) Rotational echo double resonance NMR, *J. Magn. Reson. 81*, 196-200.
15. Bodenhausen, G., and Ruben, D. J. (1980) Natural abundance nitrogen-15 NMR by enhanced heteronuclear spectroscopy, *Chem. Phys. Lett. 69*, 185-189.
16. Bielecki, A., Kolbert, A. C., de Groot, H. J. M., Griffin, R. G., and Levitt, M. H. (1990) Frequency-switched Lee-Goldburg sequences in solids., *Adv. Magn. Reson. 14*, 111-124.
17. Hong, M., Gross, J. D., Rienstra, C. M., Griffin, R. G., Kumashiro, K. K., and Schmidt-Rohr, K. (1997) Coupling amplification in 2D MAS NMR and its application to torsion angle determination in peptides, *J. Magn. Reson. 129*, 85-92.
18. Rienstra, C. M., Tucker-Kellogg, L., Jaroniec, C. P., Hohwy, M., Reif, B., McMahon, M. T., Tidor, B., Lozano-Perez, T., and Griffin, R. G. (2002) De novo determination of peptide structure with solid-state magic-angle spinning NMR spectroscopy., *Proc. Natl. Acad. Sci. USA 99*, 10260-10265.

19. Hong, M., and Griffin, R. G. (1998) Resonance Assignment for Solid Peptides by Dipolar-Mediated 13C/15N Correlation Solid-State NMR, *J. Am. Chem. Soc. 120*, 7113-7114.
20. Luo, W., and Hong, M. (2006) Determination of the oligomeric number and intermolecular distances of membrane protein assemblies by anisotropic (1)h-driven spin diffusion NMR spectroscopy, *J. Am. Chem. Soc. 128*, 7242-7251.
21. Song, Z., Kovacs, F. A., Wang, J., Denny, J. K., Shekar, S. C., Quine, J. R., and Cross, T. A. (2000) Transmembrane domain of M2 protein from influenza A virus studied by solid-state 15N polarization inversion spin exchange at magic angle NMR, *Biophys. J. 79*, 767-775.
22. Wang, C., Takeuchi, K., Pinto, L. H., and Lamb, R. A. (1993) Ion channel activity of influenza A virus M2 protein: characterization of the amantadine block., *J. Virol. 67*, 5585-5594.
23. Hu, J., Asbury, T., Achuthan, S., Li, C., Bertram, R., Quine, J. R., Riqiang, F., and Cross, T. A. (2007) Backbone Stucture of the Amantadine-Block Trans-Membrane Domain M2 Proton Channel from Influenza A Virus, *Biophys. J. 92*, 4335-4343.
24. Baldus, M., Petkova, A. T., Herzfeld, J., and Griffin, R. G. (1998) Cross polarization in the tilted frame: assignment and spectral simplification in heteronuclear spin systems., *Mol. Phys. 95*, 1197-1207.

Chapter 5

Amantadine-Induced Conformational and Dynamical Changes of the Influenza M2 Transmembrane Proton Channel

A paper published in the Proceedings of the National Academy of Sciences, USA

2008, vol. 105 (5) pp. 1483-1488

Sarah D. Cady and Mei Hong

Abstract

The M2 protein of influenza A virus forms a transmembrane proton channel important for viral infection and replication. Amantadine blocks this channel, thus inhibiting viral replication. Elucidating the high-resolution structure of the M2 protein and its change upon amantadine binding is crucial for designing antiviral drugs to combat the growing resistance of influenza A viruses against amantadine. We employed magic-angle-spinning solid-state NMR to determine the conformation and dynamics of the transmembrane domain of the protein, M2TMP, in the apo- and amantadine-bound states in lipid bilayers. 13C chemical shifts and torsion angles of the protein in DLPC bilayers indicate that M2TMP is a-helical in both states, but the average conformation differs subtly, especially at the G34-I35 linkage and V27 sidechain. In the liquid-crystalline membrane, the complexed M2TMP shows dramatically narrower lines than the apo-peptide. Analysis of the homogeneous and inhomogeneous linewidths indicates that the apo-M2TMP undergoes significant microsecond-timescale motion, and amantadine binding alters the motional rates, causing line narrowing. Amantadine also reduces the conformational heterogeneity of specific residues, including the G34/I35 pair and several sidechains. Finally, amantadine causes the helical segment N-terminal to G34 to increase its tilt angle by 3°, and the G34-I35 torsion angles cause a kink of 5° in the amantadine-bound helix. These data indicate that amantadine affects the M2 proton channel mainly by changing the distribution and exchange rates among multiple low-energy conformations, and only subtly alters the average conformation and

orientation. Amantadine-resistant mutations may thus arise from binding-incompetent changes in the conformational equilibrium.

Introduction

The M2 protein of the influenza A virus forms a membrane-bound proton channel that acidifies the endosomally trapped virus, which triggers the release of the viral RNA into the infected cell, initiating viral replication (1, 2). The cationic amine amantadine inhibits viral replication by blocking this proton channel, thus has been used for the prophylaxis and treatment of influenza A infections (3, 4). However, in the last few years amantadine resistance skyrocketed among influenza A viruses in Asia and North America (5), making it imperative to develop alternative antiviral drugs.

The M2 protein contains a transmembrane a-helical domain (6) that has the essential amantadine-sensitive proton channel activity of the intact protein (7). Mutagenesis and electrophysiological experiments showed that the residues important for proton conduction and amantadine interaction lie on one face of the helix, namely V27, A30, S31, and G34 (8, 9). Neutron diffraction data indicated that the amantadine ring is localized at ~6 Å from the center of DOPC bilayers, close to V27 (10). Fourier analysis of the periodic oscillations in the channel reversal potential, pH-sensitive current, and amantadine resistance of cysteine mutants of the M2 protein yielded a functional structure of the channel (11). The active form of the channel is a tetramer for the intact protein (12, 13) as well as the transmembrane peptide (M2TMP) (14), as shown by 19F solid-state NMR (SSNMR) of the membrane-bound peptide.

The most extensive molecular-level structural information of M2TMP came from static 15N SSNMR data of Cross and coworkers. Using uniaxially aligned lipid membranes, they determined the orientation of M2TMP in the apo- (15) and complexed (16) states from 15N chemical shift and N-H dipolar couplings. The apo-peptide is tilted by 38° from the bilayer normal (15), whereas the amantadine-complexed peptide exhibits a kink with 31° and 20° tilt angles (16). However, sample preparation conditions such as solvents, membrane composition and peptide concentration varied greatly in these studies, which may contribute

to the observed orientation difference. From the 15N orientational data no direct information on the backbone and sidechain conformations can be extracted. The sidechain conformation may be especially sensitive to amantadine binding, yet so far only one 13C-15N distance (17) and four 19F-19F distances (14, 18) have been reported. Recently, amantadine was found to cause substantial narrowing of the 15N NMR spectra (19, 20), suggesting that it either reduces the conformational heterogeneity or changes the dynamics of the protein, but which factor dominates is unknown.

To elucidate the atomic-resolution conformation and dynamics of the backbone and sidechains of this important proton channel with and without amantadine, we have employed magic-angle-spinning (MAS) 13C and 15N NMR techniques on M2TMP bound to DLPC bilayers. To identify sites of structural perturbation, we measured and compared the 13C and 15N isotropic shifts and torsion angles of eight residues spread throughout the peptide. The data indicate that amantadine most significantly perturbs the backbone of G34 and I35 and the sidechain of V27. Analysis of the homogeneous and inhomogeneous 13C linewidths in the gel and liquid-crystalline (LC) phases of the membrane indicates that the apo-peptide backbone undergoes significant motion on the microsecond timescale. Amantadine binding alters the motional rates and reduces the conformational distribution. Thus the central feature of M2TMP structure appears to be the presence of multiple low-energy conformations, which are readily modified and selected by amantadine.

Results and Discussion

M2TMP conformation with and without amantadine

We chose eight residues in M2TMP for ^{13}C and ^{15}N labeling. Based on the approximate seven-residue periodicity of the protein (*11*), these sites cover channel-lining positions (V27, A30, and G34), helix-helix interfaces (L26, I33, L38), and lipid-facing positions (A29, I35). In this way, we assess the impact of amantadine binding to M2TMP structure from all regions of the tetrameric bundle. Two peptides were synthesized that each contains four uniformly ^{13}C, ^{15}N-labeled residues. The "LAGI" sample contains labeled L26, A29, G34 and I35, and the "VAIL" sample contains labeled V27, A30, I33, and L38. Figure

5.1 shows representative ^{13}C cross-polarization (CP) MAS spectra of the peptide in DLPC bilayers with (red) and without (black) amantadine at 303 K. The ^{13}C isotropic linewidths narrow substantially upon amantadine binding. In the apo peptide many backbone signals such as G34 Cα are broad and poorly defined, while with amantadine all Cα resonances narrow and increase in intensity. Sidechain signals are also narrowed but less dramatically. This ^{13}C line narrowing is similar to that seen in ^{15}N spectra of the protein (*16, 19*). In the next section we investigate the origin of this line narrowing.

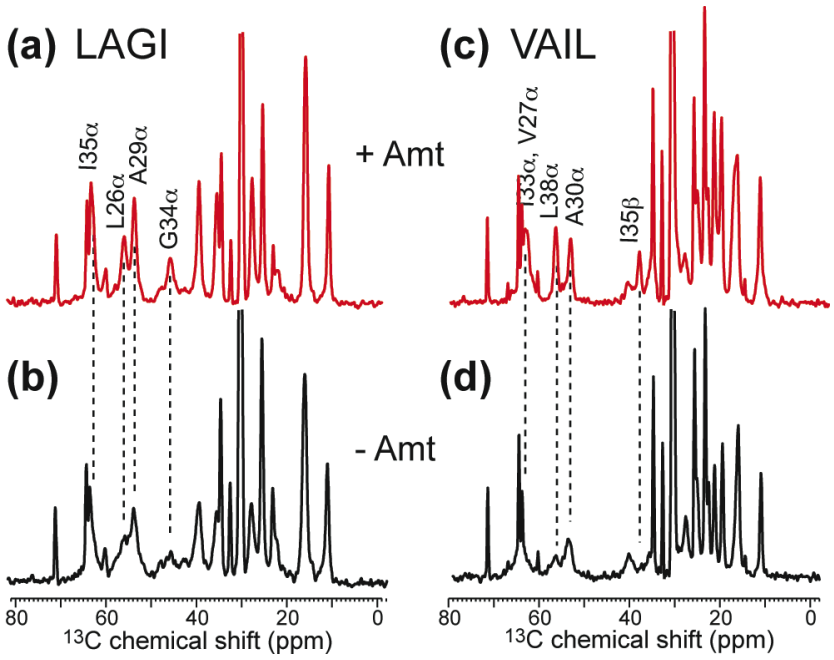

Figure 5.1. ^{13}C CP-MAS spectra of M2TMP at 303 K with (red) and without (black) amantadine. (a, b) LAGI. (c, d) VAIL. Note the significant line narrowing and intensity increase in the presence of amantadine.

To determine the M2TMP conformation and its perturbation by amantadine, we measured the ^{13}C and ^{15}N isotropic chemical shifts of the peptide without and with amantadine. ^{13}C-^{13}C 2D double-quantum (DQ) filtered correlation spectra and ^{15}N-^{13}C correlation spectra were measured at 243 K where the peptide motion is frozen. Both spectra remove all lipid natural-abundance ^{13}C signals, thus simplifying resonance assignment. Figure 5.2 shows the 2D ^{13}C-^{13}C correlation spectra of LAGI and VAIL with (red) and

without (black) amantadine. The spectra are readily assigned based on the connectivity patterns. Various chemical shift changes are observed, for example at V27α, A30β, I35γ1 and L38β. The largest Cα shift change occurs at V27, which exhibits a 1.0 ppm upfield shift in the complex. G34 Cα is not detected in the 2D ^{13}C-^{13}C correlation spectrum due to the DQ excitation condition, but its signal is visible in the 2D ^{15}N-^{13}C spectra (Figure 5.7, supporting information) and shows a downfield ^{15}N chemical shift change of 2.5 ppm. Interestingly, the two Ile residues flanking G34 also exhibit ^{15}N chemical shift changes but in opposite directions, causing their amantadine-bound ^{15}N shifts to differ by 5.8 ppm. Table 5.2 (supporting information) lists the isotropic shifts of the apo and complexed M2TMP.

Despite the chemical shift perturbations by amantadine, no change is large enough to indicate a non-helical structure (*21*). This is reflected by the positive Cα and C' secondary shifts and negative Cβ secondary shifts (Figures 5.3a-c) for all eight labeled residues. Figure 5.3d plots the amantadine-induced average absolute chemical shift changes of each residue. The maximum perturbation occurs at the channel-lining G34, followed by its adjacent I35 and I33. A second local maximum is seen at V27, consistent with its proximity to amantadine (*10*). In terms of residue location, the channel-lining residues, the interfacial residues, and the lipid-facing residues except for the G34-neighboring I35 have average chemical shift changes of 0.79 ppm, 0.46 ppm, and 0.33 ppm, respectively.

To obtain more quantitative conformational constraints, we measured ϕ, ψ, and χ_{1H} torsion angles using dipolar correlation techniques. The ϕ angles of all labeled residues except for G34 were measured using the HNCH technique (*22*), which correlates the N-H and Cα-Hα bond orientations of each residue. Most ϕ angles fall between –45° and –85°, with no large difference between the apo and complexed peptide within the angular resolution of the technique (Figure 5.4a, Table 5.1).

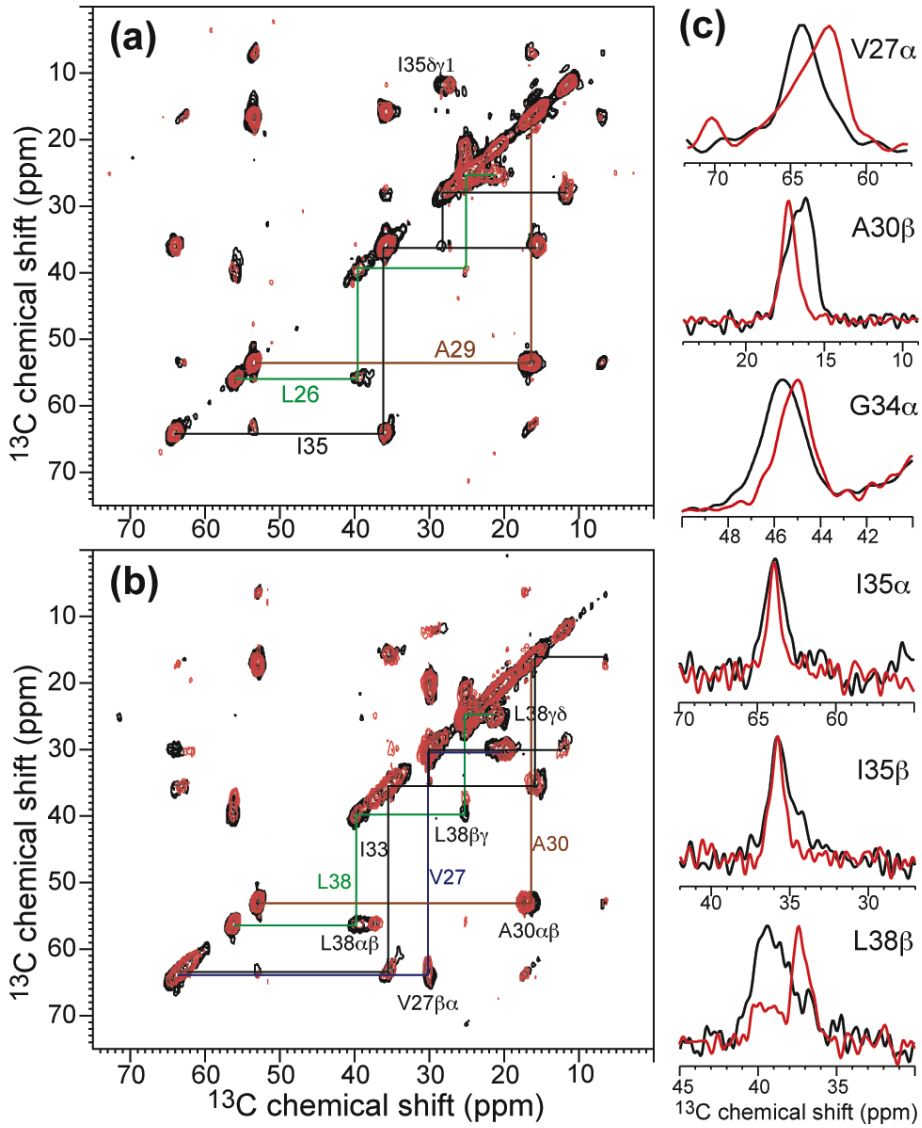

Figure 5.2. 2D ^{13}C-^{13}C DQ filtered spectra of M2TMP in DLPC bilayers without (black) and with (red) amantadine at 243 K. Intra-residue connectivities and cross peaks with chemical shift changes are indicated. (a) LAGI. (b) VAIL. (c) Selected 1D cross sections that exhibit line narrowing and chemical shift changes upon amantadine binding. The G34α trace was extracted from 1D CP spectra.

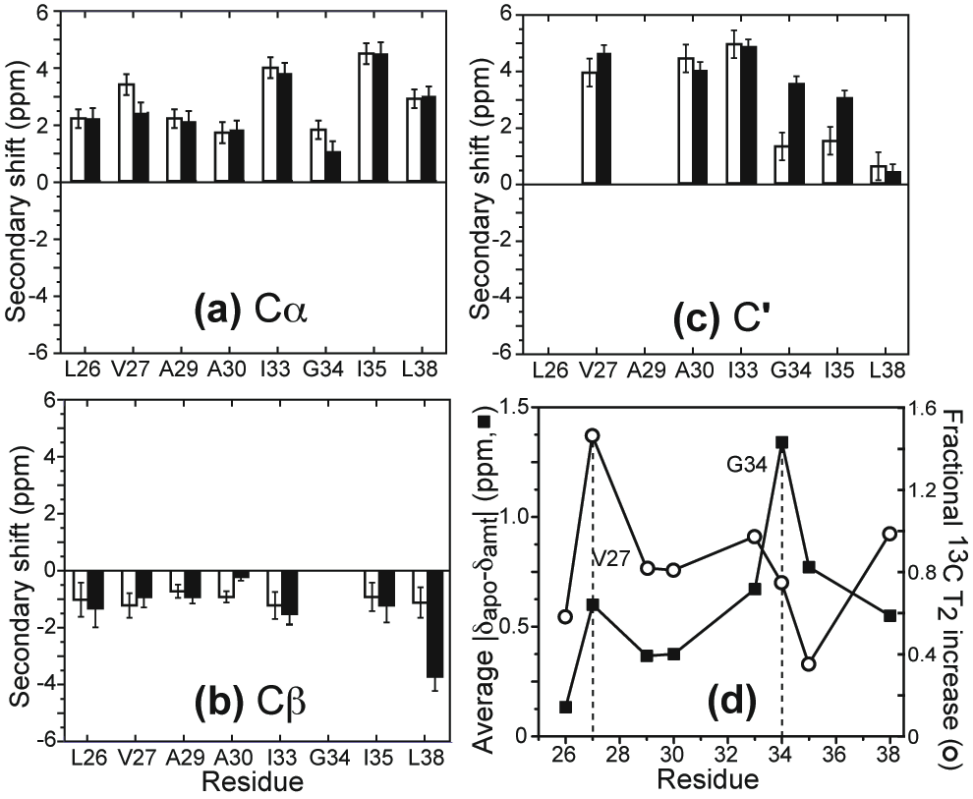

Figure 5.3. Amantadine-induced isotropic shift and T_2 changes of M2TMP. Secondary shifts are plotted for (a) Cα, (b) Cβ, and (c) C'. Open and filled bars correspond to the apo- and complexed M2TMP, respectively. The average chemical shift uncertainty is 0.35 ppm, estimated from the intrinsic linewidths of the spectra. (d) Average absolute chemical shift changes (filled squares) and fractional ^{13}C T_2 increase at 303 K (open circles). Local maxima of chemical shift and T_2 perturbation occur at V27 and G34.

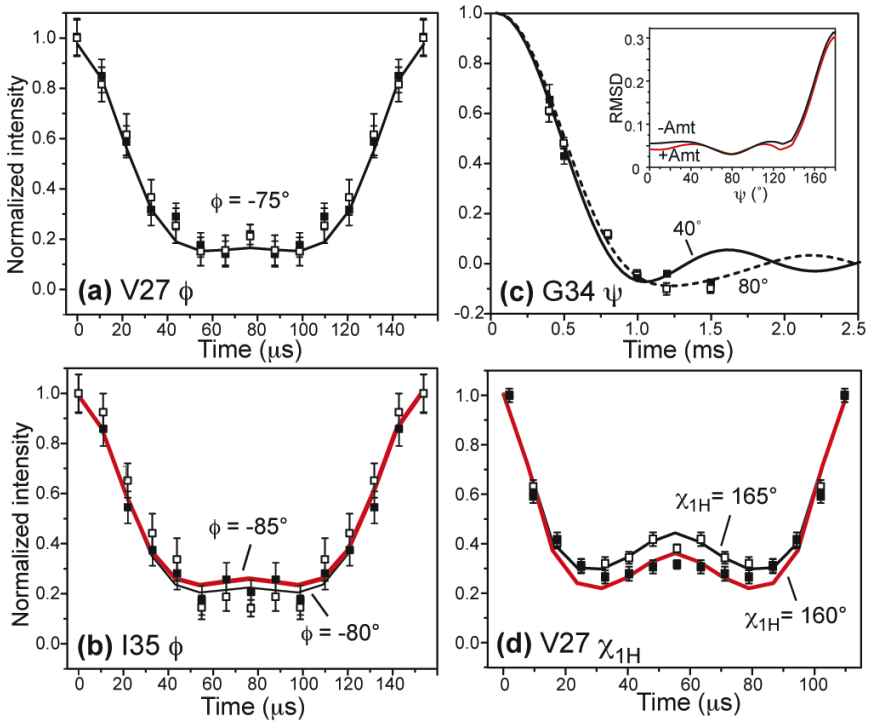

Figure 5.4. Selected torsion angle data of M2TMP without (open squares) and with (filled squares) amantadine, along with their RMSD-quantified best-fit simulations (lines). Red lines: best-fit curves for the complexed M2TMP when different from the apo-peptide. (a) V27 ϕ. (b) I35 ϕ. (c) G34 ψ. Inset shows the RMSD between the simulation and the experiment. (d) V27 χ_{1H}.

When taking into account the significant ^{15}N, $^{13}C\alpha$ and $^{13}C'$ shift changes at G34-I35, the observed I35 ϕ angles of -80° for the apo-M2TMP and -85° for the complex (Figure 5.4b) may reflect a real torsion angle difference. The ψ angle of G34 was measured using the NCCN technique. The data (Figure 5.4c) yielded a best-fit ψ angle of -80° at 243 K with and without amantadine. However, the angular resolution of the technique is limited in the α-helical region (*23*), as shown by the shallow RMSD minimum. Thus, we used the TALOS program (*24*) to predict the G34 torsion angles based on the experimental chemical shifts of the I33/G34/I35 triplet. This gave G34 (ϕ, ψ) of (-66°, -37°) and (-67°, -42) for the apo- and complexed peptide, respectively (Table 5.1). Indeed, the calculated -40° NCCN curve agrees well with the experimental data.

For the β-branched Val and Ile residues, the χ_{1H} torsion angle were obtained by correlating the Cα-Hα and Cβ-Hβ bond orientations (*25*). Here the angular resolution is much higher, ±3°, due to the nearly trans nature of the measured conformation. I33 and I35 show no χ_{1H} change, consistent with their lack of Cα/Cβ chemical shift perturbation. In contrast, the channel-lining V27 exhibits a significant χ_{1H} difference of 5° (Figure 5.4d), consistent with the 1.0 ppm Cα and Cγ1 chemical shift change at this residue (Table 5.2).

Overall, the chemical shifts and torsion angle data indicate that amantadine induces only small conformational changes in M2TMP, with the main sites of perturbation being the G34-I35 pair and V27. This small conformational change contrasts with the large and extensive dynamic changes shown below.

M2TMP dynamics and conformational heterogeneity

The 1D ^{13}C MAS spectra show dramatic differences in the linewidths of the apo- and amantadine-complexed M2TMP. In general, NMR linewidths have two contributions: inhomogeneous linewidths due to, mainly, conformational heterogeneity, and homogeneous linewidths due to relaxation induced by stochastically fluctuating local fields on the microsecond timescale and residual dipolar couplings (*26*). Homogeneous broadening is not refocused in a spin-echo experiment while inhomogeneous broadening is. Thus, to distinguish conformational heterogeneity from microsecond-timescale dynamics and to compare them between the apo- and complexed M2TMP, we measured the ^{13}C T_2 relaxation times using a Hahn-echo experiment (*27*). The echo-derived T_2 is related to the homogeneous linewidth Δ by $T_2 = 1/\pi\Delta$ (*28*). Since residual dipolar couplings resulting from imperfect ^{1}H decoupling or insufficiently fast MAS are the same between the apo and complexed peptide, any T_2 or Δ differences should mainly result from dynamic differences of the two states. Figure 5.8 (supporting information) shows representative T_2 decay curves at 303 K. All resolved sites exhibit longer T_2's with amantadine than without. This is true for both the backbone and sidechains and for both channel-lining residues and other residues (Table 5.3, supporting information). For backbone Cα, sidechain carbons, and methyl carbons, the average T_2 increases by 1.5 ms, 2.1 ms, and 2.5 ms, respectively. The T_2 increase also varies

with the residue location with respect to the channel: the three channel-lining residues experience the largest average T_2 increase of 2.0 ms, followed by T_2 increases of 1.9 ms and 1.4 ms for the interfacial and lipid-facing residues, respectively. Figure 5.3d plots the fractional ^{13}C T_2 increase of the complexed peptide over the apo-M2TMP as a function of residues, calculated as $\frac{1}{n}\sum_{i=1}^{n}\left(T_{2,+\mathrm{Amt}}^{i} - T_{2,-\mathrm{Amt}}^{i}\right)\Big/T_{2,-\mathrm{Amt}}^{i}$, where n is the number of sites measured in each residue. The largest T_2 increase is seen at V27, which again correlates with its purported close distance to the fused ring of amantadine (*10, 29*).

In ^{1}H-decoupled solids, ^{13}C T_2 relaxation times increase when motional correlation times either decrease or increase beyond the microsecond time window (*26*). Thus both fast motions in the extreme narrowing limit and slow motions in rigid solids give rise to long T_2's. Comparison of the ^{13}C T_2 at 303 K, 243 K and other temperatures (Table 5.4, supporting information) suggests that the motional rates of Cα sites in the apo-peptide are near the characteristic frequency of the T_2 minimum ($\sim 2\pi \cdot 70$ kHz) in the LC phase, and that amantadine binding increases the motional rates. This suggests that amantadine may widen the pore slightly, reducing steric hindrance and facilitating motion (*30*). Indeed, most sidechain methyl groups show an increase in the motional rates in the amantadine-bound state based on the temperature-dependent T_2's, consistent with their motion being facilitated by a widening of the pore.

To assess the conformational heterogeneity of the protein, we compare the homogeneous linewidths Δ derived from the T_2 with the apparent linewidths Δ* measured from the spectra. In the LC phase, the Cα linewidth of apo-M2TMP is almost completely homogeneously broadened by motion, as seen by the similar Δ and Δ* (Figure 5.9, supporting information). Amantadine binding reduces Δ by a factor of two. For the sidechains, conformational heterogeneity is detectable in both the apo and complexed peptide due to narrower intrinsic linewidths. To evaluate the conformational heterogeneity without different homogeneous linewidths between the apo and complexed peptide, we froze the DLPC-bound M2TMP to 243 K, where the homogeneous linewidths become similar between the two states (Table 5.5, supporting information). Under this condition, most sites show

similar Δ* and hence similar conformational heterogeneity between the apo and complexed peptide. The exceptions are G34, I35 and the sidechains of L26, A30 and L38, where the complexed peptide has significantly narrower lines, indicating reduced conformational heterogeneity. This is also seen in the cross sections of the ^{13}C 2D spectra (Figure 5.2c).

In summary, in the LC phase of the lipid bilayer, the apo-M2TMP backbone undergoes large-amplitude microsecond-timescale motion that causes significant homogeneous broadening of the ^{13}C spectra and consequent loss of intensity. Amantadine binding increases the T_2 relaxation times for all sites by changing the motional rates, thus narrowing the intrinsic linewidths. When the motion is frozen, the conformational distribution of the peptide is revealed to be reduced by amantadine at specific residues, including the G34-I35 junction and several methyl-rich sidechains.

Amantadine-induced M2TMP orientation change

We recently measured the orientation of the apo-M2TMP using a powder-sample approach that exploits fast rigid-body uniaxial diffusion of the peptide backbone around the bilayer normal (*31*). Under this condition, motionally averaged powder spectra are obtained that indicate the peptide orientation from the bilayer normal (*32*). We now use this approach to determine the orientation of M2TMP in complex with amantadine. ^{15}N-^{1}H dipolar couplings and ^{15}N chemical shift anisotropies (CSA), which are extremely sensitive to the helix orientation, were measured. Figure 5.5(a, b) shows the N-H DIPSHIFT curves of V28 and A30 at 313 K where the peptide is uniaxially mobile. Amantadine binding decreases the N-H dipolar coupling of both residues. Correlating the motionally averaged $\bar{\delta}_{//}$ N-H dipolar coupling with the $\bar{\delta}_{\perp}$ edge of the ^{15}N CSA obtained from static 1D spectra (not shown), we obtain 2D "PISA wheels" (*33, 34*) (Figure 5.5c).

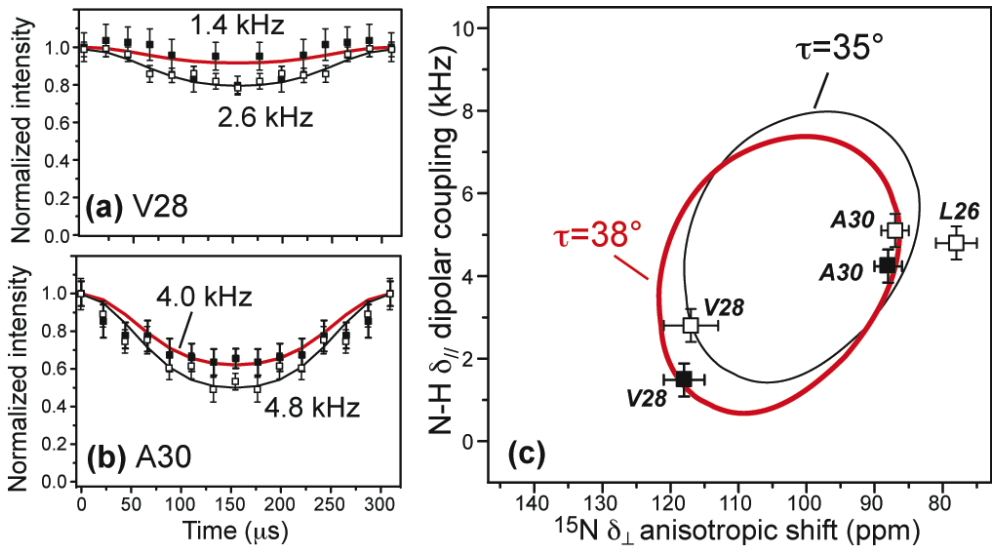

Figure 5.5. Orientation of amantadine-bound M2TMP. (a, b) ^{15}N-^{1}H dipolar coupling of unoriented M2TMP in DLPC bilayers with amantadine (filled squares, red line). For comparison, the apo-peptide data published recently are superimposed (open squares, black line) (*31*). (a) V28. (b) A30. (c) PISA wheels of M2TMP constructed from the $\delta_{//}$ N-H dipolar couplings and $\delta_{\perp}$ ^{15}N anisotropic shifts. The data fit to a wheel with a tilt angle τ of 38° (red). The apo-peptide shows a τ = 35° (open symbols and black line) (*31*).

For the apo peptide in DLPC bilayers, previous data yielded a tilt angle τ of 35° (*31*), while the current amantadine-bound M2TMP has a slightly larger τ of 38°. The rotation angle of the wheel is unchanged. The 3° increase, while small, is consistent with amantadine binding at the N-terminus of the helix, pushing it open slightly. The orientation of the segment C-terminal to G34 is not probed here since no ^{15}N labels are used in that region.

Figure 5.6 shows the chemical shift and torsion-angle constrained structure of M2TMP in the presence of amantadine, refined from the ^{15}N-NMR-derived model 1NYJ (*15*). At the G34-I35 junction, a G34 ψ angle of –42° and I35 ϕ of –85° were used. The resulting helix shows a small kink of 5° between the segments N-terminal and C-terminal to G34, visible in the top view (Figure 5.6b). The kink is defined as the angle between the average N-H bond orientation for residues 27-33 and for residues 37-43. This kink is reminiscent of the recent ^{15}N NMR data of DMPC-bound M2TMP, which showed a bend of

11˚ at G34 (*16*). We found that the exact value of the kink is sensitive to the G34/I35 torsion angles. With ψ_{34} = -60˚, the kink increases to ~16˚, while with a more ideal ϕ_{35} of –60˚, the kink is almost completely removed.

Conclusion

The NMR data here provide the first extensive set of high-resolution conformational and dynamical constraints of the backbone and sidechains of M2TMP in lipid bilayers without and with amantadine, and elucidate the nature of the spectral line narrowing caused by amantadine. The data indicate that amantadine binding to M2TMP exerts the largest effect on the dynamics and conformational heterogeneity of the protein, to a lesser extent on the average backbone and sidechain conformations, and only subtly affects the helix orientation. The apo-peptide exhibits large-amplitude microsecond-timescale motion that homogeneously broadens the NMR lines. Amantadine increases the motional rates of most backbone Ca sites, causing substantial line narrowing. It also reduces the conformational heterogeneity of certain residues, including G34, I35 and the sidechains of L26, A30 and L38. Perturbation of the average conformation mainly occurs at G34-I35 and at V27 sidechain. Combined, the data strongly suggests that conformational plasticity is essential to proton conduction and gating of the apo-channel, and at least part of amantadine's mechanism of action is to modify and select among the multiple low-energy conformations of M2TMP. This is consistent with energy surface mapping (35) and analytical ultracentrifugation data of M2TMP and its mutants (36, 37). It is possible, then, that amantadine resistance can arise from mutations that alter the protein conformational distribution and dynamics, thus preventing amantadine binding.

The observed large V27 chemical shift and T2 changes are in excellent agreement with mutagenesis data indicating strong interaction of this residue with amantadine. Mutation of V27 to Ala, Ser, Ile and Thr caused either complete or partial resistance to amantadine in various viral strains (3, 9). Thus, the interaction of amantadine with the channel is exquisitely sensitive to the size and hydrophobicity of the sidechain at this position.

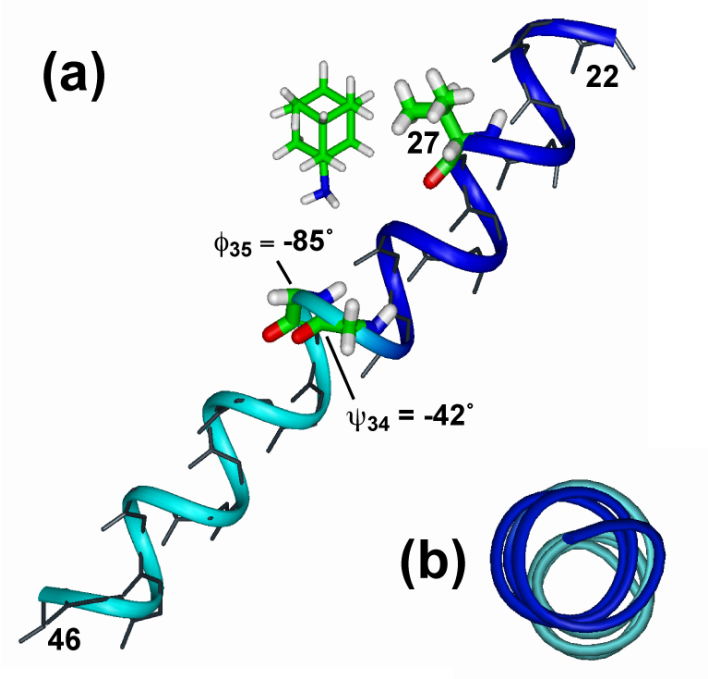

Figure 5.6. Chemical shift and torsion-angle restrained backbone and partial sidechain structure of amantadine-bound M2TMP. (a) Side view. (b) Top view. The exact position and orientation of amantadine is unknown, and is shown here only as a reference to the peptide. The G34 ψ and I35 ϕ angles create a helix kink of 5°, highlighted by the blue N-terminal and the cyan C-terminal segments.

Complexed with amantadine, the M2TMP helix shows a small degree of non-ideality in the backbone torsion angles. In particular, the deviation of the G34-I35 conformation from the ideal helix geometry causes a helix kink of 5°, which may have an effect on the inter-helical interaction of H37 imidazole rings downstream (*19*). The exact value of the kink and the exact orientation of the helix in the DLPC membrane differ slightly from those found in the DMPC membrane. Given the differences in sample preparation conditions such as membrane thickness and the state of alignment (*19, 20*), these differences further underscore the structural plasticity of the peptide. The spectra of the amantadine-bound M2TMP show a single signal for each label, thus the four helices of the tetramer are rotationally symmetric and chemically identical. This implies that in the LC phase, not only does amantadine have the same uniaxial mobility as the tetrameric bundle, but it also exchanges among the four helices on a timescale faster than the nuclear spin interactions ($< 10^{-5}$ s) (*19*).

Material and Methods

Peptides and lipids

Fmoc-protected uniformly ^{13}C, ^{15}N-labeled amino acids were either prepared in-house (*38*) or purchased from Sigma and Cambridge Isotope Laboratories. The transmembrane peptide of the M2 protein of the Udorn strain (residues 22-46) (*39*) was synthesized by PrimmBiotech (Cambridge, MA) and purified to >95% purity. The amino acid sequence is SSDPLVVAASIIGILHLILWILDRL. In addition to peptides containing multiple uniformly ^{13}C, ^{15}N-labeled residues, two peptides each containing a single ^{15}N label at V28 and A30 were synthesized for orientation measurements.

Membrane sample preparation

M2TMP was reconstituted into lipid vesicles by detergent dialysis (*18*). DLPC (1,2-dilauroyl-*sn*-glycero-3-phosphatidylcholine) lipids were chosen due to the favorable dynamics of the protein in this membrane (*31*) and the similar phase transition temperature (-2˚C) of this bilayer to biological membranes. The vesicle solution was prepared by suspending dry DLPC powder (Avanti Polar Lipids) in 1 mL phosphate buffer (10 mM Na_2HPO_4/NaH_2PO_4, 1mM EDTA, 0.1mM NaN_3) at pH 7.5, vortexing and freeze-thawing 6-8 times to create uniform vesicles of ~200 nm diameter (*40*). M2TMP powder was codissolved with the detergent octyl-β-D-glucopyranoside (OG) in 2 mL phosphate buffer to reach an OG concentration of 30 mg/mL. The M2TMP/OG solution was then mixed with the DLPC vesicle solution, giving a final OG concentration of 15 mg/mL. The mixture was vortexed for 1 hr, allowed to stand for 6-8 hrs at room temperature, then dialyzed with a 3.5 kDa cutoff against 1 L phosphate buffer at 4 °C for 3 days with buffer changes every 8-12 hrs to ensure complete removal of the detergent. The dialyzed M2TMP/DLPC solution was centrifuged at 150,000 g for 3 hours at 10˚C to give a wet pellet with ~50 wt% water. The final peptide/lipid (P/L) molar ratio is 1:15. UV-VIS spectrum of the supernatant indicated ~98% binding of the peptide to the membrane. For amantadine-bound samples, 10 mM amantadine hydrochloride was added to the phosphate buffer throughout the lipid vesicle formation and peptide assembly process.

For orientation measurements, ^{15}N-labeled M2TMP was codissolved with DLPC lipids in trifluoroethanol at a P/L of 1:20, lyophilized, then rehydrated to 50 wt% water using a pH 8.1 phosphate buffer. For amantadine-bound samples, 2 mmol of amantadine hydrochloride was added to the dry M2TMP/lipid mixture before dissolution in trifluoroethanol.

Solid-state NMR spectroscopy

Most NMR experiments were carried out on a Bruker AVANCE-600 (14.1 Tesla) spectrometer (Karlsruhe, Germany) using a 4 mm triple-resonance MAS probe. ^{13}C-^{13}C and ^{15}N-^{13}C 2D correlation and torsion angle experiments were conducted at 243 K to freeze peptide motion. All other parameters, including ^{15}N CSA, ^{15}N-^{1}H dipolar coupling, and ^{13}C T_2 relaxation times, were measured at 303 K or 313 K where the peptide is uniaxially mobile in the LC phase of the DLPC bilayer. Typical radiofrequency pulse lengths were 5 μs for ^{13}C and 3.5-4.0 μs for ^{1}H. ^{1}H TPPM (*41*) or SPINAL (*42*) decoupling of 60 – 70 kHz were applied. ^{13}C chemical shifts were referenced to the α-Gly C' signal at 176.49 ppm on the TMS scale, and ^{15}N chemical shifts were referenced to the ^{15}N signal of N-acetyl-valine at 122 ppm on the liquid ammonia scale. For G34 torsion angles extraction from TALOS, the ^{13}C chemical shifts were converted to the TSP scale by adding 1.82 ppm to the measured shifts.

2D DQ filtered ^{13}C-^{13}C correlation spectra were measured using a SPC5 sequence (*43*) under 7 kHz MAS. DQ filtration removes lipid background ^{13}C signals, thus simplifying assignment of the protein signals. 2D ^{15}N-^{13}C correlation spectra were measured using a REDOR pulse train (*44*) of 0.7 – 2.1 ms for ^{13}C-^{15}N coherence transfer (*45*).

ϕ angles were measured under 6.5 kHz MAS using the HNCH technique, with doubling of the N-H dipolar coupling to enhance the angular resolution (*22, 46*). ^{1}H-^{1}H homonuclear coupling was removed by an FSLG sequence (*47*). The HNCH data were simulated using a doubled N-H coupling of 12.0 kHz and a C-H dipolar coupling of 12.5 kHz, both scaled by the FSLG scaling factor of 0.577. These values were directly measured by C-H and N-H dipolar-shift (DIPSHIFT) correlation experiments on the protein at 243 K.

ψ angle was measured with the NCCN experiment (*23*) correlating the N_i-$C\alpha_i$ and C'_i-N_{i+1} bond orientations. Spinning speeds of 4 and 5 kHz were used to obtain multiple time points on the angle-dependent curve. χ_{1H} torsion angles (Hα-Cα-Cβ-Hβ) were measured by correlating the Cα-Hα and Cβ-Hβ bond orientations using a modified HCCH technique (*25*) under 9 kHz MAS. A HORROR sequence with a resonance condition of $\omega_1 = \omega_r/2$ (*48*) was used to selectively excite the Cα-Cβ DQ coherence, followed by a dipolar-doubled C-H DIPSHIFT period. A doubled and FSLG-scaled C-H dipolar coupling of 26.0 kHz was used to simulate the angle-dependent curves. All these torsion angles have an inherent double degeneracy due to the uniaxial nature of the dipolar coupling. The wrong angle is readily identified by the fact that it falls into either unpopulated regions of the Ramachandran diagram or the β-sheet region, which contradicts NMR chemical shifts.

^{15}N-^{1}H dipolar couplings for orientation determination were obtained from a dipolar-doubled DIPSHIFT experiment (*46, 49, 50*) under 7 kHz MAS. An FSLG sequence with an effective field of 76.5 kHz was used for ^{1}H homonuclear decoupling.

Acknowledgement

This work is supported by NSF grants MCB-0543473 and DBI-0421374. The authors thank Prof. Yoshitaka Ishii for help with the TALOS simulation.

References

1. Pinto, L. H., Holsinger, L. J., and Lamb, R. A. (1992) Influenza virus M2 protein has ion channel activity, *Cell 69*, 517-528.
2. Pinto, L. H., and Lamb, R. A. (2007) Controlling influenza virus replication by inhibiting its proton flow, *Mol. BioSyst. 3*, 18-23.
3. Wang, C., Takeuchi, K., Pinto, L. H., and Lamb, R. A. (1993) Ion channel activity of influenza A virus M2 protein: characterization of the amantadine block., *J. Virol. 67*, 5585-5594.

4. Lamb, R. A., Holsinger, K. J., and Pinto, L. H. (1994) The Influenza A virus M2 ion channel protein and its role in the influenza virus life cycle., in *Cellular Receptors of Animal Viruses* (Wemmer, E., Ed.), pp 303-321, Cold Spring Harbor Lab Press, Plainview, NY.
5. Bright, R. A., Medina, M. J., Xu, X., Perez-Oronoz, G., Wallis, T. R., Davis, X. M., Povinelli, L., Cox, N. J., and Klimov, A. I. (2005) Incidence of adamantane resistance among influenza A (H3N2) viruses isolated worldwide from 1994 to 2005: a cause for concern, *Lancet 366*, 1175-1181.
6. Duff, K. C., Kelly, S. M., price, N. C., and Bradshaw, J. P. (1992) The secondary structure of influenza A M2 transmembrane domain. A circular dichroism study, *FEBS Lett. 311*, 256-258.
7. Duff, K. C., and Ashley, R. H. (1992) The transmembrane domain of influenza A M2 protein forms amantadine-sensitive proton channels in planar lipid bilayers., *Virology 190*, 485-489.
8. Hay, A. J., Wolstenholme, A. J., Skehel, J. J., and Smith, M. H. (1985) The molecular basis of the specific anti-influenza action of amantadine, *EMBO J. 4*, 3021-3024.
9. Holsinger, L. J., Nichani, D., Pinto, L. H., and Lamb, R. A. (1994) Influenza A virus M2 ion channel protein: a structure-function analysis, *J. Virol. 68*, 1551-1563.
10. Duff, K. C., Gilchrist, P. J., Saxena, A. M., and Bradshaw, J. P. (1994) Neutron diffraction reveals the site of amantadine blockade in the influenza A M2 ion channel, *Virology 202*, 287-293.
11. Pinto, L. H., Dieckmann, G. R., Gandhi, C. S., Papworth, C. G., Braman, J., Shaughnessy, M. A., Lear, J. D., Lamb, R. A., and DeGrado, W. F. (1997) A functionally defined model for the M2 proton channel of influenza A virus suggests a mechanism for its ion selectivity, *Proc. Natl. Acad. Sci. USA 94*, 11301-11306.
12. Sakaguchi, T., Tu, Q., Pinto, L. H., and Lamb, R. A. (1997) The active oligomeric state of the minimalistic influenza virus M2 ion channel is a tetramer *Proc. Natl. Acad. Sci. USA 94*, 5000-5005.

13. Salom, D., Hill, B. R., Lear, J. D., and DeGrado, W. F. (2000) pH-dependent tetramerization and amantadine binding of the transmembrane helix of M2 from the influenza A virus, *Biochemistry 39*, 14160-14170.
14. Luo, W., and Hong, M. (2006) Determination of the oligomeric number and intermolecular distances of membrane protein assemblies by anisotropic 1H-driven spin diffusion NMR spectroscopy, *J. Am. Chem. Soc. 128*, 7242-7251.
15. Wang, J., Kim, S., Kovacs, F., and Cross, T. A. (2001) Structure of the transmembrane region of the M2 protein H(+) channel, *Protein Sci. 10*, 2241-2250.
16. Hu, J., Asbury, T., Achuthan, S., Li, C., Bertram, R., Quine, J. R., Riqiang, F., and Cross, T. A. (2007) Backbone Stucture of the Amantadine-Block Trans-Membrane Domain M2 Proton Channel from Influenza A Virus, *Biophys. J. 92*, 4335-4343.
17. Nishimura, K., Kim, S., Zhang, L., and Cross, T. A. (2002) The closed state of a H+ channel helical bundle combining precise orientational and distance restraints from solid state NMR, *Biochemistry 41*, 13170-13177.
18. Luo, W., Mani, R., and Hong, M. (2007) Sidechain conformation and gating of the M2 transmembrane peptide proton channel of influenza A virus from solid-state NMR, *J. Phys. Chem. B 111*, 10825-10832.
19. Hu, J., Riqiang, F., and Cross, T. A. (2007) The Chemical and Dynamical Influence of the Anti-Viral Drug Amantadine on the M2 Proton Channel Transmembrane Domain, *Biophys. J. 93*, 276-283.
20. Li, C., Qin, H., Gao, F. P., and Cross, T. A. (2007) Solid-state NMR characterization of conformational plasticity within the transmembrane domain of the influenza A M2 proton channel, *Biochim. Biophys. Acta 1768*, 3162-3170.
21. Zhang, H., Neal, S., and Wishart, D. S. (2003) RefDB: A database of uniformly referenced protein chemical shifts, *J. Biomol. NMR 25*, 173-195.
22. Hong, M., Gross, J. D., and Griffin, R. G. (1997) Site-resolved determination of peptide torsion angle phi from the relative orientations of backbone N-H and C-H bonds by solid-state NMR, *J. Phys. Chem. B 101*, 5869-5874.

23. Costa, P. R., Gross, J. D., Hong, M., and Griffin, R. G. (1997) Solid-State NMR Measurement of psi in Peptides: a NCCN 2Q-Heteronuclear Local Field Experiment, *Chem. Phys. Lett. 280*, 95-103.
24. Cornilescu, G., Delaglio, F., and Bax, A. (1999) Protein backbone angle restraints from searching a database for chemical shift and sequence homology, *J. Biomol. NMR 13*, 289-302.
25. Feng, X., Lee, Y. K., Sandstroem, D., Eden, M., Maisel, H., Sebald, A., and Levitt, M. H. (1996) Direct determination of a molecular torsional angle by solid-state NMR, *Chem. Phys. Lett. 257*, 314-320.
26. Rothwell, W. P., and Waugh, J. S. (1981) Tranverse relaxation of dipolar coupled spin systems under rf irradiation: detecting motions in solids., *J. Chem. Phys. 74*, 2721-2732.
27. Hahn, E. L. (1950) Spin echoes, *Phys. Rev. 80*, 580-594.
28. Lesage, A., Bardet, M., and Emsley, L. (1999) Through-bond carbon-carbon connectivities in disordered solids by NMR *J. Am. Chem. Soc. 121*, 10987-10993.
29. Sansom, M. S., and Kerr, I. D. (1993) Influenza virus M2 protein: a molecular modelling study of the ion channel, *Protein Eng. 6*, 65-74.
30. Astrahan, P., Kass, I., Cooper, M. A., and Arkin, I. T. (2004) A novel method of resistance for influenza against a channel-blocking antiviral drug, *Proteins: Struct., Funct., Bioinf. 55*, 251-257.
31. Cady, S. D., Goodman, C., Tatko, C. D., DeGrado, W. F., and Hong, M. (2007) Determining the orientation of uniaxially rotating membrane proteins using unoriented samples: a 2H, 13C, AND 15N solid-state NMR investigation of the dynamics and orientation of a transmembrane helical bundle, *J. Am. Chem. Soc. 129*, 5719-5729.
32. Hong, M., and Doherty, T. (2006) Orientation determination of membrane-disruptive proteins using powder samples and rotational diffusion: a simple solid-state NMR approach, *Chem. Phys. Lett. 432*, 296-300.
33. Marassi, F. M., and Opella, S. J. (2000) A solid-state NMR index of helical membrane protein structure and topology, *J. Magn. Reson. 144*, 150-155.

34. Wang, J., Denny, J., Tian, C., Kim, S., Mo, Y., Kovacs, F., Song, Z., Nishimura, K., Gan, Z., Fu, R., Quine, J. R., and Cross, T. A. (2000) Imaging membrane protein helical wheels, *J. Magn. Reson. 144*, 162-167.
35. Torres, J., Kukol, A., and Arkin, I. T. (2001) Mapping the energy surface of transmembrane helix-helix interactions., *Biophys. J. 81*, 2681-2692.
36. Stouffer, A. L., Nanda, V., Lear, J. D., and DeGrado, W. F. (2005) Sequence determinants of a transmembrane proton channel: an inverse relationship between stability and function, *J. Mol. Biol. 347*, 169-179.
37. Howard, K. P., Lear, J. D., and DeGrado, W. F. (2002) Sequence determinants of the energetics of folding of a transmembrane four-helix-bundle protein., *Proc. Natl. Acad. Sci. USA 99*, 8568-8572.
38. Carpino, L. A., and Han, G. Y. (1972) 9-Fluorenylmethoxycarbonyl Amin-Protecting Group, *J. Org. Chem. 37*, 3404-3409.
39. Ito, T., Gorman, O. T., Kawaoka, Y., Bean, W. J., and Webster, R. G. (1991) Evolutionary analysis of the influenza A virus M gene with comparison of the M1 and M2 proteins, *J. Virol. 65*, 5491-5498.
40. Traikia, M., Warschawski, D. E., Recouvreur, M., Cartaud, J., and Devaux, P. F. (2000) Formation of unilamellar vesicles by repetitive freeze-thaw cycles: characterization by electron microscopy and 31P-nuclear magnetic resonance, *Eur. Biophys. J. 29*, 184-195.
41. Bennett, A. E., Rienstra, C. M., Auger, M., Lakshmi, K. V., and Griffin, R. G. (1995) Heteronuclear decoupling in rotating solids., *J. Chem. Phys. 103*, 6951-6958.
42. Fung, B. M., Khitrin, A. K., and Ermolaev, K. (2000) An improved broadband decoupling sequence for liquid crystals and solids, *J. Magn. Reson. 142*, 97-101.
43. Hohwy, M., Rienstra, C. M., Jaroniec, C. P., and Griffin, R. G. (1999) Fivefold symmetric homonuclear dipolar recoupling in rotating solids: application to double-quantum spectroscopy., *J. Chem. Phys. 110*, 7983-7992.
44. Gullion, T., and Schaefer, J. (1989) Rotational echo double resonance NMR, *J. Magn. Reson. 81*, 196-200.

45. Hong, M., and Griffin, R. G. (1998) Resonance Assignment for Solid Peptides by Dipolar-Mediated 13C/15N Correlation Solid-State NMR, *J. Am. Chem. Soc. 120*, 7113-7114.
46. Hong, M., Gross, J. D., Rienstra, C. M., Griffin, R. G., Kumashiro, K. K., and Schmidt-Rohr, K. (1997) Coupling amplification in 2D MAS NMR and its application to torsion angle determination in peptides, *J. Magn. Reson. 129*, 85-92.
47. Bielecki, A., Kolbert, A. C., de Groot, H. J. M., Griffin, R. G., and Levitt, M. H. (1990) Frequency-switched Lee-Goldburg sequences in solids., *Adv. Magn. Reson. 14*, 111-124.
48. Nielsen, N. C., Bildsoe, H., Jakobsen, H. J., and Levitt, M. H. (1994) Double-quantum homonuclear rotary resonance: efficient dipolar recovery in magic-angle spinning nuclear magnetic resonance, *J. Chem. Phys. 101*, 1805-1812.
49. Huster, D., Yamaguchi, S., and Hong, M. (2000) Efficient b-Sheet Identification in Proteins by Solid-State NMR Spectroscopy, *J. Am. Chem. Soc. 122*, 11320-11327.
50. Munowitz, M. G., Griffin, R. G., Bodenhausen, G., and Huang, T. H. (1981) Two-Dimensional Rotational Spin-Echo Nuclear Magnetic Resonance in Solids: Correlation of Chemical Shift and Dipolar Interactions, *J. Am. Chem. Soc. 103*, 2529-2533.

Supporting Information

Table 5.2: ^{13}C and ^{15}N chemical shifts (ppm) of M2TMP in DLPC bilayers at 243 K without and with amantadine (Amt). Sites with chemical shift differences greater than 0.5 ppm are bolded. The letters s, m, w denote strong, medium, and weak intensities when more than one peak is observed. The ^{13}C and ^{15}N shifts are referenced to TMS and liquid NH_3, respectively.

residue	site	- Amt	+ Amt
L26	N	117.7	117.5
	CO	-	-
	Cα	55.4	55.4
	Cβ	39.7	39.4
	Cγ	25.2	25.1
	Cδ1	22.3	22.4
	Cδ2	21.2	21.3
V27	N	120.4	120.2
	CO	**177.9**	**178.6**
	Cα	**63.8**	**62.8**
	Cβ	29.8	30.1
	Cγ1	**21.0**	**20.0**
	Cγ2	19.5	19.9
A29	N	**120.9**	**121.7**
	CO	-	-
	Cα	53.3	53.2
	Cβ	16.7	16.5
A30	N	118.7	118.4
	CO	180.4	180.0
	Cα	52.8	52.9
	Cβ	**16.5**	**17.2**
I33	N	**120.2**	**118.8**
	CO	178.8	178.7
	Cα	63.3	63.1
	Cβ	35.7	35.5
	Cγ1	**28.6**	**30.1**
	Cγ2	**15.1**	**16.0**
	Cδ	11.8	12.2
G34	N	**107.1**	**106.3, 109.7**
	CO	**173.5**	**175.7**
	Cα	**45.6**	45.9, **44.8**
I35	N	**122.3**	**124.6**
	CO	**175.4**	**176.9**

	Cα	63.8	63.8
	Cβ	36.0	35.8
	Cγ1	**28.2**	**27.0**
	Cγ2	15.8	15.7
	Cδ	11.8	11.7
L38	N	**117.8**	**117.1**
	CO	175.8	175.6
	Cα	56.1	56.2
	Cβ	**39.6s,** 36.8w	39.7m, **37.0s**
	Cγ	25.2	25.0
	Cδ1	**22.3**	**23.3**
	Cδ2	**20.1**	**21.2**

Table 5.3: ^{13}C homogeneous T_2 and apparent T_2^* (ms) of M2TMP in DLPC lipid bilayers without and with amantadine (Amt) at 303 K. T_2^* is obtained from the observed linewidths by $T_2^* = 1/\pi\Delta^*$.

Residue	site	T_2^*, - Amt	T_2, - Amt	T_2^*, + Amt	T_2 , + Amt
L26	Cα	1.0	1.4	1.8	2.1
	Cβ	1.8	1.8	2.6	3.0
	Cδ1	3.2	5.8	4.7	9.2
	Cδ2	-	-	3.7	8.4
V27	Cα	1.1	1.0	1.3	3.4
	Cγ2	3.7	4.7	3.4	7.2
A29	Cα	1.1	1.3	2.0	2.5
	Cβ	2.1	5.2	2.2	9.0
A30	Cα	1.1	1.8	2.1	3.5
	Cβ	2.2	3.4	1.3	5.7
I33	Cα	1.1	1.0	1.4	3.4
	Cγ2	2.2	3.4	1.3	4.6
	Cδ	3.7	4.8	3.0	5.6
G34	Cα	0.9	1.2	1.3	2.1
I35	Cα	1.4	1.9	2.3	2.1
	Cβ	1.9	2.1	2.9	2.6
	Cγ2	2.1	2.1	2.2	3.4
	Cδ	3.5	4.9	4.1	7.1
L38	Cα	1.2	1.3	2.1	3.5
	Cβ	1.2	1.5	2.3	3.6
	Cγ	2.6	2.7	2.1	3.5
	Cδ1	3.3	4.5	3.8	8.3
	Cδ2	3.7	4.7	3.0	8.0
average		2.1	2.8	2.5	4.9

Table 5.4: ^{13}C homogeneous T_2 (ms) of M2TMP at 243 K and 303 K of M2TMP without and with amantadine (Amt).

Residue	Site	-Amt, 303 K	-Amt, 243 K	+Amt, 303 K	+Amt, 243 K
L26	Cα	1.4	3.0	2.1	2.8
	Cβ	1.8	1.8	3.0	1.5
	Cγ		2.4		
	Cδ1	5.8	3.0	9.2	
	Cδ2			8.4	
V27	Cα	1.0	2.8	3.4	3.0
	Cβ		2.4		2.5
	Cγ2	4.7	4.0	7.2	4.7
A29	Cα	1.3	3.2	2.5	2.8
	Cβ	5.2	4.6	9.0	4.9
A30	Cα	1.8	2.8	3.5	3.2
	Cβ	3.4	5.1	5.7	7.2
I33	Cα	1.0	2.8	3.4	3.0
	Cβ		2.3		2.8
	Cγ1		2.4		2.5
	Cγ2	3.4		4.6	
	Cδ	4.8	4.2	5.6	4.3
G34	Cα	1.2	3.2	2.1	2.6
I35	Cα	1.9	2.9	2.1	2.8
	Cβ	2.1	2.2	2.6	1.8
	Cγ2	2.1		3.4	
	Cδ	4.9	5.3	7.1	4.7
L38	Cα	1.3	2.9	3.5	3.2
	Cβ	1.5	1.9	3.6	2.2
	Cγ	2.7	2.7	3.5	3.0
	Cδ1	4.5	4.0	8.3	4.7
	Cδ2	4.7		8.0	

Table 5.5: ^{13}C apparent linewidths (Δ*) and homogeneous linewidths (Δ) (Hz) of M2TMP in DLPC bilayers at 243 K without and with amantadine (Amt). The apparent linewidths Δ* (±20 Hz) are read off from 2D correlation spectra, while the homogeneous linewidths Δ are obtained from T_2 measurements as $\Delta = 1/\pi T_2$. Sites of significant linewidth changes upon amantadine binding are bolded. Sites without entry are due to resonance overlap.

Residue	site	Δ*, - Amt	Δ, - Amt	Δ*, + Amt	Δ, + Amt
L26	Cα	170	100	200	110
	Cβ	**410**	180	**270**	200
V27	Cα	260	110	260	110
	Cβ	190	130	180	130
A29	Cα	160	100	140	110
	Cβ	240	70	240	70
A30	Cα	180	110	140	100
	Cβ	**310**	60	**160**	40
I33	Cα	300	110	300	110
	Cβ	260	140	230	110
	Cγ1	360	130	370	130
	Cγ2	310		280	
G34	Cα	**240**	100	**180**	120
I35	Cα	**250**	110	**130**	120
	Cβ	**240**	150	**160**	180
	Cγ1	**290**		**170**	
	Cγ2	210		210	
	Cδ	210	60	170	70
L38	Cα	190	100	150	100
	Cβ	**380**	160	**200**	150
average		258	113	207	115

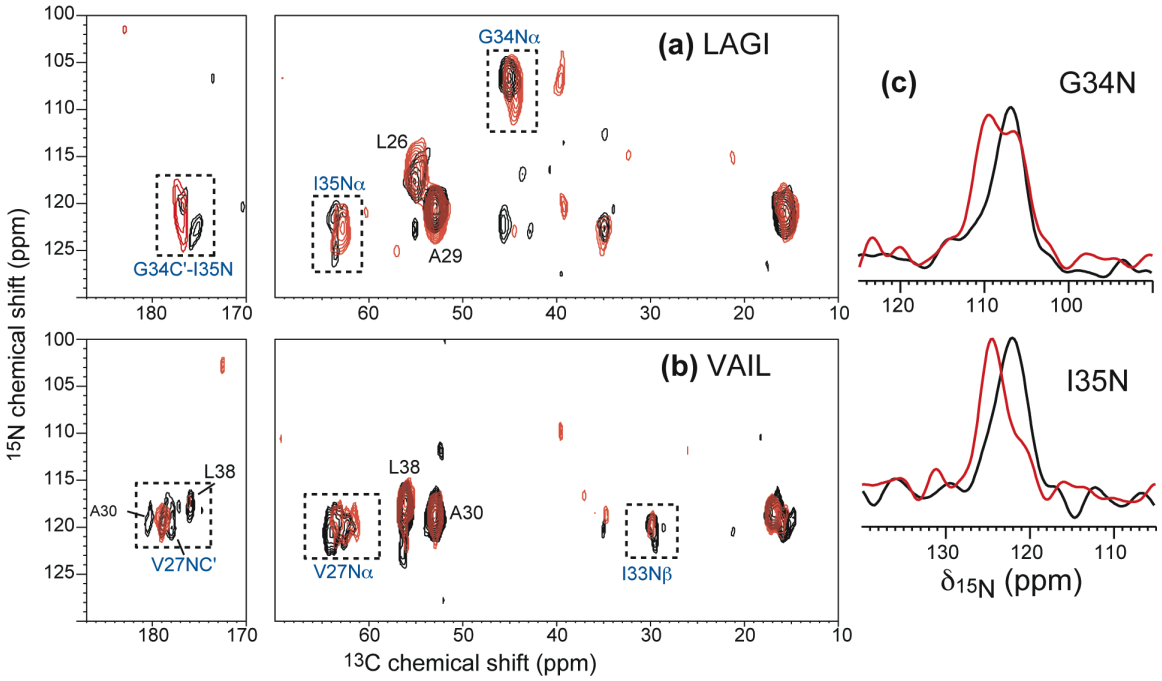

Figure 5.7 2D ^{15}N-^{13}C correlation spectra of M2TMP in DLPC bilayers with (red) and without (black) amantadine at 243 K. (a) LAGI. ^{13}C chemical shifts change for G34 Cα, G34 C' and I35 Cα, and ^{15}N shift changes are detected at G34 and I35. (b) VAIL. ^{13}C chemical shifts change at V27 Cα, C' and I33 Cβ. (c) 1D ^{15}N cross sections for G34 and I35, showing the chemical shift and linewidth changes.

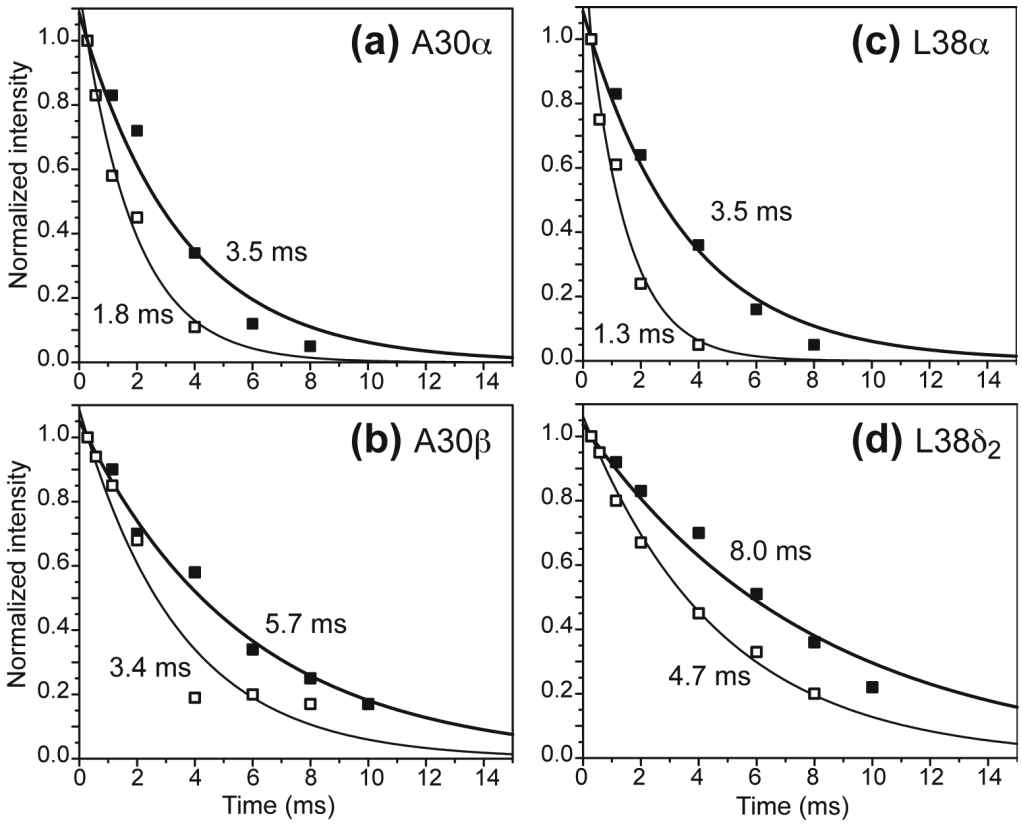

Figure 5.8 ^{13}C T_2 decay curves of representative backbone (a, c) and sidechain (b, d) carbons of M2TMP with (filled squares) and without (open squares) amantadine at 303 K. (a) A30α. (b) A30β. (c) L38α. (d) L38δ2. All carbons show longer T_2's upon amantadine binding.

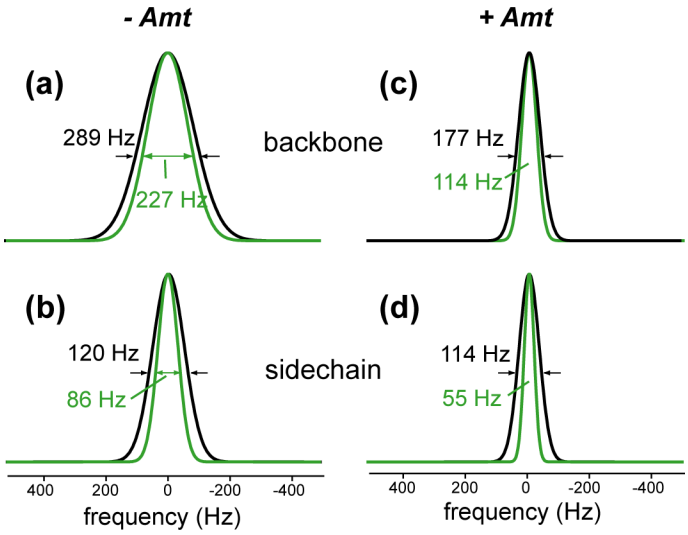

Figure 5.9 Average ^{13}C homogeneous (green) and apparent (black) linewidths of M2TMP at 303 K without (a, b) and with (c, d) amantadine (Amt). (a, c): Backbone Cα carbons. (b, d) Sidechain carbons. The homogeneous linewidths are calculated from the T_2 values (Table 3, supporting information) according to $\langle\Delta\rangle = 1/\pi\langle T_2\rangle$, then averaged for all sites within each category. The backbone Cα homogeneous linewidths are significantly narrowed by amantadine. However, the heterogeneous linewidths are difficult to compare at this temperature.

Chapter 6

Structure of Amantadine-Bound M2 Transmembrane Peptide of Influenza A in Lipid Bilayers from Magic-Angle-Spinning Solid-State NMR: the Role of Ser_{31} in Amantadine Binding

A paper published in the Journal of Molecular Biology

2009, vol. 385 (4) pp. 1127-1141

Sarah D. Cady, Tatiana V. Mishanina and Mei Hong

Abstract

The M2 proton channel of influenza A is the target of the antiviral drugs amantadine and rimantadine, whose effectiveness has been abolished by a single-site mutation of Ser_{31} to Asn in the transmembrane domain of the protein. Recent high-resolution structures of the M2 transmembrane domain obtained from detergent-solubilized protein in solution and crystal environments gave conflicting drug binding sites. We present magic-angle-spinning solid-state NMR results of Ser_{31} and a number of other residues in the M2 transmembrane peptide (M2TMP) bound to lipid bilayers. Comparison of the spectra of the membrane-bound apo and complexed M2TMP indicates that Ser_{31} is the site of the largest chemical shift perturbation by amantadine. The chemical shift constraints lead to a monomer structure with a small kink of the helical axis at Gly_{34}. A tetramer model is then constructed using the helix tilt angle and several interhelical distances previously measured on unoriented bilayer samples. This tetramer model differs from the solution and crystal structures in terms of the openness of the N-terminus of the channel, the constriction at Ser_{31}, and the sidechain conformations of Trp_{41}, a residue important for channel gating. Moreover, the tetramer model suggests that Ser_{31} may interact with amantadine amine via hydrogen bonding. While the apo and drug-bound M2TMP have similar average structures, the complexed peptide has much narrower linewidths at physiological temperature, indicating drug-induced changes of the protein dynamics in the membrane. Further, at low temperature, several residues show narrower lines in the complexed peptide than the apo peptide, indicating that amantadine

binding reduces the conformational heterogeneity of specific residues. The differences of the current solid-state NMR structure of the bilayer-bound M2TMP from the detergent-based M2 structures suggest that the M2 conformation is sensitive to the environment, and care must be taken when interpreting structural findings from non-bilayer samples.

Introduction

The M2 protein of influenza A virus forms a tetrameric proton channel that is the target of the antiviral drugs amantadine and rimantadine (*1*). The drugs were effective until recently, when a single-site mutation of S31N in the transmembrane domain of the protein caused complete resistance of the viruses to the drugs (*2*). The M2 proton channel is important for viral replication. After the virus enters the infected cell by endocytosis, the proton channel acidifies the viral core, which triggers the dissociation of the virus matrix and subsequent viral gene expression (*3*). With 97 amino acids, the M2 protein is small compared to typical ion channels, thus it is an excellent system for elucidating the structure-function relationship of ion channels. Extensive mutagenesis, electrophysiological (*4, 5*) and sedimentation experiments (*6*) have been carried out to determine the low-resolution structure and stability of this proton channel. Elucidating the high-resolution structure and the difference between the drug-free and drug-bound states is the next natural challenge that is important not only for developing new inhibitors to curb influenza infection but also for understanding the fundamental biophysics of ion channels.

The transmembrane domain of the M2 protein spanning residues 22 to 46 (Figure 6.1a) contains a histidine and a tryptophan that are crucial for proton conduction and gating (*7, 8*). This domain exhibits channel activity (*9*) and forms a parallel four-helix bundle with left-handed crossing angles. The residues facing the channel lumen versus the lipids have been identified through experiments probing the effects of mutation on proton currents and amantadine inhibition (*10*). The main channel-facing residues, V27, A30, G34 and H37, fall onto the *a* and *d* positions of a heptad repeat (Figure 6.1b). The *b*, *c*, and *f* positions of the heptad repeat face the lipids, while the *e* and *g* positions occupy the helix-helix interfaces. Apart from the transmembrane domain, the segment of the protein spanning residues 44-60

forms a membrane-proximal amphipathic helix that is important for channel stability (*11*) and is recently found to be involved in pH activation (*12*).

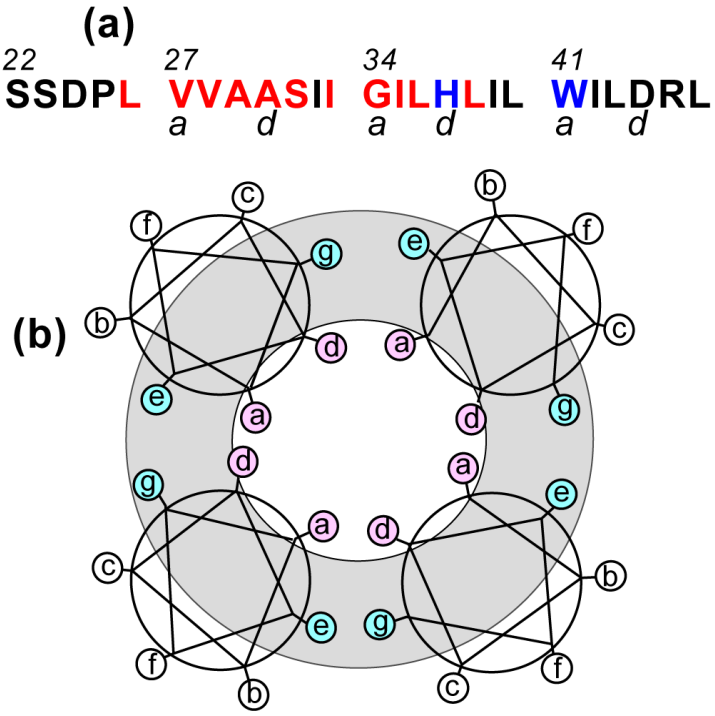

Figure 6.1. M2(22-46) sequence and its representation as a heptad repeat. (a) Amino acid sequence. The *a* and *d* residues of the heptad repeat *abcdefg* are labeled. The ^{13}C, ^{15}N-labeled residues that have been studied so far (*13*) are colored in red. H37 and W41, which are central for proton conduction and channel gating, are shown in blue. (b) Four-helix bundle organization of M2TMP. Channel-facing *a* and *d* residues are shaded in pink, and interfacial *e* and *g* residues are shaded in cyan.

Recently, two high-resolution structures of portions of the M2 protein containing the transmembrane domain were reported simultaneously (*14, 15*). One structure was obtained by X-ray crystallography and the other by solution NMR. The X-ray structure was determined on amantadine-bound M2(22-46) in the detergent octyl-β-D-glucopyranoside (OG) (*15*). The solution NMR structure was determined on rimantadine-bound M2(18-60) solubilized in DHPC micelles (*14*). Strikingly, the two structures showed very different drug binding sites: the solution NMR structure showed rimantadine to be bound at the helix-helix

interfaces of the tetramer near the C-terminus of the transmembrane domain, while the crystal structure showed amantadine bound to the channel lumen near the N-terminus. In addition, the helix orientation and the sidechain conformations of the two structures differ substantially (*16*).

These structural differences underscore the importance of examining the M2 transmembrane peptide structure using an independent technique and doing so in the most biologically relevant environment of lipid bilayers. Detergent micelles are known to cause curvature stress to membrane proteins and have been documented to affect the structure of proteins compared to bilayer-bound samples (*17*). Similarly, crystallizing hydrophobic membrane proteins in a sparse matrix of detergent molecules leaves open the question of how different the structure is from the bilayer-bound state. For these reasons, solid-state NMR (SSNMR) spectroscopy, which can be readily applied to lipid bilayers and other semi-solids, is the preferred method for determining the high-resolution structures of membrane proteins.

Until recently, the majority of SSNMR data on the M2 transmembrane peptide (M2TMP) consisted of static ^{15}N chemical shift anisotropies and N-H dipolar couplings measured on uniaxially aligned membrane samples. These data yielded very precise orientation angles of the M2TMP helices in the lipid bilayer (*18, 19*). However, the ^{15}N NMR constraints do not report the sidechain conformation nor the interhelical packing of the tetramer. Further, information on the backbone structure is only inferred by pattern recognition of the 2D N-H dipolar and ^{15}N chemical shift correlation spectra.

We recently undertook a magic-angle-spinning (MAS) SSNMR study of the structure and dynamics of M2(22-46) in lipid bilayers. Several types of structural information have been obtained so far. First, isotropic ^{13}C and ^{15}N chemical shifts of eight residues in the transmembrane domain (L26, V27, A29, A30, I33, G34, I35, and L38) were measured and compared between the apo and amantadine-complexed states (*13*) to determine structure perturbation by the drug. Second, ϕ, ψ and χ_1 torsion angles were directly measured at selected residues by dipolar correlation experiments to quantify the peptide conformation. Third, we measured the helix orientations using unoriented membrane samples and found small differences between the apo and drug-bound peptide, as well as different tilt angles in

lipid bilayers of different thicknesses (*20, 21*). Fourth, the peptide dynamics were probed by ^{2}H quadrupole NMR and various dipolar coupling and chemical shift anisotropy measurements, and were found to be dramatically altered by drug binding (*20*). Finally, we measured interhelical distances at V27, A30, L38, and W41 using ^{19}F-labeled M2TMP to constrain the helix packing in the tetrameric bundle (*22, 23*). These SSNMR results were obtained from M2TMP bound to hydrated and unoriented DLPC, DMPC or POPC membranes, which are more natural environments for membrane proteins than detergents.

In this work, we report the chemical shifts of Ser_{31}, Val_{28} and Leu_{36}, and propose a backbone structural model of M2TMP using all SSNMR constraints obtained so far. Ser_{31} has been postulated to be the main residue involved in amantadine binding. MD simulations suggested that the Ser_{31} hydroxyl group forms hydrogen bonds with the amantadine amine (*24*). This was supported by neutron diffraction experiments that showed amantadine to be positioned between Val_{27} and Ser_{31} (*25*). Mutation of Ser_{31} to Asn gives rise to the main drug-resistant mutant in current influenza A viruses. Thus, knowledge of Ser_{31} conformation in M2TMP is important for understanding how amantadine blocks the channel. The availability of chemical shifts for a contiguous segment of the peptide allows us to deduce the (ϕ, ψ) torsion angles of the protein using the well established relation between protein conformation and NMR chemical shifts (*26*). From this chemical shift constrained monomer structure, we constructed a tetramer model of the transmembrane domain using several interhelical distances measured previously. We compare this MAS-NMR model with the solution NMR, X-ray, and ^{15}N orientation-NMR structures, and suggest the binding site of amantadine.

Results

^{13}C chemical shifts of VSL-M2TMP without and with amantadine

Figure 6.2 shows the lipid-suppressed ^{13}C MAS spectra of V28, S31, L36-labeled M2TMP without (a, c) and with amantadine (b, d). The lipid background signals were suppressed by a ^{13}C-^{13}C DQ filter in (a, b) and a ^{15}N-^{13}C heteronuclear dipolar filter in (c, d). For the N-C filtered spectra, only the directly bonded Cα signals are selected due to the short

N-C recoupling time used. All spectra were measured at 243 K, in the gel phase of the membrane.

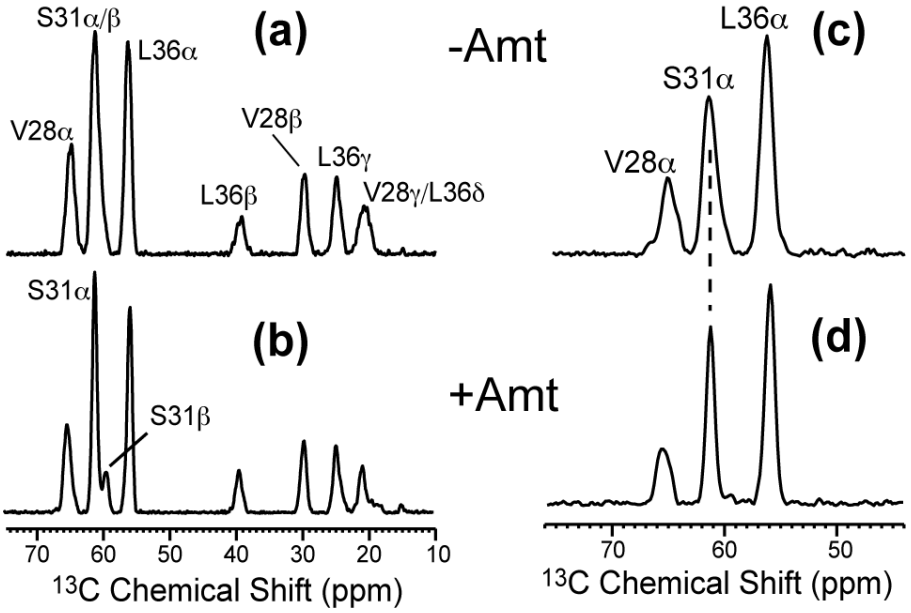

Figure 6.2. 1D ^{13}C spectra of VSL-M2TMP in DLPC bilayers at 243 K. (a) ^{13}C DQF spectrum of the apo peptide. (b) ^{13}C DQF spectrum of the amantadine-bound peptide. (c) ^{15}N-filtered ^{13}C spectrum of the apo peptide. (d) ^{15}N-filtered ^{13}C spectrum of the amantadine-bound peptide.

The main ^{13}C chemical shift difference caused by amantadine occurs at S31 Cα and Cβ: the two sites overlap completely in the apo-M2TMP spectrum (a) but become partly resolved in the amantadine-complexed spectrum (b). In addition, the ^{15}N-^{13}C filtered spectra in (c, d) show a narrower S31 Cα peak for the complexed peptide than the apo peptide. At low temperature where peptide motion is frozen, NMR linewidths reflect conformational distribution. Thus, the narrower Cα line of the complexed peptide indicates reduced conformational heterogeneity at S31 upon drug binding (see below).

Figure 6.3 shows the 2D ^{13}C-^{13}C DQF-COSY spectra to illustrate the unambiguous assignment of the ^{13}C chemical shifts. The 2D spectra further illustrate the striking difference of S31 chemical shifts between the apo- and amantadine-complexed M2TMP: while the apo peptide does not resolve the S31 Cα and Cβ peaks near 61 ppm, the complexed peptide

shows clear off-diagonal intensities indicative of chemical shift separation between Cα and Cβ (b). On the other hand, the S31 Cα/CO cross peaks are unchanged by amantadine (c). Since protein secondary structures give opposite-signed secondary shifts between Cβ on one hand and Cα and CO on the other, the absence of opposite Cα and CO shift changes from the Cβ shift change suggests that the cause for the Cβ change is packing interaction with amantadine rather than (ϕ, ψ) angle changes of the S31 backbone.

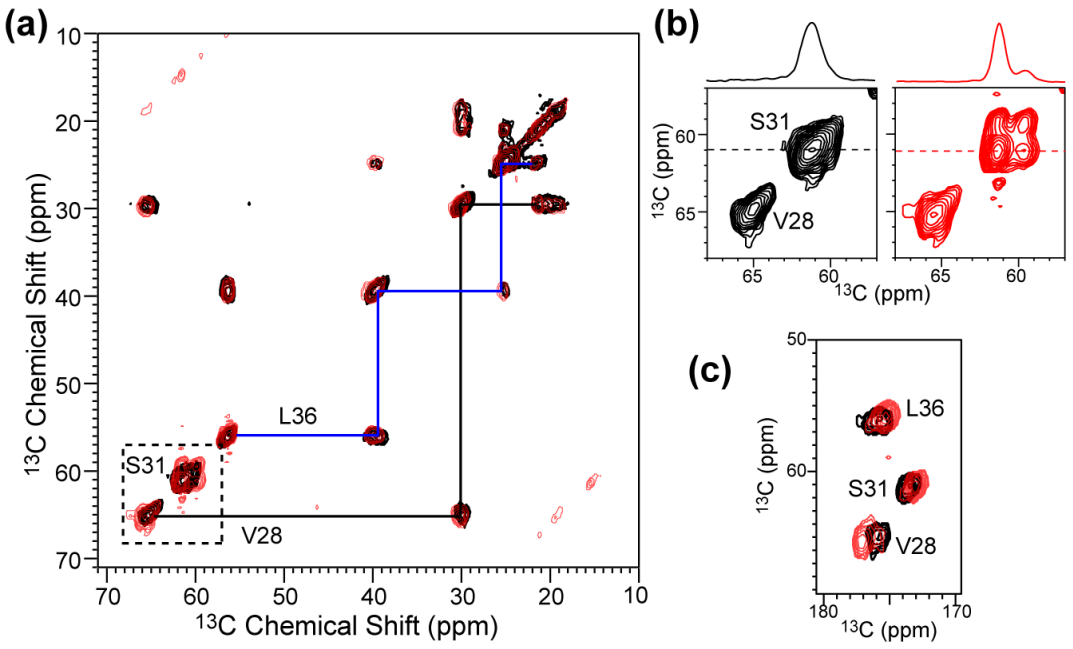

Figure 6.3. 2D ^{13}C-^{13}C DQF correlation spectra of VSL-M2TMP in DLPC bilayers at 243 K without (black) and with (red) amantadine. (a) Aliphatic region. (b) S31 and V28 region. (c) Carbonyl region.

To confirm the S31 Cβ chemical shift, we carried out a 1D CH_2-spectral editing experiment. The experiment selectively detects CH_2 groups such as Ser Cβ while suppressing the signals of all CH groups such as backbone Cα's. Figure 6.4 compares the CH_2-edited spectra (b, d) with the ^{13}C CP spectra (a, c) of the apo and complexed M2TMP. The unfiltered spectra contain all labeled peptide ^{13}C signals as well as natural abundance lipid ^{13}C signals; thus they are less resolved than Figure 6.2. The CH_2 filter suppressed the V28

and L36 Cα signals but retained S31 Cβ, L36 Cβ, and the main lipid CH_2 peaks. The method does not completely suppress the mobile CH_3 groups, however their chemical shifts do not overlap with Ser Cβ. The CH_2-edited spectra of the apo and complexed peptide (b, d) confirm the 1.0 ppm upfield shift of the S31 Cβ peak upon amantadine binding.

In addition to S31, V28 Cα and CO show significant chemical shift changes in the 2D spectra (Figure 6.3c). The CO frequency increased by 1.4 ppm while the Cα chemical shift increased by 0.7 ppm (Table 6.1). These downfield shift changes are consistent with a more ideal helical conformation in the presence of amantadine. Moreover, the CO chemical shift is sensitive to hydrogen bonding (*27*); thus the larger increase of the CO chemical shift over Cα suggests that amantadine may perturb the hydrogen-bond network around V28.

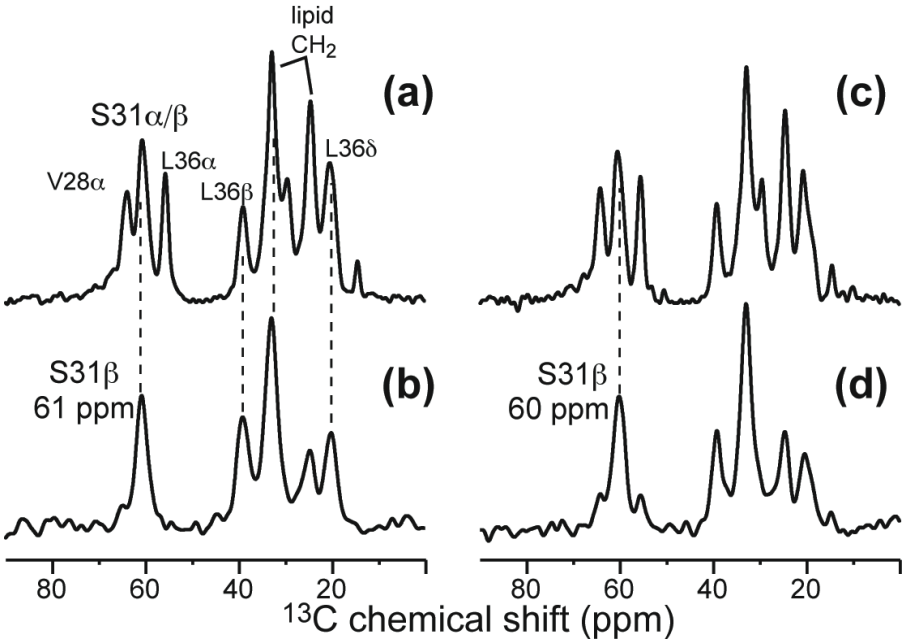

Figure 6.4. Selective detection of S31 Cβ by CH_2 editing. (a) ^{13}C CP-MAS spectrum of apo-M2TMP. (b) CH_2 edited spectrum of apo-M2TMP. (c) ^{13}C CP-MAS spectrum of amantadine-bound M2TMP. (d) CH_2 edited spectrum of bound M2TMP. Note the suppression of the Cα CH peaks in (b) and (d).

Table 6.1: ^{13}C and ^{15}N chemical shifts (ppm) of M2TMP in DLPC bilayers at 243 K without and with amantadine (Amt). Sites with chemical shift differences greater than 0.5 ppm are bolded. Letters s, m and w denote strong, medium and weak, respectively. The ^{13}C and ^{15}N shifts are referenced to TMS and liquid NH_3, respectively.

		N	CO	Cα	Cβ	Cγ	Cδ	Cε
L26	apo	117.7	176.6	55.5	39.1	25.2	23.8	21.2
	Amt	117.5	176.3	55.7	39.4	25.2	23.3	20.9
V27	Apo	120.4	177.8	63.8	29.7	21.2	19.3	
	Amt	119.9	178.1	63.9s **62.0w**	30.0	20.8	19.5	
V28	Apo	**122.8**	**175.9**	**64.8**	29.7	20.7	19.5	
	Amt	**125.9**	**177.0**	**65.4**	29.7	20.8	19.0	
A29	Apo	**120.9**	176.7	53.5	16.6			
	Amt	**121.7**	176.8	53.5	16.3			
A30	Apo	118.0w **119.4**	177.7	52.8	16.5			
	Amt	118.7	177.5	52.8	17.0			
S31	Apo	**114.7**	**173.7**	61.2	**60.8**			
	Amt	**121.4**	**173.1**	61.3	**59.8**			
I33	Apo	**120.3**	175.7	63.1	35.4	28.5	15.7 **14.9**	11.8
	Amt	**119.4**	176.0	63.2	35.4	28.3	16.0	12.0
G34	Apo	**107.1**	**173.0**	**45.7**				
	Amt1	**106.3**	173.2	45.5				
	Amt2	**109.7**	**175.0**	**45.0**				
I35	Apo	**122.3**	175.5	63.9	35.7	**28.1**	15.7	11.7
	Amt	**124.6**	175.4	63.8	35.8	**27.3**	15.6	11.6
L36	Apo	119.9	**175.8**	56.0	39.4	24.9	24.2	21.2
	Amt	119.6	**175.3**	55.8	39.5	24.7	23.8	21.2
L38	apo	**117.8**	175.8	56.1	37.5w 39.5s	25.0	24.2	**20.1**
	Amt	**117.1**	175.8	56.0	37.4m 39.6s	24.9	23.9	**21.0**

^{15}N chemical shifts of VSL-M2TMP without and with amantadine

Low-temperature 1D ^{15}N MAS spectra of the apo and complexed VSL-M2TMP are shown in Figure 6.5. The assignment of the ^{15}N peaks is based on 2D ^{15}N-^{13}C correlation spectra shown in Figure 6.6 below. Both the ^{15}N chemical shifts and ^{15}N linewidths show dramatic changes upon amantadine binding. The V28 and S31 ^{15}N peaks move downfield, and all three sites are narrowed by a factor of two. The drug-complexed peptide has FWHM of 2.0 ppm for all three sites, while the apo peptide linewidths range from 3.5 – 5.3 ppm (Table 6.2).

2D ^{15}N-^{13}C correlation spectra are shown in Figure 6.6 to provide definitive evidence of structure perturbation by amantadine. Consistent with the ^{13}C data, the most pronounced ^{15}N chemical shift change occurs at S31 (6.7 ppm), followed by V28, which has a more modest but still significant ^{15}N shift increase of 3.1 ppm. Similar to the ^{13}C data, L36 exhibits little change in its ^{15}N chemical shift.

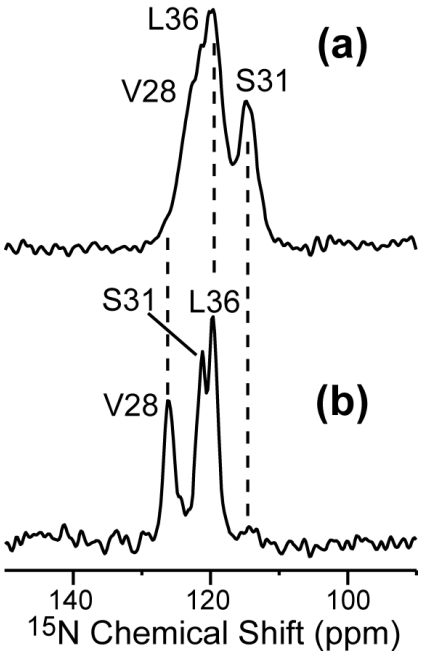

Figure 6.5. 1D ^{15}N CP-MAS spectra of VSL-M2TMP in DLPC bilayers at 243 K. (a) Without amantadine. (b) With amantadine.

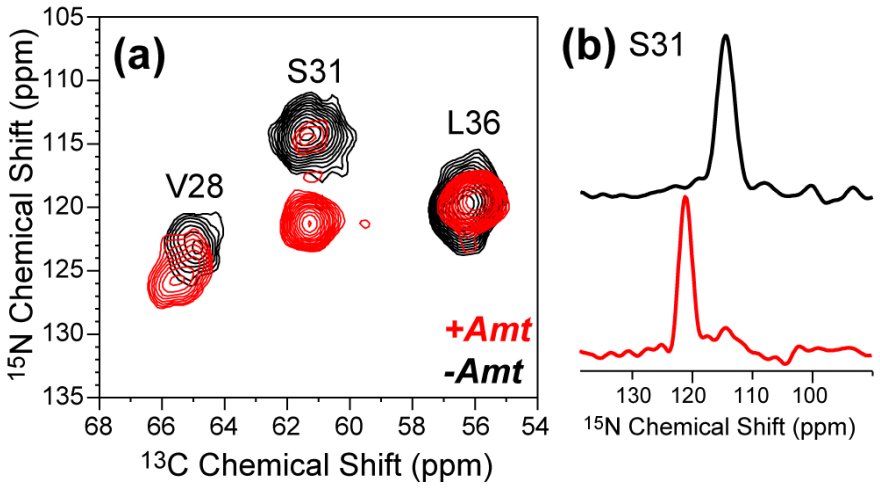

Figure 6.6. (a) 2D ^{15}N-^{13}C 2D correlation spectrum of VSL-M2TMP in DLPC bilayers at 243 K. Black: without amantadine. Red: with amantadine. (b) S31 ^{15}N cross sections.

Table 6.2. ^{13}C and ^{15}N apparent (Δ*) and intrinsic linewidths (Δ) of VSL-M2TMP at 243 K under 71 kHz ^{1}H decoupling. Significant linewidth changes between the apo and amantadine-bound samples are bolded.

Residue	site	Δ*, apo (ppm)	Δ, apo (ppm)	Δ*, + Amt (ppm)	Δ, + Amt (ppm)
V28	N	**5.3**	-	**2.0**	-
	Cα	1.4	0.60	1.3	0.60
	Cβ	1.1	0.67	1.0	0.67
	Cγ1	1.7	0.40	1.4	0.40
	Cγ2	1.3	0.40	1.6	0.40
S31	N	**3.5**	-	**2.0**	-
	Cα	**1.5**	0.60	**0.93**	0.60
	Cβ	**2.8**	0.57	**1.6**	0.57
L36	N	**4.0**	-	**2.0**	-
	Cα	1.0	0.47	0.9	0.47
	Cβ	1.3	0.73	1.1	0.73
	Cγ	1.1	0.57	1.0	0.57
	Cδ1	1.9	0.40	1.7	0.40
	Cδ2	1.4	0.40	1.4	0.40

Chemical shift perturbation at the M2TMP core

Table 6.1 summarizes all ^{13}C and ^{15}N chemical shifts measured for eleven residues, including L26, V27, V28, A29, A30, S31, I33, G34, I35, L36, and L38. This table extends the one recently reported (*13*) by the addition of V28, S31 and L36 chemical shifts, the addition of carbonyl chemical shifts for all residues, and the more accurately measured sidechain methyl chemical shifts (*13*). Figure 6.7a plots the average chemical shift change per residue due to amantadine binding:

$$\text{chemical shift perturbation} = \frac{1}{n}\sum_{i=1}^{n}\left|\delta_{apo,i} - \delta_{amt,i}\right|,$$

where n is the number of chemical shift values available in each residue. Both the ^{13}C and ^{15}N chemical shifts are included, and the absolute value of the chemical shift difference is summed to avoid cancellation of positive and negative shift changes. Figure 6.7a shows three distinct local maxima of chemical shift perturbation: S31, G34 and V28, with average chemical shift changes of 2.1 ppm, 1.1 ppm, and 0.9 ppm, respectively.

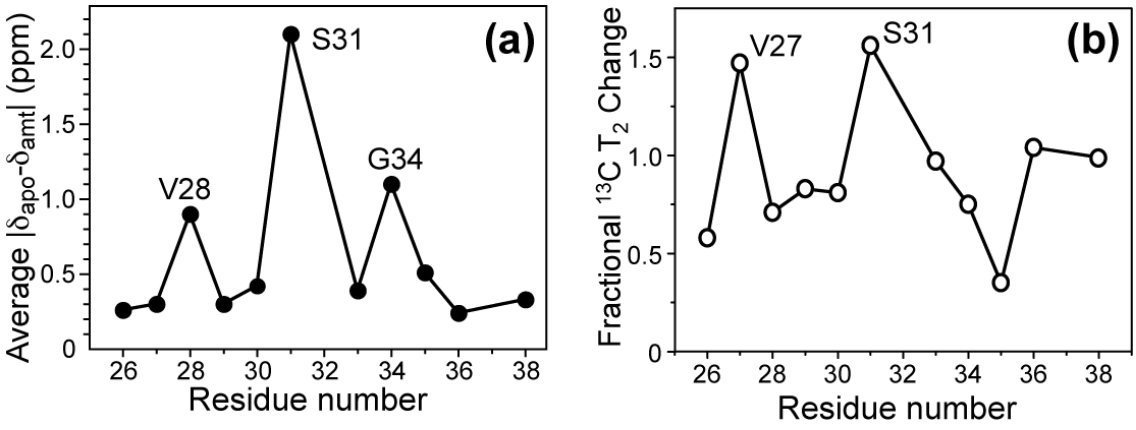

Figure 6.7. Amantadine-induced changes of M2TMP structure and dynamics in DLPC bilayers. (a) Average isotropic chemical shift changes for each residue, measured at low temperature. (b) Average ^{13}C T_2 changes, measured at 303 K.

Conformational distributions at V28, S31 and L36

While isotropic chemical shifts report the average conformation, linewidths of frozen proteins indicate the conformational distribution. Apparent linewidths (Δ*) directly read off from the spectra are indicative of conformational heterogeneity, while homogeneous linewidths (Δ) result from T_2 relaxation, which is induced by microsecond-timescale molecular motions that modulate the nuclear spin interactions. The homogeneous linewidths can be measured using spin echo experiments and are related to T_2 by $\Delta = 1/\pi T_2$. We extracted the ^{15}N and ^{13}C apparent linewidths from 2D ^{13}C-^{13}C and ^{15}N-^{13}C correlation spectra where all signals are resolved. Low temperature spectra are used since they capture all conformations present in the fluid membrane. Table 6.2 shows that the apparent linewidths of most sites in V28, S31 and L36 are similar between the apo and complexed peptide, with the exception of all amide ^{15}N sites and S31 Cα and Cβ.

To obtain the ^{13}C homogeneous linewidths, we measured the T_2 relaxation times under a ^{1}H decoupling field of 71 kHz. ^{1}H-decoupled heteronuclear T_2 is mainly sensitive to motions on the timescale of the inverse of the decoupling field, which is thus ~ 10 μs. Table 6.2 shows that the ^{13}C homogeneous linewidths are identical between the apo and complexed peptide within experimental uncertainty, indicating that all peptide motion is frozen at 243 K and does not cause different relaxation between the apo and complexed states. Thus, the narrower Δ* of S31 in the complexed peptide must be attributed to reduced conformational heterogeneity due to drug binding.

Amantadine-induced changes of M2TMP dynamics

Complementing the low-temperature chemical shift and linewidth data, we measured the ^{13}C spectra of M2TMP in the liquid-crystalline phase of the lipid bilayer to obtain information on the molecular motion of the protein. Previous data on eight other labeled residues found across-the-board line narrowing by amantadine at high temperature (*13*). This is now observed at V28, S31, and L36 as well. Figure 6.8 shows the ^{13}C CP-MAS spectra of apo and complexed VSL-M2TMP in DLPC bilayers from 243 K to 313 K. At 243 K, the

spectra show strong intensities characteristic of immobilized molecules for both the apo and complexed M2TMP. When the temperature increased to 283 K, near the phase transition temperature of the DLPC bilayer, the peak intensities decrease significantly for both samples, indicating intermediate-timescale motion. Increasing the temperature to the near-physiological 313 K partially recovered the intensities of both samples, but the amantadine-complexed peptide exhibits stronger CP intensities than the apo-peptide, especially for methylene groups such as L36 Cβ and S31 Cβ.

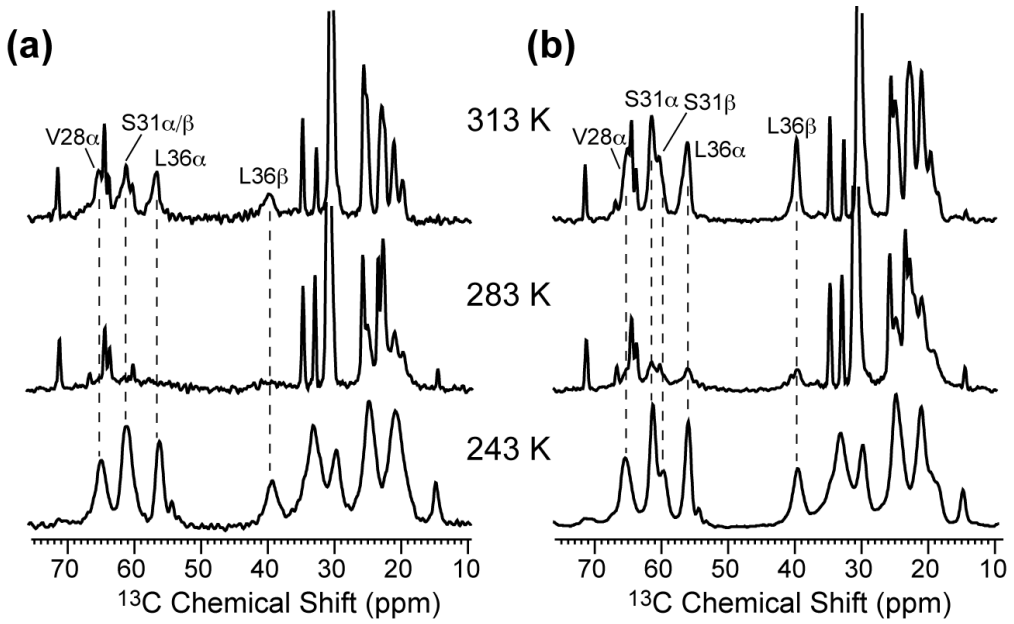

Figure 6.8. 1D ^{13}C variable-temperature CP-MAS spectra of VSL-M2TMP bound to DLPC bilayers. (a) Without amantadine. (b) With amantadine. Temperatures from top to bottom are 313 K, 283 K and 243 K.

To probe fluid-phase dynamics of M2TMP, we measured the ^{13}C T_2 of the peptide at 303 K using the Hahn-echo experiment and compared them between the apo and complexed states. Table 6.3 shows that the ^{13}C T_2 values increase by 1.5 – 4.0 fold upon drug binding, consistent with what was observed at other residues (*13*). Plotting the fractional increase of the ^{13}C T_2 for the eleven residues as

$$\text{fractional } T_2 \text{ change} = \frac{1}{n}\sum_{i=1}^{n}\frac{T_{2,amt}^{i} - T_{2,apo}^{i}}{T_{2,amt}^{i}},$$

we find two local maxima, V27 and S31 (Figure 6.7b).

Table 6.3. ^{13}C homogeneous T_2 (ms) of VSL-M2TMP at 303 K with 71 kHz ^{1}H decoupling.

Residue	site	T_2, apo	T_2 , +Amt
V28	Cα	1.0	2.5
	Cγ1	3.0	5.6
	Cγ2	2.6	4.7
S31	Cα	1.1	3.5
	Cβ		3.8
L36	Cα	1.0	3.6
	Cβ	1.1	3.5
	Cγ	2.6	7.9
	Cδ1	6.0	11.6
	Cδ2	6.0	-

Dependence of M2 structural changes on amantadine concentration and specificity of the structure changes

The above amantadine-induced chemical shift changes were measured on membrane samples prepared from buffers containing 10 mM amantadine. ^{1}H solution NMR analysis of the supernatant after the membrane is pelleted showed that the amount of amantadine bound to the membrane typically corresponded to a M2 : amantadine molar ratio of ~1 : 10. This is well in excess of the expected stoichiometric M2 : amantadine ratio, which is either 4 : 1 based on the crystal structure or 1: 1 based on the solution NMR structure. The use of excess amantadine is largely due to the concern that the lipophilic drug, which readily partitions into the lipid membrane from the aqueous solution (*28-30*), may not all end up in the channel. Nevertheless, the question arises as to whether the observed M2 chemical shift changes result from non-specific effects of amantadine on the lipid bilayer that then indirectly change the peptide structure, or whether it is due to direct amantadine-peptide interactions. To address

this question, we prepared a VSL-M2TMP sample in DLPC bilayers with a much lower M2 : amantadine molar ratio of 1 : 2, by directly titrating a quantitative amount of amantadine solution into the M2 membrane pellet. The resulting 2D spectrum (Figure 6.9c) shows that 70% of the S31 ^{15}N-^{13}Cα peak has shifted to the bound position. The 30% remaining unshifted signal can be attributed to channels without amantadine, implying that some amantadine is dispersed in the rest of the lipid bilayer. The observation of the same chemical shift perturbation at much lower amantadine levels confirm that the structural changes we detect at high concentration result from direct drug-protein interactions rather than non-specific lipid-mediated effects, as shown in Figure 6.9.

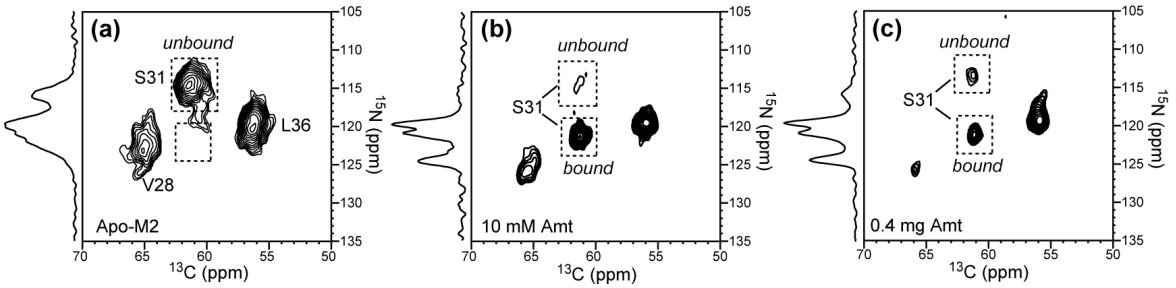

Figure 6.9. 2D ^{15}N-^{13}C correlation spectra of VSL-M2TMP in DLPC bilayers with different amounts of amantadine. The S31 ^{15}N-^{13}Cα cross peak is used to indicate the degree of amantadine binding. 1D ^{15}N CP spectra are shown projected from the indirect dimension of each spectrum. (a) No amantadine. The S31 peak is completely in the unbound position. (b) Amantadine added at 10 mM in the buffer. The M2 : amantadine molar ratio in the final membrane is ~1 : 8. Almost all S31 intensities are at the bound position. (c) Amantadine directly titrated into the membrane pellet. The M2 : amantadine molar ratio in the final pellet is ~ 1 : 2. 70% of the S31 intensity is at the bound position.

A related question is whether amantadine causes the M2 ^{13}C T_2 relaxation time changes (Figure 6.7b) by indirect and non-specific changes of the membrane dynamics. To answer this question, we prepared two DLPC samples without the M2 peptide. One sample does not contain amantadine and the other contains 10 mM amantadine in the buffer during vesicle formation. The ^{13}C T_2 relaxation times of the two DLPC samples were measured at

313 K by direct polarization Hahn echo experiments, in which identical ^{1}H decoupling field strengths (30 kHz) were used to ensure that the motion is probed on the same timescale. Figure 6.10 shows the fractional T_2 changes for all resolved DLPC carbon sites. It can be seen that all sites except the headgroup Cβ experience negligible T_2 changes of less than ±10% upon amantadine binding. Moreover, most DLPC sites show a *decrease* of ^{13}C T_2, opposite to the trend for M2TMP. Thus, amantadine does not significantly impact the lipid dynamics, and the dynamic changes of M2TMP are specifically due to peptide-drug interactions.

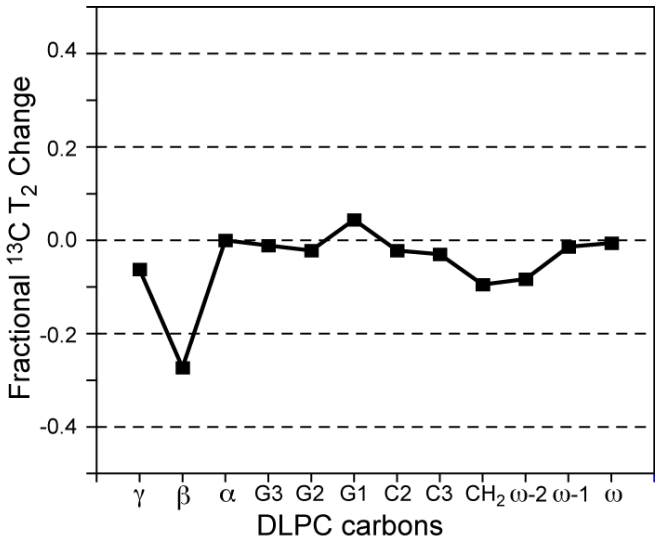

Figure 6.10. Fractional ^{13}C T_2 changes of DLPC lipid carbons upon amantadine binding at 313 K. No M2 peptide is present. The fractional change is calculated as $\left(T_{2,amt} - T_{2,apo}\right)/T_{2,apo}$.

Discussion

The goals of this study are two fold: obtain a chemical shift constrained backbone structure of M2TMP in the absence and presence of amantadine, and determine the size and nature of the drug-induced conformational change, particularly at Ser_{31}. With the consolidation of the ^{13}C and ^{15}N chemical shifts for eleven consecutive residues in the core of

the peptide, we can now use the TALOS program to predict the backbone torsion angles of the M2 peptide in the lipid bilayer.

Backbone structure of M2TMP monomer

The TALOS predicted (ϕ, ψ) torsion angles of M2TMP based on the ^{13}C and ^{15}N chemical shifts are shown in Figure 6.11 and tabulated in Table 6.S1 in Supplementary Materials. TALOS requires the chemical shifts of three consecutive residues to predict the torsion angles of the central residue. Since I32 and H37 have not been labeled in our studies but data for their neighboring residues are available, we used database ideal helical chemical shifts for these two residues as placeholders in order to extract the (ϕ, ψ) angles of their neighboring residues. The torsion angles of I32 and H37 are thus not entirely constrained (shaded points in Figure 6.11).

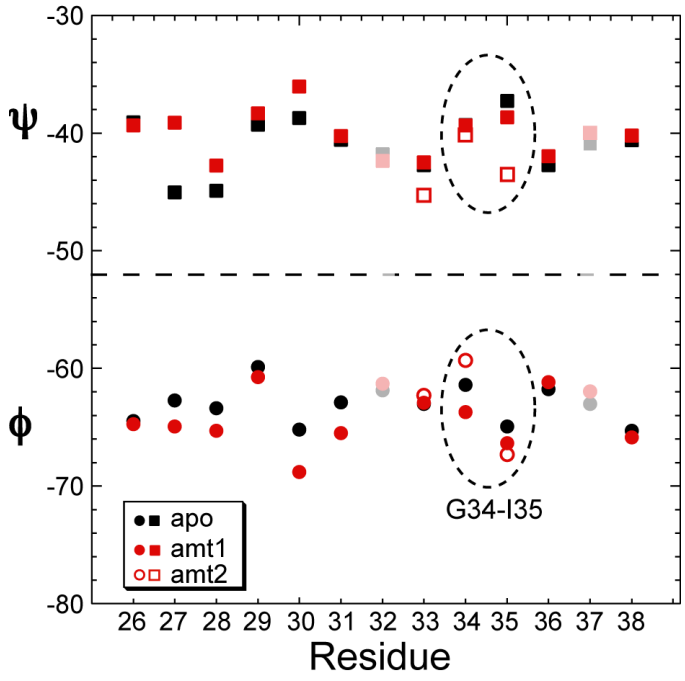

Figure 6.11. TALOS predicted (ϕ, ψ) angles for residues 26-38 of apo (black) and amantadine-complexed M2TMP (red). Filled and open red symbols denote the conformations of amt1 and amt2, which differ at G34. Residues 32 and 37 are shaded due to incomplete experimental data.

The chemical shift changes listed in Table 6.1 indicate a number of (ϕ, ψ) changes, although none of them are large enough to alter the basic helical nature of the protein. The first region of change is V27-V28, and the second is A30-S31. Interestingly, while the chemical shifts of V27 and A30 themselves are not significantly perturbed, the larger chemical shift changes of their C-terminal residues, V28 and S31, translated into significant (ϕ, ψ) changes at V27 and A30. In particular, the large ^{15}N chemical shift changes of S31 and V28 indicate that the ψ angle of A30 and V27, respectively, are significantly perturbed.

The G34-I35 pair is the third region of (ϕ, ψ) perturbation that merits attention. Not only do both residues show clear chemical shift perturbations, but also two sets of G34 ^{15}N and ^{13}C chemical shifts are present in the complexed peptide (Table 6.1). We denote the set with an upfield ^{15}N shift of 106.3 ppm as amt1, and the set with a downfield ^{15}N chemical shift of 109.7 ppm as amt2. The amt1 chemical shifts are similar to the apo values, suggesting that a population of peptide either does not bind or only weakly binds amantadine. In contrast, the amt2 chemical shifts are significantly different from the apo values, and cause larger G34 ϕ and I35 ψ changes (Figure 6.11). Overall, the TALOS predicted (ϕ, ψ) angle differences between the apo- and amt2 forms of M2TMP are on average (1.8°, 2.8°).

Figure 6.12 shows the monomer structure of the M2TMP backbone based on the TALOS (ϕ, ψ) angles. The apo structure is shown in black and gray and the amt2 structure in blue and cyan. For residues 39 down to the end of the helix, where no experimental chemical shifts are available, we used the helical torsion angles of (-59°, -44°) for both the apo and complexed peptide. Figure 6.12 shows that both helices are relatively ideal. The side views of the two models are oriented such that the N-terminus half of the helix above G34 has a tilt angle of 35° for the apo peptide and 38° for the amantadine-bound peptide. These tilt angles were measured on hydrated vesicle samples by ^{15}N NMR (*13, 20, 21*). When the N-terminal segments of the two helices are superimposed, it becomes apparent that the amt2 and apo helices diverge in the orientation of the segment C-terminal to G34. Comparing the helical axis for residues 27-33 with the helical axis for residues 35-41, we find a kink of 8° for the apo peptide and 5° for the amt2 helix. The helical axis orientations were calculated as the

average N-H vector orientation of each 7-residue segment, which approximately complete two turns of the helix.

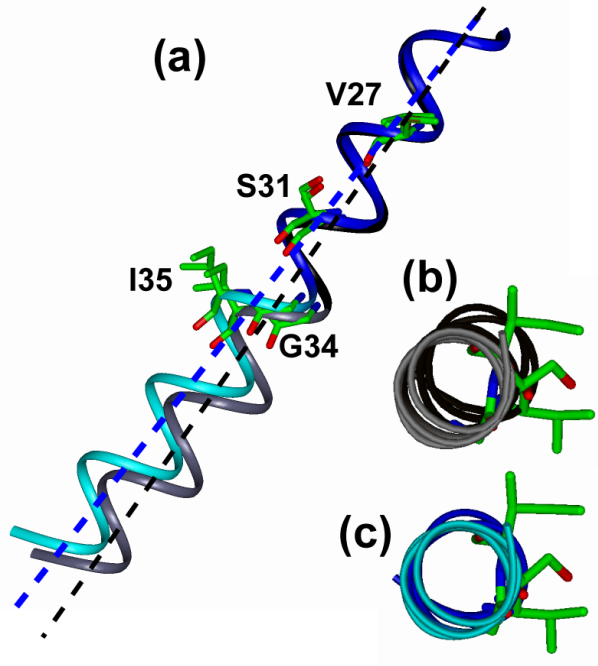

Figure 6.12. Chemical shift constrained backbone structure of the M2TMP monomer. Apo: black and gray ribbon. Amantadine-bound: blue and cyan ribbon. (a) Side view of the helix with tilt angles determined by SSNMR. (b) Top view of the apo monomer. (c) Top view of the amantadine-complexed monomer. The apo peptide has a more noticeable kink.

^{15}N chemical shift anisotropies and N-H dipolar couplings have been measured on M2TMP in glass-plate aligned DMPC/DMPG membranes using static NMR techniques. These data indicated a pronounced helix kink of 13° for the drug-complexed M2TMP (*18*). The site of the kink is G34, in good qualitative agreement with the current chemical shift data that indicate structure perturbation at G34-I35. However, the kink from the oriented-sample NMR data is much larger than deduced from the current unoriented MAS samples. While static ^{15}N anisotropic couplings are very sensitive to helix orientations, it is possible that glass-plate samples may exert additional influences on the protein orientation through

mechanical stress and hydration. In comparison, the unoriented vesicle samples should place much less stress on membrane proteins and thus provide a useful check of the protein orientation. Moreover, the membrane thickness may affect the helical kink. The aligned membrane experiments were done in DMPC and DMPG lipids while the current experiments were conducted in the thinner DLPC bilayers.

The recent solution NMR (*14*) and X-ray structures (*15*) of drug-bound and detergent solubilized M2 peptide show different kinks of the helical backbone. Comparing the same segments of 27-33 and 35-41, the solution NMR structure (PDB: 2RLF) has a minor kink of 4˚, while the refined crystal structure (PDB: 3C9J) has a larger kink of 12˚. Thus, the amt2 kink of 5˚ measured by MAS-SSNMR falls within the range of reported by all methods.

Paradoxically, the structure of the apo M2 peptide is much less known than that of the drug-bound M2. Static ^{15}N NMR data of the apo peptide suffered from broad linewidths due to unfavorable conformational dynamics of the protein (*19, 31*), which made it difficult to detect possible helix orientation differences between the N- and C-terminal segments of the helix. The MAS-NMR approach here bypasses this difficulty since its main structural constraints are *isotropic* chemical shifts, which can be measured at low temperature where motion is frozen. Based on the ^{13}C and ^{15}N isotropic chemical shifts, the helical backbone of the apo M2TMP is also not straight but has a kink of ~9˚, as shown in the top view in Figure 6.12b. While the chemical shift constrained backbone conformation are only indirect constraints of the helix orientation, the data nevertheless suggests that the presence of Gly_{34} in the peptide may cause a small kink already in the apo protein. This would not be surprising since Gly is a helix breaker in globular proteins (*32*). In membrane proteins Gly adheres to more ideal helical torsion angles (*33*), as in the case of Gly_{34}, but a small deviation from ideality is all that is required to cause a small kink of the helical axis. If confirmed, then the role of helix kink to the M2 channel activity would need to be considered. Since Gly_{34} is located roughly one turn away from His_{37}, which is responsible for proton conduction, we speculate that the kink may be required for establishing the proper His_{37} sidechain conformation. The change in the helix kink after amantadine binding may thus be relevant for proton blockage.

Backbone structure of the M2 tetramer

Based on the chemical shift constrained monomer structure, we now construct a tetramer model of amantadine-bound M2TMP using the measured helix orientation and interhelical distances. Again, the helix tilt angle is set to be 35˚ for the apo peptide (*20*) and 38˚ for the amantadine-bound peptide (*13, 21*) for the segment N-terminal to Gly_{34}. We have previously measured two ^{19}F-^{19}F interhelical distances at Trp_{41} 5-^{19}F (*23*) and Phe_{30} 4-^{19}F (*22, 34*) using ^{19}F spin diffusion NMR (*35*) . By design, these experiments measure all three distances in the symmetric tetramer, including two nearest neighbor $i - i\pm1$ distances r_{nn} and the diagonal $i - i+2$ distance, $\sqrt{2}r_{nn}$. The tetrameric nature of the channel is directly confirmed in the experiment as an equilibrium value of 1/4. We found an r_{nn} of 11.8 Å for Trp_{41} 5-^{19}F and 8.5 Å at Phe_{30} 4-^{19}F. The former constrained the Trp_{41} sidechain rotamer to t90 (χ_1=180˚, χ_2=90˚), while the latter constrained the Phe_{30} rotamer to *t* (χ_1=180˚). In addition to these two interhelical distances, we use a Gly_{34} Cα-Cα diagonal distance of 10.4 Å (*36*) in building the tetramer model.

Figure 6.13 shows the tetramer model for the amt2 peptide where the three distance restraints are indicated. For clarity we show only the diagonal distances, which are 16.7 Å, 12.5 Å, and 10.4 Å for Trp_{41} 5-^{19}F, Phe_{30} 4-^{19}F, and Gly_{34} Cα, respectively. For comparison, the tetramer structure solved by ^{15}N static NMR (PDB: 2H95), solution NMR (PDB: 2RLF), and X-ray crystallography (PDB: 3C9J) are shown in Figure 6.14b-d. A number of differences can be seen. First, both the solution NMR structure in DHPC micelles and the static ^{15}N NMR structure in DMPC bilayers give inter-helical Trp_{41} distances that are much shorter than the measured value. This discrepancy is mainly due to the different (χ_1, χ_2) angles in these models: t-90 in the solution NMR structure and (-95˚, 125˚) in the static ^{15}N NMR model. The crystal structure has the t90 rotamer for Trp_{41} and thus gives consistent interhelical distances with the ^{19}F MAS NMR result. Second, the MAS-SSNMR tetramer model is more open at the N-terminus than the solution NMR and crystal structures. At Val_{27}, the Hγ - Hγ diagonal distances in our model are ~11 Å, but are 5 – 7 Å in the other models. The relatively large pore opening at Val_{27} in our model is a direct result of the helix orientation, and is consistent with the small chemical shift perturbation of Val_{27} and the

interhelical Phe_{30} distance constraint. This large opening may be necessary to allow the drug to bind at the N-terminus. The smaller Val_{27} constriction in the solution NMR and crystal structures is a direct result of smaller tilt angles, which may be influenced by the detergent matrix used. It is well documented that the orientation of the M2 transmembrane helix is relatively plastic, readily affected by the bilayer thickness (*20, 37*). In DLPC and DMPC bilayers, both MAS and static NMR experiments point to a large helical tilt angle of about 35˚, while in POPC bilayers the tilt angle is only 26˚ (*20*).

In contrast to the openness of the channel at Val_{27}, the MAS-derived structural model shows a tight Ser_{31} constriction, with a distance of 9.0 Å between the two opposing hydroxyl oxygens. This Ser_{31} constriction is similar to the crystal structure, but tighter than the static ^{15}N NMR model (11.9 Å) and the solution NMR structure (19.4 Å) (Figure 6.14). Overall, the small Ser_{31} constriction is consistent with the large chemical shift perturbation at this site (see next section).

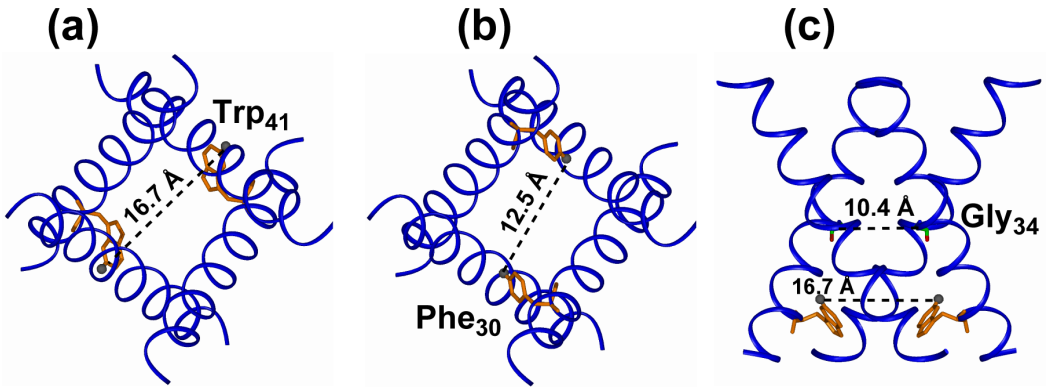

Figure 6.13. Tetramer model of M2TMP constrained by SSNMR chemical shifts, interhelical distances and helix orientations. (a) Trp_{41} 5-^{19}F distance between the two opposite helices is 16.7 Å (*23*). (b) Phe_{30} 4-^{19}F diagonal distance is 12.5 Å (*22*). (c) Side view of the tetramer, with a diagonal Gly_{34} Cα-Cα distance of 10.4 Å.

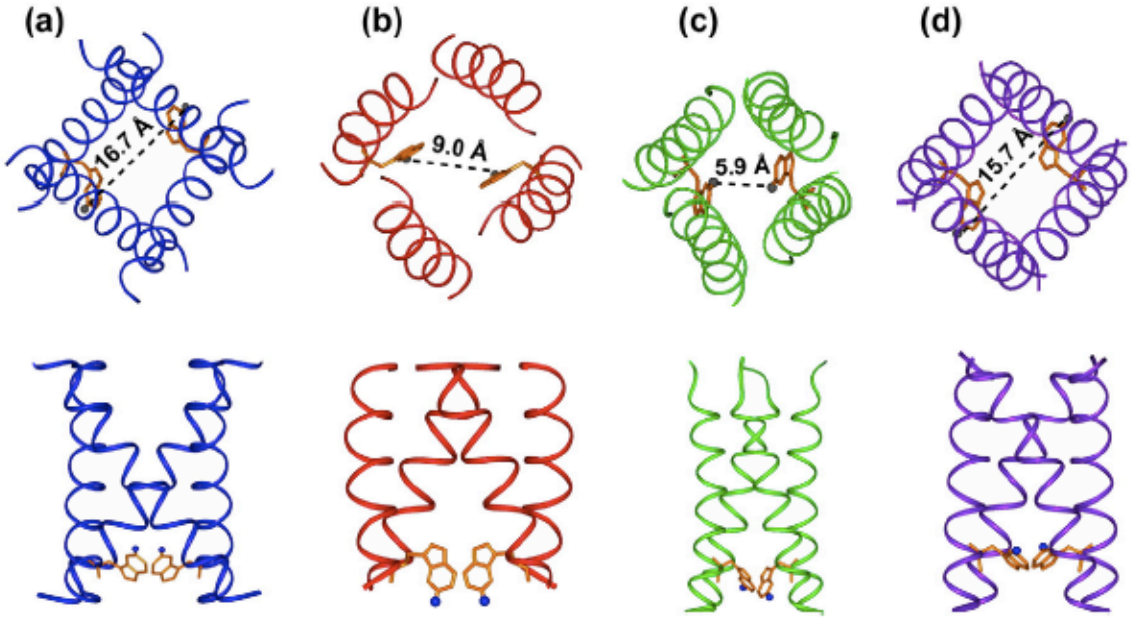

Figure 6.14. Comparison of the MAS NMR structure model with other recently published structures of drug-complexed M2. The Trp_{41} indole ring and the diagonal distance between its 5-^{19}F or Hζ3 is indicated. (a) MAS-NMR model of amantadine-bound M2TMP. (b) ^{15}N static SSNMR model of amantadine-bound M2TMP (PDB code: 2H95). (d) Solution NMR structure of rimantadine-bound M2(18-60) (PDB code: 2RLF). (d) Crystal structure of amantadine-bound M2TMP (PDB: 3C9J).

To compare the various M2 PDB structures with the current MAS-based model more quantitatively, we used the SHIFTX program (*38*) to calculate the ^{15}N, ^{13}CO, ^{13}Cα and ^{13}Cβ chemical shifts for the crystal structure (PDB: 3C9J), the solution NMR structure (PDB: 2RLF), and the oriented solid-state NMR structure (PDB: 2H95). The root-mean-square (RMS) deviations of the predicted chemical shifts from the measured values for both the apo and amantadine-bound M2TMP are summarized in Table 6.S2 (Supplementary Material). Three observations can be made. First, with the exception of the ^{13}CO shifts for the oriented NMR structure model, most ^{13}C RMS shift differences are in the range of 0.8-1.3 ppm, which are comparable to the standard RMS errors of the SHIFTX program. This suggests that the deviations are mostly due to systematic uncertainties in the prediction protocol rather than large secondary structure differences. Second, the ^{15}N chemical shifts differences are

comparable to the standard RMS error when the predicted values are compared to the measured apo chemical shifts, but the differences become almost two times larger when the predicted values are compared to the amantadine-bound chemical shifts. This further indicates the sensitivity of ^{15}N chemical shifts to long-range electrostatic effects due to ligand binding and helix packing, which are not taken into account in such chemical shift prediction programs. Third, among the three PDB structures, the oriented SSNMR structure (2H95) has the largest ^{13}C chemical shift deviations from the current data, but the smallest ^{15}N chemical shift deviations. This is consistent with the sole use of ^{15}N NMR inputs to constrain the 2H95 model.

Ser_{31} interaction with amantadine

The chemical shift perturbation plot (Figure 6.7a) indicates maximal drug-induced changes at Ser_{31} and Val_{28}, which are mainly due to the large ^{15}N chemical shift changes of these two residues. Many factors influence ^{15}N chemical shielding: in addition to (ϕ, ψ, χ) torsion angles (*39*), solvation effects and electrostatic field effects can be significant. Hydrogen bonding of the NH group can cause a deshielding of as much as 13 ppm (*40*), and γ-gauche effect through the sidechain torsion angle also affects the ^{15}N chemical shifts (*39*). However, database ^{15}N secondary shifts show only small deviations of ~ 1 ppm for the helical conformation from the random coil values (*41*). Thus, it is difficult to directly interpret the large ^{15}N chemical shift perturbation of Ser_{31}. Nevertheless, it is noteworthy that both the ^{15}N and Cβ chemical shifts of Ser_{31} in the bound peptide (Table 6.1) are well beyond the typical values for α-helical Ser (*41*), which are 114.9 ppm and 61.2 ppm, respectively, while the apo peptide's Ser_{31} chemical shifts are within the database range for α-helical Ser. This suggests that Ser_{31} is locally perturbed by amantadine through packing effects.

Early neutron diffraction (*25*) and MD simulations (*24*) both supported the N-terminus of the helical bundle to be the amantadine binding site. However, the recently published high-resolution crystal structure (*15*) and solution NMR structure (*14*) of M2 gave contradictory results on the drug binding site. The former shows an N-terminus binding site deeper than Ser_{31}, while the latter puts four rimantadine molecules per channel on the C-

terminus side at helical interfaces. Since then, a functional study of the proton conductivity of M2 mutants has been carried out that supports the N-terminus region as the primary amantadine binding site with channel inhibition properties (*42*).

While the current data do not directly probe the drug binding site, several indirect pieces of structural evidence support an N-terminus location for amantadine. First, Ser_{31} is the only residue among the three studied here whose sidechain Cβ linewidth is reduced. This may reflect sidechain conformational ordering necessary to form the appropriate hydrogen bond with amantadine. Second, the chemical shift perturbation for the segment N-terminal to G34 is extensive (Figure 6.11), with only the lipid-facing A29 and the very upstream L26 showing no torsion angles changes. Third, both V28 and L36 lie at lipid-facing positions (*b* and *c*) of the heptad repeat, but the chemical shift perturbation of the N-terminus V28 is much larger than that of the C-terminus L36.

Assuming that amantadine indeed binds the N-terminus portion of the channel, we can model the distances of amantadine from Ser_{31} in the tetramer (Figure 6.15). Using the height of amantadine found in the crystal structure as a template, we found that if the amine points to the center of the membrane, then the R_{NO} distances between Ser_{31} OH and amantadine NH_2 are 7.5 – 8.0 Å, too long for hydrogen bonding. However, if the amine points to the membrane surface, then much shorter R_{NO} distances of ~4.5 Å are found. This amine-up orientation is supported by a recent paramagnetic relaxation NMR and MD simulation study of the depth of insertion of amantadine in the absence of M2 (*29*). To decrease the R_{NO} distance further to form hydrogen bonds of 2.5 – 3.5 Å, the Ser_{31} χ_1 torsion angle would need to be changed. Due to the small sidechain, Ser does not have a single dominant χ_1 rotamer. For α-helical backbones, the most popular rotamer of *m* (χ_1= –65°) is 44% while the least popular rotamer *t* (χ_1=-170°) still has a significant presence of 22% (*43*). In our model (Figure 6.15), both the *m* and *t* rotamers give R_{NO} distance of ~4.5 Å, but shorter distances of ~3.5 Å may be reached for less canonical χ_1 angles. Ultimately, intermolecular distance experiments are necessary to test this Ser_{31} binding-site hypothesis and to determine the high-resolution structure of the amantadine binding pocket in the bilayer-bound M2.

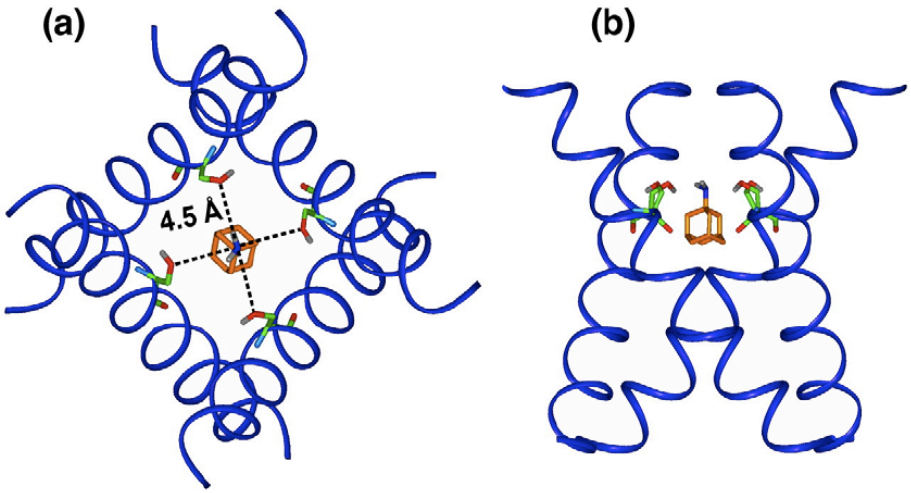

Figure 6.15. MAS-NMR M2 tetramer model with the proposed amantadine-binding site. The height of amantadine is set to be similar to that of the crystal structure. Ser_{31} sidechain O distances to the amine are indicated. The top view looks down the helix axis from the N- to the C-terminus.

Molecular dynamics of M2TMP

The conformational plasticity of the M2 peptide in lipid membranes are now well documented (*20, 31, 37*). The low ^{13}C CP intensities and short ^{13}C T_2 relaxation times for V28, S31 and L36 at high temperature all confirm the presence of intermediate-timescale conformational dynamics, which interfere with ^{1}H decoupling and the ^{1}H-^{13}C cross polarization process. In the gel phase, the motion is largely frozen, thus the distribution of conformations sampled at high temperature is shown as isotropic chemical shift distributions. The larger low-temperature linewidths of the apo peptide compared to the complexed peptides, mostly at ^{15}N sites, indicate larger conformational disorder of the apo peptide.

The nature of the M2 motion is complex. We have shown that the whole helical bundle undergoes uniaxial rotation around the bilayer normal (*20*), which explains the observation that the short ^{13}C T_2 times are not local but occur throughout the peptide. The lengthening of the T_2 upon amantadine binding (Table 6.3) can in principle result from either a decrease or increase of motional correlation times. Temperature-sensitive relaxation times

(unpublished data) indicate that the rate of motion is accelerated rather than slowed down by amantadine. Figure 6.7b indicates that most residues have similar amantadine-induced T_2 increases except for Ser_{31} and Val_{27}, whose T_2 increases are much larger. We hypothesize that the exceptionally long ^{13}C T_2 at this two sites may be caused by strong interaction with amantadine. However, the exact nature of the site-specific conformational dynamics or ordering will require further investigation.

In summary, the solid-state NMR chemical shifts and dynamic constraints measured here for Ser_{31} and other residues combine with previous data to allow the determination of a bilayer-bound structure of the transmembrane domain of this important influenza proton channel. We found that the apo and amantadine-complexed M2TMP differ in conformation mainly at three regions, V27-V28, A30-S31, and G34-I35. In particular, G34 is the site of a helical kink in both the apo and drug-bound peptide. Interhelical distances and helix orientations constrain the tetramer to be relatively open at the N-terminus, which allows the drug to enter, but tight at Ser_{31}, which suggests hydrogen bonding between the hydroxyl group and the amantadine amine. At Trp_{41} the channel has an interhelical distance of ~16.7 Å between opposing helices. Among all residues, Ser_{31} shows the largest drug-induced perturbations of chemical shifts, conformational dynamics, and conformational disorder, strongly suggesting that this residue is the amantadine binding site.

Material and Methods

Peptides and lipids

Fmoc-protected uniformly ^{13}C, ^{15}N-labeled Val, Ser, and Leu were either prepared in-house (*44*) or purchased from Sigma-Aldrich and Cambridge Isotope Laboratories. The M2 transmembrane domain of the Udorn strain (residues 22-46) (*45*) was synthesized by PrimmBiotech (Cambridge, MA) and purified to >95% purity. The amino acid sequence is SSDPL VVAASII GILHLIL WILDRL. The main peptide used in this work includes labeled residues at V28, S31, and L36 and is denoted VSL-M2TMP. Two previously studied M2TMP samples were also re-examined for their chemical shift assignment. One peptide

contains labeled residues at L26, A29, G34 and I35, and the other peptide contains labeled sites at V27, A30, I33 and L38.

Membrane sample preparation

M2TMP was reconstituted into 1,2-dilauroyl-*sn*-glycero-3-phosphatidylcholine (DLPC) bilayers by detergent dialysis (*23*). DLPC was chosen because of the favorable dynamics of the protein in this membrane (*20*) and the similar phase transition temperature (-2˚C) of this bilayer to biological cell membranes. The lipid vesicle solution was prepared by suspending dry DLPC powder (Avanti Polar Lipids) in 1 mL phosphate buffer (10 mM Na_2HPO_4/NaH_2PO_4, 1 mM EDTA, 0.1 mM NaN_3) at pH 7.5, vortexing and freeze-thawing 6-8 times to create uniform vesicles (*46*). M2TMP powder was codissolved with OG in 2 mL phosphate buffer to an OG concentration of 30 mg/mL. The M2TMP/OG solution was mixed with an equal volume of DLPC vesicles to halve the OG concentration to 15 mg/mL. The final peptide/lipid molar ratio (P/L) was 1:15. The mixture was vortexed for 1 hr, allowed to stand for 6-8 hrs at room temperature, then dialyzed with a 3.5 kDa cutoff against 1 L phosphate buffer at 4 °C for 3 days. The buffer was changed every 8-12 hrs to ensure complete removal of the detergent. The dialyzed M2TMP/DLPC solution was centrifuged at 150,000 g for 3 hours at 10˚C, resulting in a pellet containing ~50 wt% water. For most amantadine-bound samples, 10 mM amantadine hydrochloride was added to the phosphate buffer either throughout the vesicle formation and peptide reconstitution processes or before ultracentrifugation. After ultracentrifugation the percent of amantadine left in the supernatant was quantified by ^1H solution NMR and found to be roughly 60%. This gave a peptide : lipid : drug molar ratio of about 1 : 15 : 8. All membrane-bound M2 samples were thus studied at pH 7.5, corresponding to the closed state of the channel.

Solid-state NMR spectroscopy

Most SSNMR experiments were carried out on a Bruker AVANCE-600 (14.1 Tesla) spectrometer (Karlsruhe, Germany) using a 4 mm triple-resonance MAS probe. ^{13}C-^{13}C and

^{15}N-^{13}C 2D correlation experiments were conducted at 243 K to freeze peptide motion. ^{13}C T_2 relaxation times were measured at 303 K where the peptide is uniaxially mobile in the liquid-crystalline DLPC bilayer. Typical rf pulse lengths were 5 μs for ^{13}C and 3.5-4.0 μs for ^{1}H. ^{1}H TPPM (*47*) or SPINAL (*48*) decoupling field strengths of 60 – 70 kHz were applied. ^{13}C chemical shifts were referenced to the α-Gly C' signal at 176.49 ppm on the TMS scale, and ^{15}N chemical shifts were referenced to the ^{15}N signal of N-acetyl-valine at 122.0 ppm on the liquid ammonia scale.

Three types of 2D ^{13}C-^{13}C correlation experiments were carried out to assign all regions of the ^{13}C spectra. A double-quantum-filtered (DQF) COSY experiment was used to obtain lipid-free protein spectra. Double-quantum filtration was performed using the dipolar recoupling sequence SPC5 (*49*) with the sample spun at 7000 Hz. To better assign the carbonyl peaks, which are weak in the DQF-COSY spectrum due to their large chemical shift difference from the aliphatic carbons, a 2D ^{1}H-driven ^{13}C spin diffusion experiment with a 10 ms DARR mixing period (*50*) was carried out under 5333 Hz MAS. Finally, to completely resolve the sidechain methyl ^{13}C signals, a double-quantum single-quantum correlation experiment, INADEQUATE (*51, 52*), was used in which the SPC5 sequence was again used for double-quantum excitation and reconversion.

Heteronuclear 2D ^{15}N-^{13}C correlation experiments were carried out in an out-and-back fashion using the REDOR sequence (*53*) for ^{13}C-^{15}N coherence transfer (*54*). The C-N recoupling times varied between 0.7 and 2.1 ms to observe one-bond versus multiple-bond cross peaks.

To selectively detect the S31 Cβ signal that overlaps with its Cα, we carried out a methylene spectral editing experiment (*55*) at 233 K. The β pulse in the sequence that was responsible for clean suppression of the methine CH signals was optimized to be 40°. For MREV-8 (*56*) ^{1}H homonuclear decoupling, a ^{1}H pulse flip angle of 94° was used.

Structure Modeling

The M2TMP tetramer structure was modeled in Insight II (Accelrys, Inc. San Diego).

The central segment of residues 26-38 was constrained by the chemical shifts and interhelical distances except for residues I32 and H37. The final tetramer model used the wild-type residue Ala at position 30, after the mutation Phe_{30} was checked for interhelical distance restraint. The atomic coordinates of the tetrameric helical bundle have been deposited in the Protein Data Bank (accession number: 2kad). The SSNMR chemical shift restraints have been deposited in the Biological Magnetic Resonance Bank (accession number: 16020). These data will be released upon publication.

Acknowledgement

This work is funded by NSF grants MCB-0543473 to M.H. and DBI-0421374 for the 600 MHz NMR spectrometer. The authors thank Professor Bill DeGrado for discussions and sharing the refined crystal structure coordinates, and Professor Klaus Schmidt-Rohr for providing the pulse sequence for the CH_2 selection experiment.

References

1. Pinto, L. H., and Lamb, R. A. (2007) Controlling influenza virus replication by inhibiting its proton channel, *Mol. Biosyst. 3*, 18-23.
2. Bright, R. A., Medina, M. J., Xu, X., Perez-Oronoz, G., Wallis, T. R., Davis, X. M., Povinelli, L., Cox, N. J., and Klimov, A. I. (2005) Incidence of adamantane resistance among influenza A (H3N2) viruses isolated worldwide from 1994 to 2005: a cause for concern, *Lancet 366*, 1175-1181.
3. Lamb, R. A., Holsinger, K. J., and Pinto, L. H. (1994) The Influenza A virus M2 ion channel protein and its role in the influenza virus life cycle., in *Cellular Receptors of Animal Viruses* (Wemmer, E., Ed.), pp 303-321, Cold Spring Harbor Lab Press, Plainview, NY.
4. Pinto, L. H., Holsinger, L. J., and Lamb, R. A. (1992) Influenza virus M2 protein has ion channel activity, *Cell 69*, 517-528.

5. Holsinger, L. J., Nichani, D., Pinto, L. H., and Lamb, R. A. (1994) Influenza A virus M2 ion channel protein: a structure-function analysis, *J. Virol. 68*, 1551-1563.
6. Sakaguchi, T., Tu, Q., Pinto, L. H., and Lamb, R. A. (1997) The active oligomeric state of the minimalistic influenza virus M2 ion channel is a tetramer *Proc. Natl. Acad. Sci. USA 94*, 5000-5005.
7. Hu, J., Fu, R., Nishimura, K., Zhang, L., Zhou, H. X., Busath, D. D., Vijayvergiya, V., and Cross, T. A. (2006) Histidines, heart of the hydrogen ion channel from influenza A virus: toward an understanding of conductance and proton selectivity, *Proc. Natl. Acad. Sci. U.S.A. 103*, 6865-6870.
8. Tang, Y., Zaitseva, F., Lamb, R. A., and Pinto, L. H. (2002) The Gate of the Influenza Virus M2 Proton Channel Is Formed by a Single Tryptophan Residue, *J. Biol. Chem. 277*, 39880-39886.
9. Duff, K. C., and Ashley, R. H. (1992) The transmembrane domain of influenza A M2 protein forms amantadine-sensitive proton channels in planar lipid bilayers., *Virology 190*, 485-489.
10. Pinto, L. H., Dieckmann, G. R., Gandhi, C. S., Papworth, C. G., Braman, J., Shaughnessy, M. A., Lear, J. D., Lamb, R. A., and DeGrado, W. F. (1997) A functionally defined model for the M2 proton channel of influenza A virus suggests a mechanism for its ion selectivity, *Proc. Natl. Acad. Sci. USA 94*, 11301-11306.
11. Kochendoerfer, G. G., Salom, D., Lear, J. D., Wilk-Orescan, R., Kent, S. B., and DeGrado, W. F. (1999) Total chemical synthesis of the integral membrane protein influenza A virus M2: role of its C-terminal domain in tetramer assembly., *Biochemistry 38*, 11905-11913.
12. Nguyen, P. A., Soto, C. S., Polishchuk, A., Caputo, G. A., Tatko, C. D., Ma, C., Ohigashi, Y., Pinto, L. H., DeGrado, W. F., and Howard, K. P. (2008) pH-induced conformational change of the influenza M2 protein C-terminal domain, *Biochemistry 47*, 9934-9936.
13. Cady, S. D., and Hong, M. (2008) Amantadine-Induced Conformational and Dynamical Changes of the Influenza M2 Transmembrane Proton Channel, *Proc. Natl. Acad. Sci. U.S.A 105*, 1483-1488.

14. Schnell, J. R., and Chou, J. J. (2008) Structure and mechanism of the M2 proton channel of influenza A virus, *Nature 451*, 591-595.
15. Stouffer, A. L., Acharya, R., Salom, D., Levine, A. S., Di Costanzo, L., Soto, C. S., Tereshko, V., Nanda, V., Stayrook, S., and DeGrado, W. F. (2008) Structural basis for the function and inhibition of an influenza virus proton channel, *Nature 451*, 596-599.
16. Miller, C. (2008) Ion channels: coughing up flu's proton channels, *Nature 451*, 532-533.
17. Chou, J. J., Kaufman, J. D., Stahl, S. J., Wingfield, P. T., and Bax, A. (2002) Micelle-induced curvature in a water-insoluble HIV-1 Env peptide revealed by NMR dipolar coupling measurement in stretched polyacrylamide gel., *J. Am. Chem. Soc. 124*, 2450-2451.
18. Hu, J., Asbury, T., Achuthan, S., Li, C., Bertram, R., Quine, J. R., Riqiang, F., and Cross, T. A. (2007) Backbone Stucture of the Amantadine-Block Trans-Membrane Domain M2 Proton Channel from Influenza A Virus, *Biophys. J. 92*, 4335-4343.
19. Wang, J., Kim, S., Kovacs, F., and Cross, T. A. (2001) Structure of the transmembrane region of the M2 protein H(+) channel, *Protein Sci. 10*, 2241-2250.
20. Cady, S. D., Goodman, C., Tatko, C. D., DeGrado, W. F., and Hong, M. (2007) Determining the orientation of uniaxially rotating membrane proteins using unoriented samples: a 2H, 13C, AND 15N solid-state NMR investigation of the dynamics and orientation of a transmembrane helical bundle, *J. Am. Chem. Soc. 129*, 5719-5729.
21. Cady, S. D., and Hong, M. (2008) Simultaneous extraction of multiple orientational constraints of membrane proteins by 13C-detected N-H dipolar couplings under magic angle spinning, *J. Magn. Reson. 191*, 219-225.
22. Luo, W., and Hong, M. (2006) Determination of the oligomeric number and intermolecular distances of membrane protein assemblies by anisotropic (1)h-driven spin diffusion NMR spectroscopy, *J. Am. Chem. Soc. 128*, 7242-7251.
23. Luo, W., Mani, R., and Hong, M. (2007) Sidechain conformation and gating of the M2 transmembrane peptide proton channel of influenza A virus from solid-state NMR, *J. Phys. Chem. 111*, 10825-10832.
24. Sansom, M. S., and Kerr, I. D. (1993) Influenza virus M2 protein: a molecular modelling study of the ion channel, *Protein Eng. 6*, 65-74.

25. Duff, K. C., Gilchrist, P. J., Saxena, A. M., and Bradshaw, J. P. (1994) Neutron diffraction reveals the site of amantadine blockade in the influenza A M2 ion channel, *Virology 202*, 287-293.
26. Cornilescu, G., Delaglio, F., and Bax, A. (1999) Protein backbone angle restraints from searching a database for chemical shift and sequence homology, *J. Biomol. NMR 13*, 289-302.
27. deDios, A. C., and Oldfield, E. (1994) Chemical shifts of carbonyl carbons in peptides and proteins., *J. Am. Chem. Soc. 116*, 11485-11488.
28. Wang, J., Schnell, J. R., and Chou, J. J. (2004) Amantadine partition and localization in phospholipid membrane: a solution NMR study, *Biochem. Biophys. Res. Commun. 324*, 212-217.
29. Li, C., Yi, M., Hu, J., Zhou, H. X., and Cross, T. A. (2008) Solid-state NMR and MD simulations of the antiviral drug amantadine solubilized in DMPC bilayers, *Biophys. J. 94*, 1295-1302.
30. Subczynski, W. K., Wojas, J., Pezeshk, V., and Pezeshk, A. (1998) Partitioning and localization of spin-labeled amantadine in lipid bilayers: an EPR study, *J. Pharm. Sci. 87*, 1249-1254.
31. Li, C., Qin, H., Gao, F. P., and Cross, T. A. (2007) Solid-state NMR characterization of conformational plasticity within the transmembrane domain of the influenza A M2 proton channel, *Biochim. Biophys. Acta 1768*, 3162-3170.
32. O'Neil, K. T., and DeGrado, W. F. (1990) A thermodynamic scale for the helix-forming tendencies of the commonly occurring amino acids, *Science 250*, 646-651.
33. Javadpour, M. M., Eilers, M., Groesbeek, M., and Smith, S. O. (1999) Helix packing in polytopic membrane proteins: role of glycine in transmembrane helix association, *Biophys. J. 77*, 1609-1618.
34. Howard, K. P., Lear, J. D., and DeGrado, W. F. (2002) Sequence determinants of the energetics of folding of a transmembrane four-helix-bundle protein., *Proc. Natl. Acad. Sci. USA 99*, 8568-8572.

35. Buffy, J. J., Waring, A. J., and Hong, M. (2005) Determination of Peptide Oligomerization in Lipid Membranes with Magic-Angle Spinning Spin Diffusion NMR, *J. Am. Chem. Soc. 127*, 4477-4483.
36. Harris, N. L., Presnell, S. R., and Cohen, F. E. (1994) Four helix bundle diversity in globular proteins, *J. Mol. Biol. 236*, 1356-1368.
37. Duong-Ly, K. C., Nanda, V., DeGrado, W. F., and Howard, K. P. (2005) The conformation of the pore region of the M2 proton channel depends on lipid bilayer environment, *Protein Sci. 14*, 856-861.
38. Neal, S., Nip, A. M., Zhang, H., and Wishart, D. S. (2003) Rapid and accurate calculation of protein 1H, 13C and 15N chemical shifts, *J. Biomol. NMR 26*, 215-240.
39. Le, H., and Oldfield, E. (1994) Correlation between 15N NMR chemical shifts in proteins and secondary structure, *J. Biomol. NMR 4*, 341-348.
40. deDios, A. C., Pearson, J. G., and Oldfield, E. (1993) Secondary and tertiary structural effects on protein NMR chemical shifts: an ab initio approach, *Science 260*, 1491-1496.
41. Zhang, H., Neal, S., and Wishart, D. S. (2003) RefDB: A database of uniformly referenced protein chemical shifts, *J. Biomol. NMR 25*, 173-195.
42. Jing, X., Ma, C., Ohigashi, Y., Oliveira, F. A., Jardetzky, T. S., Pinto, L. H., and Lamb, R. A. (2008) Functional studies indicate amantadine binds to the pore of the influenza A virus M2 proton-selective ion channel, *Proc. Natl. Acad. Sci. USA 105*, 10967-10972.
43. Lovell, S. C., Word, J. M., Richardson, J. S., and Richardson, D. C. (2000) The penultimate rotamer library, *Proteins: Struct., Funct., Genet. 40*.
44. Carpino, L. A., and Han, G. Y. (1972) 9-Fluorenylmethoxycarbonyl Amino-Protecting Group *J. Org. Chem. 37*, 3404-3409.
45. Ito, T., Gorman, O. T., Kawaoka, Y., Bean, W. J., and Webster, R. G. (1991) Evolutionary analysis of the influenza A virus M gene with comparison of the M1 and M2 proteins., *J Virol. 65*, 5491-5498.
46. Traikia, M., Warschawski, D. E., Recouvreur, M., Cartaud, J., and Devaux, P. F. (2000) Formation of unilamellar vesicles by repetitive freeze-thaw cycles: characterization by electron microscopy and 31P-nuclear magnetic resonance, *Eur. Biophys. J. 29*, 184-195.

47. Bennett, A. E., Rienstra, C. M., Auger, M., Lakshmi, K. V., and Griffin, R. G. (1995) Heteronuclear decoupling in rotating solids., *J. Chem. Phys. 103*, 6951-6958.
48. Fung, B. M., Khitrin, A. K., and Ermolaev, K. (2000) An improved broadband decoupling sequence for liquid crystals and solids, *J. Magn. Reson. 142*, 97-101.
49. Hohwy, M., Rienstra, C. M., Jaroniec, C. P., and Griffin, R. G. (1999) Fivefold symmetric homonuclear dipolar recoupling in rotating solids: application to double-quantum spectroscopy., *J. Chem. Phys. 110*, 7983-7992.
50. Takegoshi, K., Nakamura, S., and Terao, T. (2001) C-13-H-1 dipolar-assisted rotational resonance in magic-angle spinning NMR, *Chem. Phys. Lett. 344*, 631-637.
51. Bax, A., Freeman, R., and Kempsell, S. P. (1980) Natural-abundance 13C-13C coupling observed via double-quantum coherence, *J. Am. Chem. Soc. 102*, 4849-4851.
52. Hong, M. (1999) Solid-state dipolar INADEQUATE NMR spectroscopy with a large double-quantum spectral width, *J. Magn. Reson. 136*, 86-91.
53. Gullion, T., and Schaefer, J. (1989) Rotational echo double resonance NMR, *J. Magn. Reson. 81*, 196-200.
54. Hong, M., and Griffin, R. G. (1998) Resonance Assignment for Solid Peptides by Dipolar-Mediated 13C/15N Correlation Solid-State NMR, *J. Am. Chem. Soc. 120*, 7113-7114.
55. Mao, J. D., and Schmidt-Rohr, K. (2005) Methylene spectral editing in solid-state C-13 NMR by three-spin coherence selection, *J. Magn. Reson. 176*, 1-6.
56. Rhim, W.-K., Elleman, D. D., and Vaughan, R. W. (1973) Analysis of multiple-pulse NMR in solids., *J. Chem. Phys. 59*, 3740-3749.

Supporting Information

Table 6.S1. TALOS predicted (ϕ, ψ) angles (degrees) and their uncertainties for apo-M2TMP and amantadine-bound M2TMP (amt2 form). ^{13}C and ^{15}N chemical shifts measured under MAS on membrane-bound M2TMP were used as inputs.

Residues	Apo (ϕ, ψ)	Apo (Δϕ, Δψ)	Amt2 (ϕ, ψ)	Amt2 (Δϕ, Δψ)
L26	(-64.5, -39.1)	(8.1, 12)	(-64.7, -39.3)	(8.3, 14)
V27	(-62.7, -45.0)	(6.6, 6.0)	(-64.9, -39.1)	(5.2, 10)
V28	(-63.4, -44.9)	(4.8, 2.6)	(-65.3, -42.8)	(6.1, 6.4)
A29	(-59.9, -39.3)	(2.1, 5.9)	(-60.7, -38.3)	(2.5, 6.5)
A30	(-65.2, -38.7)	(5.2, 7.0)	(-68.8, -36.0)	(6.1, 9.4)
S31	(-62.9, -40.6)	(4.0, 11)	(-65.5, -40.3)	(11, 6.6)
I32	(-61.9, -41.8)	(8.5, 4.8)	(-61.3, -42.3)	(5.8, 7.9)
I33	(-63.0, -42.7)	(3.3, 7.1)	(-62.3, -45.3)	(5.0, 6.0)
G34	(-61.4, -39.3)	(5.3, 5.5)	(-59.3, -40.1)	(5.6, 7.0)
I35	(-64.9, -37.3)	(4.3, 6.2)	(-67.3, -43.5)	(3.2, 9.5)
L36	(-62.0, -41.1)	(4.4, 3.9)	(-63.1, -40.2)	(5.0, 4.3)
H37	(-63.0, -40.8)	(3.6, 5.1)	(-62.4, -40.4)	(3.4, 5.6)
L38	(-67.2, -39.4)	(7.9, 7.9)	(-67.1, -36.5)	(7.9, 11)
RMS error		(5.0°, 6.2°)		(5.8°, 7.4°)

The TALOS (ϕ, ψ) uncertainties are larger than the torsion angle differences between the apo and amantadine-bound M2TMP, which are (1.8°, 2.8°) for (ϕ, ψ). This does not mean, however, that the structural difference between apo and amantadine-bound M2 is insignificant, since TALOS is based on the empirical correlation between database chemical shifts and protein structures, and thus has limited ability to distinguish torsion angles of perturbed protein states due to small-molecule binding.

Table 6.S2: RMS deviations (ppm) between SHIFTX-predicted chemical shifts for eleven residues of M2TMP and measured chemical shifts on bilayer samples by MAS NMR. The database standard RMS errors of SHIFTX prediction are given for comparison.

Sites	X-ray (3C9J)	Solution NMR (2RLF)	Oriented NMR (2H95)	Standard RMS error
N, apo	2.73	2.48	2.08	2.43
N, amt	4.56	4.04	3.78	
CO, apo	1.10	1.18	2.33	1.16
CO, amt	1.34	1.37	2.52	
CA, apo	0.87	0.79	1.01	0.98
CA, amt	0.97	0.80	1.13	
CB, apo	0.85	1.03	1.34	1.10
CB, amt	0.99	1.10	1.38	

Chapter 7

Accurate Measurement of Methyl ^{13}C Chemical Shifts by Solid-State NMR for the Determination of Protein Sidechain Conformation: the Influenza A M2 Transmembrane Peptide as an Example

A paper published in the Journal of the American Chemical Society

2009, vol. 131 pp. 7806-7816

Mei Hong, Tatiana V. Mishanina and Sarah D. Cady

Abstract

The use of sidechain methyl ^{13}C chemical shifts for the determination of the rotameric conformation of Val and Leu residues in proteins by solid-state NMR spectroscopy is described. Examination of the solution NMR stereospecifically assigned methyl groups shows significant correlation between the difference in the two methyl carbons' chemical shifts and the sidechain conformation. It is found that α-helical and β-sheet backbones cause different sidechain methyl chemical shift trends. In α-helical Leu's, a relatively large absolute methyl ^{13}C shift difference of 2.89 ppm is found for the most populated *mt* rotamer (χ_1=-60°, χ_2=180°), while a much smaller value of 0.73 ppm is found for the next populated *tp* rotamer (χ_1=180°, χ_2=60°). For α-helical Val residues, the dominant *t* rotamer (χ_1=180°) has more downfield Cγ2 chemical shifts than Cγ1 by 1.71 ppm, while the next populated *m* rotamer (χ_1=-60°) shows the opposite trend of more downfield Cγ1 chemical shift by 1.23 ppm. These significantly different methyl ^{13}C chemical shifts exist despite the likelihood of partial rotameric averaging at ambient temperature. We show that these conformation-dependent methyl ^{13}C chemical shifts can be utilized for sidechain structure determination once the methyl ^{13}C resonances are accurately measured by double-quantum (DQ) filtered 2D correlation experiments, most notably the dipolar DQ to single-quantum (SQ) correlation technique. The advantage of the DQ-SQ correlation experiment over simple 2D SQ – SQ correlation experiments is demonstrated on the transmembrane peptide of the influenza A M2

proton channel. The methyl chemical shifts led to predictions of the sidechain rotameric states for several Val and Leu residues in this tetrameric helical bundle. The predicted Val rotamers were further verified by dipolar correlation experiments that directly measure the χ_1 torsion angles. It was found that the chemical-shift predicted sidechain conformations are fully consistent with the direct torsion angle results; moreover, the methyl ^{13}C chemical shifts are sensitive to ~5° changes in the χ_1 torsion angle due to drug binding.

Introduction

Recent advances in extensive ^{13}C and ^{15}N labeling, multidimensional correlation methods, and improved sample preparation protocols that produce well ordered solid proteins, have enabled atomic-level three-dimensional structure determination of proteins by solid-state NMR (*1-5*). Despite the tremendous progress, most studies have so far focused on the backbone conformation and fold, with considerably lower resolution structure for the sidechains (*6*). Sidechains are important for enzyme active site chemistry and interaction with small molecules. For ion channels in lipid membranes, the positions of sidechains, as manifested by their (χ_1, χ_2) angles, have important implications for ion conduction and transport. In principle, two NMR approaches are available for determining the protein sidechain conformation. The first measures the torsion angles by correlating the dipolar couplings along the two bonds sandwiching the torsional bond of interest. For the χ_1 angle, a natural choice is to correlate the Cα-Hα and Cβ-Hβ dipolar couplings (*7, 8*). However, the dipolar-correlation based torsion angle experiments work best for β-branched residues (Val, Ile, Thr) with a single Hβ proton (*9*). For long-chain amino acids where methylene groups dominate, the torsion angle results are less easy to interpret, thus sidechain torsion angles farther away from the backbone are harder to measure. The second approach is to measure distances between sidechain carbons and backbone atoms such as the amide nitrogen (*10*). However, these experiments have limited sensitivity due to the need for long transverse mixing times, and as a result have been demonstrated only on well ordered microcrystalline proteins with long T_2 relaxation times.

In principle, the chemical shifts of sidechain carbons should reflect the sidechain torsion angles χ_1, χ_2 and so on, analogous to the influence of (ϕ, ψ) torsion angles on backbone ^{13}C chemical shifts (*11, 12*). Since chemical shifts are much easier to measure than torsion angles and distances, there is a considerable incentive to determine whether a correlation exists between the sidechain ^{13}C chemical shifts and the rotameric conformation. Indeed, chemical shielding computation indicated that the χ_1 torsion angle affects the Cγ shielding of Val (*13*): the χ_1 =180° conformation has a more shielded (upfield) Cγ1 than Cγ2 while the χ_1=-60° conformation has a more deshielded (downfield) Cγ1 resonance. A more recent computation study found the Ile Cγ1 and Cγ2 chemical shift anisotropies are sensitive to both (χ_1, χ_2) angles (*14*). Very recently, an analysis of sidechain ^{13}C chemical shifts of nine amino acids in five proteins showed a correlation between upfield shifts of the Cγ resonances and *gauche* conformations of the γ-substituents (*15*). Overall, however, efforts to predict and exploit the conformational dependence of sidechain ^{13}C chemical shifts have been quite limited, mainly due to the concern that rotameric averaging may be too extensive for clear chemical shift differences to remain at ambient temperature. The second concern is aromatic ring current effects (*16, 17*), which can affect the sidechain chemical shifts significantly. Third, for double-methyl residues Val, Leu, and Ile, stereospecific assignment of the two methyl carbons is highly desirable if not absolutely necessary to establish a clear correlation between conformation and methyl chemical shifts.

Stereospecific assignment of the two methyl ^{13}C chemical shifts of Val and Leu has been possible by solution NMR for a number of years. One approach uses fractional ^{13}C labeling to create different labeling levels of the two methyl carbons due to their different stereoselective biosynthetic pathways (*18*). A second approach measures three-bond J-couplings $^{3}J_{C\gamma N}$ and $^{3}J_{C\gamma C'}$ to give stereospecific assignment of Val residues once the Karplus equations are accurately parameterized (*19-22*). With these methods, an increasing database of proteins with known conformation and known methyl ^{13}C chemical shifts has become available. More recently, analyses of sidechain C-H residual dipolar couplings (RDCs) in partially aligned media have allowed more precise determination of rotameric populations in proteins (*23, 24*). These scalar and dipolar coupling measurements showed

that many Val, Leu and Ile residues in globular proteins in solution adopt a single rotameric state with only small fluctuations around the mean, while those that show conformational equilibria between different canonical rotamers often retain one dominant (greater than ~75%) conformation.

The 2D ^{1}H-driven ^{13}C spin diffusion experiment, due to its simplicity and robustness, has become the standard method of choice for ^{13}C-based assignment of solid proteins. For well ordered proteins with narrow linewidths, these 2D spin-diffusion based correlation spectra, a variant of which is called DARR (*25*), contain surprisingly high levels of information and allow many spin systems to be resolved and assigned. However, the DARR experiment is less useful for membrane peptides and proteins, since the high natural abundance signals of the lipids tend to obscure cross peaks near the diagonal. Moreover, membrane proteins usually have broader lines than microcrystalline proteins or fibrous proteins due to conformational and dynamic disorder induced by the lipids. While alternative MAS techniques for 2D homonuclear correlation spectroscopy have been available, direct comparisons among these techniques have not been made, especially for sidechain resonance assignment of membrane proteins. Here, we compare the 2D DARR experiment with two double-quantum-filtered (DQF) ^{13}C-^{13}C correlation experiments that are equivalent to the solution NMR DQF-COSY experiment (*26*) and the INADEQUATE experiment (*27, 28*), for the purpose of accurately measuring methyl ^{13}C chemical shifts to determine protein sidechain conformations.

We use the influenza A M2 transmembrane peptide (M2TMP) to demonstrate the accurate measurement of methyl ^{13}C chemical shifts and to verify the correlation between these shifts and the sidechain conformation of Val. The M2 protein of influenza A virus forms a proton channel in the virus envelope that is essential for viral replication (*29*). Opening of the channel acidifies the viral core, which triggers the release of the viral ribonucleoprotein complex into the host cell (*30*). A number of high-resolution structural studies have been carried out on the transmembrane domain of the M2 protein, using X-ray crystallography (*31*), solution NMR (*32*), oriented solid-state NMR (SSNMR) (*33, 34*) and magic-angle spinning SSNMR (*35, 36*). Thus, a relatively large amount of structural information is available. Using the methyl ^{13}C chemical shifts, we predict the dominant

rotameric states of five Val and Leu residues in M2TMP when bound to the lipid bilayer, and compare them with the PDB structures obtained from other methods.

Materials and Methods

M2TMP membrane sample preparation

The M2 transmembrane peptide of the Udorn strain of influenza A virus was synthesized by PrimmBiotech (Cambridge, MA) and purified to >95% purity. The amino acid sequence is SSDPL VVAASII GILHLIL WILDRL. Two peptide samples with different sets of uniformly ^{13}C, ^{15}N-labeled residues were used in this study. The first sample contains ^{13}C, ^{15}N-labeled residues at V28, S31 and L36 (VSL-M2TMP). The second sample contains ^{13}C, ^{15}N-labels at V27, A30, I33 and L38 (VAIL-M2TMP). The peptide was reconstituted into DLPC lipid vesicles by detergent dialysis as described before (*36, 37*) with a peptide/lipid molar ratio of 1:15. A pH 7.5 phosphate buffer was used for the membrane sample preparation, thus the peptide studied here corresponds to the closed state of the proton channel. Both apo and amantadine-bound M2TMP were used. For the latter, amantadine was incorporated into the membrane by using buffer solutions containing 10 mM amantadine.

Solid-state NMR experiments

SSNMR experiments were carried out on a Bruker AVANCE-600 (14.1 Tesla) spectrometer and a DSX-400 (9.4 Tesla) spectrometer (Karlsruhe, Germany). 4 mm triple-resonance MAS probes were used and samples were spun between 5 kHz and 7 kHz. Typical rf pulse lengths were 5 μs for ^{13}C and 3.5-4.0 μs for ^{1}H. ^{1}H TPPM (*38*) or SPINAL (*39*) decoupling fields of 60–70 kHz were applied. ^{13}C chemical shifts were referenced to the α-Gly C' signal at 176.49 ppm on the TMS scale.

Three 2D ^{13}C-^{13}C correlation experiments were used to measure and assign the methyl ^{13}C chemical shifts in M2TMP. The 2D DARR spin diffusion experiment was carried out with a 10 ms mixing period (*25*) under 5.333 kHz MAS. The double-quantum (DQ) filtered SQ-SQ experiment was carried out under 7 kHz MAS. The 2D dipolar-mediated

INADEQUATE-type experiment (*27, 28*) was carried out under 7 kHz MAS. For the latter two experiments, ^{13}C-^{13}C dipolar recoupling was achieved using the SPC5 sequence (*40*). All spectra were measured at 243 K where the peptide motion is frozen.

Statistical analysis of methyl chemical shifts and sidechain rotameric conformation

To identify any potential correlation between the methyl ^{13}C chemical shifts and sidechain conformation of Val and Leu, we searched the Biological Magnetic Resonance Data Bank (BMRB) and first-hand literature reports for stereospecifically assigned methyl ^{13}C chemical shifts. Most residues (62 out of 73) in α-helices were stereospecifically assigned, with an ambiguity value of 1 in the BMRB. The exceptions are two residues from Dcp2, where no ambiguity value was given, five residues from chicken cytochrome c, and two residues each from cofilin and fasciclin, which were assigned an ambiguity value of 2 (Table 7.2). The chemical shifts of these non-stereoassigned methyl groups fall within the general trend of each class, and therefore were included in the analysis. The structures of proteins with available methyl chemical shifts were downloaded from the RCSB Protein Data Bank (PDB) and visualized in Insight II (Accelrys, Inc. San Diego). A total of 19 protein structures were examined, 17 of which were solved by solution NMR and two structures (profilin IIa and yeast cytochrome c) were solved by X-ray crystallography. The sidechain χ_1 and χ_2 angles were measured as N-Cα-Cβ-Cγ1 and Cα-Cβ-Cγ1-Cδ1, respectively, in Insight II.

The Val and Leu methyl ^{13}C chemical shifts were grouped first according to the backbone conformation (helix or sheet), then according to the sidechain rotamer categories. For Val, the main rotamers are *t* (trans, χ_1=180°), *m* (minus, χ_1=-60°), and *p* (plus, χ_1=+60°) (Figure 7.1a) (*41*), using the nomenclature of the Penultimate Rotameric Library (*42*). For Leu, the main rotamers are *mt* (χ_1 = -60°, χ_2=180°), *tp* (χ_1=180°, χ_2=60°), and *tt* (χ_1=χ_2=180°) (Figure 7.1b). Our analysis focuses on the difference between the two methyl ^{13}C chemical shifts, which are not affected by possible inconsistencies in chemical shift calibration and are also less sensitive to ring current effects. The mean methyl chemical shift differences as well as the mean absolute shift differences are computed for each conformational category. The

standard deviation σ of each distribution is calculated as $\sigma = \sqrt{\frac{1}{N-1}\sum_{i=1}^{N}(x_i - \bar{x})^2}$, where x denotes the chemical shift difference. Chemical shift differences that fall beyond 2.6 times the standard deviations from the mean were discarded. This corresponds to a confidence level of 99% that these data points are anomalous or may be due to incorrect assignment. To obtain a measure of the uncertainty of the mean, we also computed the standard deviation of the mean $\sigma_{\bar{x}}$ as $\sigma_{\bar{x}} = \sigma/\sqrt{N}$.

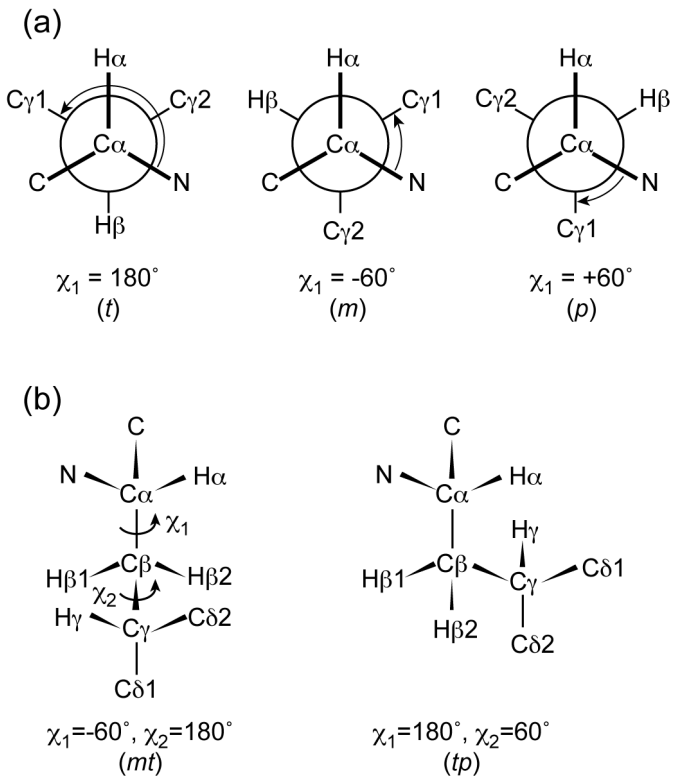

Figure 7.1. Definitions of the rotameric states of Val and Leu. (a) Val *t*, *m*, and *p* states. (b) Leu *mt* and *tp* states.

Results and Discussion

Accurate measurement of the methyl ^{13}C chemical shifts

We first compare the relative merits of three 2D ^{13}C-^{13}C correlation experiments for accurate measurement of the methyl ^{13}C chemical shifts. The first experiment correlates SQ and SQ coherences and establishes the coherence transfer by ^{13}C spin diffusion. This DARR experiment (*25*) is the solid-state analog of the solution NMR NOESY experiment. The second experiment correlates SQ coherences after passing them through a DQ filter, so that only ^{13}C sites involved in coupled spin networks are detected. This DQ-filtered SQ-SQ experiment is the solid-state analog of the DQF-COSY experiment. The third experiment correlates the dipolar-generated DQ coherence with SQ coherence, thus is analogous to the INADEQUATE experiment (*28*). While all three solid-state MAS experiments are well known, for clarity and comparison we show their pulse sequences in Figure 7.2. The DQ excitation and reconversion periods are executed back-to-back between the evolution and detection periods of the DQ filtered SQ-SQ experiment, but are separated by the evolution period in the dipolar-INADEQUATE (DQ-SQ correlation) experiment. The ^{13}C-^{13}C dipolar couplings for exciting the DQ coherences were recoupled with the SPC5 sequence (*40*), one of many recoupling sequences available (*43, 44*).

Figure 7.3 shows the three 2D correlation spectra of V28, S31, and L36-labeled M2TMP in DLPC bilayers at 243 K. The spin system connectivities are indicated in each spectrum. In the 2D DARR spectrum (a), the main resolved lipid signals along the diagonal are indicated with asterisks. It can be seen that while the Cα/Cβ cross peaks of the peptide are well resolved in the spectrum, the sidechain cross peaks, especially those involving methyl groups, cluster near and overlap significantly with the diagonal. They include the L36 Cδ signal at 20.9 ppm and the V28 Cγ signal near 19.5 ppm (d). The homogeneous linewidths of the membrane sample at this temperature are actually relatively narrow, as seen by the width of the narrow part of the diagonal ridge. Thus, the broad bulges along the diagonal indicate cross peaks that are poorly resolved from the diagonal. In particular, the Ser Cα and Cβ chemical shifts are known to be similar in α-helices (*45*), thus the broad diagonal peak around 61 ppm is due to the diagonal Cα and Cβ peaks overlapping with the true

Cα/Cβ cross peaks (g). Moreover, in the 60-70 ppm region where the Ser signals resonate, there are various lipid signals such as the headgroup Cα (59.7 ppm), the glycerol G1 (63.2 ppm) and G3 (63.9 ppm).

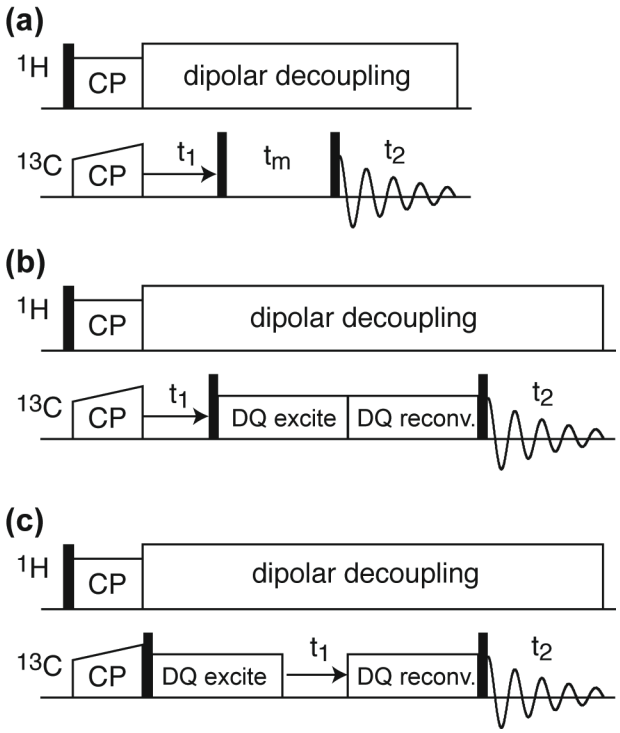

Figure 7.2. Pulse sequences for 2D ^{13}C-^{13}C correlation spectroscopy. (a) SQ-SQ correlation by DARR mixing. (b) DQ filtered SQ-SQ correlation. (c) DQ-SQ correlation. The DQ excitation and reconversion are achieved by the SPC5 recoupling scheme (*40*).

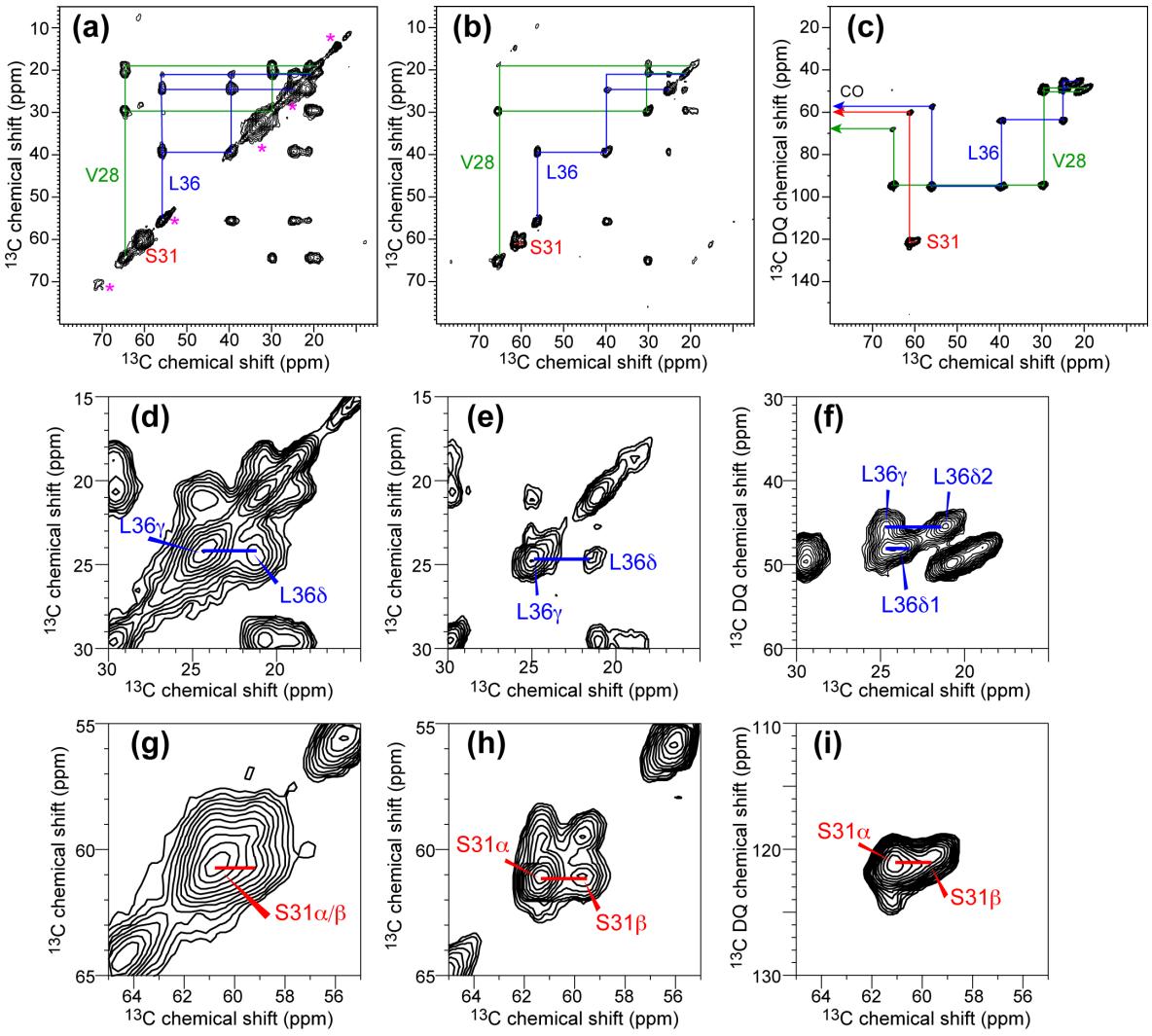

Figure 7.3. 2D ^{13}C-^{13}C correlation spectra of amantadine-complexed VSL-M2TMP in DLPC bilayers at 243 K. (a) 2D DARR spectrum with a 10 ms mixing time. (b) 2D DQ filtered SQ-SQ correlation spectrum. (c) 2D DQ-SQ correlation spectrum. Two spectral regions are selected from each 2D spectrum and amplified in (d-i). Middle row (d-f): L36 methyl ^{13}C region. Bottom row (g-i): S31 Cα and Cβ region.

The 2D DQ filtered SQ-SQ correlation experiment considerably simplifies the spectrum by removing all lipid natural abundance ^{13}C signals along the diagonal (Figure 7.3b). The Leu and Val methyl regions now show well resolved peaks, as seen in Figure 7.3e. The L36 Cγ signal at 24.9 ppm is well separated from one of the Cδ peaks at 21.3 ppm.

However, the second Leu methyl Cδ peak remains ambiguous. Based on the chemical shift databases, the second Leu methyl carbon may resonate close to the Cγ peak and thus may not be resolved from the diagonal. For the Ser Cα/Cβ cross peaks (Figure 7.3h), the DQ filtered SQ-SQ correlation spectrum shows a distinct cloverleaf pattern, which gives a relatively clear Cα-Cβ chemical shift separation of 1.7 ppm. Further verification that the upfield peak is Cβ while the downfield peak is Cα can be made by a CH_2-filter experiment that suppresses all CH signals (thus Cα) while retaining all CH_2 signals (thus Cβ) (*36*).

The remaining ambiguity of the methyl ^{13}C chemical shifts is removed by the dipolar-INADEQUATE experiment. Figure 7.3c shows the DQ-SQ correlation spectrum and the expanded Leu methyl region is shown in Figure 7.3f. Now two Leu Cγ-Cδ correlation slices can be observed, with the upfield Cδ2 peak appearing in the 45.6 ppm DQ slice while the downfield Cδ1 peak appearing in the 48.3 ppm DQ slice. The latter is close to the Cγ peak near the slope-2 diagonal of the spectrum. Importantly, since there are no un-partnered diagonal peaks in the DQ-SQ correlation spectra, two coupled resonances that have nearly identical chemical shifts simply resonate near the slope-2 line of the spectrum and can be assigned unambiguously. In the case of VSL-M2TMP, since the L36 Cγ resonance is clearly resolved in the 45.6 ppm DQ slice to be 24.7 ppm, its partner Cδ1 peak can be readily read off in the 48.3 ppm DQ slice as the difference between 48.3 ppm and 24.7 ppm, which is 23.6 ppm. Thus, the Cδ1 peak is only 1.1 ppm from the Cγ peak, which explains the difficulty of resolving the two peaks in the SQ-SQ correlation spectra (Figure 7.3a, 7.3b).

Figure 7.4 shows the three 2D spectra of VAIL-M2TMP in gel-phase DLPC bilayers. This sample contains three double-methyl residues (V27, I33, and L38), thus making their chemical shift identification difficult in the DARR spectrum. Specifically, the Val Cβ and Ile Cγ1 chemical shifts are very similar near 30 ppm, thus the Ile Cβ/Cγ1 cross peak (35.6 ppm, 28.4 ppm) is partly obscured by the Val Cβ peak and the lipid CH_2 diagonal peak (Figure 7.4d). Further, unless very long t_1 evolution times are used, the lipid CH_2 signal is often truncated, giving rise to truncation wiggles in the ω_1 dimension that interfere with the precise measurement of near-diagonal cross peaks. The long t_1 evolution times necessary for obtaining sharp lipid diagonal signals are usually excessive for the peptide signals, causing

sub-optimal use of the experimental time. The I33 Cγ1 signal at 28.4 ppm is also low and broad, which we attribute to the special spin dynamics of the Ile spin system. The two methyl groups of Ile have unequal distances from the backbone: the Cγ2 methyl group neighbors Cβ while the Cδ methyl neighbors Cγ1. The magnetization of Cγ1 between the two methyl groups appears to be disproportionally drawn to both methyl carbons, causing its low intensity in the 2D spectrum.

The DQ filtered SQ-SQ correlation spectrum (Figure 7.4b, e) shows significantly simplified Ile Cβ/Cγ1 region: the cross peak, while still weak, can now be resolved from the diagonal since the lipid CH_2 peak is suppressed. However, the strong Val Cβ diagonal signal still remains. The DQ-SQ correlation spectrum (Figure 7.4c, f) gives the highest resolution for the Ile spin system. The two Cβ/Cγ1 cross peaks are now of similar intensities and have well defined lineshapes and are well resolved from the Val Cα/Cβ and Cβ/Cγ peaks. In addition, the methyl region of the spectrum is also much better resolved, similar to Figure 7.3.

Figure 7.4(g-i) demonstrates the ability of the dipolar INADEQUATE experiment to clearly identify conformational polymorphism. The L38 Cβ exhibits two chemical shifts that are 2.4 ppm apart. This is seen in all three 2D spectra, but is most clearly manifested in the dipolar INADEQUATE spectrum, since the presence of the two Cβ shifts is confirmed by the elongated shape of the Cα peak in the DQ dimension.

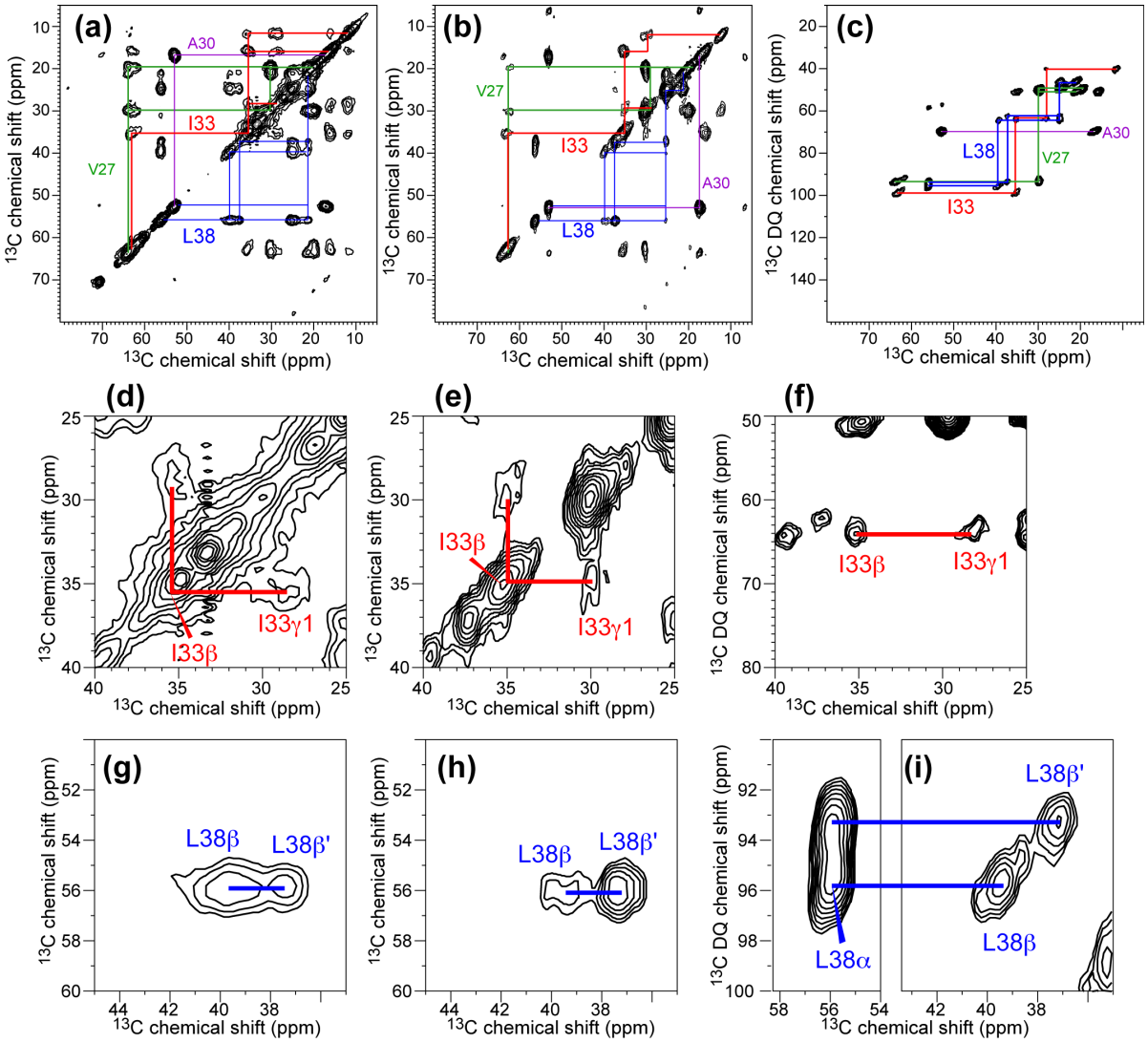

Figure 7.4. 2D ^{13}C-^{13}C correlation spectra of amantadine-complexed VAIL-M2TMP in DLPC bilayers at 243 K. (a) DARR spectrum with a 10 ms mixing time. (b) DQ filtered SQ-SQ correlation spectrum. (c) DQ-SQ correlation spectrum. Two spectral regions are selected from each 2D spectrum in (a-c) and amplified in (d-i). Middle row (d-f) I33 Cβ-Cγ1 region. Bottom row (g-i): L38 Cα-Cβ region. Note the presence of two Cβ peaks.

Methyl chemical shift changes of M2TMP between the apo and amantadine-bound states

The influenza A M2 transmembrane domain (residues 22-46) contains two Val residues (V27, V28), five Ile residues, and six Leu residues. We have labeled both Val residues and three of the Leu residues (L26, L36, and L38). Since the two Ile methyl carbons have chemical shift differences of about 5 ppm, their spectral identification usually does not pose any difficulty, and will not be discussed further.

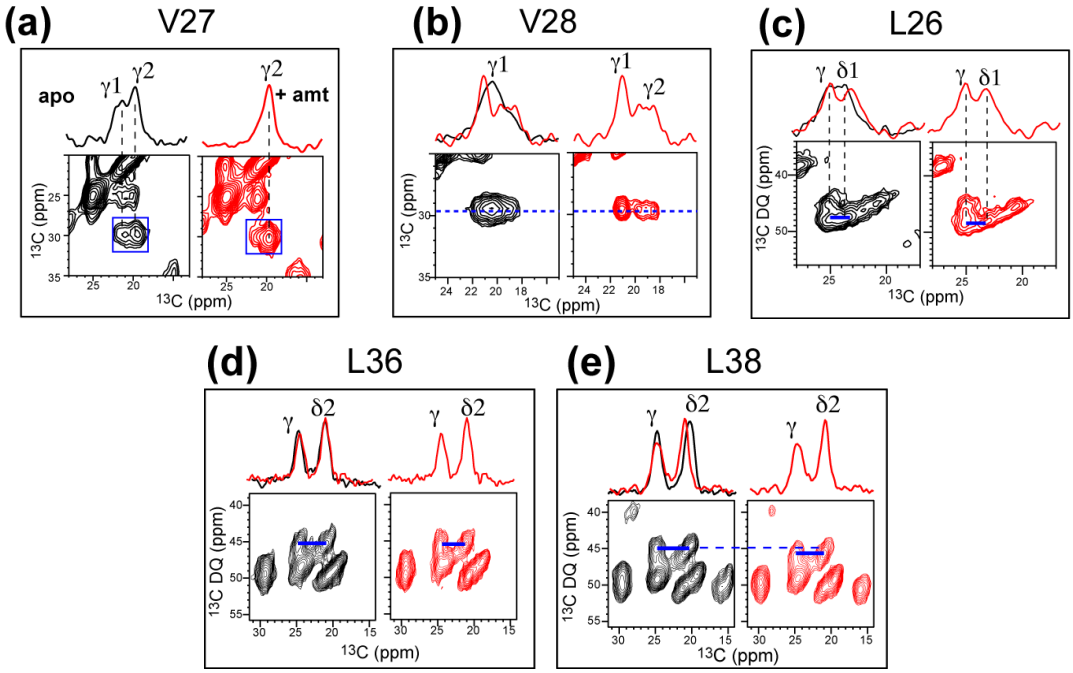

Figure 7.5. Methyl ^{13}C chemical shift changes of labeled Val and Leu residues in M2TMP in the absence (black) and presence (red) of amantadine. (a) V27 Cγ chemical shifts from 2D DARR spectra. (b) V28 Cγ chemical shifts from 2D DARR spectra. (c-e) Leu Cγ and Cδ chemical shifts from 2D DQ-SQ correlation spectra. (c) L26. (d) L36. (e) L38. Except for L36, all other residues show methyl ^{13}C chemical shift perturbations by amantadine.

The binding of the M2 channel inhibitor amantadine has been recently shown to cause noticeable changes in the ^{13}C chemical shifts of various residues (*35*, *36*). Here we focus on the methyl ^{13}C shift changes induced by the drug. Figure 7.5 compares the methyl regions of the five Val and Leu residues between the apo peptide and the amantadine-bound

peptide. The DQ-SQ correlation spectra of Leu residues and the DARR spectra of Val residues are shown, the latter because the Val Cβ/Cγ cross peaks are sufficiently separated from the diagonal. Figure 7.5 shows that four out of five residues show methyl chemical shift perturbations by amantadine. Between the two Val residues, the V27 Cγ1 intensity is weakened by amantadine binding, whereas the V28 Cγ2 intensity is increased by amantadine binding. Among the three Leu residues, L36 exhibited no chemical shift changes, whereas the L26 Cδ1 and L38 Cδ2 frequencies are shifted from their apo values. Since our methyl ^{13}C assignments are not stereospecific, below we will use the absolute values of the methyl ^{13}C chemical shift differences extracted from the protein databases to interpret the conformation of these M2 sidechains.

Table 7.1. Experimental Val and Leu methyl ^{13}C chemical shifts (ppm) [1] in apo and amantadine-bound (amt) M2TMP in DLPC bilayers.

Val		$\delta_{C\gamma 2}$	$\delta_{C\gamma 1}$	$\lvert\delta_{C\gamma 2}-\delta_{C\gamma 1}\rvert$	Rotamer[2]
V27	Apo	21.2	19.3	1.9	*t*
	Amt	20.8	19.5	1.3	*t/m*
	Soln NMR[3]	-	-	1.6	
V28	Apo	20.7	19.5	1.2	*t/m*
	Amt	20.8	19.0	1.8	*t*
	Soln NMR[3]	-	-	1.3	
Leu		$\delta_{C\delta 1}$	$\delta_{C\delta 2}$	$\lvert\delta_{C\delta 1}-\delta_{C\delta 2}\rvert$	Rotamer[2]
L26	Apo	23.8	21.2	2.6	*mt*
	Amt	23.3	20.9	2.4	*mt*
	Soln NMR[3]	-	-	0.7	
L36	Apo	24.2	21.2	3.0	*mt*
	Amt	23.8	21.2	2.6	*mt*
	Soln NMR[3]	-	-	1.5	
L38	Apo	24.2	20.1	4.1	*mt*
	Amt	23.9	21.0	2.9	*mt*
	Soln NMR[3]	-	-	1.0	

[1]. The solid-state NMR ^{13}C chemical shifts were not stereospecifically assigned and were measured at 243 K. The chemical shift are referenced to TMS.

[2]. Predicted rotameric states based on the ^{13}C solid-state NMR chemical shifts.

[3]. Solution NMR methyl ^{13}C shift differences were measured on DHPC-micelle bound M2(18-60) at ambient temperature (*32*).

Table 7.1 lists the methyl ^{13}C chemical shifts of the five Val and Leu residues in the apo and amantadine-bound M2TMP in DLPC bilayers. Overall, amantadine causes 0.5 – 1.2 ppm changes in the methyl ^{13}C chemical shift difference. To interpret these ^{13}C chemical shift changes, we turn to an analysis of the methyl chemical shift trends in protein NMR databases.

Dependence of Val and Leu methyl ^{13}C chemical shifts on protein sidechain conformation

Methyl ^{13}C chemical shifts are sensitive to a number of factors, including the sidechain conformation, which can manifest through γ-gauche effects (*46*), and ring current effects. We hypothesize that when ring current effects are excluded by considering methyl ^{13}C shift *differences* in each residue, the sidechain conformation is the main determining factor for the methyl chemical shifts. Further, we wish to determine whether distinct trends of methyl ^{13}C chemical shifts exist for different sidechain rotamers that are assigned by combinations of NOEs, RDCs, and scalar couplings. The existence of a significant correlation between the methyl chemical shifts and rotameric states would indicate that rotameric averaging, while present, is not too extensive to obliterate sidechain conformational differences. We examined the methyl ^{13}C chemical shifts of 19 proteins in the RCSB Protein Data Bank, 17 of which are solution NMR structures and 2 are X-ray crystal structures. These proteins and their BMRB and PDB accession numbers are listed in Table 7.2. The rotameric states and methyl ^{13}C chemical shifts of the α-helical Val and Leu residues among these 19 proteins are listed in the Supporting Information Tables 7.S1 and 7.S2. It is important to note from the beginning that since the conformational dependence is searched from solution NMR structures, any rotameric averaging necessarily reflects sidechain dynamics in medium to large globular proteins in solution at ambient temperature. The extent of this averaging depends on the percentage of surface-accessible residues. However, our systems of interest are membrane proteins in lipid bilayers at low temperatures, which have very little or no rotameric averaging, thus their methyl chemical shifts would correspond to purer conformational states.

Table 7.2. Proteins that were examined for investigating the conformational dependence of methyl ^{13}C chemical shifts in proteins.

Protein	PDB ID	BMRB ID
Ubiquitin	1d3z	4375
Calmodulin, N-terminus	1f70	4056
Calmodulin, C-terminus	1f71	4056
Cytochrome c, chicken	2frc	1404
GB1	2gb1	7280
Cofilin	1q8g	6004
Profilin I	1pfl	4082
Profilin IIa	2v8c	15452
Fasciclin-like protein	1w7d	6312
Talin C-terminal Domain	2jsw	15411
Dcp2 decapping enzyme	2jvb	7325
M2 (residues 23-60)	2rlf	ref. (*32*)
RNase T_1	1ygw	ref. (*21*)
P22 c2 repressor	1adr	ref. (*18*)
Malate synthase G	2jqx	ref. (*22*)
Cytochrome c, yeast	2ycc	ref. (*14*)
Phosphohistidine phosphatase	2ai6	6625
OmpX	1q9f	ref. (*54*)
Hsc-70	1ckr	ref. (*55*)

The rotameric states of proteins depend on the backbone conformation. α-helical (H) and β-sheet (S) backbones have different populations of sidechain conformations for steric reasons (*42*). Thus, we first sort the methyl ^{13}C chemical shifts by the backbone conformation. Within each backbone category, we binned the methyl ^{13}C chemical shifts according to the canonical χ_1 and χ_2 angles. Since most solution NMR data we considered have stereospecifically assigned Val Cγ1/Cγ2 and Leu Cδ1/Cδ2 chemical shifts, we first analyzed the methyl ^{13}C chemical shift difference with the sign. However, because stereospecific assignment is still not possible by solid-state NMR, we also need to investigate whether the absolute value of the methyl ^{13}C chemical shift difference can serve to distinguish different rotamers. Thus Table 7.3 lists both the sign-sensitive and absolute methyl ^{13}C shift differences of Val and Leu in α-helical and β-sheet secondary structures.

The standard deviations of the distributions are indicated, along with the standard deviations of the mean, which are reported as uncertainties (±) of the mean.

Figure 7.6 plots the α-helical Val Cγ1 and Cγ2 chemical shifts in the *t* and *m* rotamers. The *t* rotamer (χ_1 = 180°) dominates (90%) in α-helical Val's and thus has the largest number of data points. It can be seen that the Cγ2 chemical shift is more downfield (larger) than the Cγ1 shift in most cases, with an average difference of 1.71 ppm and a standard deviation of 0.52 ppm. Only two out of 21 data points in this class have upfield Cγ2 chemical shifts than Cγ1. Because of the dominance of the *t* rotamer in Val and the generally downfield Cγ2 shifts, we calculate the methyl ^{13}C shift difference for Val as $\delta_{C\gamma 2} - \delta_{C\gamma 1}$. When the absolute value of the methyl shift differences are considered, the average difference is 1.67 ppm. This trend agrees qualitatively with the recent finding of London and coworkers based on a smaller sample size of five proteins (*15*).

Table 7.3. Statistics of Val and Leu methyl ^{13}C chemical shift differences from protein databases.

Valine						
Rotamer	Population	No. residues	Mean $\delta_{C\gamma 2} - \delta_{C\gamma 1}$ (ppm)	$\sigma_{\delta_{C\gamma 2} - \delta_{C\gamma 1}}$ (ppm)	Mean $\lvert\delta_{C\gamma 2} - \delta_{C\gamma 1}\rvert$ (ppm)	$\sigma_{\lvert\delta_{C\gamma 2} - \delta_{C\gamma 1}\rvert}$ (ppm)
Helix, *t*	90%	21	1.71 ± 0.12	0.52	1.67 ± 0.11	0.51
Helix, *m*	7%	6	-1.23 ± 0.41	1.00	1.23 ± 0.41	1.00
Sheet, *t*	72%	24	-0.26 ± 0.29	1.41	1.25 ± 0.14	0.65
Sheet, *m*	20%	2	-1.95 ± 0.65	0.92	1.95 ± 0.65	0.92
Sheet, *p*	8%	5	0.28 ± 1.07	2.39	1.76 ± 0.62	1.39
Leucine						
Rotamer	Population	No. residues	Mean $\delta_{C\delta 1} - \delta_{C\delta 2}$ (ppm)	$\sigma_{\delta_{C\delta 1} - \delta_{C\delta 2}}$ (ppm)	Mean $\lvert\delta_{C\delta 1} - \delta_{C\delta 2}\rvert$ (ppm)	$\sigma_{\lvert\delta_{C\delta 1} - \delta_{C\delta 2}\rvert}$ (ppm)
Helix, *mt*	62%	15	2.89 ± 0.25	0.94	2.89 ± 0.25	1.13
Helix, *tp*	30%	15	-0.10 ± 0.24	0.90	0.73 ± 0.13	0.50
Helix, *tt*	1%	11	0.17 ± 0.35	1.15	0.90 ± 0.20	0.67
Sheet, *mt*	46%	11	1.92 ± 0.32	1.01	2.12 ± 0.24	0.75
Sheet, *tp*	36%	9	0.74 ± 0.77	2.30	2.14 ± 0.29	0.87

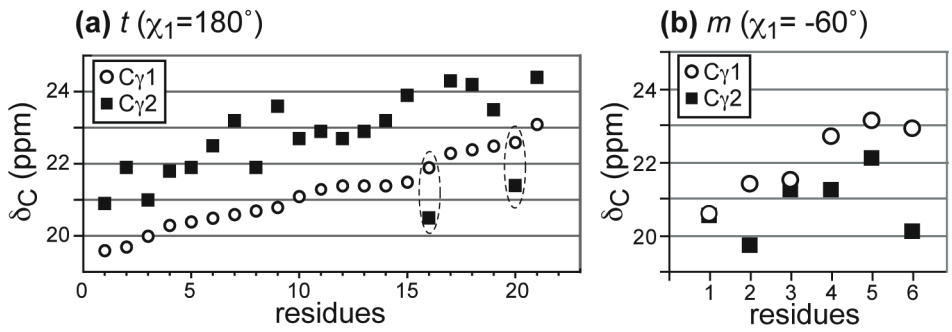

Figure 7.6. α-helical Val Cγ chemical shifts as a function of sidechain conformation from protein databases. (a) The *t* rotamer. (b) The *m* rotamer. Dashed lines in (a) indicate anomalous data points that are excluded in the statistical analysis in Table 7.3.

For the *m* rotamer of helical Val (7% abundant in proteins), the mean absolute Cγ2/Cγ1 shift difference is about 0.5 ppm smaller than the *t* rotamer. More importantly, the sign of the chemical shift difference is reversed, with the Cγ1 chemical shifts now more downfield than Cγ2. Thus, new SSNMR techniques for stereospecific assignment of the Val methyl ^{13}C chemical shifts should be able to distinguish the *t* and *m* rotamers simply based on the relative values of the Cγ1 and Cγ2 shifts. The upfield Cγ2 shift in the *m* rotamer can be well explained by the γ-gauche effect, as the Cγ2 carbon is *gauche* to both the N and C' atoms of the backbone (Figure 7.1a) and experiences steric crowding (*15, 46*). For the *p* rotamer, due to its very low occurrence in proteins (2%) and the small chemical shift sample size (5 points) we found from databases, we do not consider its methyl chemical shift trend further.

Figure 7.7 shows the Cδ1 and Cδ2 chemical shifts of α-helical Leu residues. For the dominant *mt* rotamer (62%), the stereospecifically assigned Cδ1 chemical shifts are uniformly more downfield than Cδ2, with an average difference, $\delta_{C\delta 1} - \delta_{C\delta 2}$, of 2.89 ppm and a standard deviation of 0.94 ppm (Table 7.3). The upfield Cδ2 chemical shift in this rotamer can again be understood by the steric crowding of Cδ2 to Cα through the γ-gauche effect, as visualized in Figure 7.1b. In contrast, the 30% abundant *tp* rotamer has a much

smaller absolute methyl shift difference of 0.73 ppm, and has no clear trend in which methyl carbon has larger chemical shifts. Given the significant difference in the absolute methyl shift differences, these two most populated Leu rotamers can be readily distinguished even without stereospecific assignment.

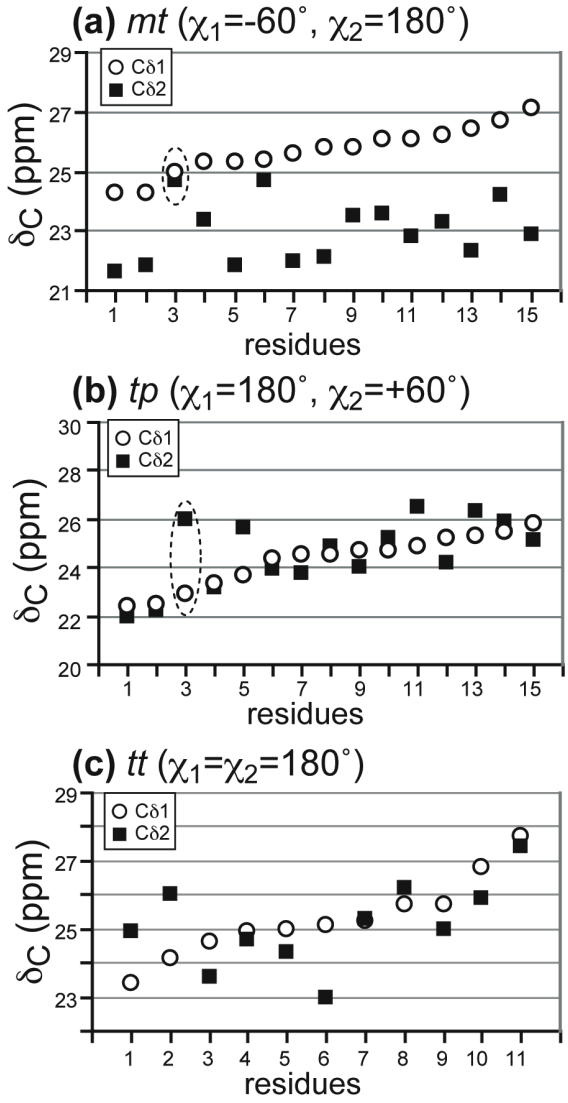

Figure 7.7. α-helical Leu Cδ methyl chemical shifts as a function of sidechain conformation from protein databases. (a) The *mt* rotamer. (b) The *tp* rotamer. (c) The *tt* rotamer. Dashed lines in (a) and (b) indicate anomalous data points that are not included in the statistical calculation in Table 7.3.

For β-sheet backbones, the Val methyl shift differences are larger for the *m* rotamer than the *t* rotamer, contrary to the trend of the helical Val's, although only a small dataset is available for the *m* rotamer. For β-sheet Leu's, the *tp* rotamer has as many positive as negative methyl ^{13}C shift differences, thus is ambiguous to distinguish from the *mt* rotamer.

The recent work of London and coworkers considered the sidechain ^{13}C chemical shifts of not only the three double-methyl residues but also six other residues in five proteins (*15*). The main finding of the paper is that steric crowding by gauche conformations of Cγ substituents causes upfield shifts of the Cγ resonances. The paper reached qualitatively similar conclusions about the methyl ^{13}C shift differences of Val and Leu as the present work. However, many quantitative details differ, mainly due to the fact that the previous work did not distinguish the α-helical and β-sheet backbone conformation, which are found here to give significantly different Cγ and Cδ shift differences. For example, while the Val *t* rotamer has much more upfield Cγ1 shifts than Cγ2 in α-helices (Table 7.3), the average difference is much smaller in β-sheets (–0.26 ppm) due to crossover of the Cγ2 and Cγ1 shifts. Another example is the Leu *tp* rotamer, which shows very different average Cδ shift differences between the helical and sheet conformations (Table 7.3). Thus, mixing of helical and sheet rotamers obscures some chemical shift trends. Expressed in terms of the chemical shift of a certain carbon in different rotamers, we find that the Leu Cδ1 average shift difference between the *tp* and *mt* rotamers in α-helices is $\delta_{C\delta1,tp} - \delta_{C\delta1,mt} = -1.4\ ppm$, but has a much smaller value of –0.1 ppm in β-sheets. This suggests that steric crowding, which causes upfield shifts of the Cδ1 resonance, is stronger in α-helical *tp* rotamers than β-sheet *tp* rotamers. Secondly, the London work analyzed the χ_1 dependence of chemical shifts separately from the χ_2 dependence. For Leu, however, whose *mt* and *tp* rotamers are predominant and few other rotamers are populated, the combined χ_1/χ_2 analysis better reflects the conformational dependence of methyl chemical shifts.

How significant is the effect of rotameric averaging, which occurs more commonly in surface-accessible residues than interior residues in globular proteins, to the statistical methyl chemical shifts obtained here? To a first approximation, the fact that clear distinctions do exist between the methyl ^{13}C shift differences of the Leu and Val rotamers indicates that

sidechain conformational equilibria in globular proteins have sufficiently limited amplitudes or significantly skewed populations. Comparison of crystal structures with solution NMR structures showed that the solution-NMR derived dominant rotamers generally agree well with the crystal structure (*21, 24*). Earlier studies of structural and fibrous proteins such as collagen (*47*), keratin intermediate filaments (*48*), and the coat protein of filamentous bacteriophages (*49*) by ^{2}H SSNMR found that Leu sidechains interconvert rapidly between the *mt* and *tp* rotamers with nearly equal populations. This extensive rotameric averaging was thought to have functional importance, one example being the distribution of mechanical stresses experienced by collagen fibrils in the organic-inorganic nanocomposites of bone. In membrane proteins, Val sidechain dynamics have been examined in bacteriorhodopsin (*50*) and gramicidin (*51*) by ^{2}H SSNMR, with the former showing no χ_1 dynamics at all while the latter showing χ_1 averaging for some of the Val residues but with a dominant rotamer. While the literature of membrane protein sidechain dynamics is still limited, it is reasonable to hypothesize that small membrane peptides would exhibit more extensive sidechain conformational motion than large membrane proteins. Compared to fibrous and membrane proteins, large globular proteins have relatively small surface areas, thus near-equal populations of rapidly interconverting rotamers should be much less common, which explains the current statistical findings. In any case, since the methyl shift trends found here likely correspond to partially averaged conformational states, the true chemical shift differences between pure rotamers will be more pronounced than given here. Therefore, solid-state NMR methyl chemical shifts measured at low temperature, where most χ_1 and χ_2 conformational dynamics are frozen, should show larger chemical shift differences between different rotamers.

Verification of the χ_1 dependence of Val methyl chemical shifts in M2TMP

Based on the above conformational dependence of methyl ^{13}C chemical shifts and the measured M2TMP Val and Leu ^{13}C chemical shifts, we can assign the rotameric states for the five Val and Leu residues. Table 7.1 shows that all three Leu residues should be assigned to the dominant *mt* rotamer, and amantadine binding, while changing the methyl shift

differences by as much as 1.2 ppm, does not change the assignment of the canonical rotamer. The particularly large methyl shift difference of L38 (4.1 ppm) in the apo state of M2TMP likely corresponds to a purer or more ideal *mt* conformation compared to L26 and L36.

For the two Val residues, the apo V27 and amantadine-bound V28 can be readily assigned to the *t* rotamer. On the other hand, the amantadine-bound V27 and the apo V28 have smaller methyl ^{13}C shift differences of about 1.2 ppm that correlate better with the *m* rotamer (Table 7.3). However, because of the relatively small methyl shift difference between the *m* and *t* Val rotamers in the absence of sign information, such an assignment may not be definitive. Thus, we directly measured the χ_1 torsion angle of Val using the HCCH dipolar correlation experiment. This serves to verify the correlation between the methyl ^{13}C chemical shifts and rotameric states of Val. This direct measurement is possible for Val because its Cβ is a branched CH group with a single proton, so that correlation of the orientation-dependent Cα-Hα and Cβ-Hβ dipolar couplings gives the relative orientation of the two C-H bonds, which is the χ_1 angle.

Figure 7.8a shows the pulse sequence of the HCCH experiment, which differs from the original experiment (*7*) in the choice of the DQ dipolar recoupling sequence and in the dipolar doubled nature of the C-H evolution period. We used the narrow-band HORROR recoupling scheme (*52*), where the ^{13}C irradiation field ω_1 is matched to half the spinning frequency ω_r, to selectively recouple the Val Cα and Cβ signals. This eliminates possible contribution of the Val Cγ-Hγ dipolar coupling to the Hα-Cα-Cβ-Hβ dipolar correlation curve. Figure 7.8b shows the first slice of the V28 HCCH 2D spectrum, indicating the clean selection of the Cα and Cβ signals. The dipolar doubling during the t_1 period is achieved by a constant time of one rotor period for homonuclear decoupling combined with moving ^{13}C 180° pulses to define the effective t_1 time (*53*). This dipolar-doubled constant-time HCCH evolution both enhances the angular resolution of the χ_1 technique and removes possible T_2 relaxation effects during t_1.

Panels (c) and (d) display the time evolution of the two Val residues under the dipolar couplings for the apo (black) and amantadine-bound (red) states. The unsymmetrized time domain data shows little intensity asymmetry for the V27 data and only minor asymmetry for

the V28 data, which is due to finite pulse length effects. For V27, the amantadine-bound peptide shows deeper dipolar dephasing than the apo state, indicating a smaller χ_1 angle. Simulations yielded a best-fit χ_1 angle of 164° for the apo peptide and 158° for the complexed peptide. Thus, amantadine binding shifts the χ_1 angle by 6° away from the *trans* conformation. This is consistent with the direction of change predicted by the methyl ^{13}C chemical shifts. For V28, the opposite is observed: the amantadine-bound peptide has shallower dipolar dephasing, giving a χ_1 angle that is 6° larger, or *closer* to the *trans* conformation, compared to the apo peptide.

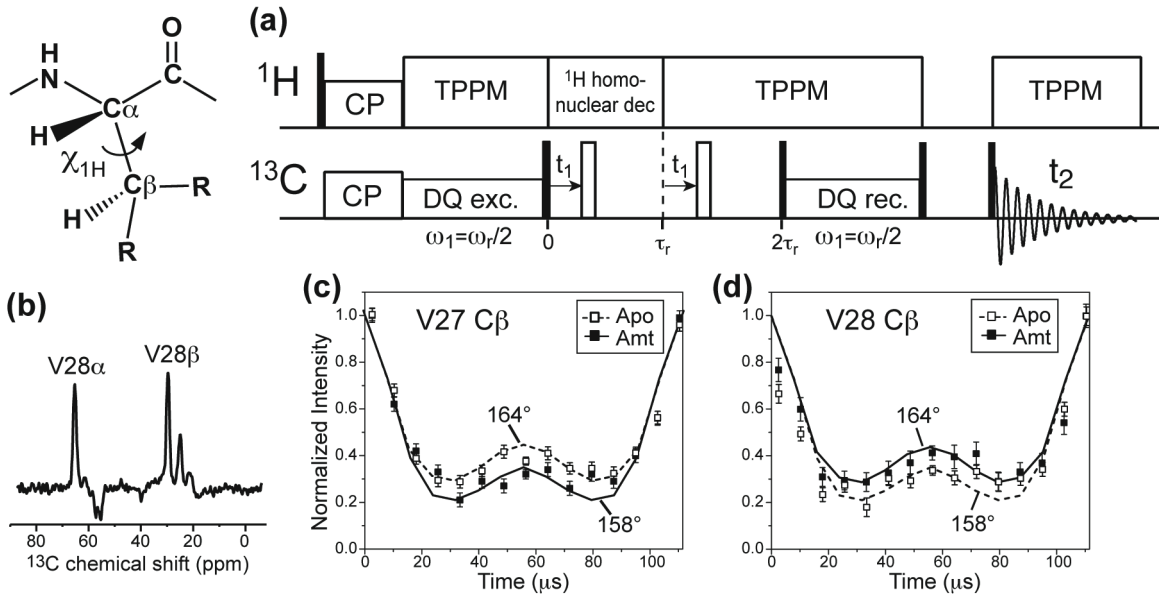

Figure 7.8. Direct measurement of the χ_1 torsion angles of V27 and V28 in M2TMP in the apo (open symbols) and amantadine-bound (filled symbols) states. (a) Double-quantum HCCH pulse sequence for correlating the Hα-Cα bond and Hβ-Cβ bond orientations to give the χ_{1H} angle, which is equal to the χ_1=N-Cα-Cβ-Cγ angle. (b) ^{13}C chemical shift dimension of the HCCH spectra of V28-labeled M2TMP. Only the Val Cα and Cβ signals are selected. (c) Unsymmetrized V27 HCCH time-domain data for the apo peptide and the amantadine-complexed peptide. The best-fit χ_{1H} angle is indicated. The bound peptide shows a 6° decrease of the χ_{1H} angle, consistent with the direction of the chemical shift change. (d) Unsymmetrized V28 HCCH data. The bound peptide has a 6° higher χ_{1H} angle than the apo peptide, consistent with the direction of the chemical shift change.

This difference is again consistent with the methyl chemical shift predictions. In addition to the consistent direction of change between the apo and Amt-bound samples for each Val residue, the HCCH data are in quantitative agreement with the methyl shift differences between V27 and V28. Namely, the V27 apo sample and V28 Amt-bound state, which have similar methyl shift differences of 1.9 ppm and 1.8 ppm, have the same HCCH-χ_1 angle of 164˚. The V27 Amt-bound state and V28 apo state, which have similar methyl shift differences of 1.3 ppm and 1.2 ppm, also have the same HCCH-χ_1 angle of 158˚. Thus, direct torsion angle experiments bear out the chemical-shift based prediction of the *t* and *m* rotamers in all four cases (Table 7.1).

Figure 7.9 shows the rotameric states of the five Val and Leu residues in amantadine-bound M2TMP in top views of the helical bundle. All three Leu residues have the *mt* rotamer, while both Val residues have the *t* rotamer. Among these five residues, L36 has the most lipid-facing location, while L38 places its methyl groups closest to the channel lumen. L26 sidechain has a more interfacial position than V27 and V28. The two recent high-resolution structures of M2TMP differed on the rotameric states of various Leu residues. For example, the solution NMR structure shows a L26 rotamer of *tp* (*32*), while the crystal structure shows a mixture of *mt* and *tp* states for L26 (*31*).

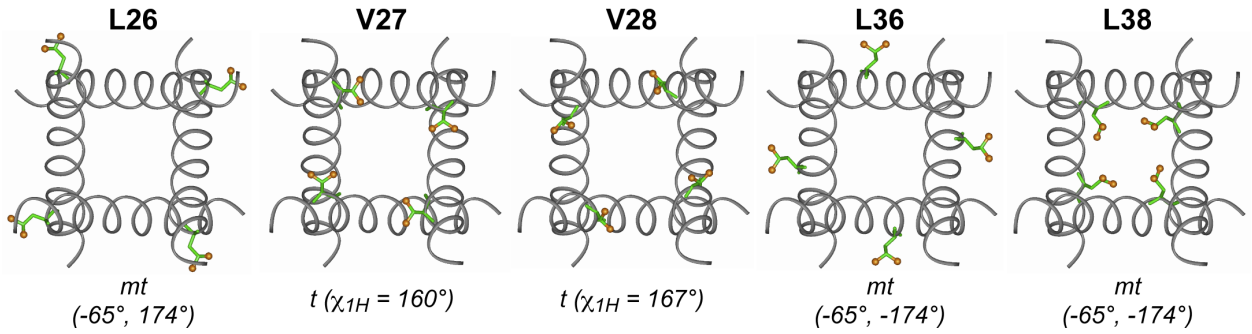

Figure 7.9. Rotameric states of Val and Leu residues determined by methyl ^{13}C chemical shifts and direct χ_1 angle measurements in amantadine-bound M2TMP. The backbone structure is for the amantadine-bound peptide (*36*) (PDB accession code: 2kad).

The rotameric difference between the solution NMR structure and solid-state NMR structure appear to be real, as the solution NMR methyl ^{13}C chemical shift differences of the three Leu residues are significantly smaller than found by solid-state NMR here (Table 7.1). This probably results from a combination of the higher temperature of the solution NMR experiments, which favor rotameric averaging, and the use of detergent micelles in the solution NMR experiments, which may lead to different sidechain conformations than in lipid bilayers.

Conclusion

We have shown that a significant statistical correlation exists between the methyl ^{13}C chemical shift differences of Leu and Val and their sidechain conformations. For α-helical Val's, the *t* rotamer has more upfield Cγ1 shifts than Cγ2, while the *m* rotamer has more upfield Cγ2 shifts than Cγ1. For α-helical Leu's, the *mt* rotamer has a large methyl shift difference of 2.9 ppm while the *tp* rotamer only has an absolute methyl shift difference of 0.73 ppm. Thus, accurate measurement of the methyl ^{13}C chemical shifts in membrane proteins, by means of 2D DQ-SQ correlation experiments, can help to determine and refine the sidechain conformation of these proteins. Application to the influenza A M2 proton channel shows that two Val's adopt the dominant *t* rotamer while three Leu residues exhibit the dominant *mt* rotamer. This work indicates that protein solid-state NMR can play an important role in understanding the conformational dependences of sidechain ^{13}C chemical shifts due to the ability to suppress rotameric averaging at low temperature. The solid-state NMR measured sidechain chemical shifts can also serve as important benchmarks for further computational analysis of the conformation dependence of sidechain chemical shifts.

Acknowledgement: This work is funded by National Science Foundation grant MCB-0543473.

References

1. Castellani, F., vanRossum, B., Diehl, A., Schubert, M., Rehbein, K., and Oschkinat, H. (2002) Structure of a protein determined by solid-state magic-angle spinning NMR spectroscopy., *Nature 420*, 98-102.
2. Franks, W. T., Zhou, D. H., Wylie, B. J., Money, B. G., Graesser, D. T., Frericks, H. L., Sahota, G., and Rienstra, C. M. (2005) Magic-angle spinning solid-state NMR spectroscopy of the beta1 immunoglobulin binding domain of protein G (GB1): 15N and 13C chemical shift assignments and conformational analysis, *J. Am. Chem. Soc. 127*, 12291-12305.
3. Petkova, A. T., Yau, W. M., and Tycko, R. (2006) Experimental constraints on quaternary structure in Alzheimer's beta-amyloid fibrils, *Biochemistry 45*, 498-512.
4. Wasmer, C., Lange, A., Van Melckebeke, H., Siemer, A. B., Riek, R., and Meier, B. H. (2008) Amyloid fibrils of the HET-s(218-289) prion form a beta solenoid with a triangular hydrophobic core, *Science 319*, 1523-1526.
5. Zech, S. G., Wand, A. J., and McDermott, A. E. (2005) Protein structure determination by high-resolution solid-state NMR spectroscopy: application to microcrystalline ubiquitin, *J. Am. Chem. Soc. 127*, 8618-8626.
6. Rienstra, C. M., Tucker-Kellogg, L., Jaroniec, C. P., Hohwy, M., Reif, B., McMahon, M. T., Tidor, B., Lozano-Perez, T., and Griffin, R. G. (2002) De novo determination of peptide structure with solid-state magic-angle spinning NMR spectroscopy., *Proc. Natl. Acad. Sci. USA 99*, 10260-10265.
7. Feng, X., Lee, Y. K., Sandstroem, D., Eden, M., Maisel, H., Sebald, A., and Levitt, M. H. (1996) Direct determination of a molecular torsional angle by solid-state NMR, *Chem. Phys. Lett. 257*, 314-320.
8. Feng, X., Verdegem, P. J. E., Lee, Y. K., Sandstrom, D., Eden, M., Bovee-Geurts, P., Grip, W. J. d., Lugtenburg, J., Groot, H. J. M. d., and Levitt, M. H. (1997) Direct determination of a molecular torsion angle in the membrane protein rhodopsin by solid-state NMR, *J. Am. Chem. Soc. 119*, 6853-6857.
9. Rienstra, C. M., Hohwy, M., Mueller, L. J., Jaroniec, C. P., B, B. R., and Griffin, R. G. (2002) Determination of multiple torsion-angle constraints in U-(13)C,(15)N-labeled

peptides: 3D (1)H-(15)N-(13)C-(1)H dipolar chemical shift NMR spectroscopy in rotating solids., *J. Am. Chem. Soc. 124*, 11908-11922.

10. Helmus, J. J., Nadaud, P. S., Höfer, N., and Jaroniec, C. P. (2008) Determination of methyl 13C-15N dipolar couplings in peptides and proteins by three-dimensional and four-dimensional magic-angle spinning solid-state NMR spectroscopy, *J. Chem. Phys. 128*, 052314.
11. deDios, A. C., Pearson, J. G., and Oldfield, E. (1993) Secondary and tertiary structural effects on protein NMR chemical shifts: an ab initio approach, *Science 260*, 1491-1496.
12. Wishart, D. S., Sykes, B. D., and Richards, F. M. (1991) Relationship between nuclear magnetic resonance chemical shift and protein secondary structure, *J. Mol. Biol. 222*, 311-333.
13. Pearson, J. G., Le, H., Sanders, L. K., Godbout, N., Havlin, R. H., and Oldfield, E. (1997) Predicting chemical shifts in proteins: structure refinement of valine residues by using ab initio and empirical geometry optimizations, *J. Am. Chem. Soc. 119*, 11941-11950.
14. Sun, H., Sanders, L. K., and Oldfield, E. (2002) Carbon - 13 NMR shielding in the twenty common amino acids: Comparisons with experimental results in proteins, *J. Am. Chem. Soc. 124*, 5486-5495.
15. London, R. E., Wingad, B. D., and Mueller, G. A. (2008) Dependence of amino acid side chain 13C shifts on dihedral angle: application to conformational analysis, *J. Am. Chem. Soc. 130*, 11097-11105.
16. Haigh, C. W., and Mallion, R. B. (1979) Ring current theories in Nuclear Magnetic Resonance, *Prog. Nucl. Magn. Reson. Spectrosc. 13*, 303-344.
17. Stamm, H., and Jackel, H. (1989) Relative ring-current effects based on a new model for aromatic-solvent-induced shifts, *J. Am. Chem. Soc. 111*, 6544-6550.
18. Neri, D., Otting, G., and Wuethrich, K. (1990) Proton and carbon-13 NMR chemical shifts of the diastereotopic methyl groups of valyl and leucyl residues in peptides and proteins, *Tetrahedron 46*, 3287-3296.
19. Vuister, G. W., and Bax, A. (1993) Quantitative J correlation: a new approach for measuring homonuclear three-bond J(HNHa) coupling constants in 15N-enriched proteins, *J. Am. Chem. Soc. 115*, 7772-7777.

20. Grzesiek, S., Vuister, G. W., and Bax, A. (1993) A Simple and Sensitive Experiment for Measurement of JCC Couplings Between Backbone Carbonyl and Methyl Carbons in Isotopically Enriched Proteins, *J. Biomol. NMR 487-493*.
21. Karimi-Nejad, Y., Schmidt, J. M., Rüterjans, H., Schwalbe, H., and Greisinger, C. (1994) Conformation of valine side chains in ribonuclease T1 determined by NMR studies of homonuclear and heteronuclear 3J coupling constants, *Biochemistry 33*, 5481-5492.
22. Tugarinov, V., and Kay, L. E. (2004) Stereospecific NMR Assignments of Prochiral Methyls, Rotameric States and Dynamics of Valine Residues in Malate Synthase G, *J. Am. Chem. Soc. 126*, 9827-9836.
23. Chou, J. J., Case, D. A., and Bax, A. (2003) Insights into the mobility of methyl-bearing side chains in proteins from (3)J(CC) and (3)J(CN) couplings, *J. Am. Chem. Soc. 125*, 8959-8966.
24. Mittermaier, A., and Kay, L. E. (2001) Chi1 torsion angle dynamics in proteins from dipolar couplings, *J. Am. Chem. Soc. 123*, 6892-6903.
25. Takegoshi, K., Nakamura, S., and Terao, T. (2001) C-13-H-1 dipolar-assisted rotational resonance in magic-angle spinning NMR, *Chem. Phys. Lett. 344*, 631-637.
26. Piantini, U., Sorensen, O. W., and Ernst, R. R. (1982) Multiple quantum filters for elucidating NMR coupling networks., *J. Am. Chem. Soc. 104*, 6800-6801.
27. Bax, A., Freeman, R., and Kempsell, S. P. (1980) Natural-abundance 13C-13C coupling observed via double-quantum coherence, *J. Am. Chem. Soc. 102*, 4849-4851.
28. Hong, M. (1999) Solid-state dipolar INADEQUATE NMR spectroscopy with a large double-quantum spectral width, *J. Magn. Reson. 136*, 86-91.
29. Pinto, L. H., and Lamb, R. A. (2006) The M2 Proton Channels of Influenza A and B Viruses, *J. Biol. Chem. 281*, 8997-9000.
30. Lamb, R. A., Holsinger, K. J., and Pinto, L. H. (1994) The Influenza A virus M2 ion channel protein and its role in the influenza virus life cycle., in *Cellular Receptors of Animal Viruses* (Wemmer, E., Ed.), pp 303-321, Cold Spring Harbor Lab Press, Plainview, NY.

31. Stouffer, A. L., Acharya, R., Salom, D., Levine, A. S., Di Costanzo, L., Soto, C. S., Tereshko, V., Nanda, V., Stayrook, S., and DeGrado, W. F. (2008) Structural basis for the function and inhibition of an influenza virus proton channel, *Nature 451*, 596-599.
32. Schnell, J. R., and Chou, J. J. (2008) Structure and mechanism of the M2 proton channel of influenza A virus, *Nature 451*, 591-595.
33. Hu, J., Asbury, T., Achuthan, S., Li, C., Bertram, R., Quine, J. R., Fu, R., and Cross, T. A. (2007) Backbone structure of the amantadine-blocked trans-membrane domain M2 proton channel from Influenza A virus, *Biophys. J. 92*, 4335-4343.
34. Wang, J., Kim, S., Kovacs, F., and Cross, T. A. (2001) Structure of the the transmembrane region of the M2 protein H+ channel., *Prot. Sci. 10*, 2241-2250.
35. Cady, S. D., and Hong, M. (2008) Amantadine-Induced Conformational and Dynamical Changes of the Influenza M2 Transmembrane Proton Channel, *Proc. Natl. Acad. Sci. U.S.A 105*, 1483-1488.
36. Cady, S. D., Mishanina, T. V., and Hong, M. (2009) Structure of amantadine-bound M2 transmembrane peptide of influenza A in lipid bilayers from magic-angle-spinning solid-state NMR: the role of Ser31 in amantadine binding, *J. Mol. Biol. 385*, 1127-1141.
37. Luo, W., Mani, R., and Hong, M. (2007) Sidechain conformation and gating of the M2 transmembrane peptide proton channel of influenza A virus from solid-state NMR, *J. Phys. Chem. 111*, 10825-10832.
38. Bennett, A. E., Rienstra, C. M., Auger, M., Lakshmi, K. V., and Griffin, R. G. (1995) Heteronuclear decoupling in rotating solids., *J. Chem. Phys. 103*, 6951-6958.
39. Fung, B. M., Khitrin, A. K., and Ermolaev, K. (2000) An improved broadband decoupling sequence for liquid crystals and solids, *J. Magn. Reson. 142*, 97-101.
40. Hohwy, M., Rienstra, C. M., Jaroniec, C. P., and Griffin, R. G. (1999) Fivefold symmetric homonuclear dipolar recoupling in rotating solids: application to double-quantum spectroscopy., *J. Chem. Phys. 110*, 7983-7992.
41. Markley, J. L., Bax, A., Arata, Y., Hilbers, C. W., Kaptein, R., Sykes, B. D., Wright, P. E., and Wüthrich, K. (1998) Recommendations for the presentation of NMR structures of proteins and nucleic acids, *Pure & Appl. Chem. 70*, 117-142.

42. Lovell, S. C., Word, J. M., Richardson, J. S., and Richardson, D. C. (2000) The penultimate rotamer library, *Proteins: Struct., Funct., Genet. 40*.
43. Lee, Y. K., Kurur, N. D., Helmle, M., Johannessen, O. G., Nielsen, N. C., and Levitt, M. H. (1995) Efficient dipolar recoupling in the NMR of rotating solids. A sevenfold symmetric radiofrequency pulse sequence, *Chem. Phys. Lett. 242*, 304-309.
44. Kristiansen, P. E., Carravetta, M., van Beek, J. D., Lai, W. C., and Levitt, M. H. (2006) Theory and applications of supercycled symmetry-based recoupling sequences in solid-state nuclear magnetic resonance, *J. Chem. Phys. 124*, 234510.
45. Zhang, H., Neal, S., and Wishart, D. S. (2003) RefDB: A database of uniformly referenced protein chemical shifts, *J. Biomol. NMR 25*, 173-195.
46. Grant, D. M., and Paul, E. G. (1964) Carbon-13C magnetic resonance. II. Chemical Shift Data for the Alkanes, *J. Am. Chem. Soc. 86*, 2984-2990.
47. Batchelder, L. S., Sullivan, C. E., Jelinski, L. W., and Torchia, D. A. (1982) Characterization of leucine side-chain reorientation in collagen-fibrils by solid-state 2H NMR, *Proc. Natl. Acad. Sci. U. S. A. 79*, 386-389.
48. Mack, J. W., Torchia, D. A., and Steinert, P. M. (1988) Solid-state NMR studies of the dynamics and structure of mouse keratin intermediate filaments, *Biochemistry 27*, 5418-5426.
49. Colnago, L. A., Valentine, K. G., and Opella, S. J. (1987) Dynamics of fd coat protein in the bacteriophage, *Biochemistry 26*, 847-854.
50. Kinsey, R. A., Kintanar, A., Tsai, M. D., Smith, R. L., Janes, N., and Oldfield, E. (1981) First observation of amino acid side chain dynamics in membrane proteins using high field deuterium nuclear magnetic resonance spectroscopy, *J. Biol. Chem. 256*, 4146-4149.
51. Lee, K. C., Huo, S., and Cross, T. A. (1995) Lipid-peptide interface: valine conformation and dynamics in the gramicidin channel, *Biochemistry 34*, 857-867.
52. Nielsen, N. C., Bildsoe, H., Jakobsen, H. J., and Levitt, M. H. (1994) Double-quantum homonuclear rotary resonance: efficient dipolar recovery in magic-angle spinning nuclear magnetic resonance, *J. Chem. Phys. 101*, 1805-1812.

53. Hong, M., Gross, J. D., Rienstra, C. M., Griffin, R. G., Kumashiro, K. K., and Schmidt-Rohr, K. (1997) Coupling Amplification in 2D MAS NMR and Its Application to Torsion Angle Determination in Peptides, *J. Magn. Reson. 129*, 85-92.

54. Hilty, C., Wider, G., Fernández, C., and Wüthrich, K. (2003) Stereospecific assignments of the isopropyl methyl groups of the membrane protein OmpX in DHPC micelles, *J. Biomol. NMR 27*, 377-382.

55. Hu, W., and Zuiderweg, E. R. P. (1996) Stereospecific assignments of Val and Leu methyl groups in a selectively 13C-labeled 18 kDa polypeptide using 3D CT-(H)CCH-COSY and 2D1JC-C edited heteronuclear correlation experiments, *J. Magn. Reson. 113*, 70-75.

Supporting Information

Table 7.S1: Val methyl Cγ chemical shifts in α-helical proteins.

Protein	Residue number	Rotamer	$\delta_{C\gamma 1}$ (ppm)	$\delta_{C\gamma 2}$ (ppm)	$\delta_{C\gamma 2} - \delta_{C\gamma 1}$ (ppm)
Malate syn.	490	Ht	19.6	20.9	1.3
Malate syn.	666	Ht	19.7	21.9	2.2
Ubiq.	26	Ht	20	21	1.0
Malate syn.	365	Ht	20.3	21.8	1.5
P22	33	Ht	20.4	21.9	1.5
Malate syn.	24	Ht	20.5	22.5	2.0
Cal. N	35	Ht	20.6	23.2	2.6
Cofilin	143	Ht	20.7	21.9	1.2
Cal. C	108	Ht	20.8	23.6	2.8
Malate syn.	166	Ht	21.1	22.7	1.6
Cal. C	91	Ht	21.4	22.9	1.5
Cal. C	142	Ht	21.4	23.2	1.8
Malate syn.	20	Ht	21.5	23.9	2.4
GB1	29	Ht	21.9	20.5	-1.4
M2	27	Ht	21.3	22.9	1.6
M2	28	Ht	21.4	22.7	1.3
Dcp2	150	Ht	22.3	24.3	2.0
Malate syn.	656	Ht	22.4	24.2	1.8
Cal. C	121	Ht	22.5	23.5	1.0
Cal. N	55	Ht	22.6	21.4	-1.2
RNase T1	16	Ht	23.1	24.4	1.3
Cyt. C	3	Hm	20.6	20.5	-0.1
Malate syn.	701	Hm	21.4	19.7	-1.7
Profilin I	60	Hm	21.5	21.2	-0.3
Cofilin	29	Hm	22.7	21.2	-1.5
Talin	2400	Hm	23.1	22.1	-1.0
Malate syn.	553	Hm	22.9	20.1	-2.8
Cofilin	14	Hp	22.4	24.9	2.4
Malate syn.	608	Hp	20.7	21.9	1.2
Cyt. C	11	Hp	21.3	19.7	-1.6
Talin	2360	Hp	23	23.3	0.3
Profilin I	40	Hp	22	19.4	-2.6

Table 7.S2. Leu methyl Cδ chemical shifts in α-helical proteins.

Protein	Residue number	Rotamer	$\delta_{C\delta1}$ (ppm)	$\delta_{C\delta2}$ (ppm)	$\delta_{C\delta1} - \delta_{C\delta2}$ (ppm)
Cyt. C	98	Hmt	24.3	21.6	2.7
Dcp2	223	Hmt	24.3	21.8	2.5
Cal. N	18	Hmt	25	24.7	0.3
Cofilin	128	Hmt	25.3	21.8	3.5
Cal. N	69	Hmt	25.4	24.7	0.7
P22	17	Hmt	25.6	22	3.6
Profilin IIa	134	Hmt	25.8	22.1	3.7
Cal. N	48	Hmt	25.8	23.5	2.3
Cal. C	112	Hmt	26.1	23.6	2.5
Cal. N	39	Hmt	26.1	22.8	3.3
Profilin I	134	Hmt	26.2	23.3	2.9
P22	64	Hmt	26.4	22.3	4.1
Malate syn.	696	Hmt	26.7	24.2	2.5
Profilin IIa	123	Hmt	27.1	22.9	4.2
Fasciclin	39	Htp	22.4	22	0.4
Fasciclin	79	Htp	22.5	22.2	0.3
Cal. N	32	Htp	22.9	26	-3.1
Cyt. C	35	Htp	23.3	23.2	0.1
Talin	2424	Htp	23.7	25.6	-1.9
Dcp2	235	Htp	24.4	23.9	0.5
P22	65	Htp	24.5	23.8	0.7
Talin	2346	Htp	24.5	24.9	-0.4
Talin	2393	Htp	24.7	25.2	-0.5
Talin	2438	Htp	24.9	26.5	-1.6
Malate syn.	291	Htp	25.3	26.3	-1.0
Talin	2470	Htp	25.5	25.9	-0.4
Talin	2407	Htp	25.8	25.1	0.7
Cal. C	105	Htt	24.1	26	-1.9
Malate syn.	285	Htt	24.6	23.6	1.0
Malate syn.	576	Htt	24.9	24.7	0.2
Malate syn.	128	Htt	25	24.3	0.7
P22	53	Htt	25.2	25.3	-0.1
Malate syn.	286	Htt	25.7	26.2	-0.5
Dcp2	231	Htt	25.7	25	0.7
Talin	2456	Htt	26.8	25.9	0.9
Cyt. C	94	Htt	27.7	27.4	0.3

Chapter 8

Effects of Amantadine on the Dynamics of Membrane-Bound Influenza A M2 Transmembrane Peptide Studied by NMR Relaxation

A paper to be published in the Journal of Biomolecular NMR

In press

Sarah D. Cady and Mei Hong

Abstract

The molecular motions of membrane proteins in liquid-crystalline lipid bilayers lie at the interface between motions in isotropic liquids and in solids. Specifically, membrane proteins can undergo whole-body uniaxial diffusion on the microsecond time scale. In this work, we investigate the ^{1}H rotating-frame spin-lattice relaxation ($T_{1\rho}$) caused by the uniaxial diffusion of the influenza A M2 transmembrane peptide (M2TMP), which forms a tetrameric proton channel in lipid bilayers. This uniaxial diffusion was proved before by ^{2}H, ^{15}N and ^{13}C NMR lineshapes of M2TMP in DLPC bilayers. When bound to an inhibitor, amantadine, the protein exhibits significantly narrower linewidths at physiological temperature. We now investigate the origin of this line narrowing through temperature-dependent ^{1}H $T_{1\rho}$ relaxation times in the absence and presence of amantadine. Analysis of the temperature dependence indicates that amantadine decreases the correlation time of motion from 2.8 ± 0.9 μs for the apo peptide to 0.89 ± 0.41 μs for the bound peptide at 313 K. Thus the line narrowing of the bound peptide is due to better avoidance of the NMR time scale and suppression of intermediate time scale broadening. The faster diffusion of the bound peptide is due to the higher attempt rate of motion, suggesting that amantadine creates better-packed and more cohesive helical bundles. Analysis of the temperature dependence of $\ln\left(T_{1\rho}^{-1}\right)$ indicates that the activation energy of motion increased from 14.0 ± 4.0 kJ/mol for the apo peptide to 23.3 ± 6.2 kJ/mol for the bound peptide. This higher activation energy indicates that excess

amantadine outside the protein channel in the lipid bilayer increases the membrane viscosity. Thus, the protein-bound amantadine speeds up the diffusion of the helical bundles while the excess amantadine in the bilayer increases the membrane viscosity.

Introduction

Nuclear magnetic resonance has long been used as a tool for measuring molecular dynamics over a broad range of time scales, from the fast picosecond – nanosecond regime (*1*), to the slow microsecond – millisecond regime (*2-4*), and to the ultra-slow supra-second regime (*5, 6*). Some of the most interesting applications are to biomolecules, where molecular dynamics has a particularly strong connection to function (*7-9*). In solution NMR studies of biomolecular dynamics, ^{15}N relaxation NMR has been the method of choice and the Lipari-Szabo model-free formalism (*10, 11*) has provided a simple theoretical framework to separate the effects of internal anisotropic motions from whole-body isotropic motion and to extract the amplitudes and rates of internal motion.

In the solid state, the lack of isotropic molecular tumbling considerably simplifies studies of internal motions by NMR. Many solid-state NMR techniques directly probe the amplitudes of internal motions, most notably ^{2}H quadrupolar NMR (*12*), which has exquisite angular resolution but no chemical resolution, and ^{1}H-X dipolar coupling techniques under magic-angle spinning (MAS), which have chemical site resolution (*13-15*). Nuclear spin relaxation times (T_1, T_2 and $T_{1\rho}$) have also been used to determine the correlation times and activation energies of motional processes such as methyl three-site jumps and aromatic ring flips. Combined, these amplitude and rate measurements have provided detailed information on the dynamics of structural proteins such as collagen and silk (*12, 16*), enzymes (*17*), and lipid membranes (*18, 19*). Molecular motions of synthetic polymers (*20-22*) and small molecules (*23*) have also been investigated extensively using solid-state NMR.

The dynamic environment of liquid-crystalline lipid bilayers lies at the interface between isotropic fluids and rigid solids and hence presents unique challenges to understanding membrane protein dynamics. While membrane protein sidechain motions have been studied by NMR for decades (*24-27*), whole-body uniaxial rotational diffusion of

membrane proteins has been less examined by NMR. As the symmetry axis of the lipid bilayer, the bilayer normal is the axis around which phospholipids undergo nanosecond rotational diffusion (*28, 29*). Membrane proteins can also undergo such rotational diffusion, because the same principle that underlies the phospholipid motion, which is Brownian diffusion in a two-dimensional fluid (*30*), also applies to membrane proteins. A number of examples of this uniaxial diffusion have now been reported for membrane peptides and proteins (*31-38*). Their NMR fingerprints include powder lineshapes with reduced anisotropy and an asymmetry parameter (η) of 0, vanishing intensity at the isotropic chemical shift of non-spinning cross polarization (CP) spectra, and narrow lines in macroscopically aligned samples whose alignment axis deviates from the static magnetic field (*39-41*).

The influenza A M2 protein forms a proton channel in the virus envelope that is important for the virus life cycle (*42, 43*). Acidification of the virus interior uncoats the viral RNA and releases it into the host cell. Amantadine binds the M2 proton channel and prevents its opening, thus inhibiting viral replication (*44, 45*). The protein forms a tetrameric helical bundle in the membranes of both whole cells (*46*) and synthetic lipids (*47*). It undergoes uniaxial diffusion at a rate of $\sim 10^5\ s^{-1}$ in DLPC bilayers based on ^{2}H NMR spectra and the 2D Brownian diffusion theory (*48, 49*). The motional axis is the bilayer normal, which is also the helical bundle axis. Since the TM helices have tilt angles of ~38° in DLPC bilayers (*50*), the rotational diffusion has large amplitudes. Combined with the fact that the motional rate is not orders of magnitude different from the ^{1}H-^{13}C and ^{1}H-^{15}N dipolar couplings, the motion strongly impacts the NMR spectra: the ambient-temperature ^{1}H-decoupled ^{13}C and ^{15}N spectra of the protein in lipid bilayers are severely exchange-broadened under both MAS and static conditions (*48, 51*). Interestingly, upon amantadine binding, the resonances in both MAS and static solid-state NMR spectra of the protein sharpen considerably. This line narrowing was also observed in solution NMR spectra of M2(18-60) bound to DHPC micelles when an excess of the analogous rimantadine was added (*52*).

Previously we have compared the ^{1}H-decoupled ^{13}C T_2 relaxation times of the apo and bound M2TMP in DLPC bilayers to understand the amantadine-induced line narrowing. We found that the bound peptide has 30-150% longer ^{13}C T_2 than the apo state at 303 K (*50, 53*),

indicating that the line narrowing has a significant contribution from dynamic changes of the protein. However, the nature of this amantadine-induced relaxation time increase has not been elucidated.

In this work, we have measured and analyzed temperature-dependent ^{1}H $T_{1\rho}$ relaxation times of the apo and amantadine-bound M2TMP to better understand its motional properties. We quantify the rates and activation energies of the M2TMP microsecond motion in the absence and presence of amantadine. We find that amantadine increases the motional rates approximately three fold at 313 K by increasing the attempt rates, thus alleviating intermediate time scale broadening and narrowing the spectral lines. Further, excess amantadine in the bilayer increases the activation energy of the motion, whose physical origin will be discussed.

Material and Methods

Peptides and lipids

FMOC-protected uniformly ^{13}C, ^{15}N-labeled amino acids were either prepared in-house (*54*) or purchased from Sigma-Aldrich and Cambridge Isotope Laboratories. The M2 transmembrane domain (residues 22-46) of the Influenza A Udorn strain (*55*) was synthesized by PrimmBiotech (Cambridge, MA) and purified to >95% purity. The amino acid sequence is SSDPL VVAASII GILHLIL WILDRL. Three labeled peptides were used in this work, each with three to four uniformly ^{13}C, ^{15}N-labeled residues. They are LAGI (L26, A29, G34 and I35), VAIL (V27, A30, I33 and L38), and VSL (V28, S31 and L36).

Membrane sample preparation

M2TMP was reconstituted into 1,2-dilauroyl-*sn*-glycero-3-phosphatidylcholine (DLPC) bilayers by detergent dialysis (*47*). The lipid vesicle solution was prepared by suspending dry DLPC powder in 1 mL phosphate buffer (10 mM Na_2HPO_4/NaH_2PO_4, 1 mM EDTA, 0.1 mM NaN_3) at pH 7.5, vortexing and freeze-thawing 6 times to create uniform vesicles (*56*). M2TMP was dissolved in octyl-β-D-glucopyranoside (OG) in 2 mL phosphate

buffer, then mixed with an equal volume of DLPC vesicles, and dialyzed against the phosphate buffer at 4 °C for 3 days. The final peptide/lipid molar ratio was 1:15. The dialyzed peptide-DLPC solution was centrifuged at 150,000 g to give a pellet containing ~50 wt% water. For the amantadine-bound samples, 10 mM amantadine hydrochloride was added to the phosphate buffer. After pelleting, the amount of amantadine remaining in the supernatant was quantified by ^{1}H solution NMR, and the bound fraction indicates a peptide : amantadine molar ratio of ~1 : 8 (*53*). All membrane-bound M2 samples were thus studied at pH 7.5, corresponding to the closed state of the channel.

Solid-state NMR spectroscopy

NMR experiments were carried out on a Bruker AVANCE-600 (14.1 Tesla) spectrometer (Karlsruhe, Germany) using a 4 mm MAS probe. ^{1}H $T_{1\rho}$ measurements were carried out using a Lee-Goldburg (LG) spin lock sequence shown in Figure 8.1 (*27*). The initial two 90° and 35° ^{1}H pulses prepare the ^{1}H magnetization to be alternately parallel and antiparallel to the ^{1}H spin lock axis, which lies at the magic angle $cos^{-1}\left(1/\sqrt{3}\right)$ from the static magnetic field in the yz plane. The spin-lock effective field strength, ω_e, was fixed at 2π x 61.2 kHz in all experiments, since $T_{1\rho}$ depends on ω_e (Equations 8.1-8.2). The samples were spun at 7000 Hz during all experiments. Six or seven spin lock time points τ_{SL} were measured between 0 and 8 ms to obtain the ^{1}H $T_{1\rho}$ at each temperature, and six or seven temperatures were measured per peptide to provide a sufficient number of data points in the $\ln\left(T_{1\rho}^{-1}\right)$ versus inverse temperature plot (Figure 8.5) to extract the dynamic parameters. The NMR probe and samples were equilibrated for 30 minutes at each temperature before tuning and data acquisition. The ^{1}H LG-CP period had the same field strength as the LG spin lock period, but had a constant contact time of 300 μs. Typical radiofrequency (rf) pulse lengths were 5 μs for ^{13}C and 3.5-4.0 μs for ^{1}H. ^{13}C chemical shifts were referenced to the α-Gly ^{13}C' signal at 176.49 ppm on the TMS scale.

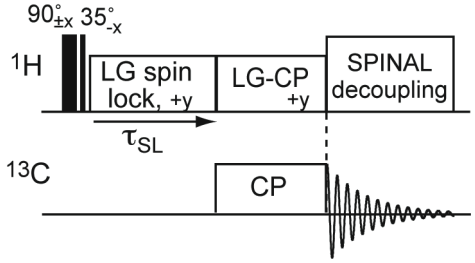

Figure 8.1. ^{13}C-detected ^{1}H Lee-Goldburg spin lock pulse sequence used to measure ^{1}H $T_{1\rho}$ relaxation times. The ^{1}H magnetization is spin-locked for a variable time τ_{SL}. The LG spin-lock and LG-CP have the same field strength.

The ^{1}H $T_{1\rho}$'s were measured between 313 K and 243 K on six membrane samples with and without amantadine. The activation energy E_a, correlation time prefactor τ_0, and correlation time τ were extracted by least-square linear fits of the $\ln\left(T_{1\rho}^{-1}\right)$ to 1000/T curves on the high temperature side using Equations 8.8-8.10. For the apo VAIL sample, artificially high $T_{1\rho}$ values were observed at 313 K, thus the apo and amantadine-bound VAIL-M2TMP data analysis did not include the 313 K data.

C-H dipolar order parameters were measured at 313 K under 7000 Hz MAS using a dipolar-doubled DIPSHIFT experiment (*57*) where ^{1}H homonuclear decoupling was achieved by the frequency-switched Lee-Goldburg sequence (*58*). The dipolar-doubled sequence suppresses the apparent T_2 relaxation by making the total homonuclear decoupling time constant at one rotor period. The t_1 evolution time was controlled by the position of a ^{13}C π pulse in the rotor period.

Theory

The membrane protein rotational diffusion of interest generally occurs on the microsecond time scale based on the 2D Brownian diffusion theory (*30*). Motions on this time scale can be probed by ^{1}H-decoupled *S*-spin spin-spin relaxation times (T_2) and rotating-frame spin-lattice relaxation times ($T_{1\rho}$). The T_2 relaxation times of an *S* spin dipolar coupled to an *I* spin under conditions of random isotropic motion and *I* spin rf decoupling depends on

the spectral density at the decoupling field strength (*23*), which is typically 50-100 kHz. However, measurement of ^{13}C T_2 by the Hahn-echo experiment in uniformly ^{13}C-labeled residues in proteins has the shortcoming that ^{13}C-^{13}C scalar coupling contributes to the time-dependent intensity decay, unless a selective ^{13}C π pulse is applied to remove the scalar interaction. Given the small chemical shift dispersion among the aliphatic carbons in proteins, very soft π pulses, which necessitate multiple experiments with shifted ^{13}C offsets, would be required to obtain homonuclear and heteronuclear decoupled ^{13}C T_2's of all sites. A simpler alternative, then, for probing microsecond time scale motion is to measure the $T_{1\rho}$, since it is primarily sensitive to spectral densities at the frequency of the spin-lock field (*2*), which is also 50 – 100 kHz.

To obtain site-specific relaxation times, we measure the ^1H $T_{1\rho}$ through the directly bonded ^{13}C sites by transferring the ^1H magnetization to ^{13}C, and by using spin-diffusion-free Lee-Goldburg spin lock instead of transverse spin lock (*59*). The effective spin lock field is thus tilted at the magic angle, $cos^{-1}\left(1/\sqrt{3}\right)$, from the static magnetic field. The ^1H magnetization, prepared along the direction of the spin-lock field (Figure 8.1), can only undergo spin-lattice relaxation in the rotating frame.

The ^1H $T_{1\rho}$ relaxation in ^{13}C-labeled molecules is driven by fluctuating ^1H-^1H and ^1H-^{13}C dipolar couplings due to random molecular motions. The orientation-dependent relaxation rate depends on spectral densities, $J(\omega)$, at the spin lock field ω_e, $2\omega_e$, Larmor frequencies ω_H, ω_C, and the sum and difference of ω_H and ω_C (*27, 60*). Since the Larmor frequencies are three to four orders of magnitude larger than ω_e (ω_H = 2π x 600 MHz, ω_C = 2π x 150 MHz, and ω_e = 2π x 61.2 kHz in our experiments), for motions in the tens to hundreds of kilohertz regime, one can safely ignore the spectral density terms at the Larmor frequencies. Taking into account magic-angle spinning at a frequency ω_R, the powder averaged $T_{1\rho}$ for the rotating-frame relevant part is (*61*):

$$\left\langle T_{1\rho}^{-1}\right\rangle = \Delta M_2\left(S,\delta_{CH},\delta_{HH},\beta\right)\cdot\left[J\left(2\omega_e+2\omega_R\right)+J\left(2\omega_e-2\omega_R\right)+J\left(2\omega_e+\omega_R\right)+J\left(2\omega_e-\omega_R\right)\right] \quad (8.1)$$

Here ΔM_2 is the product of the dynamic portion of the dipolar second moment and orientational terms that transform spin interaction tensors from their molecule-fixed principal axis frames to the rotor frame (*61*). The dynamic portion of the dipolar second moment is approximately $\left(1-S^2\right)$ times the rigid-limit dipolar second moment, where the order parameter *S* represents the orientation-invariant part of the interaction. In solid-state NMR, the order parameter can be independently measured by various dipolar chemical-shift correlation experiments (*15, 27, 62*). The dependence of ΔM_2 on the C-H (δ_{CH}) and H-H (δ_{HH}) dipolar couplings in Equation 8.1 reflects the fact that the ^{13}C-detected ^{1}H $T_{1\rho}$ relaxation is driven by C-H and H-H dipolar couplings. β is the angle between B_0 and the spin-lock field and is $cos^{-1}\left(1/\sqrt{3}\right)$ in our experiments.

For motions with a single correlation time τ, the spectral density is given by (*10*):

$$J(\omega_i) = \frac{\tau}{1+\omega_i^2\tau^2}, \tag{8.2}$$

Explicitly writing the spectral density terms in Equation 8.1, we obtain

$$\left\langle T_{1\rho}^{-1}\right\rangle = \Delta M_2\left(S,\delta_{CH},\delta_{HH},\beta\right)\cdot\left[\frac{\tau}{1+\left(2\omega_e+2\omega_R\right)^2\tau^2}+\frac{\tau}{1+\left(2\omega_e-2\omega_R\right)^2\tau^2}+\frac{\tau}{1+\left(2\omega_e+\omega_R\right)^2\tau^2}+\frac{\tau}{1+\left(2\omega_e-\omega_R\right)^2\tau^2}\right] \tag{8.3}$$

The dependence of $T_{1\rho}$ on correlation time τ can be considered in three regimes. In the long correlation time or strong collision limit where $2\omega_e\tau >> 1$, Equation 8.3 is approximated as:

$$\left\langle T_{1\rho}^{-1}\right\rangle \approx \Delta M_2\left(S,\delta_{CH},\delta_{HH},\beta\right)\cdot\left[\frac{1}{\left(2\omega_e+2\omega_R\right)^2}+\frac{1}{\left(2\omega_e-2\omega_R\right)^2}\right.$$
$$\left.+\frac{1}{\left(2\omega_e+\omega_R\right)^2}+\frac{1}{\left(2\omega_e-\omega_R\right)^2}\right]\cdot\frac{1}{\tau},\qquad 2\omega_e\tau>>1 \tag{8.4}$$

In the short correlation time or weak collision regime, Equation 8.3 is simplified to:

$$\left\langle T_{1\rho}^{-1}\right\rangle \approx 4\Delta M_2\left(S,\delta_{CH},\delta_{HH},\beta\right)\cdot\tau,\qquad 2\omega_e\tau<<1 \tag{8.5}$$

In the intermediate motional regime where $2\omega_e\tau=1$, for $\omega_e >> \omega_R$, the relaxation rate is the fastest, corresponding to a $T_{1\rho}$ minimum.:

$$\left\langle T_{1\rho}^{-1}\right\rangle \approx 2\Delta M_2\left(S,\delta_{CH},\delta_{HH},\beta\right)\cdot\tau,\qquad 2\omega_e\tau=1 \tag{8.6}$$

For an activated motional process, the correlation time is given by the Arrhenius law:

$$\tau=\tau_0 e^{E_a/RT}, \tag{8.7}$$

where E_a is the activation energy and τ_0 is the prefactor describing the attempt rate of motion. The larger the attempt rate, the smaller the τ_0, and the shorter the correlation time τ. Substituting τ into Equation 8.5, we find that E_a can be extracted from a plot of $\ln\left(T_{1\rho}^{-1}\right)$ versus 1000/T in the short τ limit:

$$\ln\left\langle T_{1\rho}^{-1}\right\rangle = \ln\left(4\Delta M_2\tau_0\right) + \frac{E_a}{1000R}\cdot\frac{1000}{T}, \quad 2\omega_e\tau << 1 \tag{8.8}$$

Equation 8.8 indicates that the natural logarithm of relaxation rates is linear with 1000/T with a slope of $E_a/1000R$ in the short correlation time regime. Moreover, the pre-exponential factor τ_0 can be extracted from the intercept of the linear fit. For this purpose, we use the second moment expression from Mehring, which takes into account both C-H and H-H dipolar relaxation as well as the LG spin lock factor (*27, 60*):

$$4\Delta M_2\tau_0 = \left(1-S^2\right)\left(\frac{3}{10}\delta_{HH}^2 + \frac{1}{15}\delta_{CH}^2\right)\tau_0, \quad 2\omega_e\tau << 1 \tag{8.9}$$

The motional correlation time is fully determined once the activation energy E_a and the pre-exponential factor τ_0 are obtained from the slope and the intercept, respectively.

In principle, an alternative method to determine the pre-exponential factor τ_0 is to exploit the $T_{1\rho}$ minimum temperature, where $2\omega_e\tau = 1$. However, as we show below, the $T_{1\rho}$ minima observed for membrane-bound M2TMP result from the lipid phase transition, and are thus not the true minima of a single motional process. On the other hand, the lipid-induced $T_{1\rho}$ minima should not affect the high-temperature slopes or intercepts, thus the activation energy E_a and τ_0 can still be extracted reliably from these features.

The $T_{1\rho}$ in the long correlation time limit can in principle also be used to extract E_a and τ. Equations 8.4 and 8.5 indicate that the slope of the $\ln\left(T_{1\rho}^{-1}\right)$ plot with 1/T on the low temperature side has the same magnitude but the opposite sign from that of the high temperature side. But this scenario is true only if a single motional process with the same E_a persists throughout the temperature range. Thus, the lipid phase transition makes this assumption invalid. Since our purpose is to understand the physiological temperature

dynamics of M2TMP, below we will analyze only the high temperature regime of the $T_{1\rho}$ data to extract M2TMP motional parameters.

Results

Site-specific 1H T1r relaxation times were measured on six membrane samples with three sets of labeled residues (LAGI, VAIL, and VSL) without and with amantadine. The eleven labeled residues are distributed from position 26 to 38 in the transmembrane domain, with I32 and H37 being the only residues not measured in this range.

Figure 8.2 shows representative 13C spectra of LAGI-M2TMP in the apo- and amantadine-bound states at 313 K, 273 K and 243 K. At 313 K, the amantadine-bound peptide has narrower linewidths than the apo peptide, whereas at 243 K the peptide signals of the two samples have similar intensities and linewidths, indicating immobilization of both states of the peptide. At 273 K, both the apo and bound peptide spectra exhibit significant exchange broadening with very low 13C intensities. This broadening coincides with the gel to liquid-crystalline phase transition temperature (271 K) of the DLPC membrane, indicating that the M2TMP motion responsible for the exchange broadening is intimately associated with the phase property of the lipid bilayer. The VAIL and VSL spectra exhibit similar temperature dependences and are given in the Supporting Information (Figures 8.S1, 8.S2). The fact that the amantadine-bound samples show narrower and higher backbone Ca signals than the apo samples at high temperature (50) indicates dynamic differences induced by amantadine, the nature of which are analyzed below.

1H T1r were measured at six to seven temperatures between 313 and 243 K. Figure 8.3 displays representative T1r decay curves at 313 K, 273 K, and 243 K as a function of spin-lock time. The decay curves are well fit by single exponential functions, where the decay constants correspond to T1r. At 313 K, the T1r decays are slower for the amantadine-bound peptide than for the apo peptide for all residues, indicating the bound peptide has longer T1r's. At 273 K, the 1H T1r's are significantly shorter than the high-temperature values for both the apo and bound peptides, and the bound peptide has marginally longer T1r's than the apo peptide. At 243 K, the T1r values increase significantly over the high

temperature values, and there is no longer a consistent difference between the apo and bound peptide.

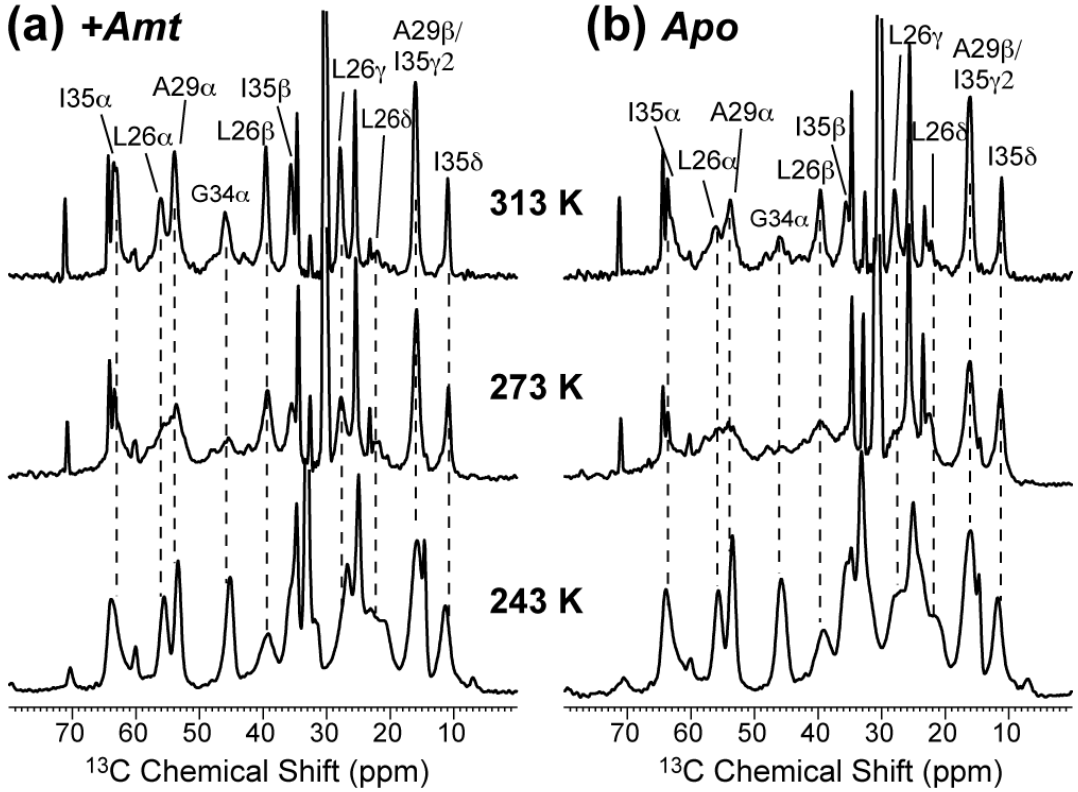

Figure 8.2. 1D ^{13}C CP-MAS spectra of LAGI M2TMP in DLPC bilayers at 313 K, 273 K, and 243 K. (a) With amantadine. (b) Without amantadine.

Supporting information Table 8.S1-8.S3 lists all $T_{1\rho}$ values for backbone Hα, sidechain Hβ, and sidechain methyl protons in the apo and bound M2TMP at all temperatures.

Figure 8.4 shows the ^{1}H $T_{1\rho}$'s as a function of 1000/T (K^{-1}) for representative backbone and sidechain sites. All curves have a V shape, indicative of passage through the fastest relaxing intermediate motional regime. Between the apo and bound peptides, the minimum $T_{1\rho}$ positions match well, with relatively similar $T_{1\rho}$ values as well as the transition temperature T_C. On the high temperature side of the minimum, the bound peptide has progressively longer $T_{1\rho}$'s than the apo peptide with increasing temperature, indicating that M2TMP has shorter correlation times in the presence of amantadine (Equation 8.5). On the low temperature side, the apo and bound peptides have smaller $T_{1\rho}$ differences for the small number of temperatures measured.

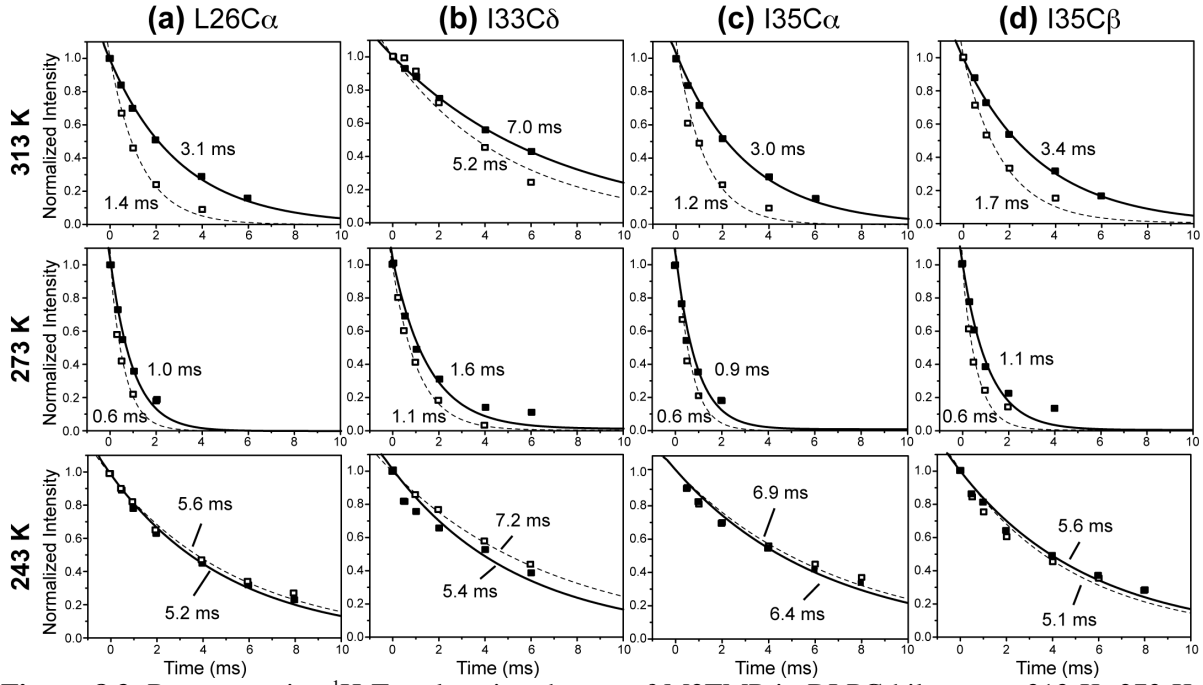

Figure 8.3. Representative ^{1}H $T_{1\rho}$ relaxation decays of M2TMP in DLPC bilayers at 313 K, 273 K, and 243 K. (a) L26 Cα, (b) I33 Cδ, (c) I35 Cα, and (d) I35 Cβ. The apo data are shown as open squares and fit by dashed lines. The amantadine-bound data are shown as filled squares and fit by solid lines. The decay constants are indicated for all sites.

To quantify the amantadine-induced dynamic differences of M2TMP, we convert the $T_{1\rho}$ plots to $\ln\left(T_{1\rho}^{-1}\right)$ and extract the activation energy and correlation time prefactor τ_0 using Equations 8.8 and 8.9. Figure 8.5 shows $\ln\left(T_{1\rho}^{-1}\right)$ as a function of 1000/T for a number of Hα sites. As expected, the shapes of the plots are roughly inverted from those of Figure 8.4, with the amantadine-bound peptide showing smaller relaxation rates than the apo peptide at physiological temperature. On the high temperature side of the $T_{1\rho}$ minimum, $\ln\left(T_{1\rho}^{-1}\right)$ is roughly linear with inverse temperature for most sites, thus supporting the assumption that the rotational diffusion can be regarded as an activated process (*vide infra*). Moreover, the amantadine-bound peptide has more positive slopes than the apo peptide, indicating larger E_a. Least-square linear fits of the high-temperature side of the $\ln\left(T_{1\rho}^{-1}\right)$ curves yielded the activation energies, listed in Table 8.1. The amantadine-bound peptide has an average E_a of

23.3 kJ/mol, which is 66% larger than the average E_a of 14.0 kJ/mol for the apo peptide. The average experimental uncertainty of the E_a is 17%. The standard deviation of the E_a distributions is 6.2 kJ/mol for the bound peptide and 4.2 kJ/mol for the apo peptide. Figure 8.6 compares the E_a values of the apo and bound peptides for each Hα site. With the exception of G34, the E_a's are relatively uniform across all residues, given the experimental uncertainty. The small E_a distribution is consistent with the approximation that the main motional process driving $T_{1\rho}$ relaxation is whole-body uniaxial diffusion rather than segmental motion. In addition, the E_a ratio between the bound and apo peptides for each site is relatively uniform, with an average ratio of 1.73 and a standard deviation of 0.35.

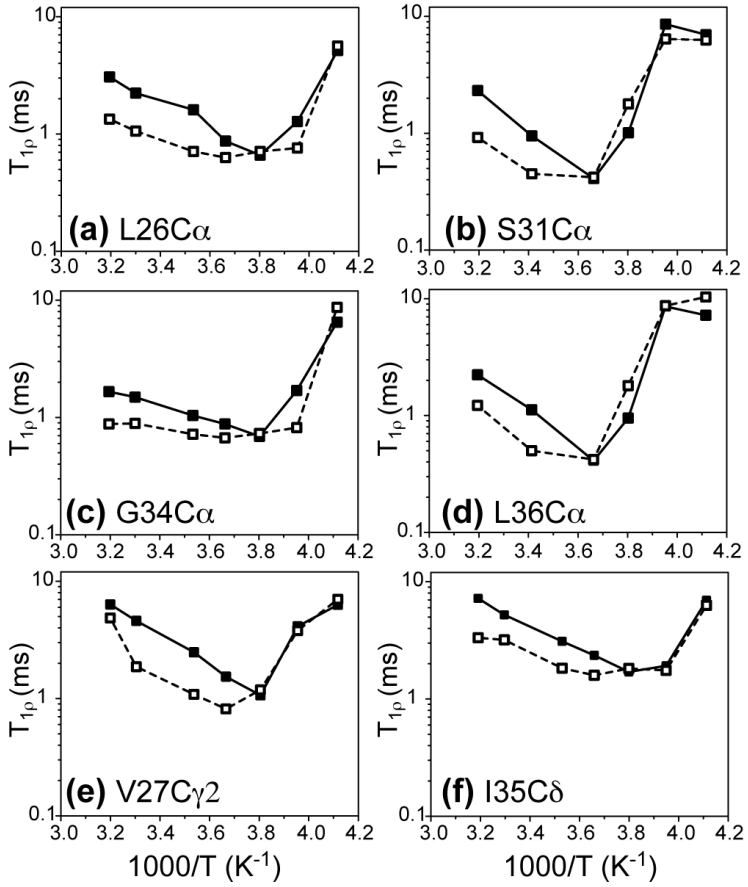

Figure 8.4. ^{1}H $T_{1\rho}$ versus 1000/T for representative M2TMP Cα sites in the apo (open squares and dashed line) and amantadine-bound (closed squares and solid line) states in DLPC bilayers. (a) L26 Cα, (b) S31 Cα, (c) G34 Cα, (d) L36, (e) V27 Cγ2, (f) I35 Cδ.

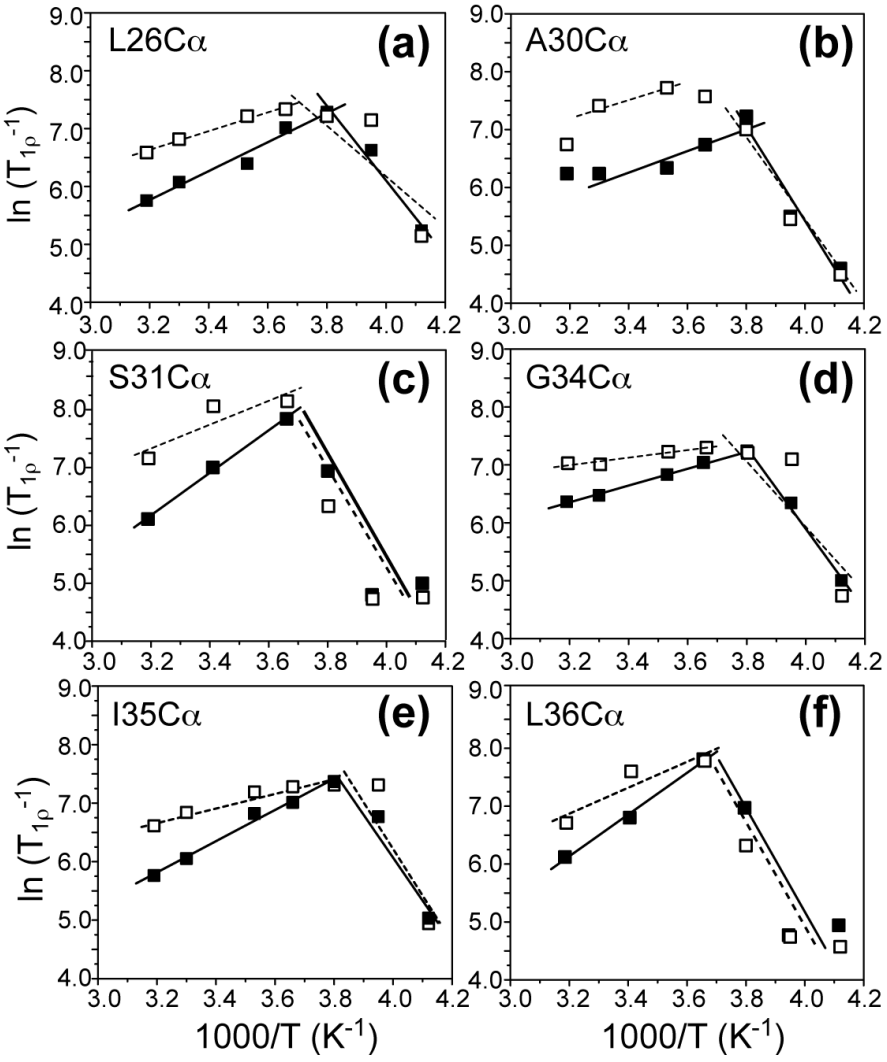

Figure 8.5. $\ln\left(T_{1\rho}^{-1}\right)$ versus 1000/T curves for representative Cα sites of M2TMP. (a) L26. (b A30. (c) S31. (d) G34. (e) I35. (f) L36. The apo data are shown as open squares and fit by dashed lines, and the amantadine-bound data are shown as filled squares and fit by solid lines.

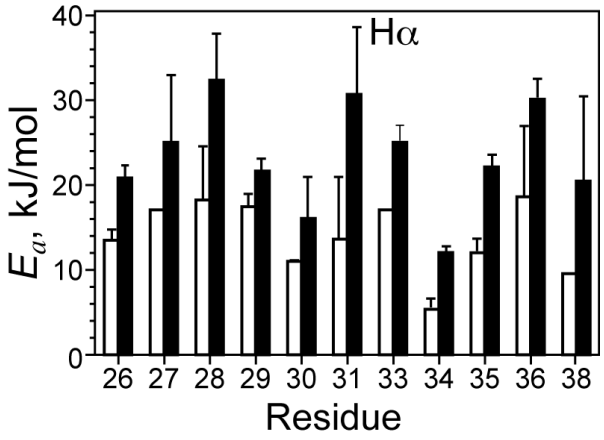

Figure 8.6. Activation energy E_a (kJ/mol) extracted from the high-temperature slopes of the Hα $\ln\left(T_{1\rho}^{-1}\right)$ versus 1000/T curves. The amantadine-bound M2TMP (filled bars) has larger activation energies than the apo peptide (open bars).

To obtain the motional correlation times, we need the C-H order parameters and E_a (Equations 8.7 and 8.9). The Cα-Hα order parameters (Table 8.1) are found to be similar between the apo and bound peptides, indicating that the amantadine-induced spectral line narrowing is not due to amplitude changes but due to rate changes. Using the high-temperature intercepts and S_{CH}, we calculated τ_0 and $\tau_{313\,K}$ for the apo and amantadine-bound M2TMP (Table 8.1). The bound peptide exhibits smaller τ_0 values, indicating higher attempt rates. As a result, the average $\tau_{313\,K}$ is shorter for the bound peptide (0.89 ± 0.41 μs) than the apo peptide (2.8 ± 0.9 μs). The three-fold reduction of $\tau_{313\,K}$ in the presence of amantadine is qualitatively consistent with the two-fold longer $T_{1\rho}$, since $T_{1\rho}^{-1}$ is linear with τ in the short τ regime (Equation 8.5). The magnitude of $\tau_{313\,K}$ is also reasonable, as it is similar to or shorter than the inverse of the spin lock field of 2.7 μs. In other words, the amantadine-bound M2TMP has a shorter correlation time than the characteristic time scale of the spin-lock field, thus alleviating exchange broadening, while the apo peptide correlation time is closer to the NMR time scale, thus giving rise to broader lines. Decreasing the temperature to 273 K increased the τ to 6.0 μs and 3.4 μs for the apo and bound peptides, respectively.

It is also interesting to examine the sidechain ^{1}H $T_{1\rho}$ trends. Table 8.S3 shows that the methyl proton $T_{1\rho}$'s are much longer than the backbone Hα $T_{1\rho}$'s and are relatively similar between the apo and bound peptides at high temperatures. Figure 8.7 shows representative $\ln\left(T_{1\rho}^{-1}\right)$ plots of two methyl groups and one methine Cβ site. The methyl protons have more similar high-temperature slopes between the apo and bound peptides, with an apparent activation energy difference of only 20% between the two states. The similarities can be attributed to three-site jumps of the methyl groups that are additional to the uniaxial diffusion, which reduce the dynamic difference between the apo and bound peptide. In comparison, the Cβ sites show more distinct activation energies between the apo and bound states, consistent with the Hα $T_{1\rho}$ behavior.

Table 8.1. E_a, τ_0, and τ_{313K} of M2TMP in DLPC bilayers in the absence and presence of amantadine extracted from Hα $T_{1\rho}$'s. The 313 K $T_{1\rho}$ and S_{CH} are also listed along with their uncertainties (superscript).

Residue	Amantadine-bound peptide					Apo peptide				
	E_a (kJ/mol)	τ_0 (ns)	τ_{313K} (μs)	$T_{1\rho}^{313K}$ (ms)	S_{CH}	E_a (kJ/mol)	τ_0 (ns)	τ_{313K} (μs)	$T_{1\rho}^{313K}$ (ms)	S_{CH}
L26	$20.9^{1.3}$	0.25	0.76	$3.1^{0.1}$	$0.42^{0.02}$	$13.5^{1.3}$	10.3	1.9	$1.3^{0.1}$	$0.44^{0.02}$
V27	$25.1^{7.8}$	0.03	0.40	$4.0^{0.3}$	$0.33^{0.04}$	17.1^{-}	3.8	2.8	$1.4^{0.1}$	$0.31^{0.02}$
V28	$32.4^{5.4}$	0.004	1.07	$2.6^{0.3}$	$0.46^{0.04}$	$18.3^{6.2}$	2.1	2.4	$1.2^{0.1}$	$0.46^{0.04}$
A29	$21.7^{1.3}$	0.18	0.76	$3.5^{0.1}$	$0.44^{0.02}$	$17.5^{1.3}$	1.7	1.4	$1.7^{0.1}$	$0.46^{0.02}$
A30	$15.9^{4.7}$	2.32	4.3	$1.9^{0.2}$	$0.60^{0.02}$	11.0^{-}	62.9	1.1	$1.2^{0.1}$	$0.60^{0.07}$
S31	$30.7^{7.8}$	0.0086	1.1	$2.3^{0.3}$	$0.50^{0.02}$	$13.6^{7.2}$	15.0	2.8	$0.9^{0.1}$	$0.40^{0.02}$
I33	$25.1^{1.8}$	0.027	0.40	$4.0^{0.3}$	$0.46^{0.02}$	17.1^{-}	4.4	3.2	$1.4^{0.1}$	$0.31^{0.02}$
G34	$12.1^{0.4}$	17.5	1.8	$1.7^{0.1}$	$0.60^{0.02}$	$5.4^{0.9}$	514	4.1	$0.9^{0.1}$	$0.69^{0.09}$
I35	$22.2^{1.3}$	0.16	0.79	$3.1^{0.1}$	$0.42^{0.02}$	$12.0^{1.3}$	18.0	1.9	$1.3^{0.1}$	$0.42^{0.02}$
L36	$30.2^{2.1}$	0.010	1.1	$2.2^{0.2}$	$0.48^{0.04}$	$18.6^{8.1}$	1.8	2.3	$1.2^{0.1}$	$0.44^{0.02}$
L38	$20.6^{9.9}$	0.18	0.48	$2.9^{0.2}$	$0.35^{0.02}$	9.6^{-}	96.6	3.8	$1.3^{0.1}$	$0.33^{0.07}$
Mean	23.3 ±6.2		0.89 ±0.41	2.8 ±0.8		14.0 ±4.2		2.8 ±0.9	1.3 ±0.2	

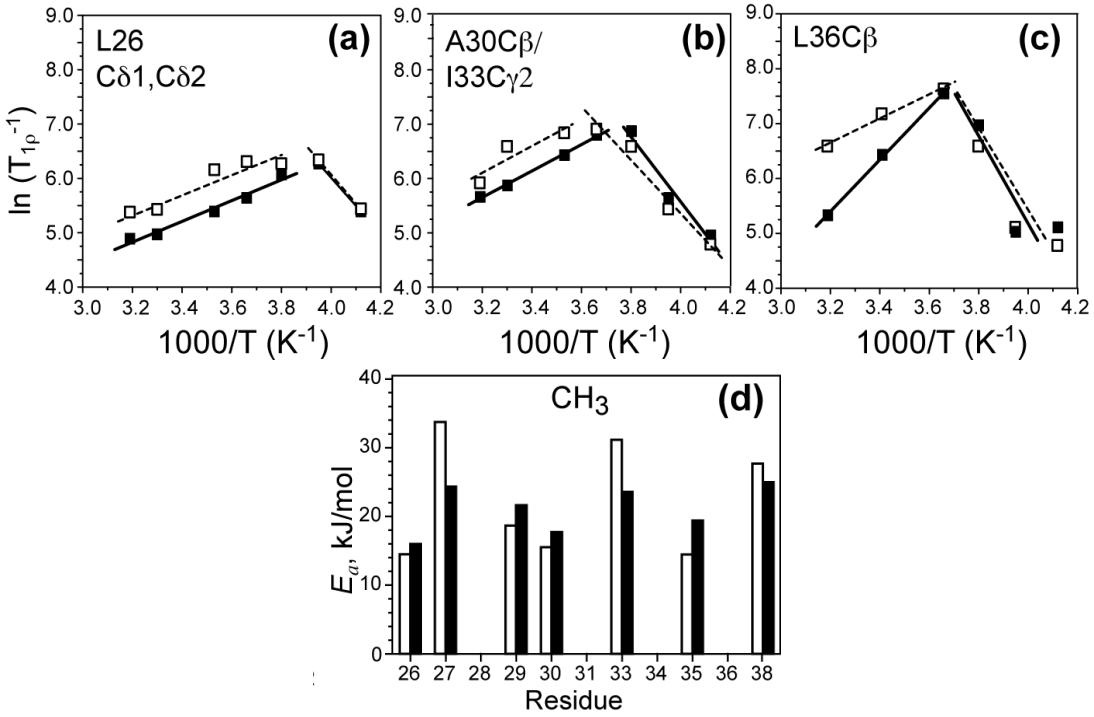

Figure 8.7. (a-c) $\ln\left(T_{1\rho}^{-1}\right)$ versus 1000/T curves for several M2TMP sidechains. (a) L26 methyl Cδ1/ Cδ2. (b) A30 Cβ and I33 Cγ2 methyl groups. (c) L36 Cβ. Apo data: open squares and dashed lines. Amantadine-bound data: filled squares and solid lines. (d) Activation energy (kJ/mol) of the methyl protons. The average E_a difference between the apo and bound peptides is ~20%.

Discussion

M2TMP uniaxial diffusion is the main motion driving $T_{1\rho}$ relaxation

The motivation for this work is to quantify the motion of M2TMP that is responsible for exchange broadening of its NMR spectra in phosphocholine bilayers at physiological temperatures, and to understand the origin of amantadine-induced line narrowing.

The exchange broadening is due to microsecond motion of the peptide that interferes with ^{13}C-^{1}H and ^{15}N-^{1}H dipolar decoupling and cross polarization. We assign the motion to whole-body uniaxial rotational diffusion of the M2 helical bundle. The presence of this uniaxial diffusion has been previously shown based on the lineshapes of ^{2}H quadrupolar spectra, ^{15}N static powder spectra, and ^{15}N-^{1}H and ^{13}C-^{1}H dipolar couplings (*48*). Two lines of evidence support the assignment of the $T_{1\rho}$ relaxation mechanism to this uniaxial diffusion.

First, all eleven measured residues exhibit rapid $T_{1\rho}$ relaxation at high temperatures, and all $T_{1\rho}$ values are increased by amantadine. Such across-the-board effects can only result from a whole-body motion. Second, the two-dimensional Brownian diffusion theory of Saffman and Delbrück predicts a rate of $10^5\ s^{-1}$ for the uniaxial diffusion of the M2 helical bundle, which agrees well with the time scale probed by the $T_{1\rho}$ experiments.

The presence of whole-body motion does not exclude additional internal motions. Sidechain motions are certainly present, although they do not interfere with the extraction of the rates and activation energy of uniaxial diffusion from the backbone Hα $T_{1\rho}$ data. The clearest manifestation of sidechain motions is the fact that the methyl protons have longer $T_{1\rho}$'s than the backbone protons, and the methyl ^{1}H $T_{1\rho}$'s are similar between the apo and bound peptides at high temperatures (Table 8.S3). These observations are not surprising, since the fast methyl rotation on the nanosecond time scale pre-averages the dipolar second moment, and thus reduce the relaxation rates (Equation 8.1). The local nature of the methyl rotation also makes the motion less sensitive to amantadine binding. The full $T_{1\rho}$ dependence includes spectral densities at the ^{1}H and ^{13}C Larmor frequencies, which are more relevant time scales for the methyl rotation. Thus, Equation 8.1 does not apply fully to methyl groups. Since the main purpose of this study is to understand the motion that causes exchange broadening of the NMR spectra, but sidechain methyl ^{13}C signals do not suffer from exchange broadening, we do not consider the combined motion of three-site jumps and uniaxial diffusion experienced by the methyl groups further. Another manifestation of possible segmental motions is the distribution of E_a. Specifically, the G34 E_a is two standard deviations lower than the average, suggesting the local motion at this residue (*vide infra*).

Correlation time of M2TMP diffusion and origin of spectral line narrowing by amantadine

The three-fold shorter correlation time of the amantadine-bound M2TMP (Table 8.1) explains the amantadine-induced line narrowing of the peptide spectra. The faster motional rates better avoid the intermediate time scale condition, thus alleviating line broadening. The faster diffusion rates result from the one to two orders of magnitude reduction of the

prefactor τ_0, as obtained from the high-temperature intercepts of the $\ln\left(T_{1\rho}^{-1}\right)$ curves. The intercept depends both on τ_0 and the dipolar second moment (Equation 8.9), whose exact magnitude differs somewhat between different theories, depending on how many spin interactions are included and whether the MAS or the static condition is operative (*27, 60, 61*). However, the ratio of the intercepts between the apo and bound peptide depends only on τ_0. Thus, the relative size of τ_0 between the apo peptide (long τ_0) and the bound peptide (short τ_0) is unambiguous.

The shorter τ_0 of the amantadine-bound M2TMP indicates higher attempt rates of motion, which suggest that the M2 helices form better-packed tetramers in the presence of amantadine. Amantadine may interact with all four helices of the tetramer, thus serving as a non-covalent linker that brings the four helices together to form a more cohesive tetrameric bundle. A more cohesive helical bundle can diffuse faster, and would also have structurally and dynamically more homogeneous individual helices. This interpretation is consistent with the relative lack of correlation time distribution for the bound peptide (*vide infra*), as manifested by the sharpness of the $T_{1\rho}$ minima, and is also consistent with disulfide cross linking data that indicate increased tetramer association in the presence of amantadine (*63*). Thus, the reduced τ_0 of the bound M2TMP suggests that amantadine is centrally located in the pore of the channel, shared by all four helices, consistent with the binding site seen in a recent crystal structure (*64*). In comparison, a solution NMR study (*52*) found four rimantadine molecules at the lipid-facing surface of each channel. It is difficult to imagine how this surface binding motif would homogenize the peptide conformation and speed up its motion.

A question that is beyond the scope of the current study is the correlation time distribution of apo M2TMP, which is manifested by the broad $T_{1\rho}$ minima of the apo peptide. The τ distribution suggests that without amantadine, the M2 helical bundles are floppier, with more internal degrees of freedom, and may exhibit dynamic heterogeneities between different tetramers. Such dynamic heterogeneity may be functionally relevant, as it may allow the apo peptide to adopt appropriate conformations to achieve its many functions, including channel activation, gating, and inhibition.

The activation energy of M2TMP uniaxial diffusion is related to membrane viscosity

A basic assumption in our dynamic analysis is that the rotational diffusion of a membrane protein in lipid bilayers can be considered an activated process that follows an Arrhenius law (Equation 8.7). The linearity of the observed $\ln\left(T_{1\rho}^{-1}\right)$ with respect to 1000/T at high temperatures (Figure 8.5) validates this assumption, but it is of interest to consider the physical basis for the activated diffusion. Membrane protein diffusion in lipid bilayers requires the availability of free volume in the vicinity of the protein, which is achieved by discrete hopping of the lipid molecules. Thus, activated lateral and rotational diffusion of membrane proteins has its molecular origin in the free volume theory of liquids (*65, 66*). Considered in this light, the activation energy essentially reflects the macroscopic viscosity of the membrane. Higher activation energies indicate higher viscosities. Thus, the higher E_a of the amantadine-bound peptide indicates that excess amantadine increases the membrane viscosity. If this is true, then the lipid ^{1}H $T_{1\rho}$ values should be affected by the excess amantadine outside the channel in the bilayer, in the same manner as the protein.

Examination of several resolved lipid ^{13}C signals confirms that there is indeed an amantadine-induced increase of the lipid E_a. Figure 8.8 shows the $\ln\left(T_{1\rho}^{-1}\right)$ curves of the lipid glycerol G3 and the acyl chain C2 signals. The excess-amantadine-containing membrane clearly has larger slopes than the amantadine-free membrane, similar to the peptide $T_{1\rho}$ behavior. The amantadine-bound samples in our experiments contain 8-fold molar excess of amantadine to the peptide, or 32-fold excess amantadine to the channel. The excess amantadine partitions into the bilayer (*67, 68*). Paramagnetic relaxation enhancement NMR data indicate that amantadine is located at the interfacial region of the DMPC bilayer with the amine group pointing to the surface (*69*). This depth and orientation are consistent with the amphipathic nature of amantadine, with its hydrophobic adamantane cage close the hydrocarbon core and its polar ammonium moiety pointing to the polar region of the bilayer.

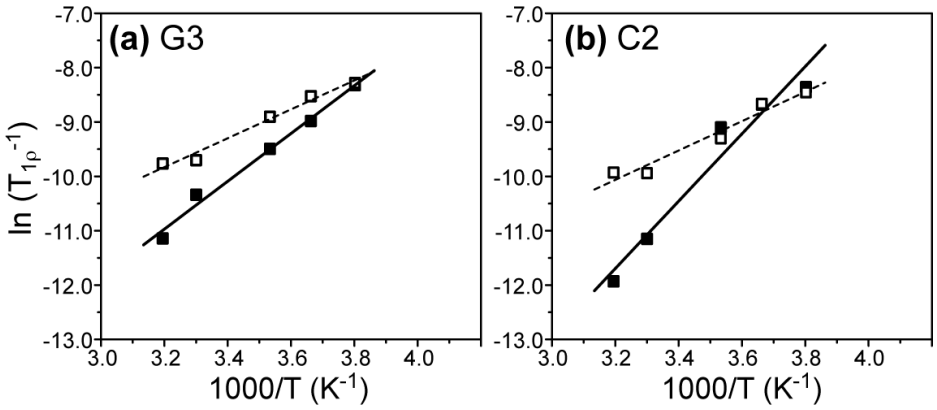

Figure 8.8. $\ln\left(T_{1\rho}^{-1}\right)$ versus 1000/T curves for several lipid ^{13}C signals in M2TMP-containing DLPC bilayers. (a) Glycerol backbone G3. (b) Acyl chain C2. Apo data: open squares and dashed lines; Amantadine-bound data: filled squares and solid lines.

Our recently measured lipid ^{13}C T_2 relaxation times at 313 K in peptide-free DLPC bilayers showed no discernible difference between amantadine-containing and amantadine-free bilayers (*53*), in contrast to the current lipid ^{1}H $T_{1\rho}$ data. This discrepancy is likely due to the presence of the peptide in the current measurements but the lack of the peptide in the previous T_2 experiments. Membrane viscosity is a function of molecular crowding: peptide-containing bilayers have much smaller free volumes for amantadine than pure lipid bilayers, thus amantadine may cause detectable fluidity changes only in M2-containing bilayers.

The viscosity origin of the activation energy of M2TMP diffusion also explains the asymmetric slope of the $\ln\left(T_{1\rho}^{-1}\right)$ curves on the two sides of the $T_{1\rho}$ minimum. Both the apo and bound peptides have steeper slopes or larger apparent activation energies on the low temperature side. Since this $T_{1\rho}$ minimum is associated with phase transition of the DLPC bilayer, the slope increase at low temperature is caused by the significant viscosity increase of the gel-phase membrane compared to the liquid-crystalline phase. Thus, the M2TMP rotational diffusion is not a single motional process above and below the lipid phase transition temperature, in contrast to most other motions that have been characterized by NMR (*23, 70*).

The viscosity origin of the activation energy may also partly explain the E_a distribution among the residues. Since a perfectly rigid-body motion should have a single E_a, the observed E_a distribution beyond the experimental uncertainty must reflect additional motions, which may result from varying membrane viscosity across the bilayer thickness. The abnormally low E_a of G34 may then be partly due to the location of G34 at the center of the TM helix and thus at the center of the bilayer, which has the lowest viscosity due to large-amplitude motions of the lipid chain ends. While the exact nature of the local G34 motion is unknown, the conclusion of increased conformational flexibility is consistent with a large number of NMR parameters for this site: its ^{15}N anisotropic chemical shifts, N-H dipolar coupling (*71*), and ^{15}N isotropic chemical shifts were all found to change with drug binding (*53, 72*) and membrane composition (*73*).

The lipid-mediated influences of excess amantadine on the diffusion dynamics of M2TMP do not change the previous conclusion that the protein-bound amantadine causes site-specific conformational changes through direct amantadine-protein interactions. The structural changes are manifested as chemical shift perturbations that are highly site specific, with residues S31, G34, and V28 exhibiting large chemical shift perturbations while other residues showing little changes (*50, 53*).

Conclusion

The temperature-dependent ^{1}H $T_{1\rho}$ relaxation times shown here indicate that the uniaxial diffusion of the M2TMP in liquid-crystalline DLPC bilayers causes efficient ^{1}H $T_{1\rho}$ relaxation, and the diffusion rates are increased by amantadine through an increase in the attempt frequencies. The average motional correlation time at 313 K is 0.89 μs for the bound peptide and 2.8 μs for the apo peptide. The faster diffusion of the bound peptide suggests that amantadine induces more homogeneous and better-packed M2TMP tetramers by coordinating with all four helices. Thus, the well documented amantadine-induced NMR line narrowing is due to suppression of the intermediate time scale broadening.

From the linear relation of $\ln\left(T_{1\rho}^{-1}\right)$ with 1/T at high temperature, we extracted the

activation energy of the M2 uniaxial diffusion. The average E_a is 23.3 kJ/mol for the bound peptide and 14.0 kJ/mol for the apo peptide. The higher E_a of the bound peptide is attributed to larger membrane viscosity by excess amantadine, which is confirmed by the lipid $T_{1\rho}$ data.

Similar exchange broadening of the apo protein and line narrowing of the bound protein have also been reported for solution NMR spectra of M2(18-60) in DHPC micelles (*52*). There, the exchange broadening of the apo protein spectra was alleviated by the addition of 40 mM rimantadine. At 53-fold molar excess to the protein (0.75 mM), the excess rimantadine is expected to significantly increase the viscosity of the micelle interior, which may affect the dynamics of the micelle-bound rimantadine in a way that facilitates the observation of its NOEs with the protein.

The present study illustrates the rich information that can be obtained from temperature-dependent relaxation studies of membrane proteins. Compared to most relaxation NMR studies so far, which were targeted to either small molecules with a single motion (*23*) or macromolecules with a well-defined local motion (*74*), the present study examines the rates and energetics of the global motion of a membrane protein (*75*). It gives a glimpse into the energetic driving force behind membrane protein uniaxial diffusion, which is not easily obtained by other biophysical techniques (*28*).

References

1. Mandel, A. M., Akke, M., and Palmer, A. G. (1996) Dynamics of ribonuclease H: Temperature dependence of motions on multiple time scales, *Biochemistry 35*, 16009-16023.
2. Schaefer, J., Stejskal, E. O., and Buchdahl, R. (1977) Magic-Angle C-13 NMR Analysis of Motion in Solid Glassy Polymers, *Macromolecules 10*, 384-405.
3. Palmer, A. G., Kroenke, C. D., and Loria, J. P. (2001) Nuclear magnetic resonance methods for quantifying microsecond-to-millisecond motions in biological macromolecules, *Meth. Enzymol. Part B: NMR of Biol. Macromolecules 339*, 204-238.

4. Shaw, W. J., Long, J. R., Campbell, A. A., Stayton, P. S., and Drobny, G. P. (2000) A solid state NMR study of dynamics in a hydrated salivary peptide adsorbed to hydroxyapatite, *J. Am. Chem. Soc. 122*, 7118-7119.
5. Schmidt, C., Blumich, B., and Spiess, H. W. (1988) Deuteron two-dimensional exchange NMR in solids., *J. Magn. Reson. 79*, 269-290.
6. deAzevedo, E. R., Hu, W. G., Bonagamba, T. J., and Schmidt-Rohr, K. (2000) Principles of centerband-only detection of exchange in solid-state nuclear magnetic resonance, and extension to four-time centerband-only detection of exchange, *J. Chem. Phys. 112*, 8988-9001.
7. Palmer, A. G., Williams, J., and McDermott, A. (1996) Nuclear magnetic resonance studies of biopolymer dynamics, *J. Phys. Chem. 100*, 13293-13310.
8. Kay, L. E. (1998) Protein dynamics from NMR, *Nature Struct. Biol. supplement*, 513-517.
9. Ishima, R., and Torchia, D. A. (2000) Protein dynamics from NMR, *Nat. Struct. Biol. 7*, 740-743.
10. Lipari, G., and Szabo, A. (1982) Model-Free Approach to the Interpretation of Nuclear Magnetic-Resonance Relaxation in Macromolecules .1. Theory and Range of Validity, *J. Am. Chem. Soc. 104*, 4546-4559.
11. Clore, G. M., Szabo, A., Bax, A., Kay, L. E., Driscoll, P. C., and Gronenborn, A. M. (1990) Deviations from the simple 2-parameter model-free approach to the interpretation of N-15 nuclear magnetic relaxation of proteins, *J. Am. Chem. Soc. 112*, 4989-4991.
12. Jelinski, L. W., Sullivan, C. E., and Torchia, D. A. (1980) 2H NMR study of molecular motion in collagen fibrils, *Nature 284*, 531-534.
13. Munowitz, M., Aue, W. P., and Griffin, R. G. (1982) Two-dimensional separation of dipolar and scaled isotropic chemical shift interactions in magic angle NMR spectra, *J. Chem. Phys. 77*, 1686-1689.
14. Schaefer, J., Mckay, R. A., and Stejskal, E. O. (1983) Dipolar rotational spin-echo 13C NMR of polymers, *J. Magn. Reson. 52*, 123-129.

15. Hong, M., Yao, X. L., Jakes, K., and Huster, D. (2002) Investigation of molecular motions by Lee-Goldburg cross-polarization NMR spectroscopy, *J. Phys. Chem. B 106*, 7355-7364.
16. Yang, Z., Liivak, O., Seidel, A., LaVerde, G., Zax, D. B., and Jelinski, L. W. (2000) Supercontraction and backbone dynamics in spider silk: 13C and 2H NMR studies., *J. Am. Chem. Soc. 122*, 9019-9025.
17. Williams, J. C., and McDermott, A. E. (1995) Dynamics of the flexible loop of triosephosphate isomerase: the loop motion is not ligand gated., *Biochemistry 34*, 8309-8319.
18. Blume, A., Rice, D. M., Wittebort, R. J., and Griffin, R. G. (1982) Molecular dynamics and conformation in the gel and liquid-crystalline phases of phosphatidylethanolamine bilayers., *Biochemistry 21*, 6220-6230.
19. Smith, R. L., and Oldfield, E. (1984) Dynamic structure of membranes by deuterium NMR, *Science 225*, 280-288.
20. Schaefer, D., Spiess, H. W., Suter, U. W., and Fleming, W. W. (1990) 2D solid-state NMR studies of ultraslow chain motion: glass transition in aPP versus helical jumps in iPP., *Macromolecules 23*, 3431-3439.
21. Schaefer, J., Stejskal, E. O., and Mckay, R. A. (1984) Phenylalanine ring dynamics by solid-state 13C NMR, *J. Magn. Reson. 57*, 85-92.
22. Hagemeyer, A., Schmidt-Rohr, K., and Spiess, H. W. (1989) 2D NMR experiments for studying molecular order and dynamics in static and rotating solids, *Adv. Magn. Reson. 13*, 85-130.
23. Rothwell, W. P., and Waugh, J. S. (1981) Transverse Relaxation of Dipolar Coupled Spin Systems under Rf-Irradiation - Detecting Motions in Solids, *J. Chem. Phys. 74*, 2721-2732.
24. Kinsey, R. A., Kintanar, A., Tsai, M. D., Smith, R. L., Janes, N., and Oldfield, E. (1981) First observation of amino acid side chain dynamics in membrane proteins using high field deuterium nuclear magnetic resonance spectroscopy, *J. Biol. Chem. 256*, 4146-4149.
25. Opella, S. J. (1986) Protein dynamics by solid state nuclear magnetic resonance, *Methods in Enzym. 131*, 327-361.

26. Lee, K.-C., Hu, W., and Cross, T. A. (1993) 2H NMR determination of the global correlation time of the gramicidin channel in a lipid bilayer, *Biophys. J. 65*, 1162-1167.
27. Huster, D., Xiao, L. S., and Hong, M. (2001) Solid-state NMR investigation of the dynamics of the soluble and membrane-bound colicin Ia channel-forming domain, *Biochemistry 40*, 7662-7674.
28. Gennis, R. B. (1989) *Biomembranes: Molecular Structure and Function*, Springer, New York.
29. Bloom, M., Evans, E., and Mouritsen, O. G. (1991) Physical properties of the fluid lipid-bilayer component of cell membranes: a perspective, *Q. Rev. Biophys. 24*, 293-397.
30. Saffman, P. G., and Delbruck, M. (1975) Brownian motion in biological membranes, *Proc. Natl. Acad. Sci. U. S. A. 72*, 3111-3113.
31. Macdonald, P. M., and Seelig, J. (1988) Dynamic properties of gramicidin A in phospholipid membranes, *Biochemistry 27*, 2357-2364.
32. Prosser, R. S., Davis, J. H., Mayer, C., Weisz, K., and Kothe, G. (1992) Deuterium NMR relaxation studies of peptide-lipid interactions, *Biochemistry 31*, 9355-9363.
33. Pauls, K. P., MacKay, A. L., Söderman, O., Bloom, M., Tanjea, A. K., and Hodges, R. S. (1985) Dynamic properties of the backbone of an integral membrane polypeptide measured by 2H-NMR, *Eur. Biophys. J. 12*, 1-11.
34. Hong, M. (2007) Structure, topology, and dynamics of membrane peptides and proteins from solid-state NMR spectroscopy, *J. Phys. Chem. B. 111*, 10340-10351.
35. Yamaguchi, S., Huster, D., Waring, A., Lehrer, R. I., Tack, B. F., Kearney, W., and Hong, M. (2001) Orientation and Dynamics of an Antimicrobial Peptide in the Lipid Bilayer by Solid-State NMR, *Biophys. J. 81*, 2203-2214.
36. Hong, M., and Doherty, T. (2006) Orientation determination of membrane-disruptive proteins using powder samples and rotational diffusion: a simple solid-state NMR approach, *Chem. Phys. Lett. 432*, 296-300.
37. Lewis, B. A., Harbison, G. S., Herzfeld, J., and Griffin, R. G. (1985) NMR structural analysis of a membrane protein: bacteriorhodopsin peptide backbone orientation and motion, *Biochemistry 24*, 4671-4679.

38. Tian, F., Song, Z., and Cross, T. A. (1998) Orientational constraints derived from hydrated powder samples by two-dimensional PISEMA, *J. Magn. Reson. 135*, 227-231.
39. Park, S. H., Mrse, A. A., Nevzorov, A. A., De Angelis, A. A., and Opella, S. J. (2006) Rotational diffusion of membrane proteins in aligned phospholipid bilayers by solid-state NMR spectroscopy, *J. Magn. Reson. 178*, 162-165.
40. Aisenbrey, C., and Bechinger, B. (2004) Investigations of polypeptide rotational diffusion in aligned membranes by 2H and 15N solid-state NMR spectroscopy, *J. Am. Chem. Soc. 126*, 16676-16683.
41. Glaser, R. W., Sachse, C., Durr, U. H., Wadhwani, P., and Ulrich, A. S. (2004) Orientation of the antimicrobial peptide PGLa in lipid membranes determined from 19F-NMR dipolar couplings of 4-CF3-phenylglycine labels, *J. Magn. Reson. 168*, 153-163.
42. Pinto, L. H., Holsinger, L. J., and Lamb, R. A. (1992) Influenza virus M2 protein has ion channel activity, *Cell 69*, 517-528.
43. Pinto, L. H., and Lamb, R. A. (2007) Controlling influenza virus replication by inhibiting its proton flow, *Mol. BioSyst. 3*, 18-23.
44. Hay, A. J., Wolstenholme, A. J., Skehel, J. J., and Smith, M. H. (1985) The molecular basis of the specific anti-influenza action of amantadine, *EMBO J. 4*, 3021-3024.
45. Wang, C., Takeuchi, K., Pinto, L. H., and Lamb, R. A. (1993) Ion channel activity of influenza A virus M2 protein: characterization of the amantadine block., *J Virol. 67*, 5585-5594.
46. Sakaguchi, T., Tu, Q., Pinto, L. H., and Lamb, R. A. (1997) The active oligomeric state of the minimalistic influenza virus M2 ion channel is a tetramer *Proc. Natl. Acad. Sci. USA 94*, 5000-5005.
47. Luo, W., and Hong, M. (2006) Determination of the oligomeric number and intermolecular distances of membrane protein assemblies by anisotropic (1)H-driven spin diffusion NMR spectroscopy, *J. Am. Chem. Soc. 128*, 7242-7251.
48. Cady, S. D., Goodman, C., Tatko, C. D., DeGrado, W. F., and Hong, M. (2007) Determining the orientation of uniaxially rotating membrane proteins using unoriented samples: a 2H, 13C, AND 15N solid-state NMR investigation of the dynamics and orientation of a transmembrane helical bundle, *J. Am. Chem. Soc. 129*, 5719-5729.

49. Kovacs, F. A., and Cross, T. A. (1997) Transmembrane four-helix bundle of influenza A M2 protein channel: structural implications from helix tilt and orientation, *Biophys. J. 73*, 2511-2517.
50. Cady, S. D., and Hong, M. (2008) Amantadine-induced conformational and dynamical changes of the influenza M2 transmembrane proton channel, *Proc. Natl. Acad. Sci. U. S. A. 105*, 1483-1488.
51. Li, C., Qin, H., Gao, F. P., and Cross, T. A. (2007) Solid-state NMR characterization of conformational plasticity within the transmembrane domain of the influenza A M2 proton channel, *Biochim. Biophys. Acta 1768*, 3162-3170.
52. Schnell, J. R., and Chou, J. J. (2008) Structure and mechanism of the M2 proton channel of influenza A virus, *Nature 451*, 591-595.
53. Cady, S. D., Mishanina, T. V., and Hong, M. (2009) Structure of Amantadine-Bound M2 Transmembrane Peptide of Influenza A in Lipid Bilayers from Magic-Angle-Spinning Solid-State NMR: The Role of Ser31 in Amantadine Binding, *J. Mol. Biol. 385*, 1127-1141.
54. Carpino, L. A., and Han, G. Y. (1972) The 9-Fluorenylmethoxycarbonyl Amino-Protecting Group, *J. Org. Chem 37*, 3404-3409.
55. Ito, T., Gorman, O. T., Kawaoka, Y., Bean, W. J., and Webster, R. G. (1991) Evolutionary analysis of the influenza A virus M gene with comparison of the M1 and M2 proteins, *J. Virol. 65*, 5491-5498.
56. Traikia, M., Warschawski, D. E., Recouvreur, M., Cartaud, J., and Devaux, P. F. (2000) Formation of unilamellar vesicles by repetitive freeze-thaw cycles: characterization by electron microscopy and P-31-nuclear magnetic resonance, *Eur. Biophys. J. 29*, 184-195.
57. Hong, M., Gross, J. D., Rienstra, C. M., Griffin, R. G., Kumashiro, K. K., and Schmidt-Rohr, K. (1997) Coupling Amplification in 2D MAS NMR and Its Application to Torsion Angle Determination in Peptides, *J. Magn. Reson. 129*, 85-92.
58. Bielecki, A., Kolbert, A. C., de Groot, H. J. M., Griffin, R. G., and Levitt, M. H. (1990) Frequency-switched Lee-Goldburg sequences in solids, *Adv. Magn. Reson. 14*, 111-124.

59. van Rossum, B. J., de Groot, C. P., Ladizhansky, V., Vega, S., and de Groot, H. J. M. (2000) A method for measuring heteronuclear (H-1-C-13) distances in high speed MAS NMR, *J. Am. Chem. Soc. 122*, 3465-3472.

60. Mehring, M., Mehring, M., and Diehl, P. e. (1983) *Principles of high resolution NMR in solids*, Berlin ; New York : Springer-Verlag, Berlin ; New York.

61. Fares, C., Qian, J., and Davis, J. H. (2005) Magic angle spinning and static oriented sample NMR studies of the relaxation in the rotating frame of membrane peptides, *J. Chem. Phys. 122*, 194908.

62. Schmidt-Rohr, K., Clauss, J., and Spiess, H. W. (1992) Correlation of structure, mobility, and morphological information in heterogeneous polymer materials by two-dimensional wideline-separation NMR spectroscopy, *Macromolecules 25*, 3273-3277.

63. Cristian, L., Lear, J. D., and DeGrado, W. F. (2003) Use of thiol-disulfide equilibria to measure the energetics of assembly of transmembrane helices in phospholipid bilayers., *Proc. Natl. Acad. Sci. USA 100*, 14772-14777.

64. Stouffer, A. L., Acharya, R., Salom, D., Levine, A. S., Di Costanzo, L., Soto, C. S., Tereshko, V., Nanda, V., Stayrook, S., and DeGrado, W. F. (2008) Structural basis for the function and inhibition of an influenza virus proton channel, *Nature 451*, 596-599.

65. Galla, H. J., Hartmann, W., Theilen, U., and Sackmann, E. (1979) On two-dimensional passive random walk in lipid bilayers and fluid pathways in biomembranes, *J. Membr. Biol. 48*, 215-236.

66. Cohen, M. H., and Turbill, D. (1959) Molecular transport in liquids and glasses, *J. Chem. Phys. 31*, 1164-1169.

67. Subczynski, W. K., Wojas, J., Pezeshk, V., and Pezeshk, A. (1998) Partitioning and localization of spin-labeled amantadine in lipid bilayers: an EPR study, *J. Pharm. Sci. 87*, 1249-1254.

68. Wang, J., Schnell, J. R., and Chou, J. J. (2004) Amantadine partition and localization in phospholipid membrane: a solution NMR study, *Biochem. Biophys. Res. Commun. 324*, 212-217.

69. Li, C., Yi, M., Hu, J., Zhou, H. X., and Cross, T. A. (2008) Solid-state NMR and MD simulations of the antiviral drug amantadine solubilized in DMPC bilayers, *Biophys. J. 94*, 1295-1302.

70. Douglass, D. C., and Jones, G. P. (1966) Nuclear magnetic relaxation of n-alkanes in rotating frame, *J. Chem. Phys. 45*, 956-963.

71. Hu, J., Asbury, T., Achuthan, S., Li, C., Bertram, R., Quine, J. R., Fu, R., and Cross, T. A. (2007) Backbone structure of the amantadine-blocked trans-membrane domain M2 proton channel from Influenza A virus, *Biophys. J. 92*, 4335-4343.

72. Wang, J., Cady, S. D., Balannik, V., Pinto, L. H., DeGrado, W. F., and Hong, M. (2009) Discovery of spiro-piperidine inhibitors and their modulation of the dynamics of the M2 proton channel from influenza A virus, *J. Am. Chem. Soc.*, in press.

73. Luo, W., Cady, S. D., and Hong, M. (2009) Immoblization of the influenza A M2 transmembrane peptide in virus-envelope mimetic lipid membranes: a solid-state NMR investigation, *Biochemistry*, Epub ahead of print.

74. Batchelder, L. S., Sullivan, C. E., Jelinski, L. W., and Torchia, D. A. (1982) Characterization of leucine side-chain reorientation in collagen-fibrils by solid-state 2H NMR, *Proc. Natl. Acad. Sci. U. S. A. 79*, 386-389.

75. Reuther, G., Tan, K. T., Vogel, A., Nowak, C., Arnold, K., Kuhlmann, J., Waldmann, H., and Huster, D. (2006) The lipidated membrane anchor of full length N-Ras protein shows an extensive dynamics as revealed by solid-state NMR spectroscopy, *J. Am. Chem. Soc. 128*, 13840-13846.

Supporting Information

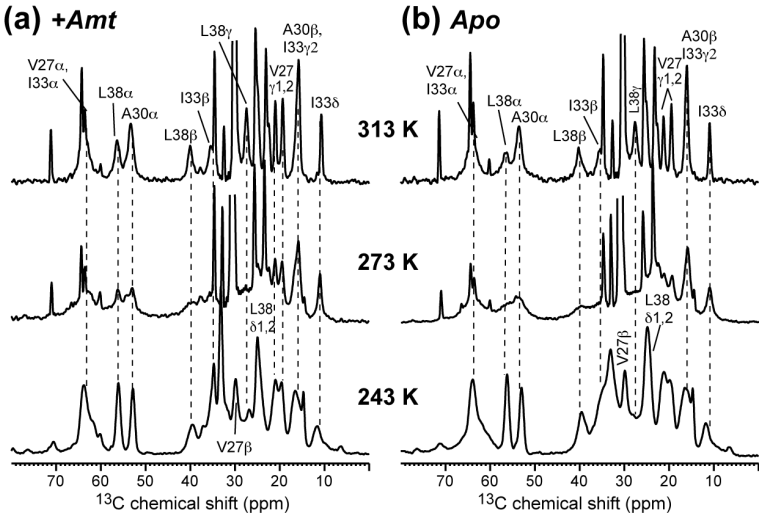

Figure 8.S1. 1D ^{13}C CP-MAS spectra of VAIL-M2TMP in DLPC bilayers at 313 K, 273 K, and 243 K. (a) With amantadine. (b) Without amantadine.

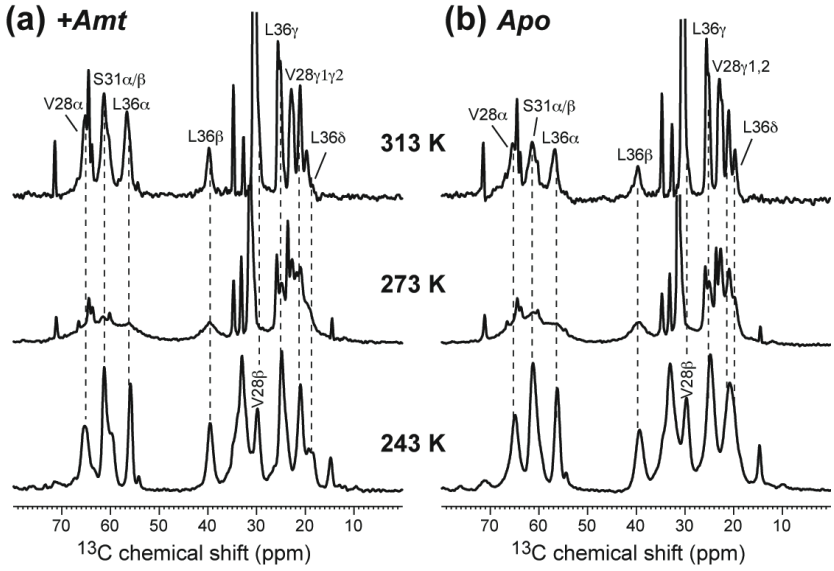

Figure 8.S2. 1D ^{13}C CP-MAS spectra of VSL-M2TMP in DLPC bilayers at 313 K, 273 K, and 243 K. (a) With amantadine. (b) Without amantadine.

Table 8.S1. Hα $T_{1\rho}$'s (ms) of M2TMP in the apo and amantadine (Amt) bound states in DLPC bilayers at various temperatures.

Site		313 K	303 K	293 K	283 K	273 K	263 K	253 K	243 K
L26	Apo	1.3	1.1		0.71	0.63	0.71	0.76	5.6
	Amt	3.1	2.2		1.6	0.87	0.66	1.3	5.2
V27	Apo	1.4	0.6		0.39	0.46	0.78	3.4	6.6
	Amt	4.0	3.2		2.6	1.6	0.66	3.4	7.1
V28	Apo	1.2		0.5		0.42	1.9	6.6	7.1
	Amt	2.6		0.8		0.41	1.5	6.9	5.8
A29	Apo	1.7	1.5		0.87	0.63	0.71	0.85	9.4
	Amt	3.5	2.3		1.3	0.93	0.69	1.7	8.8
A30	Apo	1.2	0.60		0.44	0.51	0.90	4.3	11.1
	Amt	1.9	1.9		1.7	1.2	0.72	4.1	9.9
S31	Apo	0.92		0.45		0.42	1.8	6.4	6.3
	Amt	2.3		0.95		0.41	1.0	8.6	7.0
I33	Apo	1.4	0.63		0.39	0.46	0.78	3.4	6.6
	Amt	4.0	3.2		2.6	1.6	0.66	3.4	7.1
G34	Apo	0.88	0.89		0.72	0.67	0.73	0.82	8.7
	Amt	1.7	1.5		1.0	0.88	0.69	1.7	6.5
I35	Apo	1.3	1.1		0.75	0.68	0.66	0.66	7.1
	Amt	3.1	2.4		1.1	0.90	0.63	1.2	6.5
L36	Apo	1.2		0.50		0.42	1.8	8.7	10.3
	Amt	2.2		1.1		0.41	0.95	8.6	7.2
L38	Apo	1.3	0.5		0.39	0.49	0.75	3.9	10.4
	Amt	2.9	2.8		2.9	2.0	0.74	3.7	8.1

Table 8.S2. Hβ $T_{1\rho}$'s (ms) of M2TMP in the apo and amantadine-bound states in DLPC bilayers at various temperatures.

Site		313 K	303 K	293 K	283 K	273 K	263 K	253 K	243 K
L26	Apo	1.9	1.5		0.81	0.70	0.74	0.76	8.7
	Amt	4.3	3.5		1.5	1.2	0.80	1.1	3.2
V27	Apo							2.9	4.8
	Amt							3.4	5.0
V28	Apo	0.83		0.41		1.1	2.0	6.5	6.0
	Amt	1.5		0.31			1.4	6.3	5.4
A29	Apo	2.9	2.5		1.4	1.8	1.3	1.3	7.0
	Amt	6.3	4.8		2.3	2.0	1.3	1.6	7.8
A30	Apo	2.7	1.4		1.1	1.0	1.4	4.3	8.3
	Amt	3.6	2.9		1.7	1.2	1.1	3.7	7.3
S31	Apo	0.92		0.46		0.42	1.8	6.8	5.9
	Amt	3.2		0.94			1.0	7.6	5.9
I33	Apo	1.6	0.74		0.39	0.50	0.78	2.5	3.9
	Amt	2.5	2.8		1.6	1.3	0.82	4.3	3.8
I35	Apo	1.7	1.3		0.73	0.64	0.69	0.73	5.1
	Amt	3.4	2.6		1.3	1.0	0.70	1.6	5.6
L36	Apo	1.3		0.74		0.47	1.3	5.9	8.1
	Amt	4.7		1.6		0.51	0.91	6.3	5.8
L38	Apo	1.4	0.71		0.39	0.42	0.55	3.0	6.8
	Amt	1.6	1.3		0.80	0.60	0.49	1.8	6.7

Table 8.S3. Methyl ^{1}H $T_{1\rho}$'s (ms) in M2TMP in the apo and amantadine-bound states in DLPC bilayers at various temperatures.

Site		313 K	303 K	293 K	283 K	273 K	263 K	253 K	243 K
L26 Cδ	Apo	4.8	4.5		2.3	1.9	2.0	1.8	4.5
	Amt	7.5	7.0		4.6	3.5	2.3	1.9	4.7
V27 Cγ	Apo	4.9	1.9		1.2	0.82	1.2	3.8	7.0
	Amt	6.3	4.6		2.5	1.5	1.1	4.1	6.3
V28 Cγ	Apo	1.9				1.4	2.5	8.0	7.1
	Amt	3.6				0.98	1.9	6.8	6.1
A29 Cβ	Apo	2.9	2.5		1.4	1.8	1.3	1.3	7.0
	Amt	6.3	4.8		2.3	2.0	1.3	1.6	7.8
A30 Cβ	Apo	2.7	1.4		1.2	1.0	1.4	4.3	8.3
	Amt	3.6	2.9		1.7	1.2	1.1	3.7	7.3
I33 Cγ2	Apo	5.2	2.1		1.3	1.1	1.3	3.1	7.2
	Amt	3.6	2.9		1.7	1.2	1.1	3.7	7.3
I33 Cδ	Apo	5.2	2.1		1.3	1.1	1.3	3.1	7.2
	Amt	7.0	5.0		2.5	1.6	1.4	3.2	5.4
sI35 Cγ2	Apo	2.9	2.5		1.4	1.8	1.3	1.3	7.0
	Amt	6.3	4.8		2.3	2.0	1.3	1.6	7.8
I35 Cδ	Apo	3.4	3.2		1.8	1.6	1.8	1.8	6.3
	Amt	7.3	5.3		3.1	2.4	1.7	1.9	7.0
L36 Cδ	Apo	5.7				1.8	2.5	8.3	8.5
	Amt	4.9				1.3	2.5	8.1	6.5
L38 Cδ	Apo	4.4	2.4		1.4	1.1	1.4	3.1	5.9
	Amt	6.8	4.5		2.4	1.4	1.2	3.6	5.1

Appendix A

Synthesis of ^{15}N Labeled Amantadine

Introduction

The following synthesis of ^{15}N labeled amanatdine is adapted from Stetter, H., J. Mayer, M. Schwarz, and K. Wulff. 1960. Über Verbindungen mit Urotropin-Struktur. 16. Beiträge zur Chemie der Adamantyl-(1)-Derivate. *Chemische Berichte-Recueil*. 93: 226–230. The original manuscript is written in German the procedure was kindly translated by Professor Klaus Schmidt-Rohr. The original synthesis was not for ^{15}N labeled product, so the reagents and glassware required for the procedure have been scaled accordingly. I will note where significant changes have been made from the original synthesis to improve experimental yield in order to make the most of the ^{15}N-labeled acetonitrile. As with any isotopically labeled synthesis, a practice run with unlabeled materials is strongly encouraged. Product numbers listed are accurate as of 2009.

The synthesis proceeds in two basic steps: the formation of a carbocation from the bromoadamantane to form the adamantyl amide, and the subsequent saponification of the amide to form the amine. The final step is acidification of the free amine to form a water-soluble salt. (Scheme A.1) The formation of the amide produces a product of high yield and purity, with experimental yields of 60-95% depending on the protocol used (see Part I). However, the saponification step and subsequent purification is somewhat low yield, with a final amantadine·HCl product yield of around 6%. A full ampule of $CH_3C^{15}N$ should yield approximately 20 mg of ^{15}N amantadine·HCl, which is more than sufficient for several NMR samples.

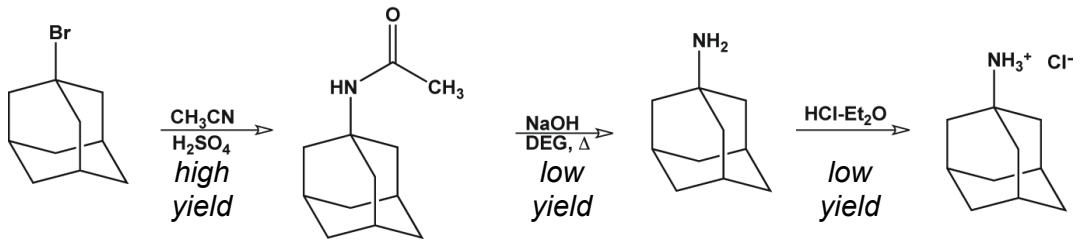

Scheme A.1. Synthesis of 1-aminoadamantane, or amantadine, from bromoadamantane. For the ^{15}N labeled product, $CH_3C^{15}N$ is used as a starting material.

Experimental Procedure

Part I Reactants: synthesis of adamantyl amide from 1-bromoadamantane.

Apparatus:

- Stir plate
- Round bottom flask, 5 mL (larger if needed)
- Micro stir bar, ~0.5 cm (Fisher Scientific)
- Plastic syringe for H_2SO_4 addition
    - Sigma-Aldrich Part # Z230723-1PAK (100/Pak)
    - Green, 1 mL, graduated in 0.1 mL increments.
- Micropipette, 1 mL tip size
- 100 mL beaker
- Small Büchner funnel and vacuum apparatus
- Filter paper to fit Büchner funnel
- 20 mL scintillation vial for final product

Reactants:

- 0.621 mL (500 mg ampule) of ^{15}N acetonitrile
    - Cambridge Isotopes Product # NLM-175-0.5

Other reactants scale as follows:

- 320 mg 1-bromoadamantane
    - Sigma-Aldrich Product # 109223
- 0.48 mL concentrated H_2SO_4
- 8.0 mL of chilled H_2O

Reactants for purification:

- 5.0 M NaOH as needed, for neutralization
- 5% solution (by weight) of sodium thiosulfate, as needed to remove remaining yellow bromine residue

NOTE: In the original procedure, the limiting reagent is 1-bromoadamantane. Obviously we want the limiting reagent to be the more expensive ^{15}N-acetonitrile, which also serves as the solvent. Although the Stetter, et al. protocol calls for only ~80mg of 1-bromoadamantane at this scale (for 500 mg of ^{15}N acetonitrile), this amount in this list of reagents is adjusted to use more of the ^{15}N label in the acetonitrile (320 mg of 1-bromoadamantane is listed above). Additional condition scanning can be conducted with unlabeled materials, but in my experience 6 times the published amount of bromoadamantane did not dissolve adequately in acetonitrile solution, but 4 times the amount dissolved adequately and gave significantly higher amounts of the amide. Note that if the reaction is scaled up in this manner, product yields for the first step will be 50-80% compared to 90-95% for the original protocol (relative

to 1-bromoadamantane). However, it is possible to make more than three times as much of the amide as would have been made in the original protocol despite the lower relative yields. The final solution in the morning may have solid stuck to the side that did not react, this will go away upon purification. The final solution will also be significantly more viscous than if only 80 mg bromoadamantane is used.

Part I Procedure: synthesis of adamantyl amide from 1-bromoadamantane.

1-bromoadamantane is measured out directly in the 5 mL round-bottom flask (RBF), which also contains the 0.5 cm stir bar. ^{15}N acetonitrile is added directly from the ampule with stirring until some solid dissolves. It is not necessary to completely dissolve the solid before addition of the acid. 0.48 mL of concentrated H_2SO_4 is added dropwise over 3-5 minutes using the 1 mL graduated syringe. After approximately 75% of the H_2SO_4 has been added, bubbles and white precipitate form in the vial. The solution will warm slightly, but not approaching boiling. Approximately 30-45 minutes after the addition of H_2SO_4, small amounts of bromine gas will begin to evolve, as evidenced by a brown/red residue on the rim of the vial. Loosely cap with a septa overnight. At this point, the solution is slightly yellow and precipitate remains.

In the morning, the solution is red/brown and translucent (Figure A.1). Stop the reaction 20-24 hours after the H_2SO_4 was added. Pouring the red/brown solution into chilled H_2O stops the reaction. White precipitate immediately forms. (**NOTE:** It is **not** recommended to use a glass pipette to extract the red solution out of the flask, because the final solution is very viscous and will stick to the glass pipette. If water is used to wash out the pipette, precipitate will form on the inside of the glass and it is very difficult to remove.) If the red solution is sticking to the sides of the RBF, it will be necessary to add cold water to the RBF and attempt to extract the solid with a glass pipette or spatula.

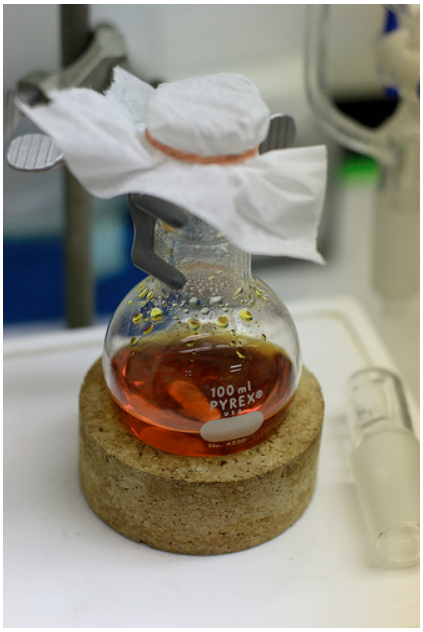

Figure A.1: Synthesis of adamantyl amide from 1-bromo-adamantane. The solution is red-orange in color and translucent after an overnight reaction with concentrated H_2SO_4.

Neutralize the solution with 5.0 M NaOH, and test with pH paper to ensure a pH of 7.0 – 9.0. Filter the solution with the filter paper and Büchner funnel, connected to a vacuum apparatus to remove most of the water. Transfer the solid to a 20 mL scintillation vial and dry overnight in a lyophilizer or an oven. If using the lyophilizer, freeze the sample in liquid nitrogen before putting under vacuum. If some yellow bromine residue remains, the product can be washed with a 5% solution (by weight) of sodium thiosulfate to remove residual the bromine.

Part II Reactants: saponification of adamantyl amide by NaOH in diethylene glycol.

Apparatus:

- Hot plate
- Sand
- A small open dish for the sand bath (less than 4" in diameter)
- Thermometer rated to at least 200 °C
- 10 mL round bottom flask with 14/20 neck
- Small condenser with 14/20 neck

- Chilled water supply and tubing to connect condenser
- Plastic micropipette, 1 mL tip size
- 14/20 septa
- Large gauge disposable needle, size 18G 1 ½" (Pink label #305196)
- Ring stand and small clamp
- 20 mL scintillation vials (several)

Reactants:

- X g of product (adamantyl amide) from first step
- 2X g of NaOH, crushed
- 20X mL of diethylene glycol

Part II Procedure: saponification of adamantyl amide by NaOH in diethylene glycol.

Directly weigh out the crushed NaOH into the 10 mL round bottom flask. Add the appropriate amount of diethylene glycol (digol) to the flask using the 1 mL micropipette tip and swirl slightly to distribute the NaOH throughout the solvent. At this time, also weigh out an appropriate amount of adamantyl amide into a small vial. Place the thermometer in the sand bath next to the round bottom flask, and place the flask in the sand so that half of it is covered. Gently heat the NaOH solution in the sand bath at ~70 °C to try and get some of the solid to dissolve. After about an hour, or when a slight yellow tinge appears in the solution, add the premeasured adamantyl amide. The solids are not highly soluble in the digol at this temperature. Bury the flask back in the sand bath, clamp the condenser apparatus to the ring stand, and insert into the round bottom flask. Wrap a small amount of Teflon tape around the joint to prevent leakage. Plug the top of the condenser with a 14/20 septa and insert a large gauge needle into it for venting. Attach the tubes to the condenser, start the chilled water and turn the hot plate to the appropriate setting (for the FisherSci hot plate, the setting is between 150-180 on the temperature dial). Reflux the solution with the sand at 130-140 °C for 12-18 hours. If specks of solid remain, reflux for another few hours. It will turn yellow after a short time and then brown after a few hours.

When the solution is done refluxing, turn off the hot plate and remove the flask from the sand, allowing it to cool completely. Dilute the digol solution with room temperature water until it is thin enough to be pipetted out of the flask. Using a glass pipette, transfer the digol solution into a 20 mL scintillation vial, using as much water as needed to rinse out the flask completely. Also rinse off the condenser apparatus with water or ether directly into the

10 mL RBF or the extraction vial. If this is not done, white product will be seen on the condenser after it is allowed to cool and dry off.

Part III Reactants: acidification and purification of amantadine.

Apparatus:

- Ring stand and small clap
- 20 mL scintillation vials (several)
- Funnel
- Filter paper
- Pasteur pipettes and bulbs
- 6" hypodermic needle and glass syringe
- Balloon filled with N_2 gas attached to a syringe with a small gauge needle

Reactants:

- Diethyl ether
- Magnesium sulfate
- 2M HCl in ether
    - Sigma-Aldrich Product # 455180
- Water
- Methylene chloride
- 0.1 M HCl, aqueous

Part III Procedure: acidification and purification of amantadine.

The digol solution will be extracted in the 20mL scintillation vial or a larger vial or a small separatory funnel if needed. For the 20 mL scintillation vial scale: using ~10-15mL of ether each time, extract the digol solution 3-4 times, shaking and venting the vial to ensure complete extraction. The layers will separate into organic and aqueous layers – we will be keeping the organic layer, which contains the amine (aminoadamantane/amantadine at this point) free base. With the scintillation vial this extraction involves siphoning the digol layer out of the vial with a Pasteur pipette, and transferring to a separate vial. The final ether/free amine solution will be quite yellow with brown bubbles of digol coming in and out of solution when it is shaken. Dry the ether/free amine solution over magnesium sulfate for ~30 minutes and filter through a filter paper and funnel into a clean vial.

In order to prevent spillage, fasten the final vial containing ether/free amine to a ring stand with a clamp. The ether/free amine solution will be acidified using neat HCl in ether solution or by bubbling HCl gas through the solution. For the neat HCl in ether, insert the N_2 filled balloon/needle into the septa sealed lid of the ether container. This is to ensure that the headspace remains inert after removing liquid. Insert the 6" hypodermic needle carefully into the septa, being sure to hold in the plunger as the pressure from the HCl/ether gas may cause it to rise. Carefully extract 2mL of the ether solution and inject it into the vial containing the ether/free amine solution. A white precipitate will form immediately. If needed, inject more HCl/ether into the ether/free amine vial to ensure complete acidification. After a few moments, brown greasy digol will begin to crash out on the sides.

Dry down the ether/amantadine·HCl solution under a stream of N_2 gas. The final product will be quite impure at this point. Once almost all of the ether has been removed, bring the product back up in ~10 mL water and shake to rinse the sides. Finally, add ~10mL of methylene chloride and shake to mix, venting the vial after shaking. Most of the brown impurity will go into the $MeCl_2$ layer, while small white amt·HCl precipitate remains in the water layer. After a few moments, the amt·HCl will dissolve into the water layer. Using the same procedure as before, siphon off the $MeCl_2$, and keep the layer in a separate vial. Extract a few more times until the $MeCl_2$ does not absorb any more color. Back-extract the $MeCl_2$ with 0.1 M HCl (aqueous) to ensure no free amine remains in the organic layer. Combine the water layers and wait a few minutes until any remaining $MeCl_2$ falls to the bottom, and remove the small amount via Pasteur pipette. Freeze and lyophilize the final product. A small amount of greasy brown residue may remain, but continue lyophilizing until all of the digol evaporates. Some brown residue may remain after lyophilization, but it should be pure enough by NMR (~95%) for the final use with protein samples. If necessary, the final product can be extracted with $MeCl_2$ a few more times or recrystalized.

To recrystalize, add a few drops of ethanol to the final dried product. This will be enough to solubilize the entire amount of product and impurity. Fill the rest of the 20mL scintillation vial with ether, and place in the 4 °C fridge or freezer overnight. Small brownish crystals will crash out and eventually sink to the bottom. After a day or two, remove most of the ether and transfer it to another vial to continue recrystallizing any

remaining product, although the amount will be small. Lyophilize the crystals that have collected at the bottom and bring back up in D_2O for analysis. Or, the crystals can be brought up directly in water and lyophilized, producing a very fluffy white powder resembling lyophilized lipids. These crystals will be very pure. Final purity of ^{15}N amt·HCl is confirmed through ^{1}H solution NMR and ^{15}N solid-state NMR.

Figure A.2: Recrystalization of amt·HCl in ethyl ether and ethanol.

Experimental Results and NMR Spectra

- Adamantyl amide from Step I: 250-270 mg, 40-80% yield relative to bromoadamantane depending on amount of bromoadamantane used.
- Amt·HCl after recrystallization: 6-9 mg, 5-6% yield relative to adamantyl amide. (8.5 mg amt·HCl from 215.6 mg adamantyl amide.)
- Amt·HCl purity before recrytallization: 46 %. After recrystallization: 92 %.

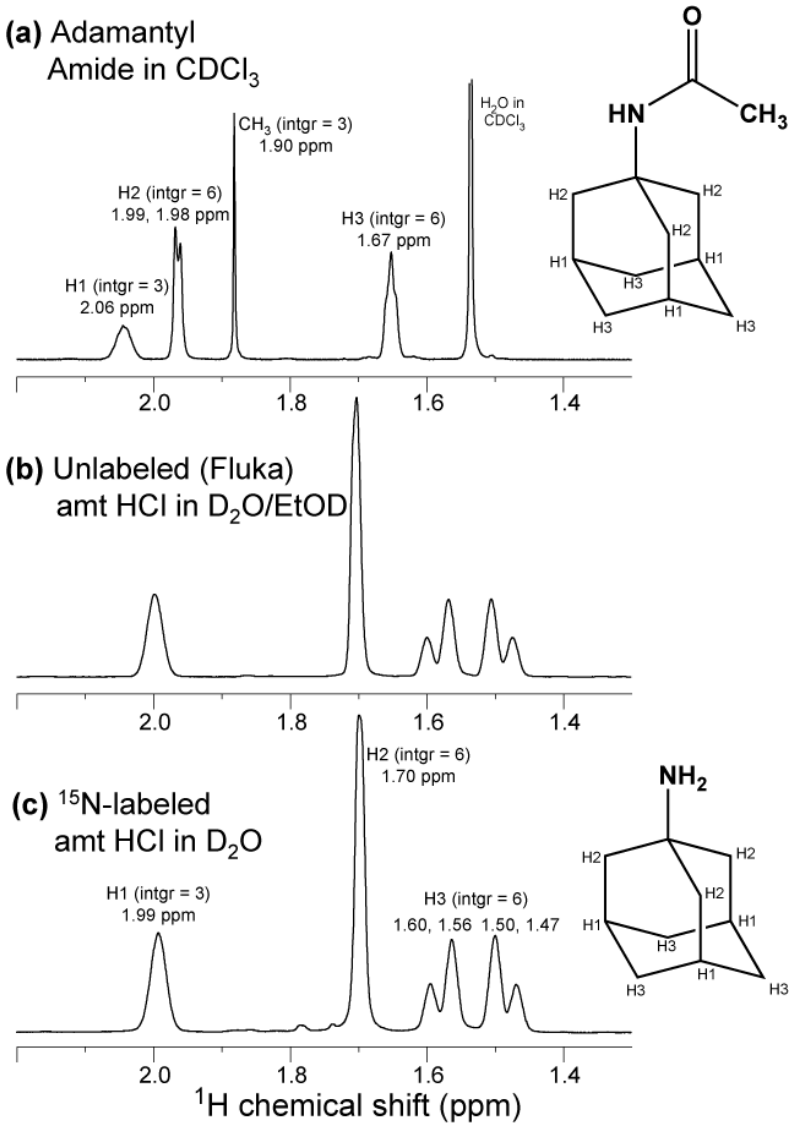

Figure A.3: ^{1}H solution NMR spectra of (a) adamantyl amide in CH_3Cl, (b) commercial unlabeled amt·HCl (Fluka) in D_2O/EtOD and (c) recrystallized ^{15}N amt·HCl in D_2O.

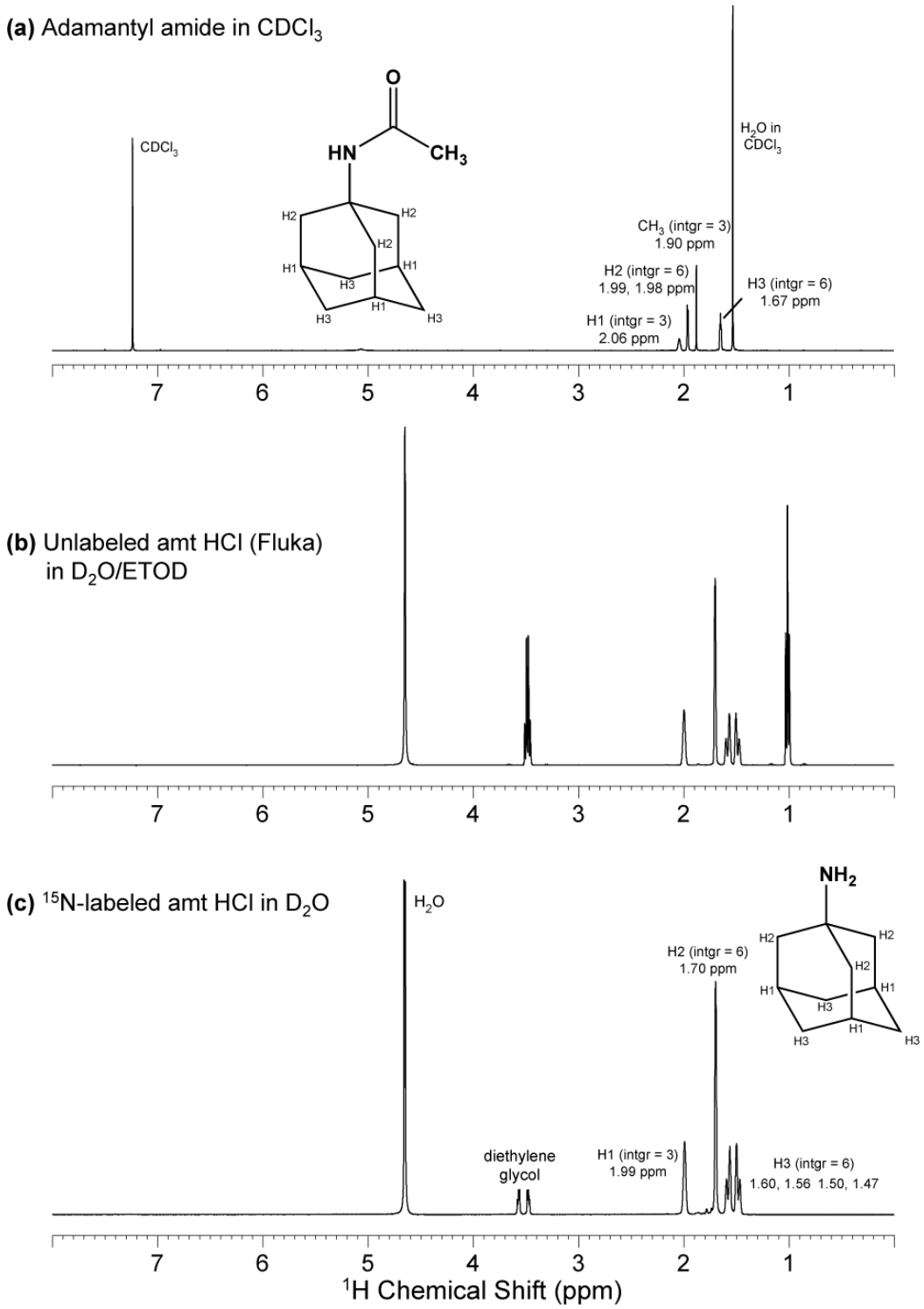

Figure A.4: Full ^{1}H solution NMR spectra of (a) adamantyl amide in CH_3Cl, (b) commercial unlabeled amt·HCl (Fluka) in D_2O/EtOD and (c) recrystallized ^{15}N amt·HCl in D_2O. ~3.5 ppm peak in (c) is residual diethylene glycol, an ~8% impurity in this sample after recrystallization.

Appendix B

Temperature calibration of 4 mm MAS probes using ^{207}Pb chemical shift

Introduction

In solid-state NMR, accurate knowledge of sample temperature is often an important consideration. When a sample is subjected to magic angle spinning (MAS), the various airflows involved, the physical rotation of the sample at a high rate, the high magnetic field, and multiple radiofrequency pulses (*1*) can all lead to changes of the sample temperature inside the MAS rotor. Most NMR probes are designed with the sample thermocouple in the stator, but it is difficult to measure the sample heating or temperature gradients that may be occurring inside the rotor. The purpose of this study is to determine the effects of high versus low airflow from the variable temperature unit, especially at low temperature, in order to have accurate temperature reporting for the variable temperature $T_{1\rho}$ data shown in Chapter 8.

The ^{207}Pb chemical shift of lead nitrate, $Pb(NO_3)_2$, has been shown to be linearly sensitive to temperature changes over the range of 143 K to 423 K (*2*). This temperature range also provides desirable ^{207}Pb linewidths under MAS. At ambient temperatures, the chemical shift change that occurs with a 0.5 K temperature change is equal to the spectral linewidth of the $Pb(NO_3)_2$ peak. Previous studies (*2*) have shown that temperature changes as small as 0.1 K can be observed through ^{207}Pb chemical shift changes given enough signal to noise. Thus, $Pb(NO_3)_2$ can be used as a probe to measure the effects of variable temperature air flow and sample temperature gradients within the rotor. ^{207}Pb chemical shift varies linearly with temperature, and it has been shown experimentally (*2*) that the chemical shift changes at the rate of 0.753 ppm/K. By conducting a series of experiments at several temperatures, we are able to observe the relationship between the variable temperature air flow and sample temperature.

Sample Packing and Data Acquisition

The $Pb(NO_3)_2$ powder was obtained from Dr. Sam Houk's laboratory at Iowa State University. Two samples with different types of sample packing were prepared for this study. The first sample packing, shown in Figure B.1a, contains a 4 mm PTFE spacer at the bottom of the rotor, with approximately 120 mg of $Pb(NO_3)_2$ packed on top of the spacer. In this sample, the $Pb(NO_3)_2$ is not constrained to a uniform density, so there may be a gradient of sample concentration throughout the rotor as the lead nitrate is a loose powder. This sample also contained a large amount of material, which was intended to fill the majority of the rotor for observation of sample temperature gradients. The second sample packing, shown in Figure B.1b, contains a 4 mm PTFE spacer at the bottom of the rotor, and a 2 mm PTFE spacer on top of the sample powder. Approximately 40 mg of $Pb(NO_3)_2$ powder is sandwiched tightly between the spacers in order to produce a compact sample that cannot shift in the rotor, and should not experience much of a temperature gradient.

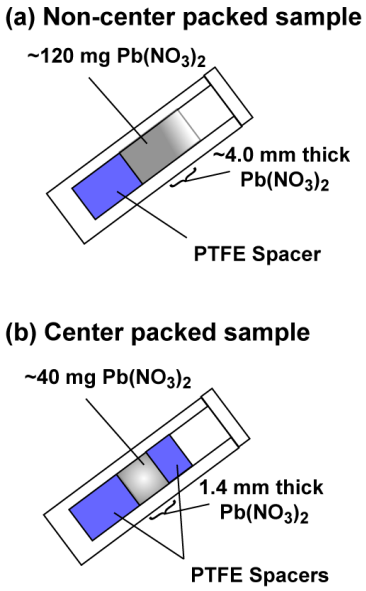

Figure B.1. Rotor packing of $Pb(NO_3)_2$ for variable-temperature air flow calibration. (a) Non-center packed sample contains a 4 mm PTFE spacer at the bottom of rotor and approximately 120 mg of $Pb(NO_3)_2$. (b) Center packed sample contains approximately 40 mg of $Pb(NO_3)_2$, sandwiched between a 4 mm PTFE spacer at the bottom of rotor and a 2 mm spacer at the top of the rotor.

NMR experiments were carried out on a Bruker AVANCE-600 (14.1 Tesla) spectrometer (Karlsruhe, Germany) using a 4 mm MAS probe. The spinning speed was 7 kHz for all experiments in order to simulate conditions used for most membrane protein samples on this machine. Spectra were obtained with a single pulse experiment in four scans with an acquisition time of 51 ms. Although the $Pb(NO_3)_2$ peak was not calibrated to tetramethyl lead (*3*), the spectrometer reference value was calculated such that at 273 K the chemical shift of $Pb(NO_3)_2$ was near -3810 ppm. Bielecki, et al. arbitrarily calibrated the 273 K peak to be 0 ppm since the absolute chemical shift is unimportant, only the relative chemical shift change with temperature is of interest.

Flow Calibration and Variable Temperature Data

As mentioned above, the goal of this study was to determine how different flow rates from the variable temperature unit affect the sample temperature, and whether or not the stator thermocouple gives an accurate temperature reading when the VT air is at a high flow rate. Not only can the flow rate be adjusted in the EDTE window in Topspin or XWinNMR, there is also a manual flow control knob inside the Variable Temperature Unit in the spectrometer cabinet. When the top of the case is removed, a small black knob can be found on the upper right-hand corner when facing the case. When adjusting the airflow in this fashion, the VT air hose should be connected to a flow meter, and the airflow in the EDTE window should be at the maximum value of 2000 L/h. To adjust the airflow, pull the knob towards the left-hand side of the case, and turn until the desired flow is obtained.

The flow meter used to calibrate these experiments consisted of three flow meters attached to one hose, each reading a maximum value of 10 L/min. The resultant flow is read as a combination of the three flow meters, for example 10/10/9 equals 10 L/min, 10 L/min and 9 L/min respectively, for a total flow of 29 L/min. The reading was taken when the EDTE window flow rate was set at 2000 L/h, and the airflow knob was manually adjusted to obtain the appropriate flow readings. When the flow meters read 10/10/9 (“high flow”) this corresponds to a total flow rate of approximately 1740 L/h, which is close to the EDTE value of 2000 L/h. When the flow meters read 6/6/7 (“low flow”) this corresponds to a total flow

rate of approximately 1140 L/h. Thus the EDTE window flow rate does not necessarily equal the actual flow out of the VT air hose, and care must be taken to ensure appropriate flow.

The resultant spectra are shown in Figure B.2. The temperatures reported for each set of spectra are the EDTE window readings, however it will be shown that this reading may not be completely accurate. For the non-center packed sample, only the "high flow" base value of 10/10/9 was used, and at each temperature the EDTE flow rate was set to be the minimum flow required to stabilize the sample temperature. These spectra are show in red in Figure B.2. For the center packed sample, the same procedure was followed for the blue spectra shown in Figure B.2. Additionally, at low temperatures, a higher flow rate was used to demonstrate that excessive VT airflow causes the temperature inside the sample to be lower than the thermocouple is reporting. These spectra are shown in green. For the center packed sample, a series of spectra at the "low flow" setting of 6/6/7 was also acquired, which are shown in black in Figure B.2.

For the non-center packed sample, the ^{207}Pb spectra at most temperatures show an obvious distribution of chemical shifts due to the loose packing of the $Pb(NO_3)_2$ powder and a temperature gradient within the sample. The high flow spectra for the center packed sample also show a downfield shift relative to the low flow spectra at 313 K, indicating the temperature inside the sample is actually higher than that measured by the thermocouple. At low temperature, the sample also shows a large distribution of temperatures. These are fit separately in Figure B.3 to demonstrate the difference in slope.

Figure B.3 shows the ^{207}Pb chemical shift as a function of temperature for (a) the non-center packed sample, (b) the center packed sample at high flow and the (c) the center packed sample at low flow. For the non-center packed sample (Figure B.3a), the slope of 0.81 ppm/K deviates significantly from the theoretical value of 0.753 ppm/K. This indicates that the sample temperature is significantly different from the stator thermocouple reading. Additionally, at the lowest temperatures (263 -243 K), a second peak can be plotted and fit. The slope for the second peak is 1.28 ppm/K, indicating that a portion of the non-centerpacked sample is at a much lower temperature than the thermocouple is reading. The temperature distribution of the non-center packed sample at 243 K is greater than 7 K.

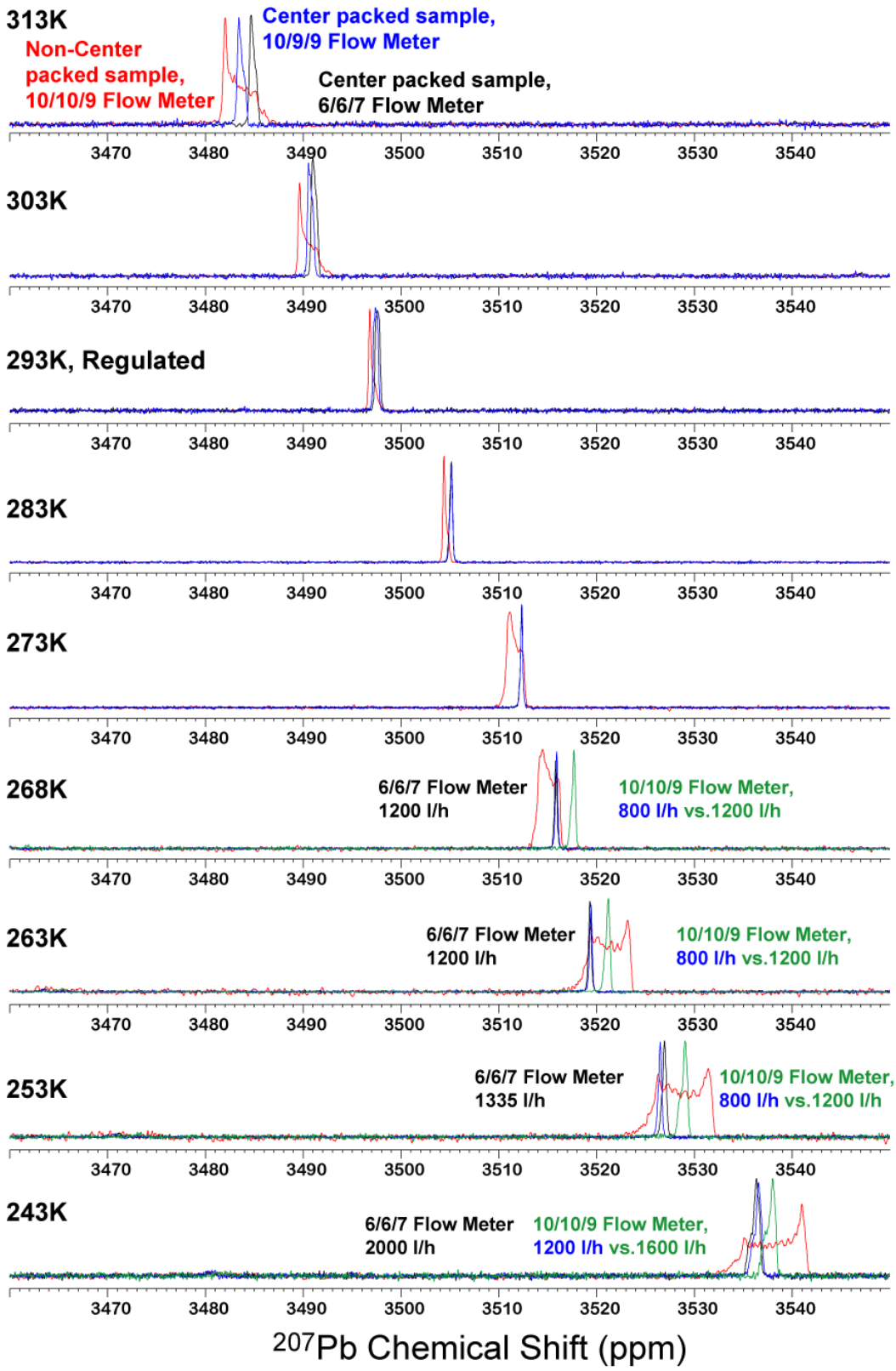

Figure B.2. Variable temperature ^{207}Pb solid-state NMR spectra of $Pb(NO_3)_2$ at 7 kHz spinning speed.

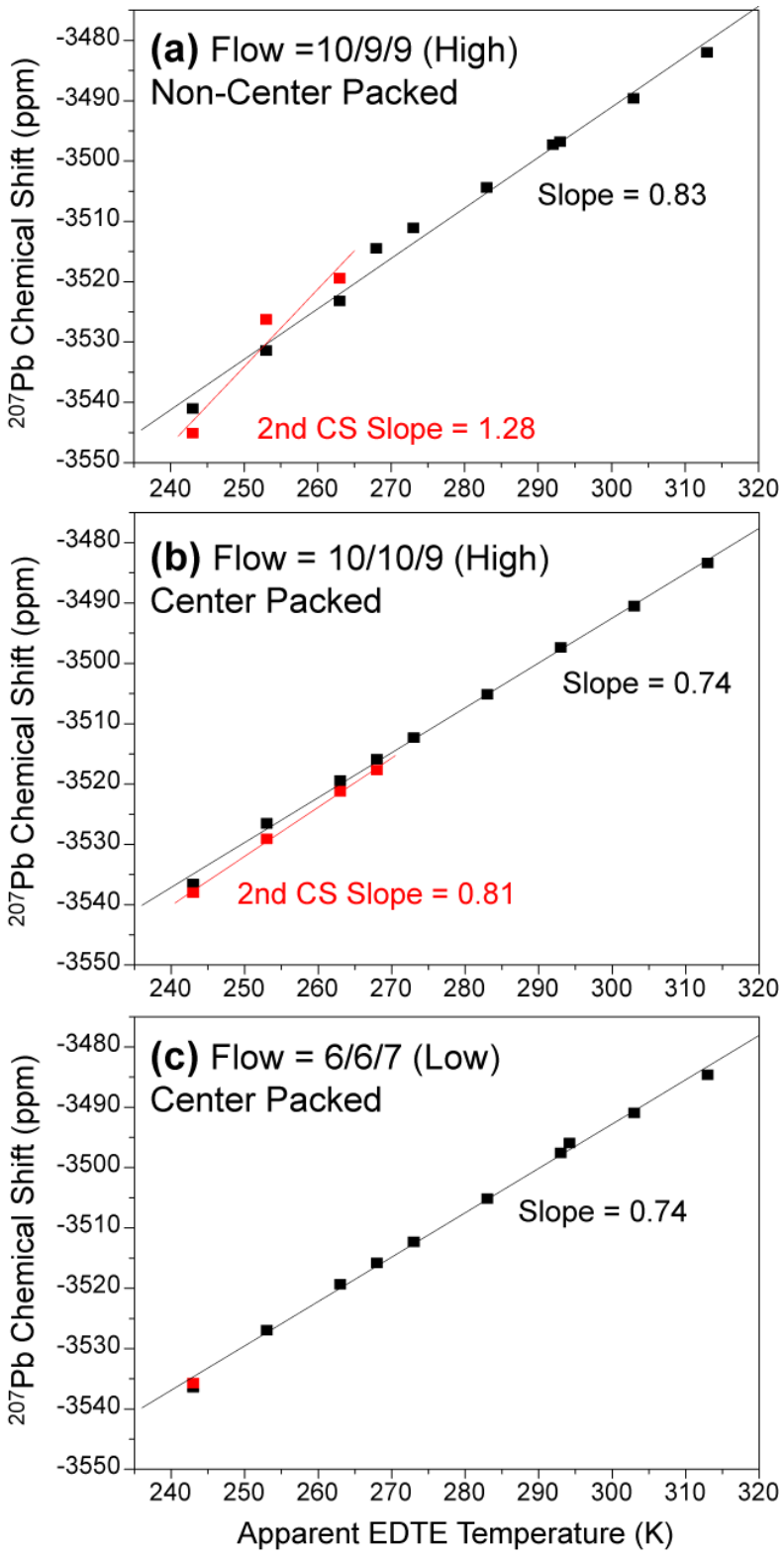

Figure B.3. Variable temperature $Pb(NO_3)_2$ chemical shift as a function of apparent temperature.

This temperature distribution is calculated by taking the difference in chemical shift of the most upfield and most downfield points of the spectrum, and may be slightly larger depending on the chemical shift values.

Both high and low flow temperature series for the center packed sample (Figures B.3b and c) show a slope of 0.74 ppm/K, which is close to the theoretical value of 0.753 ppm/K. This indicates that the thermocouple in the stator is reading a temperature very close to the actual temperature inside the rotor. Our slope measurement of 0.74 ppm/K means that the temperature reading over 100 K range may vary up to 1.3 K from the actual sample temperature. Since we typically measure samples within a 70 K range, this effect is minimal. When a higher flow rate for the VT air is used for the center packed sample, the internal sample temperature is lower than the thermocouple reading, by about 1.9 K at the lowest temperature of 243 K. Thus it is important to use the minimum flow require to reach the desired sample temperature.

Conclusion

This study has attempted to measure the reliability of the stator thermocouple temperature reading versus the actual temperature inside the sample rotor. We have shown through a series of ^{207}Pb NMR spectra, that a center packed sample shows good temperature homogeneity throughout the rotor. We have also shown that using a high flow of VT air can cause temperature gradients throughout the sample. When very high flows are used, we measure up to 1.9 K deviation from the thermocouple reading. Thus, it is important to take these factors into consideration when conducting a series of variable temperature experiments, especially when relaxation data is extracted from the temperature series.

References

1. Stringer, J. A., Bronnimann, C. E., Mullen, C. G., Zhou, D. H. H., Stellfox, S. A., Li, Y., Williams, E. H., and Rienstra, C. M. (2005) Reduction of RF-induced sample heating with a scroll coil resonator structure for solid-state NMR probes, *Journal of Magnetic Resonance 173*, 40-48.
2. Bielecki, A., and Burum, D. P. (1995) Temperature-Dependence of Pb-207 Mas Spectra of Solid Lead Nitrate - an Accurate, Sensitive Thermometer for Variable-Temperature Mas, *Journal of Magnetic Resonance Series A 116*, 215-220.
3. Lutz, O., and Nolle, A. (1980) Nuclear Magnetic Shielding Tensors of Pb-207(2+) in Pb(NO3)2, *Z Phys. B Con. Mat. 36*, 323-328.

Appendix C

Sample Dialysis and Transfer of Hydrated Lipid Gels via Centrifugation

Introduction

This appendix will summarize the preparation, ultracentrifugation and transfer of hydrated liposome pellets containing hydrophobic peptides for solid-state NMR experiments. The focus of this work has been the M2 transmembrane peptide (M2TMP) of the influenza A virus, thus the preparation method detailed here is geared towards the incorporation of hydrophobic transmembrane peptides into lipid vesicles.

Buffer Preparation

All samples prepared for the work included in this dissertation have been studied at a neutral pH of 7.0-7.5. The preparation included here will produce a buffer in this range. If the pH is to be much above or below this range, change the buffer precursors accordingly to obtain proper pH and buffering capacity.

This buffer recipe will produce 100 mM phosphate buffer with 10 mM EDTA and 0.1 mM NaN_3. This buffer is ten times the concentration used in dialysis. To prepare the final buffer, use 100 mL of the concentrated buffer and dilute to 1 L with distilled/deionized water. Finally, adjust the pH of the dilute buffer with a small amount (generally 2-5 mL) of 1 M NaOH or HCl to obtain the desired pH.

The phopsphate ions serve as the buffering medium, whereas EDTA is a water softener to prevent heavy metals from binding to the sample, and NaN_3 is used as a protease killer to ensure the sample is not contaminated with bacteria from the air or other surfaces. Weigh out all buffer reagents and add directly to a 1 L bottle, and add 1 L of distilled/deionized water and mix or shake until all reagents are dissolved.

Buffer Reagents:

Na_2HPO_4, sodium hydrogen phosphate, approximately 11.9 g

NaH_2PO_4, sodium dihydrogen phosphate, approximately 4.1 g

EDTA, ethylenediaminetetraacetic acid, approximately 3.7 g

NaN_3, sodium azide, approximately 0.065 g

Sample Preparation and Dialysis

All samples prepared for the work included in this dissertation include only a single lipid such as DLPC, POPC or DMPC. Other preparations, including the viral membrane mixing, are covered elsewhere (*1*). Most samples were prepared with a molar ratio of 1 peptide to 15 lipids. The detergent dialysis protocol is covered in the group literature (*2*), but will be expanded upon here with additional notes and pictures.

The lipid vesicle solution is prepared by suspending dry lipid powder in 1 mL phosphate buffer (10 mM Na_2HPO_4/NaH_2PO_4, 1 mM EDTA, 0.01 mM NaN_3) at pH 7.5, vortexing and freeze-thawing 6 times to create uniform vesicles (*3*). M2TMP is dissolved in octyl-β-D-glucopyranoside (OG) in 2 mL phosphate buffer, and then mixed with an equal volume of lipid vesicles. Typically 30 mg of OG is used to solvate 5-6 mg of M2TMP. The final solution of lipid, peptide and detergent is vortexed for 1 hr and allowed to stand for 6-8 hrs at room temperature. At this point, a length of dialysis tubing should be prepared by soaking 4-5" of tube in the dialysis buffer. After the bag has been hydrated, use a tube clip to close one of the ends (Figure C.1). The sample mixture can now be added to the dialysis tubing using the 1 mL micropipette. Ensure that the tip of the micropipette is inside of the bag before releasing the solution. This transfer is usually conducted with a large weigh boat set under the dialysis tube to catch any spillage. Rinse the vial 2-3 times with small aliquots of buffer to ensure complete transfer. If possible, the final solution volume should be approximately 3-3.5 mL so that the entire volume can be contained in one ultracentrifuge tube. Clip the other end of the dialysis tube, leaving some air space in the tube. The solution is dialyzed with a 3.5 kDa cutoff against 1 L phosphate buffer at 4 °C for 3 days with buffer

changes every 8-12 hrs to ensure complete removal of the detergent. After dialysis, the sample is transferred again with the 1 mL micropipette directly to a 4 mL ultracentrifuge tube. Rinse the dialysis bag with 2-3 small aliquots of clean buffer, and fill any remaining headspace in the ultracentrifuge tube with buffer until only 2-3 mm remain at the top of the tube. The dialyzed peptide-lipid solution is centrifuged at 150,000 g (55,000 rpm) and 4 °C to give a pellet containing ~50 wt% water.

Figure C.1. Dialysis tube filled with a solution, and clipped on both ends with tube clips (*4*).

Sample Transfer via Ultracentrifugation

Previously, hydrated liposome samples were packed into the rotor by scraping the pellet out of the ultracentrifuge tube. However, this transfer method could be inconvenient and lossy at times. The ultracentrifugation method was originally developed to transfer microcrystalline proteins. Advantages of this method are that there is less sample stuck to centrifuge tube walls and packing tools. Transfer can be difficult if the sample is too dry, as it will stick to the sides of pipette tips, or if the sample is too wet it can overspill the rotor. In previous experience, this transfer method does not work well for viral membrane samples. Additionally, if KEL-F rotor insert is being used, one can only have 35-40 mg total size sample.

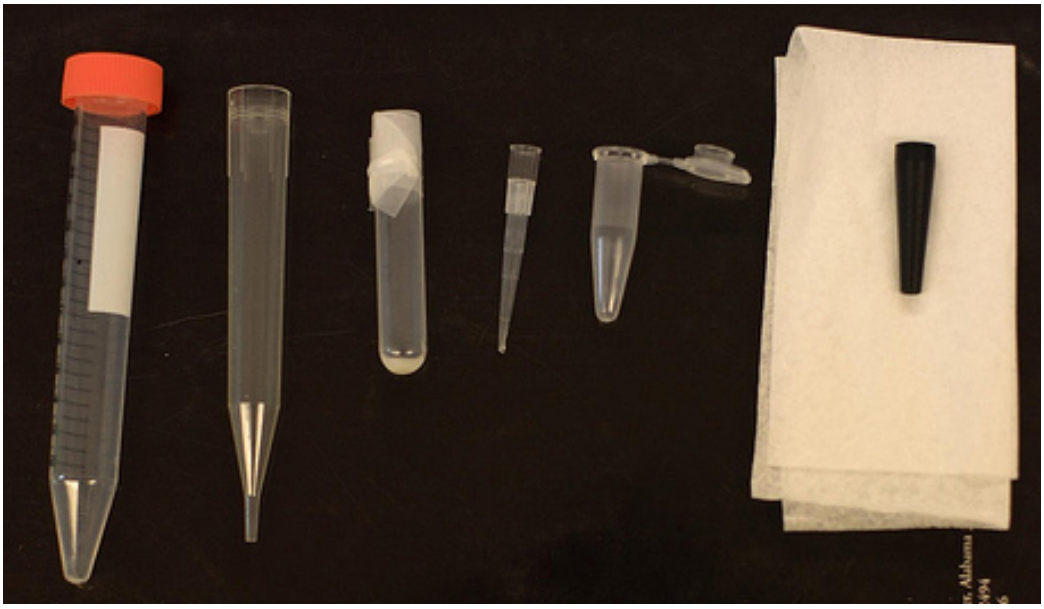

Figure C.2: Equipment required from left to right: 15 mL centrifuge tube, 5 mL pipette tip, 4 mL ultracentrifuge tube (with pellet sample at bottom), 200 uL **flame-sealed** pipette tip, 1.5 mL Eppendorf tube, rotor-holding funnel, rotor or rotor insert (not pictured).

Figure C.2 displays the equipment required for the centrifugation sample transfer. The Iowa State University Machine Shop manufactured the funnel pictured at far right especially for our group. Also, the 200 μL pipette tip has been flame-sealed by briefly dragging the pipette tip across a Bunsen burner flame.

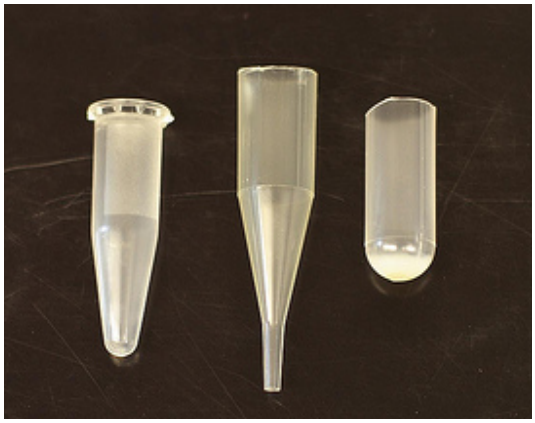

Figure C.3: Eppendorf tube with cap clipped, 5 mL pipette tip cut to approximately 2" in length and ultracentrifuge tube cut to approximately 1".

Figure C.3 shows how to trim the Eppendorf tube, the 5 mL pipette tip and ultracentrifuge tube so that the pieces will fit into the 15 mL orange cap centrifuge tube. Figure C.4 shows the final assembly: the clipped ultracentrifuge tube fits into the 5 mL pipette tip, which fits into the 200 µL flame-sealed pipette tip. The entire assembly is inserted into the black funnel and rests in the clipped Eppendorf tube. It is important to clip the 5 mL pipette tip and the ultracentrifuge tube such that the final assembly is not too tall to fit into the orange cap tube. Weigh the sealed pipette tip before transfer

Figure C.4: Sample transfer assembly. (a) Clipped ultracentrifuge tube fits into clipped 5 mL pipette tip, which rests in 200 µL flame-sealed pipette tip and black funnel. The entire assembly rests in the Eppendorf tube with cap removed. (b) The assembly needs to fit inside a 15 mL orange cap tube.

The final assembly pictured in figure C.4b is then centrifuged for 2-3 minutes, or until the pellet has transferred into the sealed pipette tip. At this point, weigh the pipette tip to ensure that most of the sample has been transferred, and calculate sample transfer efficiency.

If the pellet is too heavy for packing, the sample can be dried slightly through lyophilization or in the dessicator. Drug can also be added to the peptide sample at this point.

Figure C.5: Liposome sample that has been transferred to a sealed pipette tip.

At this point, the 5 mL pipette tip and ultracentrifuge tube can be discarded if the entire sample has been spun down. Weigh a rotor with insert (if using). The black funnel is engineered such that the pipette tip will fit at the top, and the rotor can be inserted in the bottom. The rotor can be placed at the bottom of the Eppendorf tube and the pipette tip can be clipped and placed back in the black funnel and slipped over the rotor. Spin down the sample for another 2-3 minutes to transfer into the rotor. Weigh the rotor and calculate transfer efficiency. Typically 85-90% of the sample is transferred.

Troubleshooting

- Occasionally the pellet will be too dry after ultracentrifugation. A uniform and well-hydrated pellet is much easier to transfer. Clip the ultracentrifuge tube to 1" and add 5-10 μL of H_2O to the pellet. Wrap in Parafilm and allow to sit in the incubator at 30-35 °C for 12-24 hours.

- If the rotor gets too full, it may prevent the entire sample from spinning out of the clipped pipette tip. If this happens, wrap the pipette tip with a thin layer of Parafilm near the top where it rests in the black funnel. This should elevate the tip enough such that the sample will be able to spin into the rotor.
- If residual sample is stuck to the sides of any of the transfer tubes, the residue can be washed into an Eppendorf tube or sealed pipette tip and lyophilized to dryness. The resultant powder can be rehydrated and added to the rotor.

References

1. Luo, W., Cady, S. D., and Hong, M. (2009) Immobilization of the Influenza A M2 Transmembrane Peptide in Virus-Envelope Mimetic Lipid Membranes: A Solid-State NMR Investigation, *Biochemistry 48*, 6361-6368.
2. Luo, W., and Hong, M. (2006) Determination of the oligomeric number and intermolecular distances of membrane protein assemblies by anisotropic 1H-driven spin diffusion NMR spectroscopy, *J. Am. Chem. Soc. 128*, 7242-7251.
3. Traikia, M., Warschawski, D. E., Recouvreur, M., Cartaud, J., and Devaux, P. F. (2000) Formation of unilamellar vesicles by repetitive freeze-thaw cycles: characterization by electron microscopy and 31P-nuclear magnetic resonance, *Eur. Biophys. J. 29*, 184-195.
4. Littrel, M. (2009) Closing a dialysis tube with a clip., *Washington University Chemistry Website*.